Modelling the mechanisms of dynamic cerebral autoregulation and cerebrovascular reactivity in the human brain

by

Natali van Zijl

Thesis submitted for the degree
of
Doctor of Philosophy
in the Department of Engineering Science
at the University of Oxford

Supervisors:
Prof. Stephen Payne & Prof. Daniel Bulte

March 2025

Abstract

Healthy cerebral blood flow (CBF) control is vital to maintain sufficient oxygen perfusion to brain tissue and prevent brain damage. CBF is therefore controlled by, amongst others, two main global mechanisms: dynamic cerebral autoregulation (dCA), that responds to changes in arterial blood pressure (ABP) to keep steady state CBF near constant, and dynamic cerebrovascular reactivity (dCVR) that responds to vasoactive substances such as CO_2. However, CBF control is impaired in a range of cerebrovascular diseases, including stroke and dementia, and treatments are limited by the lack of understanding of the underlying mechanisms of dCA and dCVR.

This thesis investigated the mechanisms that govern dCA and dCVR by combining physiological modelling with time series analysis under different physiological conditions. Simple physiological models of the CBF mechanisms were developed and model parameters were optimised with experimentally-derived impulse responses (IRs). dCA was investigated by representing its myogenic and metabolic responses each by a gain and time constant in a physiological model, to disentangle their contributions. Parameters were optimised with a dataset where CBF was represented by cerebral blood velocity (CBv) measured with transcranial Doppler ultrasonography (TCD) under different physiological conditions, where normocapnia and thigh cuff conditions represented intact dCA and hypercapnia represented impaired dCA. Both the myogenic and metabolic responses were found to be impaired (p-values < 0.001) and the metabolic response to be specifically slowed down (p-values < 0.001) in hypercapnia.

dCVR was investigated by representing the vasculature's response to changes in CO_2 by a gain and two time constants in a physiological model. The model produced the

CO_2-flow IR shape most commonly reported in previous data-driven literature, an improvement on models that include the effects of CO_2 with only one time constant. Model parameters were optimised with the TCD dataset under normocapnia and hypercapnia, and one dCVR time constant was found to be significantly affected by physiological condition (p-values < 0.001, except one analysis where p-value < 0.05), becoming smaller in hypercapnia compared to normocapnia. Potential sex-specific effects on the gain (p-value < 0.05) and time constants (p-values < 0.001) were also found. The dCVR model was expanded for use with a dataset where CBF was represented by blood-oxygen-level-data (BOLD) measured with functional magnetic resonance imagining (fMRI). A group comparison was performed between postpartum women and controls but significant differences were not found in the brain regions investigated in this thesis. Brain region was, however, found to significantly affect all model parameters (p-values < 0.001), highlighting the spatial heterogeneity of dCVR and motivating application of the dCVR physiological model with BOLD-fMRI data.

The results of this thesis contribute to the understanding of the complexities of dCA and dCVR and how they are affected under different physiological conditions. For dCA, specific mechanisms could be investigated, and for dCVR, a first link between the growing body of data-driven dCVR studies and its underlying physiology was presented, using both TCD data, as is typical for the dCA community, and BOLD-fMRI data, which is typical for the dCVR community.

Acknowledgements

Thank you, thank you, thank you. My DPhil has been far from a smooth journey, and it is with a grateful heart that I am writing this last piece of my thesis. First and foremost, thank you to my supervisors: Stephen Payne, for your calm, steady support from beginning to end, and Daniel Bulte, for reminding me of the joy to be found in discovering the intricacies of human physiology. I would also like to thank my research group for fostering a curious, supportive environment, where I always felt comfortable asking questions and giving my input. I am immensely grateful to the Rhodes Trust, and especially Mary Eaton, for your unwavering support (financial and otherwise) in making my dream of pursuing a PhD come true.

I express my sincere gratitude to all of the academics who helped me along the way. Thank you to Abhirup Banerjee for helping me with my statistical analysis and your encouragement over many cups of tea. Thank you to David Simpson and Tony Birch for letting me use your data, as well as your insightful comments on my work. Thank you to Joana Pinto for letting me use your data, your expert help crafting abstracts and applications, and your eagerness to help in any way possible.

Then to my community here in Oxford - thank you for welcoming me into your homes and hearts. Thank you to Helene-Mari and Koot, for your mentorship and support in and out of academia. Thank you to the friends I’ve made at Oxford Community Church, for being my home away from home. A special thank you goes to Hannah, for your intentional friendship and support in the big things and the small things. A big thank you also goes to the women of the Oxford University Water Polo Club, for welcoming me to a new sport when I did not know if I would be able to play sport again.

To my dear friends and family back home - thank you for the long phone calls and the quality time during my visits to South Africa. I always felt so loved and supported, even from a continent away. A special thank you to Megan and Nicole, for the consistent check-ins to talk about both serious and everyday things. Then to my mom - thank you for your tireless support and for listening to all of my concerns; I do not think it is possible to pray more prayers than you did these last few years. To my dad - thank you for being my academic role model and for always making time for me when I needed help. To my husband, Kyle - thank you for being my rock, for moving to Oxford with me, and for your steadfast confidence in me. You made this possible.

Most of all, thank you to God, for teaching me to walk with You in between the miracles.

Publications and conferences

Journal papers

1. **van Zijl, N.**, Banerjee, A., Payne, S.J. 2024. Modeling the mechanisms of non-neurogenic dynamic cerebral autoregulation. IEEE Transactions on Biomedical Engineering. DOI: 10.1109/TBME.2024.3463873.
2. **van Zijl, N.**, Bulte, D.P., Payne, S.J. 2024. Quantifying dynamic cerebrovascular reactivity under different physiological conditions. IEEE Transactions on Biomedical Engineering. (Under review)

Conference presentations

1. **van Zijl, N.**, Payne, S.J. Identifying the different mechanisms that govern dynamic cerebral autoregulation. Computational & Mathematical Biomedical Engineering (CMBE) 2022 Proceedings Vol. 2. June 29, 2022. (Oral)
2. **van Zijl, N.**, Payne, S.J. Identifying the mechanisms that govern cerebral autoregulation. The 9th World Congress of Biomechanics. July 10-14, 2022, Taipei, Taiwan. (Oral)
    - Best Paper Award (Honourable Mention)
3. **van Zijl, N.**, Banerjee, A., Payne, S.J. Identifying the mechanisms of intact and impaired dynamic cerebral autoregulation. The 31st International Symposium on Cerebral Blood Flow and Metabolism. June 12-15, 2023, Brisbane, Australia. (Poster)
4. **van Zijl, N.**, Bulte, D.P., Payne, S.J. A model of dynamic cerebrovascular reactivity. BioMedEng24. September 5-6, 2024, London, United Kingdom. (Poster)
5. **van Zijl, N.**, Pinto, J., Payne, S.J., Bulte, D.P. Modeling dynamic cerebrovascular reactivity in the postpartum period using BOLD-fMRI. Organization for Human Brain Mapping Annual meeting. June 24-28, 2025, Brisbane, Australia. (Accepted)

Table of contents

Nomenclature

Symbols		
b_j	-	Basis function number j
C_a	ml/mmHg	Compliance of small (regulating) arteries
C_c	ml/mmHg	Compliance of capillaries
c_j	-	Expansion coefficient for basis function number j
C_v	ml/mmHg	Compliance of veins
f_r	-	Regulating compartment resistance fraction
f_v	-	Venous compartment resistance fraction
G_a	-	dCVR gain, active in small arteries
h_{CO2}	-	CO_2-flow IR
h_p	-	Pressure-flow IR
M	-	System memory
$\overline{p_i}$	mmHg	Baseline intramural pressure
p	-	Model order
$\overline{P_a}$	mmHg	Baseline ABP
ΔP_a^*		Perturbation from baseline ABP as a fraction of baseline ABP
$P_{a,co2}$	mmHg	Arterial CO_2 partial pressure
$\overline{P}_{a,co2}$	mmHg	Baseline arterial CO_2 partial pressure
$\overline{P_c}$	mmHg	Baseline critical closing pressure
P_{ic}	mmHg	Intracranial pressure
P_v	mmHg	Pressure of large veins
P_1	mmHg	Pressure of small (regulating) arteries
P_2	mmHg	Pressure of capillaries
P_3	mmHg	Pressure of small veins
Δq^*		Perturbation from baseline flowrate as a fraction of baseline flowrate
q_{la}	ml/s	Flowrate in large arteries
Δq_{la}^*	-	Perturbation from baseline flowrate as a fraction of baseline flowrate in large arteries
R_c	mmHg s/ml	Resistance of capillaries
R_{la}	mmHg s/ml	Resistance of large (non-regulating) arteries
R_{lv}	mmHg s/ml	Resistance of large veins
R_{sa}	mmHg s/ml	Resistance of small (regulating) arteries

Symbols		
R_{sv}	mmHg s/ml	Resistance of small veins
S_E		Elastic sensitivity coefficient
S_M		Myogenic sensitivity coefficient
S_V		Metabolic sensitivity coefficient
SD		Standard deviation
V_a	ml	Total arterial volume
V_c	ml	Volume of capillaries
V_{la}	ml	Volume of large (non-regulating) arteries
V_{sa}	ml	Volume of small (regulating) arteries
V_v	ml	Volume of veins
α		Exponential decay parameter
λ		Box Cox transformation parameter
τ_M	s	Myogenic time constant
τ_V	s	Metabolic time constant

Abbreviations and acronyms	
ABP	Arterial blood pressure
ACAs	Anterior cerebral arteries
ACoA	Anterior communicating artery
AIC	Akaike Information Criterion
ANOVA	Analysis of variance
ARI	Autoregulation index
BIC	Bayesian Information Criterion
BOLD	Blood-oxygen-level-dependent
CA	Cerebral autoregulation
CARNet	Cerebrovascular Research Network
CBF	Cerebral blood flow
CBFV	Cerebral blood flow velocity
CBv	Cerebral blood velocity
CBV	Cerebral blood volume
CO_2	Carbon dioxide
CPP	Cerebral perfusion pressure
CrCP	Critical closing pressure
CSF	Cerebral spinal fluid
CT	Computed tomography
CVR	Cerebrovascular reactivity

Abbreviations and acronyms	
dCA	Dynamic cerebral autoregulation
dCVR	Dynamic cerebrovascular reactivity
DVM	Discrete Volterra model
EEs	Elementary effects
FFT	Fast Fourier transform
fMRI	Functional magnetic resonance imaging
FO	First order
FOTD	First order time delay
GE-EPI	Gradient echo echo-planar imaging
ICAs	Internal carotid arteries
ICP	Intracranial pressure
IR	Impulse response
IR_{init}	Initial value of the impulse response
LLA	Lower limit of autoregulation
MCA	Middle cerebral artery
MISO	Multiple-input-single-output
ML	Machine learning
MNI	Montreal Neurological Institute
MP-RAGE	Magnetization prepared - rapid gradient echo
MRI	Magnetic resonance imaging
m/v	Multivariate
NMSEs	Normalised mean squared error
NVC	Neurovascular coupling
$PaCO_2$	Arterial partial pressure of CO_2
PCoAs	Posterior communicating arteries
PCAs	Posterior cerebral arteries
PDM	Principal dynamic modes
$PetCO_2$	End-tidal partial pressure of CO_2
ROR	Rate of regulation
RS	Resting state
SISO	Single-input-single-output
SNR	Signal-to-noise ratio
SO	Second order
SOTD	Second order time delay
sCA	Static cerebral autoregulation

Abbreviations and acronyms	
SD	Standard deviation
SF	Sampling frequency
SR	Step response
SSE	Sum of squared errors
SVD	Singular value decomposition
TCD	Transcranial Doppler ultrasound
TE	Echo time
TFA	Transfer function analysis
TR	Repetition time
ULA	Upper limit of autoregulation
u/v	Univariate
VAs	Vertebral arteries

CHAPTER 1

Introduction

This thesis investigates the mechanisms of dynamic cerebral autoregulation (dCA) and dynamic cerebrovascular reactivity (dCVR) by combining physiological and data-driven modelling.

1.1.Background

The brain is an important, complex, and major energy-consuming organ in the human body. Despite representing only 2-3% of body mass, it accounts for 20% of metabolism and 14% of blood flow [1]. This tight link between cerebral metabolism and cerebral blood flow (CBF) is because the brain has limited capacity to store the oxygen and nutrients it needs to function, so it relies on CBF to provide a sufficient and continuous supply – to the extent that an interruption in CBF can lead to brain cell death within minutes [2].

Maintaining sufficient blood flow to the brain is therefore vital for brain health. Fortunately, the human body has a group of built-in, overlapping mechanisms that collectively act to control CBF so that sufficient oxygen and nutrients are continuously delivered to brain tissue [3]. Two of these mechanisms are global in nature, responding to changes in the systemic circulation: cerebral autoregulation (CA) and cerebrovascular reactivity (CVR). CA acts in response to changes in arterial blood pressure (ABP) in order to maintain steady state CBF near constant, and can do so successfully over an ABP range of approximately ±50% change from baseline [3]. CVR acts in response to vasoactive substances such as carbon dioxide (CO_2) in the blood, regulating both CBF to match local metabolic demand and pH around functional brain tissue to maintain homeostasis [4].

Unsurprisingly, impaired CA and/or CVR has been implicated in a range of cerebrovascular diseases, including stroke [5], hypotension [6], vascular occlusions [7], and dementia [8] – leading causes of death and disability worldwide [9]. Important insights into such pathological conditions in the brain, e.g., stroke type and location, can be gained via imaging techniques such as computed tomography (CT) and magnetic resonance imaging (MRI) – but they are limited by resolution. For example, MRI can achieve voxel sizes as small as 1 mm but blood vessels in the cerebral vasculature have diameters in the order of μm, with the average diameter of a capillary being 6 μm.

Modelling and computational techniques are therefore valuable to "fill the gaps" that imagining techniques cannot see. Furthermore, CBF control refers to the relationships between CBF and other variables such as CO_2 and ABP, so direct measurements themselves cannot provide assessment of CVR or CA. Some form of modelling or analysis is required to provide insights into the state of CA in health and disease. The quantitative approach of modelling is specifically valuable to help identify quantitative metrics and so set clinical guidelines.

CA has been assessed using both physiological models and data-based analysis techniques. Studies first focussed on the steady state response of CA, termed static CA (sCA), mostly due to temporal resolution limitations in measurements. This research was valuable nonetheless, and yielded the Lassen curve that shows how steady state CBF measurements remain relatively constant over a range of steady state ABP measurements. Later, the development of transcranial Doppler ultrasonography (TCD) allowed cerebral blood velocity (CBv) to be measured at a high temporal resolution, which opened up investigations into the temporal aspects of CA, leading to the term dCA.

However, most dCA studies have aimed at assessing dCA as a whole and determining whether dCA as a whole is intact or impaired. Some physiological models have attempted to model detailed pathways of dCA, but such detailed models require large amounts of parameters, making it difficult or impossible to validate them with experimental data. The underlying mechanisms that contribute to dCA are therefore still poorly understood in both physiological and pathophysiological conditions – which prohibits the development of informed and targeted clinical treatments. For example, in patients with high blood pressure and impaired dCA, it remains unclear whether blood pressure lowering medications would be beneficial or have severe CBF implications [10].

CVR has mostly been assessed using data-driven approaches. Most often, the steady state response, termed static CVR (sCVR), is determined as the ratio between measured changes in CBv and expired CO_2 in response to a breath-hold. sCVR has been assessed in clinical practice to evaluate cerebrovascular function in patients with carotid artery stenosis [11], hypertension [12], stroke [13], and heart failure [14], and a related impairment has been linked to cerebral ischemic events [13].

Although some earlier studies have estimated a CVR delay, the term dCVR was only introduced in 2019 [15], and most dCVR studies have also been from a data-driven perspective. By their nature, these data-driven studies cannot give insights into the underlying mechanisms of dCVR. The effects of CO_2 have been included in physiological models, but typically as a simple first order model to account for a confounding effect during investigation of dCA instead of investigation of dCVR itself. The mechanisms underlying dCVR, despite their clear relevance to cerebrovascular health, therefore remain poorly understood under both physiological and pathophysiological conditions.

1.2.Aim and objectives

The aim of this thesis is to investigate the mechanisms of dynamic CBF control by combining physiological and data-driven modelling approaches. Specifically, the two main global mechanisms of CBF control, dCA and dCVR, are investigated. This aim is achieved by addressing the following objectives:

1. Investigate the mechanisms of dCA under different physiological conditions by combining physiological modelling TCD with time series analysis.
2. Investigate the mechanisms of dCVR under different physiological conditions by combining physiological modelling with TCD time series analysis.
3. Investigate the mechanisms of dCVR under different physiological conditions by combining physiological modelling with time series analysis of data from a second modality: blood-oxygen-level-dependent (BOLD) data from functional MRI (fMRI).

The first objective is addressed in Chapter 3, the second objective is addressed in Chapter 4, and the third objective is addressed in Chapter 5.

1.3.Research scope

This thesis is focussed on the two main global CBF control mechanisms: CA and CVR. The scope of this thesis is limited to these two global CBF control mechanisms, therefore excluding local CBF control mechanisms such as neurovascular coupling (NVC). Furthermore, CA and CVR are investigated in terms of their dynamic components, dCA and dCVR, in this thesis, therefore excluding consideration of sCA and sCVR. Lastly, the scope of this thesis is limited to modelling dCA and dCVR in humans, not animals.

1.4.Thesis organisation

This thesis is organised as follows: Chapter 2 is a literature review that provides an overview of the physiology of the cerebral vasculature and CBF control, focussing on dCA and dCVR, and the current state of the art of measurements, physiological models, and data-based analysis of dCA and dCVR. Chapter 3 focusses on dCA, separating out two of its underlying mechanisms by combining a physiological model and transfer function analysis (TFA) of a TCD dataset under different physiological conditions.

Chapter 4 shifts the focus to dCVR, presenting a physiological model of dCVR that produces the CO_2-flow impulse response (IR) shape found in most previous studies and using it in conjunction with a TCD dataset under different physiological conditions. Chapter 5 expands the dCVR model for use with BOLD-fMRI data and performs a group comparison between postpartum women and controls on brain hemisphere and brain region levels.

Finally, Chapter 6 summarises and discusses the thesis' findings along with the limitations, and presents avenues for future work to build on the findings of this thesis. All the work presented in this thesis was done by the author (NvZ) unless specifically stated otherwise.

CHAPTER 2

Literature review

2.1.Cerebral vasculature

The brain has limited nutrient storage capacity, so it requires blood flow to provide a sufficient and continuous supply of oxygen and other nutrients to meet its metabolic demand. This blood flow is supplied to the brain via an interconnected system of blood vessels that penetrate to every part of the brain, termed the cerebral vasculature and partially shown in Figure 2.1.

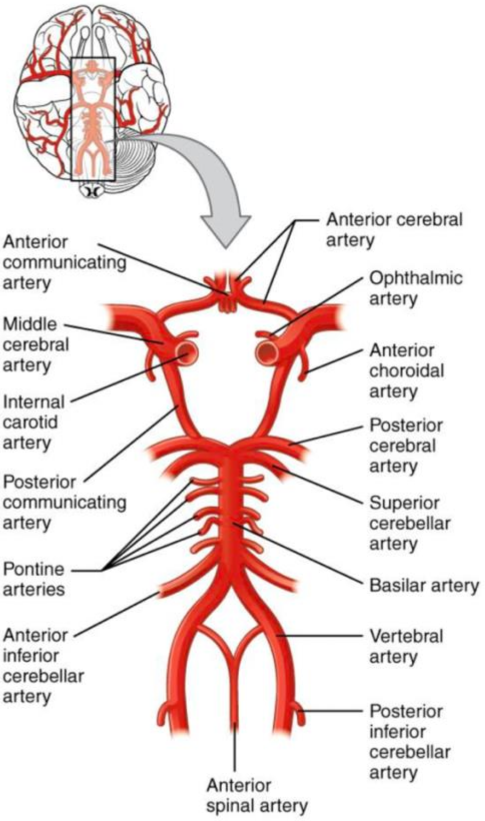

Figure 2.1. Major arteries in the cerebral vasculature. Reproduced without change from OpenStax College [16] under license http://creativecommons.org/licenses/by/3.0/.

Four large arteries enter the brain: the left and right internal carotid arteries (ICAs) from the front, and the left and right vertebral arteries (VAs) from the back. These arteries then join the circle of Willis, which also includes the left and right anterior cerebral arteries (ACAs), the anterior communicating artery (ACoA), and the posterior communicating arteries (PCoAs) - allowing for collateral flow and hence continued perfusion in the presence of a blockage in a major artery. From there, six main arteries supply blood to the brain tissue: the left and right middle cerebral arteries (MCAs), the left and right ACAs, and the left and right posterior cerebral arteries (PCAs). Branching off from these arteries are many smaller arteries, arterioles, and capillaries that supply blood to all regions of the brain [17].

It should be noted that numerous studies have reported significant variations in the circle of Willis between individuals. In an early study of 350 human brains by Crossman and Neary [18] only around half (52 %) had a complete circle of Willis. The later study of 500 subjects by Papantchev *et al.* [19] corroborated this, showing that 58.6% of the subjects had some variation in the circle of Willis. Papantchev *et al.* [19] also divided the variations into different types, where the most common deviation (in 35.6% of all subjects) was found to be hypo- or aplasia of the left PCoA - meaning that the area supplied by the left MCA is at most risk of hypoperfusion.

Variation in the circle of Willis will not necessarily have a negative impact on perfusion, but it is likely to affect the response of the vasculature to any changes in blood supply. For example if there is a sudden blockage in a large blood vessel, a more complete circle of Willis could allow for greater compensation via collateral flow [20]. However, CBF control mechanisms, such as dCA and dCVR will also play a role in the response to interrupted blood flow, as is discussed further in the following section.

2.2.Cerebral blood flow control

There is a tight link between CBF and metabolism and any interruption in the supply of blood flow to the brain can lead to brain cell death within minutes [2]. It is therefore vital to maintain sufficient blood flow to the brain, so CBF is controlled by a group of overlapping mechanisms that collectively ensure sufficient oxygen and nutrient delivery to brain tissue [3]. These overlapping responses create a notable feature of CBF control, namely its redundancy that allows for robust control under challenging circumstances, an important level of protection against brain damage [21].

Ainslie and Duffin [4] categorised the different stimuli that affect CBF, all with different sensitivities and different time scales, into five categories: CO_2, cell activity, cardiac output, cerebral perfusion pressure (CPP), and nerve activity. The scope of this thesis is limited to the effects of CPP and CO_2 (see Section 1.3), which are set by the wider systemic circulation and can be termed global stimuli. The response of CBF to CPP and CO_2 is termed dCA and dCVR respectively. These global control mechanisms likely interact with the wider systemic circulation, but in dCA or dCVR studies, CPP and CO_2 are typically set as boundary conditions to assess the control mechanisms in isolation. This section provides an overview of dCA and dCVR, as well as an explanation of compliance as the manipulated variable in both mechanisms.

2.2.1.Dynamic cerebral autoregulation

CA refers to a collection of mechanisms that act collectively to maintain steady state CBF near constant despite changes in CPP. It is considered in two ways: as sCA and as dCA. The scope of this thesis is limited to dCA but sCA is also explained here to provide context for dCA. sCA refers to the steady state ABP-CBF relationship, which is measured over minutes or hours [22] [23] and is shown by the Lassen curve (Figure 2.2 (a)). The CBF response is relatively flat (i.e., has low sensitivity) over approximately ±50% changes from baseline ABP [3], and the lower limit of autoregulation (LLA) and upper limit of autoregulation (ULA) indicate the saturation points where the blood vessels are completely constricted or dilated.

dCA refers to the transient response of CBF to changes in ABP, with a time scale of seconds, and is the focus of most current research and clinical assessment of CA in patients [24]. Simultaneously taken, continuous measurements of CBF and ABP show greater variability in CBF than indicated by Lassen's curve for sCA, indicating that the speed of ABP changes has a large effect on how well CA performs. dCA can therefore be thought of as a high pass filter [25], where high frequency oscillations in the ABP signal pass on to the CBF (because CA takes too long to respond to quick changes), while low frequency oscillations are attenuated by CA, so they are not passed on as much to the CBF.

The transient response of CBF to changes in ABP exhibits biphasic behaviour: first a quick, passive response and then a slightly slower, active response (i.e., dCA) [3], as shown in Figure 2.2(b). Take the example where ABP decreases. Since blood vessel walls have compliance, a decrease in ABP leads to a decrease in vessel wall radius and hence an increase in resistance to flow, so CBF decreases in the passive response. The active response (i.e., dCA) then counters the passive response by increasing vessel radius in response to a drop in ABP. dCA restores CBF close to its original value, although there is always a slight drop in CBF when ABP decreases. Importantly, the fact that dCA must overcome the passive response means that the active response is a strong process and even small changes in its strength can yield large differences in physiological behaviour.

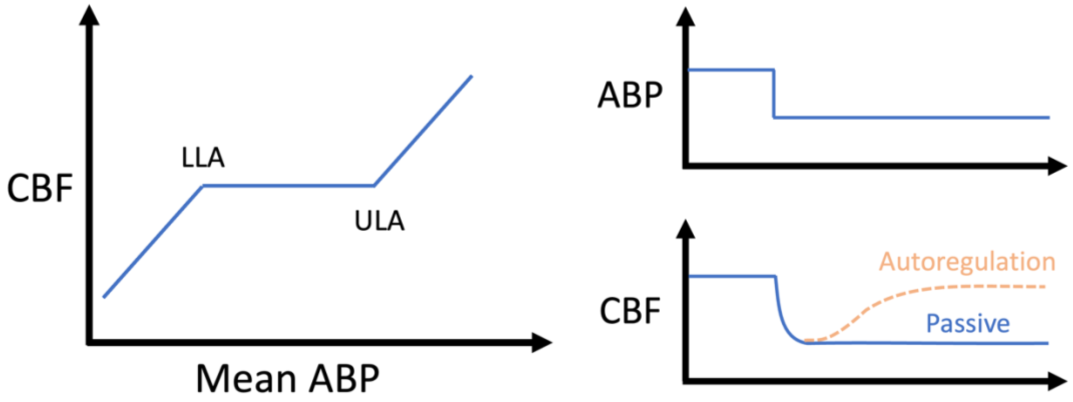

(a) (b)

Figure 2.2. (a) Lassen curve showing static cerebral autoregulation. (b) Biphasic response of CBF to a drop in ABP, adapted from cvphysiology.com. ABP: arterial blood pressure, CBF: cerebral blood flow, LLA: lower limit of autoregulation, ULA: upper limit of autoregulation.

The collection of different mechanisms that govern dCA are most commonly defined as the myogenic, metabolic, and neurogenic responses [26] [3] [27] [28], shown in Figure 2.3. dCA is therefore seen as a group of mechanisms that collectively act to control CBF, although most studies warn that these mechanisms are simplified terms for complex pathways that remain poorly understood and that they do overlap and should not be viewed as fully independent from one another. The myogenic response is driven by CPP, which acts on the cerebral vasculature to give an active response to maintain the desired CBF by overcoming the passive response. The myogenic response seems to play a dominant role in dCA during changes in ABP, but since it is not the only response involved, it has been difficult to determine its precise contribution to overall CA [21].

The metabolic response is described as a feedback system, where changes in vasoactive substances (e.g., O_2, CO_2) drive local vasodilation and so increase CBF [29]. However, it has been found that the increase in CBF after neural activity (i.e., activity that increases the metabolic demand) can exceed the current metabolic demand [30], and can even occur under conditions of abundance in glucose and O_2 [31]. This makes it unlikely that the feedback system of the metabolic response is completely responsible for the changes in CBF observed in response to neural activity; and the metabolic processes alone may be too slow to explain the fast increase in CBF after neural activity. The neurogenic response has therefore been proposed as a feedforward theory, wherein there is coupling between the local neurons and cerebral vasculature [29] - although this pathway is the most difficult to measure and therefore the most poorly understood. It is now thought that the coupling of CBF to brain activity derives from a combination of the feedback metabolic response and the feedforward neurogenic response [21].

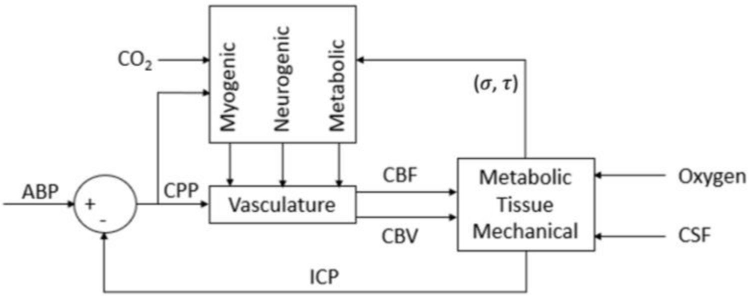

Figure 2.3. Block diagram of the main mechanisms that govern cerebral autoregulation, adapted from [26]. ABP: arterial blood pressure. CPP: cerebral perfusion pressure, CBF: cerebral blood flow, CBV: cerebral blood volume, ICP: intracranial pressure, CSF: cerebral spinal fluid, σ: direct stress on blood vessel walls, τ: shear stress on blood vessel walls. The label containing σ and τ is placed in brackets to indicate that it does not exist in the original diagram in [26] but is included here for completeness, as it represents the current school of thought regarding the variables that the mechanisms of CA may be responding to.

However, the term "cerebral autoregulation" has been taken to mean different things across different studies, encompassing more or fewer responses or mechanisms. In some studies, CA is limited to the control of CBF in response to changes in ABP (as in this thesis), while other studies expand it to the wider field of CBF control, where areas such as CVR (discussed in Section 2.2.2) and NVC are also included. This likely stems from the uncertainty around how different responses or mechanisms work together to control CBF. The recent review by Claassen *et al.* [21] discusses this uncertainty and highlights the question of whether the different pathways in CA (i.e., myogenic, metabolic, neurogenic) represent an orchestrated effort to maintain CBF constant in response to changes in ABP, or whether they constitute fail-safe mechanisms to ensure robust control. To sketch this more clearly, a hypothetical example is provided, where ABP drops and the myogenic mechanism fails to maintain CBF. In such a case, cerebral metabolism could be affected, which could prompt the metabolic mechanism to promote vasodilation to restore CBF. Due to the redundancy, it is difficult to determine whether a mechanism constitutes a primary mechanism in CA or whether it is an independent mechanism that provides redundancy due to overlapping functional effects. This motivates the use of mathematical models or data-driven approaches to aid in disentangling the contribution of each pathway to overall CA and overall CBF control.

2.2.2.Dynamic cerebrovascular reactivity

CVR refers to the ability of the cerebral vasculature to respond to changes in a vasoactive substance, typically arterial partial pressure of CO_2 ($PaCO_2$). Importantly, CO_2 is tightly coupled to pH, and increases in CO_2 are accompanied by decreases in perivascular pH (i.e., the pH in the spaces surrounding blood vessels), and it is this decrease in perivascular pH that is actually believed to affect changes in vessel compliance and hence CBF [32]. However, most studies investigate CVR by delivering and measuring CO_2 as the stimulus, as discussed in Section 2.3.2.

Similarly to CA, CVR has both static and dynamic components, termed sCVR and dCVR, and the scope of this thesis is limited to dCVR but sCVR is also described here to provide context for dCVR. sCVR refers to the steady state relationship between $PaCO_2$ and CBF, typically quantified as the ratio of changes in CBF to change in $PaCO_2$ [3]. Within the limits 20-60 mmHg $PaCO_2$, the $PaCO_2$-CBF relationship is sensitive and near-linear, with saturation limits that correspond to the limits of arterial compliance [33] [34] [35], as shown in Figure 2.4. Impaired CVR could therefore be due to inability of the vasculature to respond to changes in $PaCO_2$ (i.e., damaged vasculature) or due to a shift in baseline conditions nearer to one of the saturation limits where the vasculature has less capacity to respond.

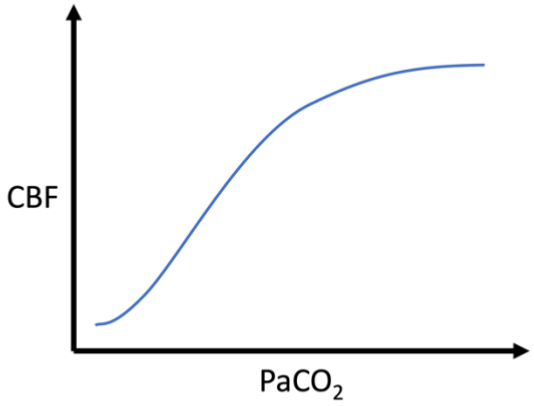

Figure 2.4. Sigmoidal curve showing static cerebrovascular reactivity. CBF: cerebral blood flow, $PaCO_2$: arterial partial pressure of carbon dioxide.

Most research to date has focussed on sCVR, e.g., [36] [37] [38]. Although they caution that there is variability in literature, Ainslie and Duffin [4] derived the average "normal" sCVR across three experimental animal studies, [39] [33] [40], and one experimental human study, [41], as around 3.8% increase in CBF for every mmHg increase in $PaCO_2$ within the $PaCO_2$ range of 35-55 mmHg. Differences between the hypercapnic and hypocapnic ranges have been found, where sCVR is higher in the former [42] [43], potentially due to larger influence of vasodilator than vasoconstrictor mediators on cerebrovascular tone [44] or a protective mechanisms to prevent cerebral ischaemia during transient drops in $PaCO_2$ that can occur in both physiological situations (e.g., exercise, postural changes) and pathophysiological states (e.g., asthma, anxiety attacks, sleep apnea) [4].

The term dCVR was introduced more recently by Prokopiou *et al.* [15], referring to the transient changes in CBF that occur in response to changes in $PaCO_2$. Recent studies, such as the study by Marmarelis *et al.* [45], also use the term, CO_2 dynamic vasomotor reactivity, to refer to dCVR. Traditionally, understanding dCVR (even before the term itself was introduced) has been mostly quantified and regressed out as "physiological noise" to aid in interpretation of the BOLD-fMRI signal (see Section 2.3.1.1) or dCA, e.g., [46], but more recent studies have found differences in dCVR between healthy and diseased states [47] [45] [48], indicating that understanding dCVR and how it is affected in different physiological and pathophysiological conditions is useful in itself. In contrast to dCA, which can be thought of as a high-pass filter (see Section 2.2.1), Peng *et al.* [46] states that dCVR appears to behave like a low-pass filter, where only low frequency oscillations in CO_2 are passed on to the CBF. It should be noted, however, that the way CO_2 content in the blood is measured is inherently limited to a low sampling frequency (SF; as explained in Section 2.3.1.3), which would limit observation of any effects of CO_2 on CBF to lower frequencies.

Notably, both sCVR and dCVR exhibit a high degree of variability across the brain [49] [50] [48]. This is revealed by the use of fMRI, where change in %BOLD is taken as a direct marker for CBF (see Section 2.3.1.1). In fact, Sobczyk *et al.* [51] illustrated the wide variety in the sigmoidal curve of sCVR in different regions of the brain within individual subjects, ranging from "normal" to "moderate" to "abnormal" responses all within the same subject. Abnormal responses may be due to the "steal" effect in some cases, where some brain regions exhibit negative sCVR, as CBF is reduced in those regions in favour of more CBF in other regions [52], although it is typically an indication of pathology. The "steal" effect is a strong independent risk factor for ischaemic stroke and occurs in regions where elderly patients typically develop white matter disease or leukoaraiosis [52] [53].

2.2.3.Compliance as the manipulated variable to control cerebral blood flow

dCA and dCVR both act to control CBF, as discussed in Section 2.2.1 and Section 2.2.2 respectively, and since they have access to the same “vascular plumbing”, both do so by manipulating the compliance of blood vessels. Compliance refers to the ability of a vessel to stretch in response to pressure and can be understood as the manipulated variable for CBF control by considering haemodynamics and Poiseuille’s law.

According to haemodynamics, blood flow is controlled by the pressure gradient and vascular resistance. Pressure gradient, however, is set by the systemic circulation (and is the disturbance variable in dCA; see Section 2.2.1), so only vascular resistance is left as a potential manipulated variable to control CBF [54] [55]. According to Poiseuille’s law [56], resistance is a function of vessel radius, vessel length and haematocrit, where haematocrit is the volume ratio of red blood cells to total blood. Vessel length and haematocrit are mostly constant with respect to time, with exceptions over long time scales, so vascular resistance and hence CBF is controlled via changes in vessel radius. This allows for fine control, since vessel resistance is inversely proportional to vessel radius to the power of four [56], meaning that small changes in radius can cause large changes in resistance and hence CBF. Vessel radius, in turn, is a function of applied pressure and vessel compliance, where applied pressure is again set by the systemic circulation (and is the disturbance variable in dCA). This leaves compliance as the manipulated variable used to control CBF [3]. Indeed, most haemodynamic models include CBF control via some form of compliance feedback response, as discussed in Section 2.4.1.

The underlying pathways by which the compliance is adjusted are outside the scope of this thesis, but briefly, compliance is adjusted by contraction or dilation of the smooth muscle cells in the vessel wall. Contraction is mostly governed by increases in intracellular calcium, which is often assumed to be related to direct stress on the vessel wall (although experimental data, e.g., [57], only supports a response to stretch of the vessel wall), and dilation by increases in nitric oxide, which can be formed in response to shear stress on the vessel wall. Traditionally, it has been assumed that this occurs only at the arteriolar level, but recently it has been debated whether pericytes at the capillary level also contribute to CBF control, although supporting evidence has not yet been observed *in vivo* in humans [58]. For more detail about the pathways underlying compliance adjustment in CBF control and potential pericyte contributions, the reader is referred to the comprehensive reviews by Claassen *et al.* [21] and Krishnamurthy *et al.* [59], and Hartmann *et al.* [58] respectively.

2.3.Measurements of dynamic cerebral autoregulation and cerebrovascular reactivity

dCA and dCVR can be assessed by simultaneous measurements of CBF and the relevant stimulant: CPP and CO_2 concentration in the blood respectively. Currently, these assessments are mostly limited to experimental research studies, although it is starting to become common practice to continuously monitor sCA (see Section 2.2.1) in patients after trauma [60]. To the best of the author’s knowledge, a simple assessment of sCVR using TCD (see Section 2.3.1.1) and a breath hold (see Section 2.3.2) is sometimes performed in a clinical setting but is not continuously monitored during any pathology.

The measurements of dCA and dCVR can be taken using a variety of different methods, each with their own advantages and limitations, and using different protocols, e.g., to induce greater variability in the signals or to investigate the effects of different physiological states. Notably, other factors also affect CBF and may act as confounding variables when trying to isolate the effects of blood pressure and CO_2, so experimental studies often measure additional variables in order to regress out their effects on CBF. For example, in dCA studies, CO_2 is often also measured, since it has such a large effect on CBF. This section provides an overview of the most commonly used methods of measuring CBF, blood pressure, and arterial CO_2, as well as typical measurement protocols for dCA and dCVR.

2.3.1.Physiological measurements

2.3.1.1. Cerebral blood flow

CBF can be measured using various techniques, including near infra-red spectroscopy, fMRI, and TCD. For a more complete summary of the different techniques available, the reader is referred to the book by Payne [27], but this discussion is limited to TCD and fMRI, as they are the most commonly used methods of measuring CBF in dCA and dCVR studies.

TCD measures the velocity of the red blood cells in the MCA, which gives a measurement of CBv (termed CBF velocity, CBFV, in older literature). The main advantage of TCD is high temporal resolution, which can be around 200 Hz, although that comes at the cost of spatial resolution [61]. It should also be highlighted that TCD measures CBv, not CBF, where knowledge of the dynamic cross-sectional area of the blood vessel is required to convert between the two. Changes in cross-sectional area are typically taken to be negligible and CBv is used as a direct marker for CBF - although the main motivation behind this is likely the difficulty in measuring small changes in vessel diameter, as there is no direct evidence either for or against it. TCD is most commonly used to quantify changes in CBF in dCA studies, e.g., [62] [63], as well as in some dCVR studies, e.g., [43] [45].

fMRI measures the BOLD signal, which relies on changes in deoxyhaemoglobin, where deoxyhaemoglobin is the protein that transports oxygen in the blood when it does not have oxygen molecules attached to it [64]. Changes in the BOLD signal are used as a surrogate for changes in CBF, although the BOLD signal is a function of both CBF and metabolism, and most studies assume a constant metabolism when a neural task is not performed [64]. The main advantage of fMRI is its good spatial resolution, which is why it is the most commonly used modality for CVR studies [65], as it can quantify regional variability of CVR (see Section 2.2.2). However, the spatial resolution comes at the cost of lower temporal resolution. BOLD-fMRI sequences can be optimised for either better spatial resolution, achieving a resolution of less than 1 mm, or better temporal resolution, achieving a resolution of 0.8 seconds, and for dCVR studies, temporal resolution is typically most important. fMRI is not typically used for CA studies, as changes in CPP are attenuated at the capillary level where the BOLD signal originates.

The modalities, TCD and fMRI, although both commonly used as surrogates for CBF, measure different things. These differences make it difficult to compare results from studies of dCA and dCVR that used different modalities, although more recent studies have shown that the information gathered from multi-modal measurements can be complementary [3]. This also motivates the development of models of dCA and dCVR that can be validated or used in conjunction with multiple modalities.

2.3.1.2. Blood pressure

ABP is typically used as a marker for CPP, as CPP is the difference between ABP and intracranial pressure (ICP; the pressure exerted by the skull on the brain) and ICP is relatively low and exhibits only small changes under normal conditions [21]. ABP is measured in dCA studies, but not typically in studies focussing on dCVR, as they mostly use the BOLD-fMRI signal as the surrogate for CBF (see Section 2.3.1.1), which originates in the capillary bed, where fluctuations in pressure and hence CPP are smaller.

ABP can be measured using invasive and non-invasive methods. Invasive methods can provide more direct and hence accurate measurements but can only be performed under limited conditions; while non-invasive methods are often more appropriate for vulnerable subjects such as stroke patients and are therefore more widely used. For dCA studies, the non-invasive Finapres device is most commonly used, as it can provide continuous ABP measurements with high temporal resolution, which can be around 200 Hz [66]. It works by applying pressure to a peripheral artery to maintain arterial blood volume constant by matching the ABP. However, it should be noted that this measurement is typically made in the finger, so its use inherently assumes that the peripheral ABP is the same in the finger and the brain, despite the distance between them. Two studies, [66], [67], have investigated the validity of using ABP measurements obtained from a Finapres device in dCA studies, and both found only small biases (which can be corrected for) in dCA indices (see Section 2.4.2) compared to the same indices determined using invasive ABP measurement methods.

2.3.1.3. Arterial carbon dioxide

The arterial concentration of CO_2 can be measured invasively or non-invasively. Invasive measurements can be taken via blood gas analysis [34], but this requires blood to be drawn from the patient or subject. The only available non-invasive measure of arterial CO_2 ($PaCO_2$) is respiratory end-tidal CO_2 ($PetCO_2$), which has been shown to closely resemble $PaCO_2$ measured by blood gas analysis when using a sequential gas delivery circuit [34].

However, there are two main disadvantages to $PetCO_2$ as a surrogate for $PaCO_2$ in studies of dynamic CA and CVR. First, its sampling rate is inherently limited to one sample per breath, which is around 0.1 to 0.2 Hz, and any intra-breath variations in $PaCO_2$ cannot be captured. Secondly, $PetCO_2$ as a surrogate for $PaCO_2$ works on the assumption that the last bit of air that a person exhales represents the composition of the air in their lungs, which is in equilibrium with the CO_2 content in their arteries. Measurements of $PetCO_2$ are therefore only reliable if the subject completely empties their lungs every time they breath out, which is typically not the case.

2.3.2.Measurement protocols

dCA and dCVR are typically assessed by recording the relevant physiological measurements (see Section 2.3.1) with recording lengths of at least 5 min [69]. These recordings can be taken under spontaneous fluctuations or protocols that induce larger fluctuations in ABP or $PaCO_2$. Spontaneous fluctuations can be seen as sufficient to stimulate dCA, as they contain beat-to-beat changes in ABP, and this has been used in numerous dCA studies, e.g., [63] [70]. dCVR has also been assessed using spontaneous fluctuations in $PaCO_2$, e.g., [15], [45]. This method is more appropriate for fragile patients, but the smaller amplitude in ABP or $PaCO_2$ fluctuations can result in less reliable estimates of dCA or dCVR respectively [69].

Protocols that induce larger fluctuations in ABP or $PaCO_2$ give a better signal-to-noise ratio (SNR), but they can also create “physiological noise” and are not always suitable for fragile subjects [69]. Various dCA protocols exist, such as head up tilt, fixed breathing, sit-to-stand manoeuvres, and random repetitive thigh cuff compression where blood pressure cuffs are repetitively inflated and subsequently deflated around a subject’s thighs. For a more comprehensive summary of the main characteristics of protocols for assessment of dCA, the reader is referred to the review by Simpson *et al.* [69]. For CVR studies, larger fluctuations in $PaCO_2$ can also be induced with various protocols, including breath holds, hyperventilation, or changes in inspired CO_2 administered via a mask (typically air with 5% CO_2).

The dCA protocols can be performed under normocapnia or hypercapnia, where normocapnia refers to a normal level of CO_2 in the blood and hypercapnia refers to elevated levels of CO_2 in the blood. Normocapnia is typically used to assess intact dCA and hypercapnia is used to simulate and assess impaired dCA. Specifically, a 5 % level of CO_2 is taken as a marker of impaired dCA [71]. It has been shown that hypercapnia significantly affects the NVC both at rest and during stimulation, so it is thought that the metabolic response of dCA specifically is impaired in this state [62] [72].

dCVR can also be assessed during both normocapnia and hypercapnia, but only using spontaneous fluctuations of $PaCO_2$, since larger induced fluctuations in $PaCO_2$ repetitively moves the physiological state between normocapnia and hypercapnia. Hypercapnia has not been specifically used to simulate impaired dCVR, but it is reasonable to expect a different physiological response, as hypercapnia would cause a shift in baseline conditions nearer to the upper saturation limit in the sigmoidal curve shown in Figure 2.4 (see Section 2.2.2). To date, dCVR has only been assessed by inducing larger fluctuations in $PaCO_2$ or at resting state during normocapnia.

2.4.Current models of dynamic cerebral autoregulation and cerebrovascular reactivity

dCA and dCVR have both been investigated and assessed using physiological models and data-driven analyses, although dCA is more established than dCVR in current literature. This section provides an overview of, first, the range of physiological models of dCA and dCVR that have been developed, second, the different data-based analysis methods used to assess dCA and dCVR, and last, combined approaches that used both physiological models and data-driven analysis.

2.4.1.Physiological models

Various models of dCA have been developed to describe the underlying physiological processes that govern dCA, providing considerable insight into these processes. Fewer models of dCVR have been developed, and typically the effects of CO_2 are included in models that focus primarily on dCA. On one side, there are simple, high-level models where sections of the vasculature are lumped into compartments, which are typically used to model the whole brain or large sections of the brain. On the other side, there are intricate models that describe specific mechanical and biochemical pathways involved in dCA and/or dCVR or take spatial heterogeneity of the brain into account, which have large computational costs as they are scaled up.

2.4.1.1. Compartment models

Compartment models typically model the CBF control mechanisms using an equivalent electrical circuit [27]. The sections of vasculature that are lumped into compartments are modelled using the concepts of pressure drop along a vessel being equivalent to voltage, flow rate of blood being equivalent to current, electrical resistance being equivalent to hydraulic resistance, inertia of blood being equivalent to inductance, and compliance of the vasculature being equivalent to capacitance. This is a substantial approximation, but it allows for models where parameters have some physiological meaning, while keeping the number of parameters low enough to be estimated using experimental data.

Such compartmental models have been used to develop whole brain models of cerebral circulation, for example the model by Ursino [73], which was the first to attempt to model the whole brain circulation as well as being the first to include dCA. dCA was modelled by assuming the inverse of vessel resistance was adjusted in response to changes in driving pressure though a low-pass filter with a gain and time constant (i.e., one overall feedback mechanism was used to describe dCA). The model showed good agreement with a number of experimental tests [74], and subsequently formed the basis of the majority of the following fundamental models of dCA, e.g., [75] [76], where the main changes have been differences in the number of arterial compartments (compared to the one compartment in the original model) and changes in the dCA pathways. The flow feedback parameter was proposed as a measure of CA strength by Ursino and Giulioni [77] and interpreted as such by later studies, e.g., [3]

Versions of the model by Ursino and Giulioni [77] have been extended to include dCVR, where feedback is based on flow and arterial CO_2 [78] [34] – although the resulting plots of CBF as a function of both ABP and $PaCO_2$ have generally been validated against animal data [33] [79] [80] [40]. In the model by Payne [81], CBF is controlled by dCA, dCVR, and NVC to investigate the interaction between the different CBF control mechanisms. In all these models, as well as in [34] [78] [81], dCVR was modelled as a first order response, with a gain and time constant, of arterial compliance to changes in the logarithm of $PaCO_2$ to emphasise that the response is linearly correlated with pH in the perivascular space (see Section 2.2.2) – except in [81], where a first order response was still used but in response to a function involving the hyperbolic tangent function of $PaCO_2$ that provided the best fit to the data of [40]. It has not yet been investigated whether first order models, with or without a time delay, adequately describe dCVR or whether previous studies have only used them as a first, simplest option.

There have been some attempts to separate out the different mechanisms of dCA (see Section 2.2.1), such as the model by Spronck *et al.* [82] that proposed a physiological model of CBF regulation with four feedback mechanisms: myogenic and shear-stress based responses to represent dCA, and neurogenic and metabolic responses to represent NVC. Each feedback mechanism was represented using a gain and time constant in the model but fitted parameter values were only obtained for the myogenic gain and time constant, the shear-stress gain, and the neurogenic gain and time constant. These parameter values were found by first "switching off" the NVC in the model while the myogenic and shear-stress response were fitted to experimental squat-to-stand dCA data; then keeping the myogenic and shear-stress values constant at the values found in their fitting and fitting the neurogenic response (and excluding the metabolic response according to preliminary fitting results) to NVC experimental data. The fact that the dCA and NVC responses were not fitted at the same time limits direct comparison of their parameter values, so the study only compared the myogenic and shear-stress responses and found that the myogenic response dominates dCA. Despite its limitations, this type of model shows the value of differentiating between different feedback mechanisms so that physiological meaning can be assigned to different components.

Payne [83] attempted to separate out the contributions of the myogenic and metabolic mechanisms of sCA by developing a simplified, physiological model of sCA with only 7 parameters. The myogenic response, taken to be purely associated with vasoconstriction, was found to be dominant over the metabolic response, which was taken to be purely associated with vasodilation. However, it should be noted that the model was limited to sCA, which leaves a gap for this approach to be extended to include dynamics and so allow for more detailed comparison to experimental data as well as insight into the time scales at which the myogenic and metabolic responses operate.

The models mentioned so far were used for population studies, where model parameters were selected or optimised to reflect average values for a population (i.e., group of people) as opposed to an individual subject. A recent study by Robles *et al.* [84] proposed a simple cerebrovascular resistance and compliance model to distinguish between intact and impaired dCA in individual patients based on two resistance parameters and two compliance parameters. Notably, the study emphasised the Genetic Algorithm that was used for parameter optimisation more than the physiological model itself, so this optimisation method could potentially be applied to other models that are sufficiently simple to make them applicable on an individual basis too.

2.4.1.2. Including biochemical pathways

There have also been physiological models of dCA where lumped compartment models have been extended by replacing overall feedback equations with specific biochemical pathways – with varying degrees of detail about chemical and metabolite production and transportation, e.g., [85] [86] [87] [88] [88]. In the model by Banaji *et al.* [85], both the dCA and dCVR mechanisms are modelled with detailed biomechanical pathways. Daher and Payne [89] provide a more detailed model specifically of dCVR, showing that the vasculature may respond to changes in tissue CO_2 rather than arterial CO_2 during hypercapnia, although it also included spatial heterogeneity (as discussed further below) via implementation within a multiscale network where the capillary bed was treated as a porous medium. However, these more detailed models tend to have large numbers of parameters to describe the required levels of detail, which makes validation with experimental data difficult.

2.4.1.3. Network models

Spatial heterogeneity of the brain has been taken into account using network models to distinguish between different parts of the brain and different generations of blood vessels with different ranges of diameters and properties, e.g., [90] [91] [92] [93]. Typically, one of two main approaches is used: either the model focusses on large vessels and, if smaller vessels are included, they are modelled as lumped compartments; or the model focusses on the capillary bed and treats larger vessels as a constant pressure supply. Major challenges with these types of models are the lack of validation due to resolution limitations of imagining techniques, and the rapid increase in complexity and hence computational demand as the number of compartments of individual vessels is increased – although the latter may be addressed by using homogenisation of blood flow in such networks, as developed by El-Bouri and Payne [94].

To the best of the author's knowledge, no network model has been developed with the explicit aim of disentangling the contributions of different mechanisms of dCA – although Milanovic *et al.*, 2021 [95] and Coccarelli *et al.* [96] did make use of network models to investigate specific details underlying dCA. Milanovic *et al.*, 2021 [95] incorporated a network model within a lumped parameter model to investigate the role of pericytes in dCA, concluding that pericytes appear to play a fundamental role in the rate of dCA. Coccarelli *et al.* [96] coupled a network model with a model of vascular smooth muscle cell contractile machinery to investigate the time-dependent behaviour of dCA at both single vessel and network levels, although only a partial network of a rat's cerebral vasculature was used, hindering comparison with experimental flow measurements. The effect of dCA on the pathways underlying dCVR was also investigated within a multiscale network [89].

2.4.1.4. Simplicity vs accuracy

It is therefore clear that physiological models require a balance between simplicity and accuracy. Simple models are rough approximations of the underlying physiology they are trying to capture, but they allow for parameter estimation from available data – although it should be noted that even simplified models such as those by Payne [81] and Ursino *et al.* [78] still have 26 and 24 parameters respectively. More accurate models hopefully represent more closely what is truly happening physiologically, but this leads to more parameters to estimate, which is rarely possible with the limited data availability and so significantly limits the use of these models.

2.4.2.Data-based analysis

Data-based analysis techniques can be used to estimate and quantify the relationship between clinically measurable, dynamic variables to give insights into the state of dCA and dCVR. For dCA, these measurable variables are typically ABP and CBv, and for dCVR, these variables are typically $PetCO_2$ and CBv or BOLD-fMRI (see Section

2.3.1). This section provides an overview of the main types of data-based analysis techniques that have been applied to dCA and dCVR in literature but is restricted to techniques that assume a linear relationship between the relevant variables, as they are most commonly used and deemed acceptable when investigating small fluctuations around baseline values. For a more comprehensive review of time domain analysis methods that can be used to assess dCA, and include the effects of CO_2 (i.e., dCVR), the reader is reviewed to the recent white paper [97] published on behalf of the Cerebrovascular Research Network (CARNet).

2.4.2.1. Simple metrics

Various simple metrics of dCA have been developed. A popular metric is the autoregulation index (ARI) proposed by Tiecks *et al.* [98], which assumes that dCA can be described by a second order model. Although the ARI model assumes a specific structure, it does not have an explicit physiological basis and is therefore included here as a data-based metric. Tiecks *et al.* [98] proposed 10 template dCA step responses (SR; see Section 2.4.2.3) with different parameter values in the second order model, each corresponding to an ARI value ranging from 0-9, with 0 meaning no autoregulation is taking place and 9 meaning that maximal autoregulation is taking place. This allows for a simple, quantified comparison between subjects, but is crude in the sense that the complex mechanisms that make up dCA are summarised in a single number. Other simple dCA metrics include the rate of regulation (RoR) [99], which is the speed of the initial response of cerebrovascular resistance to a decrease in ABP induced by deflation of a thigh cuff; and Pearson's correlation coefficient [100] [101], where little or no correlation between ABP and CBv (i.e., coefficient close to zero) indicates intact autoregulation, and positive correlation (i.e., $0 <$ coefficient < 1) indicates a coupling between ABP and CBv and therefore impaired autoregulation.

Pearson's coefficient has also been used to quantify a delay in the CVR response as a metric of the temporal aspect of CVR. The delay is quantified as the shift at which Pearson's correlation coefficient between the $PetCO_2$ and BOLD-fMRI signals is maximised, which were typically recorded during externally induced changes in $PaCO_2$ (see Section 2.3.2). A single delay can be determined for the whole brain, such as in [50] [51] [102], or a delay can be determined for each voxel, such as in [103] [104] [105] [106]. Poublanc *et al.* [107] took this a step further by looking at the correlation between the measured BOLD-fMRI signal and a BOLD-fMRI signal predicted from the $PetCO_2$ signal instead of the $PetCO_2$ signal itself. The predicted BOLD-fMRI signal was calculated as the convolution of the $PetCO_2$ signal with a haemodynamic response function (i.e., the IR), which was taken as a first order exponential function.

Poulin *et al.* [7] quantified both a delay and a time constant for the dCVR response, by fitting a first order with time delay model to the CBv response to an externally stimulated change in $PaCO_2$. Poulin *et al.* [108] extended this approach by quantifying a delay and time constant for two components, a slow one and a fast one, meaning that the overall response was described as second order. Again, these models assume specific structures but do not have explicit physiological bases, so they are discussed here as data-based analyses instead of in Section 2.4.1 as physiological models.

2.4.2.2. Transfer function analysis

TFA is a data-based technique that is commonly used to assess dCA [25], so it is covered here in some detail. TFA has more recently also been applied to dCVR [109]

[48]. It examines the behaviour between the input and output of a linear, stationary system in the frequency domain. In the case where the system is dCA, the input is ABP and the output is CBv; in the case where the system is dCVR, the input is $PetCO_2$ and the output is CBv or BOLD-fMRI (depending on the modality). The transfer function therefore quantifies the extent to which the ABP or $PetCO_2$ signal is reflected in the CBv/BOLD-fMRI signal, and is calculated from the time series as (eqn 2.1) [110]:

$$\mathrm{H(f)} = \mathrm{S_{xy}}(f) S_{xx}(f) \tag{2.1}$$

where $S_{xx}(f)$ (eqn 2.2) [110] and $S_{xy}(f)$ (eqn 2.3) [110] are calculated as:

$$\mathrm{S_{xx}(f)} = E[X(f)X^*(f)] \tag{2.2}$$

$$\mathrm{S_{xy}(f)} = E[X(f)Y^*(f)] \tag{2.3}$$

where X and Y are the power spectra of ABP and CBv respectively in dCA, and the power spectra of $PetCO_2$ and CBv/BOLD-fMRI respectively in dCVR; E indicates expectation (i.e., average); and * indicates the complex conjugate. Different studies compute the power spectra differently, but typically the input (ABP or $PetCO_2$) and output (CBv or BOLD-fMRI) time series are pre-processed, divided into segments and smoothed before being transformed using the fast Fourier transform (FFT) with superposition, whereafter the average of the result is calculated. The recently updated white paper [111] published on behalf of the CARNet provides recommendations for selecting methods and hyperparameters for TFA with the aim of providing a standard implementation of TFA in dCA research. TFA can also be applied in a multivariate approach, where multiple inputs, e.g., both ABP and $PetCO_2$, can be considered [46].

The transfer function is typically converted to a gain and phase, accompanied by the coherence, to provide an indication of the linear association between the input (ABP or $PetCO_2$) and output (CBv or BOLD-fMRI). The gain is the ratio of the output (CBv/BOLD-fMRI) to the input (ABP or $PetCO_2$). For dCA, a low gain represents efficient dCA (i.e., good attenuation of the oscillations) and an increasing gain represents impaired dCA (i.e., poor attenuation of the oscillations) [25]. Physiologically, a negative phase shift (typically reported as a positive number and termed “phase lead” or “phase” in the literature) is expected between ABP and CBv, which indicates intact dCA; while a phase tending close to zero indicates completely impaired dCA [25].

For dCVR, a reduced gain represents reduced CVR and an increased phase represents a slower response. Duffin *et al.* [109] showed that certain regions of the brain exhibit a slower response or a reduced response and that conventional sCVR analysis, where sCVR is quantified as the ratio of changes in CBF to changes in $PetCO_2$ [3], incorrectly characterises regions of slow CVR response as low or negative reactivity due to its calculation of sCVR as a linear temporal correlation without correction of delayed responses or slowed dynamics. A subsequent study by Leung *et al.* [48] corroborated that conventional sCVR analysis underestimates vessel reactivity compared to when dynamics are incorporated via TFA and showed that the effect is more prominent in patients with sickle cell disease. These studies therefore propose that TFA more accurately characterises the CVR response in its entirety, as it accounts for both the magnitude of response and the dynamic aspect of the response. Such an approach can provide additional information about the dCVR response and so provide insight into the mechanisms that govern dCVR – specifically where dCVR is impaired in cerebrovascular diseases.

Despite its wide use in dCA research, TFA has not been widely accepted for assessing dCA in clinical practice, motivating the need to further improve the TFA-derived metrics to distinguish clearly between intact and impaired dCA. A valuable goal would be to improve the technique (or a new workflow that somehow incorporates TFA) to the extent where it could give real-time or at least useful-time insights into whether dCA is intact or impaired, and potentially even which mechanism is impaired, in a bed-side monitoring setting. A recent study by Liu *et al.* [112] turned to machine learning (ML) to achieve this. The study proposed a semi-supervised ensemble learning strategy using an autoencoder and two classifiers to optimise feature extraction of TFA to improve discriminative power (i.e., to differentiate significantly) when classifying dCA as either intact or impaired. The approach was shown to outperform generic TFA and statistical analysis in identifying significant differences in features between subject groups with known intact and impaired dCA, promoting further development of ML techniques for impaired dCA detection.

ML limitations should be born in mind, however, as they typically require large amounts of data for training and are prone to overfitting if there are insufficient data available for testing. This is especially relevant in dCA or dCVR assessment, as subjects of interest are typically vulnerable patients; or dCA impairment is simulated as hypercapnic healthy subjects, but recordings taken during hypercapnia are no longer than 5 min to prevent health risks [69]. ML techniques also constitute black-box approaches, making their results more difficult to interpret and reducing confidence in results where the ground truth cannot be known and therefore cannot be used for comparison. For example, training data would be labelled as “intact dCA” or “impaired dCA” although this cannot be known with complete certainty. A possible way to attenuate this uncertainty at least somewhat, could be to use a hybrid approach that incorporates physiological knowledge in data-driven approaches to assess dCA or dCVR, which is further discussed in Section 2.4.3.

2.4.2.3. Impulse and step responses

The IR of dCA and dCVR can be estimated with various methods, including direct IR estimation, TFA, basis expansion methods, and autoregressive models with exogenous input (ARX) [97], and the SR is the result of integrating the IR. Direct IR estimation and TFA are more flexible but may be more sensitive to noise, whereas ARX models and basis expansion methods are more robust under low SNR conditions such as in resting state data, but do contain some estimation bias by restricting the IR shape.

In direct IR estimation, the IR can be estimated as the product of the autocorrelation matrix of the input (ABP or $PetCO_2$) and the cross-correlation vector of the input and output (CBv/BOLD-fMRI), such as in [113]. Using TFA, the IR can be obtained by applying the inverse fast Fourier transform (FFT) to the transfer function, and the SR is the result of integrating the IR, such as in [71] and [114]. An ARX model predicts the future output (CBv/BOLD-fMRI) based on previous output and input (ABP and/or $PetCO_2$) values, where the number of previous values to include (i.e., model order) can be selected based on previous literature or the Akaike information criterion (AIC) or Bayesian information criterion (BIC) [97].

Panerai *et al.* [115] used an ARX model (although they refer to it as an autoregressive-moving average model, which is typically done in dCA literature [97]) in an attempt to disentangle some of the underlying mechanisms of dCA. This is of particular interest and discussed here in some detail, as most current research only focusses on distinguishing between intact and impaired dCA as a whole, but it would be valuable to go a step beyond “impaired dCA” and be able to provide information on how dCA is impaired, i.e., provide insights into which mechanisms of dCA are impaired, as this could potentially allow for targeted treatment. Panerai *et al.* [115] found that myogenic activity is mainly expressed through changes in the resistance-area product, where resistance and area refer to the vessel resistance and cross-sectional vessel area respectively. The study also aimed to show that the metabolic response is mainly expressed through changes in the critical closing pressure (CrCP), where CrCP refers to the value of ABP where the blood vessel collapses and CBF becomes zero - although the results could not clearly confirm this from the available data. In a subsequent study, Panerai *et al.* [63] used sub-component analysis to break down the changes in CBv into separate contributions of ABP, CrCP and RAP. Their analysis of the results showed that both RAP and CrCP contribute significantly to the dCA response (i.e., the changes in CBv), and that the CrCP response (not the RAP response) explains the depression in dCA observed during hypercapnia. However, there is more work to be done to disentangle the contributions of different mechanisms to dCA – especially in terms of identifying the relative speeds at which the mechanisms act.

Basis expansion methods are based on the understanding that the kernel of the first order discrete Volterra model (DVM) is equivalent to the IR. The IR function is expanded in terms of an orthonormal set of discrete time basis functions. Laguerre basis functions are typically used for the dCA IR [97], and the recent review paper by Shams *et al.* [116] recommends spherical Laguerre basis functions for the dCVR IR[1]. “Principal dynamic modes” (PDM) have also been used as basis functions to estimate both the dCA and dCVR IRs and SRs [45], where the PDMs are estimated for each input (ABP and/or

---

[1] An overview of basis expansion methods is provided here, but more detail (including relevant equations) of the basis expansion method using spherical Laguerre basis functions is provided in the methods section of Chapter 4 (see Section 4.2.3).

$PetCO_2$) via Singular Value Decomposition (SVD) of a rectangular matrix that is composed of all kernels that were estimated using Laguerre basis functions.

A typical dCA IR for a subject with no known pathological conditions is well established in current literature. It shows an undershoot just before one second, followed by a rapid return to baseline with a potential slight overshoot [27]. The corresponding SR shows a slight overshoot before rapidly settling down to a baseline value [27], which clearly shows the biphasic behaviour of the passive response followed by the active response of dCA (see Figure 2.2(b) in Section 2.2.1). However, it should be noted that the amplitudes of IRs and SRs can vary significantly according to the type of dCA test used to derive them (e.g., thigh cuff, spontaneous fluctuations) [27]. The dCVR IR is not as well established in current literature, but the recent review by Shams *et al.* [116] describes the dCVR IR shape as starting at zero, rising to a positive peak, sometimes exhibiting an undershoot, and settling to baseline, and they used this shape as the ground truth in a simulated case study to test different IR estimation methods. Step increases or decreases in $PaCO_2$ have been approximated in experimental studies, and the CBF response, which would approximate a SR, is simply a respective increase or decrease until the new steady state value is reached.

2.4.3.Combined physiological models and data-based analysis

Physiological models and data-based analysis of dCA and dCVR both have their own advantages and disadvantages. In physiological models, the main advantage is that the parameters can be linked to some physiological meaning; but often these parameters cannot be measured, making validation with experimental data difficult or impossible. Furthermore, physiological models typically have a large number of parameters, essentially rendering them black-box models, as it is not possible to gain insights into the mechanisms that govern dCA and dCVR from them.

In data-based analysis methods, no assumptions are made about underlying physiology, meaning that no prior knowledge of the system is required. However, results can be difficult to interpret for this exact reason, as it is not always straightforward to link patterns in the data to physiological meaning. Due to the complementary nature of the advantages and disadvantages of physiological models and data-based analysis techniques, a hybrid approach such as physiologically informed, data-based analysis may be promising. Such as approach could leverage the information contained in data by linking it to physiologically meaningful parameters or could use known physiology to constrain data-based analysis inputs or outputs.

Despite the fact that Panerai [26] mentioned that such a hybrid approach combining mathematical models of well-known physiological phenomena with heuristically identifiable components may aid in pinpointing specific phenomena responsible for clinically relevant disturbances in 2004 already, only a few studies have investigated such an approach for dCA and none have done so for dCVR. To the best of the author's knowledge, only Payne and Tarassenko [114] ventured in this direction for dCA, by combining TFA with a physiological model to interpret clinical data. The study developed a physiological model that closely resembles a second order transfer function and optimised parameter values using the IRs obtained from applying TFA to the data, obtaining physiologically reasonable parameter values. In this case, the parameter values related to overall dCA, but there is scope to apply this approach using a different physiological model, where the mechanisms of dCA are more clearly separated to aid in disentangling the contributions of these mechanisms in dCA. There is also scope to apply such an approach to a simple physiological model of dCVR.

2.5.Summary

In this chapter, relevant literature was discussed to provide an overview of the physiology of CBF control with an emphasis on dCA and dCVR, how dCA and dCVR can be measured, and current modelling approaches that aid in understanding and assessment of dCA and dCVR. Both physiological models and data-based analysis methods were discussed, and both were found to be more established in application to dCA than dCVR in current literature, with dCVR being more prominent in data-based literature than physiological models. Building on this previous literature, the following chapters present the application of a hybrid approach combining a simplified physiological model with data-based analysis to disentangle the different mechanisms of dCA, and a similar approach to link the growing body of data-based dCVR research to a physiological model as a first step towards improving mechanistic understanding under different physiological conditions, using both TCD and BOLD-fMRI as measurement modalities.

CHAPTER 3

Modelling the mechanisms of non-neurogenic dynamic cerebral autoregulation

A version of this chapter is published as:

- ***van Zijl, N.**, Banerjee, A., Payne, S.J. 2024. Modeling the mechanisms of non-neurogenic dynamic cerebral autoregulation. IEEE Transactions on Biomedical Engineering. DOI: 10.1109/TBME.2024.3463873.*

Subsets of the results in this chapter were presented at the following conferences:

- ***van Zijl, N.**, Payne, S.J. Identifying the different mechanisms that govern dynamic cerebral autoregulation. Computational & Mathematical Biomedical Engineering (CMBE) 2022 Proceedings Vol. 2. June 29, 2022.*
- ***van Zijl, N.**, Payne, S.J. Identifying the mechanisms that govern cerebral autoregulation. The 9th World Congress of Biomechanics. July 10-14, 2022, Taipei, Taiwan.*
- ***van Zijl, N.**, Banerjee, A., Payne, S.J. Identifying the mechanisms of intact and impaired dynamic cerebral autoregulation. The 31st International Symposium on Cerebral Blood Flow and Metabolism. June 12-15, 2023, Brisbane, Australia.*

Abstract

dCA refers to a collection of mechanisms that act to maintain steady state CBF near constant despite changes in ABP, but which is known to become impaired in various cerebrovascular diseases. Currently, the mechanisms of dCA and how they are affected in different physiological conditions are poorly understood. The objective of this study was to disentangle the magnitudes and time scales of the myogenic and metabolic *responses of dCA, in order to investigate how each mechanism is affected in impaired dCA. A physiological model of dCA was developed, where both the myogenic and metabolic responses were represented by a gain and time constant. Model parameters were optimised with pressure-flow IRs under normocapnia, thigh cuff, and hypercapnia conditions. The IRs were derived by applying TFA to experimental recordings of ABP (Finapres), $PetCO_2$ (capnograph), and CBv (TCD in bilateral MCAs). The myogenic gain to time constant ratio was significantly smaller (p-values < 0.001 using both univariate and multivariate TFA), and the metabolic time constant was significantly larger (p-values < 0.001 using both univariate and multivariate TFA) in hypercapnia compared to normocapnia. Both the myogenic and metabolic responses were shown to be affected in impaired dCA, and the metabolic response was shown to be slowed down. This study contributes to the understanding of the complexities of dCA and how it is affected in different physiological conditions.*

3.1.Introduction

dCA acts to control the transient response of CBF to changes in ABP. It aims to maintain steady state CBF and hence oxygen delivery relatively constant to prevent brain damage but is known to become impaired in various cerebrovascular diseases. A recent review by Sarwal *et al.* [117] states that proposed clinical interventions to optimise CA status have yet to demonstrate clear clinical benefit, although emerging clinical evidence does show the feasibility of directly targeting autoregulation with therapies, for example, reduction of post-operative delirium [118] and better subsequent memory test performance [119] in patients with autoregulation-guided management, and demonstrated feasibility of autoregulation-based blood pressure targets for acute ischemic stroke patients undergoing thrombectomy [120]. Increasing understanding of the complexities of dCA will enhance the ability to translate this knowledge into future clinical trials. Specifically, the mechanisms of dCA are generally agreed upon to consist of myogenic, metabolic, and neurogenic responses [26], but their interaction and how they are individually affected in different physiological and pathophysiological conditions remain poorly understood, despite considerable research into the underlying processes.

Numerous physiological models of dCA have been developed to describe these underlying physiological processes that govern dCA, for example [88], [121], [73]. However, more detailed models that aim to truly represent what is happening physiologically require many parameters to be estimated during experimental validation, which is rarely possible with the limited data availability, significantly limiting their use. Data-driven techniques such as TFA [25] have also been used to assess dCA, and Payne and Tarassenko [114] combined TFA with a physiological model to interpret clinical data. However, these studies have mainly focused on determining whether dCA as a whole is intact or impaired. Currently, it is still unclear how the individual mechanisms of dCA are each affected in impaired dCA, although this could be valuable in understanding the different types of impairment.

Few attempts have been made to separate out the different mechanisms of dCA. Spronck *et al.* [82] developed a physiological model of CBF regulation with four feedback mechanisms: myogenic and shear-stress based responses to represent CA, and neurogenic and metabolic responses to represent NVC. However, the CA and NVC parameters were optimised separately due to the large number of parameters; and data from only one physiological condition was used, so there was no investigation into how the mechanisms are affected in different conditions. A previous study by Payne [83], which forms the basis for the model developed in this chapter, developed a simplified model of sCA, where the myogenic response was taken to be purely associated with vasoconstriction and the metabolic response to be purely associated with vasodilation. However, the study was based purely on sCA, which limits comparison with experimental data. Robles *et al.* [84] also aimed to quantify the separate contributions of the myogenic and metabolic responses of dCA as they are represented by changes in vascular resistance and compliance, but again did not investigate separate dynamics for the two mechanisms.

The aim of this chapter is therefore to disentangle both the magnitude and time scales of the metabolic and myogenic responses of dCA in different physiological conditions. The work aims to provide new insights into fundamental processes that govern dCA by interpreting individual mechanisms of dCA and how they are affected in different conditions. The myogenic and metabolic responses were selected for inclusion in the model in preference to the neurogenic response, as the coupling between local neurons and cerebral vasculature is difficult to measure, making it the most poorly understood pathway.

The rest of this chapter is organised as follows: Section 3.2. presents the methodology used in this chapter, including model development and incorporation of experimental data, as well as the statistical and sensitivity analyses; Section 3.3 provides the results of the model fit, sensitivity analysis, and optimised parameter values; Section 3.4 presents the main findings and study limitations, placing them in the context of current literature; and finally, Section 3.5 summarises the conclusions of this chapter.

3.2. Materials and methods

3.2.1. Model development

Both second order and first order models were developed[2] to find the simplest model that could describe dCA with acceptable accuracy while fitting experimental data robustly.

3.2.1.1. Second order model

A second-order model of dCA was developed as an extension of the sCA model by Payne [83]. A detailed derivation of the sCA model and its extension to a dCA model are provided in Appendix A.1, but briefly, the radius, r, of a single arteriole responds to changes in internal pressure, p, and pressure gradient, ∇p:

$$\Delta r^* = S_{r,p}\Delta p^* + S_{r,\nabla p}\Delta(\nabla p)^* \tag{3.1}$$

where Δ refers to a perturbation from baseline and the star superscript denotes a value as a fraction of its baseline value. The coefficients $S_{r,p}$ and $S_{r,\nabla p}$ are dependent on the elastic, myogenic, and metabolic responses, each only represented by sensitivity coefficients (S_E, S_M, S_V respectively) in the static model, but with the myogenic and metabolic responses modelled as first order responses (in the Laplace domain) here:

$$S_{r,p} = \frac{1 - \frac{S_M}{\tau_M s + 1}}{2\frac{S_M}{\tau_M s + 1} - \frac{S_V}{\tau_V s + 1} + S_E - 1} \tag{3.2}$$

---

[2] Work on the first order models is included in this chapter to provide further context about the selection of the second order model; it is not included in the published article.

$$S_{r,\nabla p} = \frac{\dfrac{S_V}{\tau_V s + 1}}{2\dfrac{S_M}{\tau_M s + 1} - \dfrac{S_V}{\tau_V s + 1} + S_E - 1} \tag{3.3}$$

The single vessel model was implemented within a full vasculature model using an electrical equivalent model, giving the overall pressure-flow transfer function:

$$\Delta q^* / \Delta P_a^* = S_{q,a} \tag{3.4}$$

where q is the flowrate, P_a is ABP, and $S_{q,a}$ is:

$$S_{q,a} = \left(\frac{\bar{P}_a}{\bar{P}_a - \bar{P}_c}\right) \times \left(\frac{\dfrac{1}{4f_r} + \left(\dfrac{\bar{P}_a - \bar{P}_c}{2\bar{p}}\right) S_{r,p} + \dfrac{1}{f_r} S_{r,\nabla p}}{\dfrac{1}{4f_r} + \left(\dfrac{\bar{P}_a - \bar{P}_c}{2\bar{p}}\right)(1 - f_r - 2f_v) S_{r,p} + \left(\dfrac{1}{f_r} - 1\right) S_{r,\nabla p}}\right) \tag{3.5}$$

with parameter values provided in Table 3.1. First order models were selected for the myogenic and metabolic responses so that the overall pressure-flow model is second order and can achieve the characteristic biphasic pressure-flow IR.

The overall transfer function was derived analytically using Mathematica and is provided in Appendix A.1. This transfer function was limited to five free parameters so that Mathematica could provide an accurate analytical solution for a polynomial with a maximum order of five. Since the main interest lies in disentangling the myogenic and metabolic responses, a time constant was not incorporated for the elastic response, and the model free parameters are shown in Table 3.1.

The overall transfer function is not strictly proper, so it was divided into a constant term and strictly proper term using the methodology outlined by Giller and Mueller [122], as explained in Appendix A.1. The strictly proper term was then converted to the time domain using the inverse Laplace transform to obtain the IR for parameter optimisation with data.

Table 3.1. Parameter values in the second order dCA model.

Parameter	Value	Units	Description	Source
Fixed parameters				
$\overline{P_a}$	100	mmHg	Baseline ABP	[123]
$\overline{P_c}$	30	mmHg	Baseline critical closing pressure	[123]
$\bar{p}$	57	mmHg	Baseline intramural pressure	[83]
f_r	0.6881	-	Regulating compartment resistance fraction	[124]
f_v	0.2572	-	Venous compartment resistance fraction	[124]
Free parameters				
S_M		-	Sensitivity coefficient/gain for myogenic response	
S_V		-	Sensitivity coefficient/gain for metabolic response	
S_E		-	Sensitivity coefficient/gain for elastic response	
τ_M		s	Time constant for myogenic response	
τ_V		s	Time constant for metabolic response	

3.2.1.2. First order models[2]

The first order models were derived similarly to the second order model, but with only one time constant instead of two. In the first case, only the myogenic response has a time constant (τ_M), such that (3.2) and (3.3) become (3.6) and (3.7) respectively:

$$S_{r,p} = \frac{1 - \dfrac{S_M}{\tau_M s + 1}}{2\dfrac{S_M}{\tau_M s + 1} - S_V + S_E - 1} \tag{3.6}$$

$$S_{r,\nabla p} = \frac{S_V}{2\dfrac{S_M}{\tau_M s + 1} - S_V + S_E - 1} \tag{3.7}$$

In the second case, only the metabolic response has a time constant (τ_V), such that (3.2) and (3.3) become (3.8) and (3.9) respectively:

$$S_{r,p} = \frac{1 - S_M}{2S_M - \dfrac{S_V}{\tau_V s + 1} + S_E - 1} \tag{3.8}$$

$$S_{r,\nabla p} = \frac{\frac{S_V}{\tau_V s + 1}}{2S_M - \frac{S_V}{\tau_V s + 1} + S_E - 1} \tag{3.9}$$

In both cases, the overall transfer function Q(s)/P_A(s) has a first order polynomial as the numerator and the denominator. When the transfer function is written as the sum of a constant and a strictly proper transfer function (as shown in Appendix A), the strictly proper transfer function has the form of a strictly proper first order transfer function.

3.2.2.Data[3]

The dataset used for this chapter was from an experimental vital sign dataset[4] [125] recorded from 20 healthy young adult subjects (Table 3.2) in supine position with head elevation in Southampton General Hospital. The dataset includes raw signals for ABP and CBv and processed signals for ABP, CBv and $PetCO_2$, with a representative recording shown in Figure 3.1. Raw signals for ABP (Finapres) and CBv (TCD in the left and right MCAs) were recorded at 125 Hz. Processed ABP and CBv signals were beat-averaged, interpolated with a cubic spline, and resampled at 10 Hz. The $PetCO_2$ signal was constructed by extracting end-tidal values from a respiratory CO_2 trace (infrared capnograph), interpolating with a cubic spline, and resampling to 10 Hz.

---

[3] The section "Data processing" from the published article is split into two sections here: "3.2.2. Data" and "3.3.3. Data-based impulse response derivation", to allow space for a more detailed description (including the addition of Table 3.2, Figure 3.1, and Figure 3.2) of the data.

[4] Data collection and pre-processing to produce beat-averaged ABP and CBv time series and $PetCO_2$ time series at 10 Hz were performed by Dr Dragana Nikolic, Prof David Simpson, and Dr Tony Birch.

Recordings were taken for five sessions approximately one week apart (8.9 ± 6.4 days), each time under three physiological conditions:

1. Normocapnia: at rest, with no gas challenge (18 min).
2. Thigh cuff: repetitive inflation/deflation of thigh cuffs, with no gas challenge (5 min).
3. Hypercapnia: at rest, with 5% CO2 gas challenge (5 min).

The dataset therefore contains 100 recordings per physiological condition, all used individually to increase the sample size. Due to poor quality or missing signals for any of the physiological measurements, three normocapnia and eight hypercapnia recordings were excluded, so 97 normocapnia, 100 thigh cuff, and 92 hypercapnia recordings were used for analysis. The data were further processed for this work by filling missing values (where artefacts had been removed) using linear interpolation (Figure 3.2), which was done for 62, 23, and 39 normocapnic, thigh cuff, and hypercapnic recordings respectively. Lastly, recordings were sub-sampled to 1 Hz for this chapter, according to the SF most widely used for IRs in the literature [114], and their z-scores were used for analysis.

Table 3.2. Demographic and physiological features of the subjects in the vital sign dataset [125].

Sex	10 male, 10 female
Age	25.5 ± 3.5 years
Height	168.3 ± 12.3 cm
Weight	64.5 ± 16.4 kg
Body mass index	22.6 ± 4.5 kg m^{-2}
Systolic blood pressure	119.6 ± 15.4 mmHg
Diastolic blood pressure	70.5 ± 8.3 mmHg

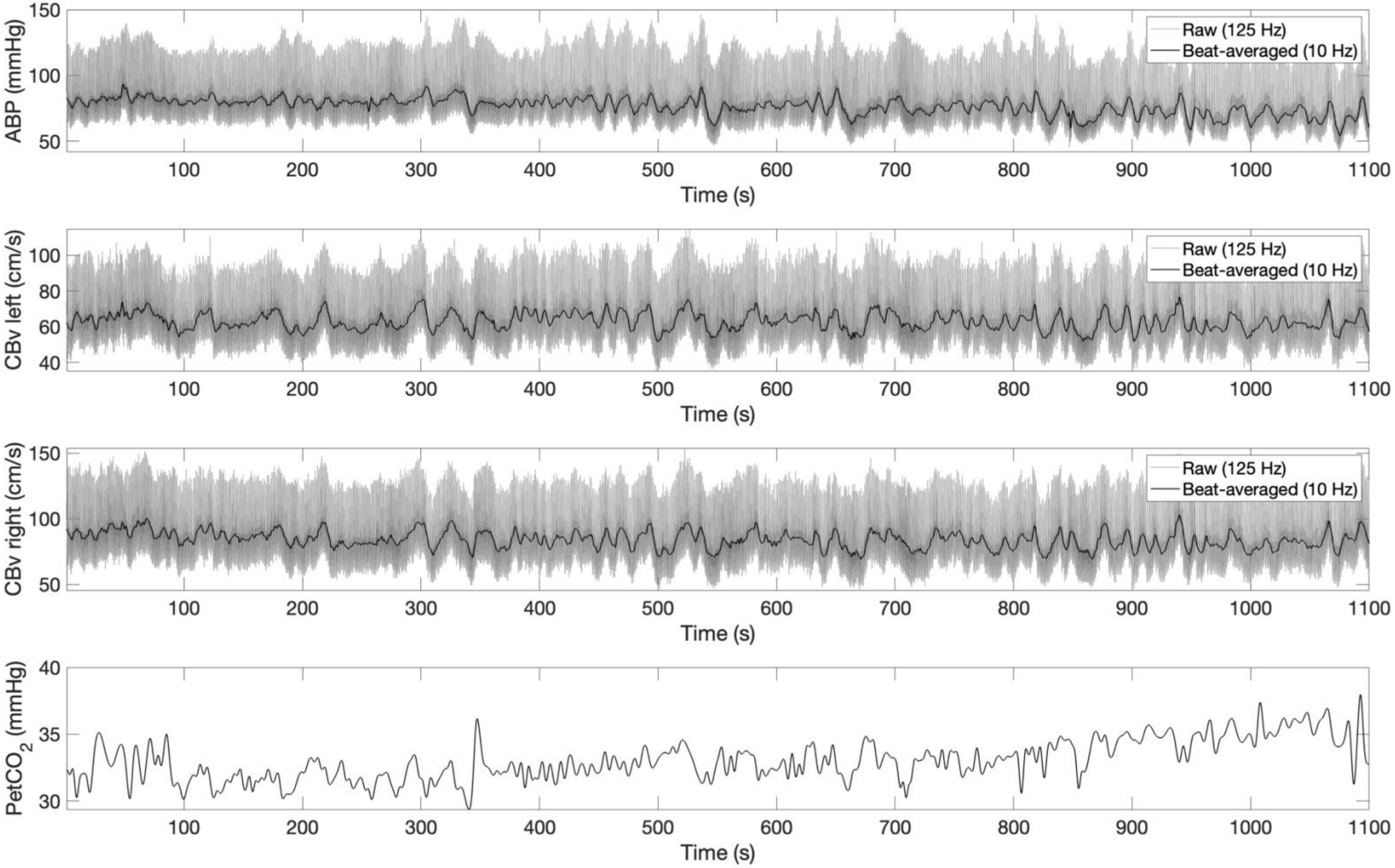

Figure 3.1. Raw (125 Hz) and processed (10 Hz) signals for a representative recording under normocapnia. ABP: arterial blood pressure, CBv: cerebral blood velocity, PetCO$_2$: end-tidal carbon dioxide partial pressure.

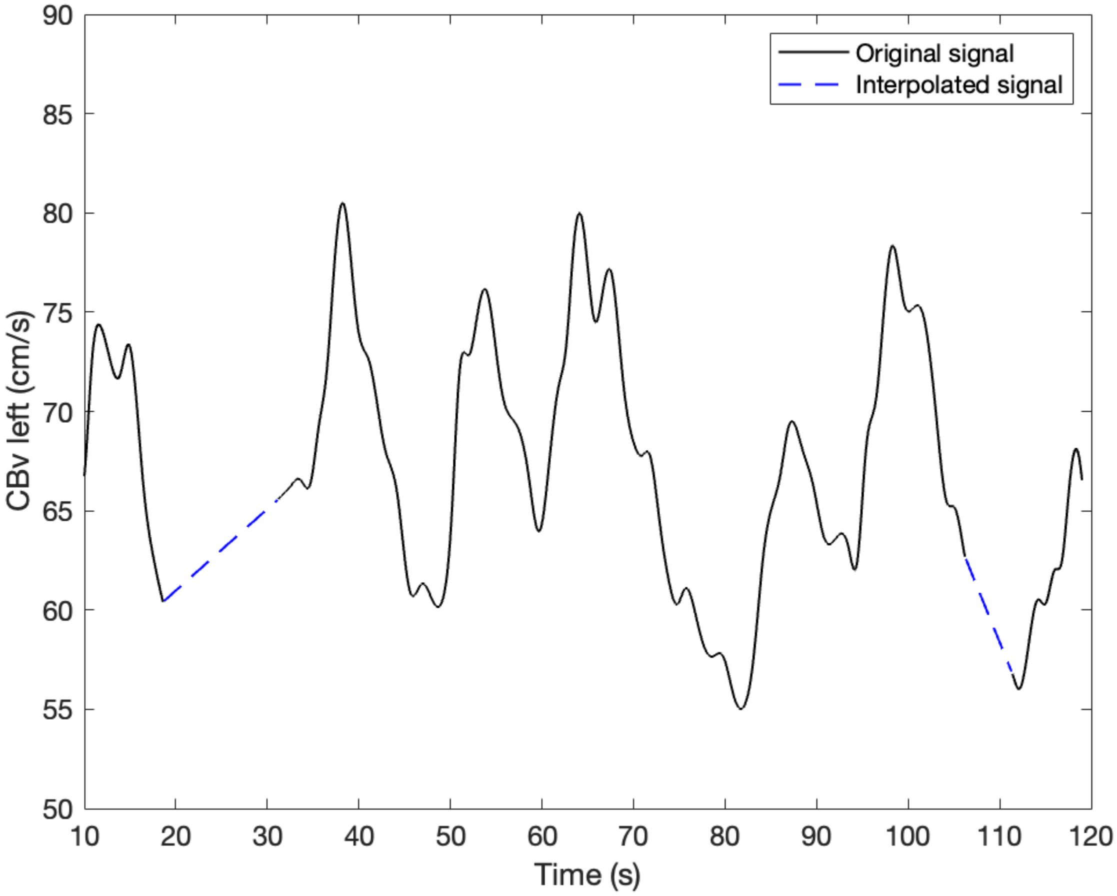

Figure 3.2. Representative CBv recording to demonstrate how missing values were filled using linear interpolation. CBv: cerebral blood velocity.

3.2.3.Data-based impulse response derivation[3]

Two sets of pressure-flow IRs were derived for each condition, using TFA (See Section 2.4.2.2) followed by the inverse FFT:

1. Using univariate (u/v) TFA with ABP as input and CBv as output (Figure 3.3A).
2. Using multivariate (m/v) TFA with both ABP and $PetCO_2$ as inputs and CBv as output (Figure 3.3B).

The TFA tool by CARNet and extension for m/v TFA by Peng *et al.* [46] were used in MATLAB, and hyperparameters were set according to recommendations from the revised white paper published on behalf of CARNet [111]. Only IRs with a mean squared coherence larger than the critical value of 0.190 in the 0.15 Hz - 0.25 Hz frequency range, proposed by Panerai *et al.* [126] to select plausible SRs, were accepted and used for model parameter optimisation. Optimising model parameters using an IR follows the approach from [114], which is advantageous because the IR represents the linear component independently from non-linear components, so it is not affected by potential nonlinearities in the pressure-flow relationship.

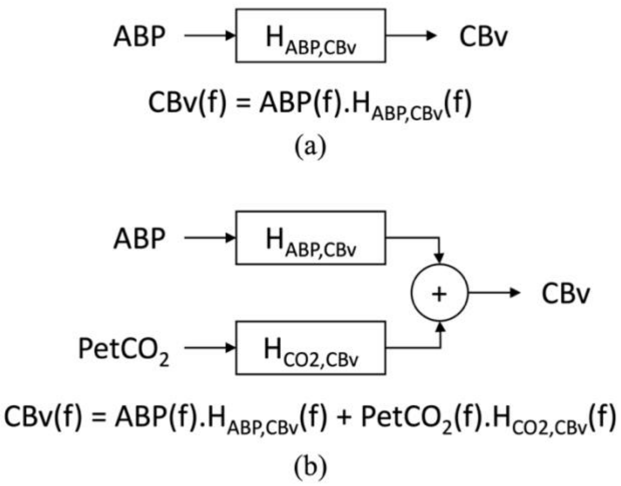

Figure 3.3. (a) Univariate model of CBv. (b) Multivariate model of CBv.

3.2.4.Parameter optimisation

Model parameters were optimised by fitting the model to each of the experimentally derived pressure-flow IRs, using the lsqnonlin function in MATLAB. The model parameter S_E was kept constant at 12, the average value estimated in [83] using the sCA model, since a scaling effect between parameter values was observed in preliminary fitting results where all five free parameters were optimised. The four parameters that describe the myogenic (S_M, τ_M) and metabolic (S_V, τ_V) responses were constrained to be non-negative to maintain physiological plausibility. Initial conditions for the parameters were obtained by pre-fitting the model to the five sample ABP and CBv recordings available on the CARNet website (www.car-net.org). The parameter sets that had the 5% largest sum of squared errors (SSE) during the fitting procedure were excluded to ensure sufficient goodness of fit for the parameter values used in further analysis.

3.2.5.Statistical analysis

Values of each parameter that were found to be further than three multiples of the quartile deviation away from the median were removed as outliers. A linear mixed effects model was fitted to the optimised values of each model parameter to account for the non-independence introduced into the data by multiple recordings from the same subject. Brain hemisphere and physiological condition were set as fixed effects and subject as a random effect:

$$MP = \beta_0 + \beta_1 * PC + \beta_2 * BH + \beta_3 * (PC \times BH) + u_{subject} + \epsilon \qquad (3.10)$$

where MP is model parameter, PC is physiological condition, BH is brain hemisphere, β_0 is the fixed effects intercept, $\beta_1, \beta_2, \beta_3$ are the coefficients for the fixed effects and their interaction, $u_{subject}$ is the random intercept for each subject, and ϵ is the residual error. Normality of the resulting residuals was tested for using the D'Agostino-Pearson test, as normally distributed residuals is a required condition for analysis with linear mixed effects models, and when it is not met, anything that is inferred from the linear mixed effects model is inconclusive. In cases where the residuals were not normally distributed, the linear mixed effects model was fitted to the transformed parameter values and the residuals checked for normality again; the square root, cube root, logarithm, and Box Cox transforms were tested.

Two-Way Analysis of Variance (ANOVA) was performed on the linear mixed effects model to test for significant effects of brain hemisphere and the three physiological conditions of normocapnia, thigh cuff, and hypercapnia. Since Two-Way ANOVA on the linear mixed effects model can only test whether a fixed effect (e.g., physiological condition) or interaction effect has a significant effect on the model parameter, but not between which pairs of group means the significant difference is (e.g., between normocapnia and hypercapnia, or between normocapnia and thigh cuff, or between thigh cuff and hypercapnia), *post-hoc* analysis was performed to assess the significance of differences between pairs of group means. Multiple comparisons were accounted for by using Tukey's correction during *post-hoc* analysis, as it is a popular choice to correct for multiple comparisons and more powerful than the Bonferroni correction. The p-values smaller than 0.05 were regarded as statistically significant. All statistical analyses and figures were prepared using R statistical software version 4.2.2.

3.2.6.Sensitivity analysis

A sensitivity analysis was performed to investigate the robustness of model parameter optimisation for each parameter. Since this study aims to gain insights into the mechanisms that govern dCA by interpreting the physiologically meaningful parameter values optimised from fitting experimentally derived IRs to the model, it is necessary to check whether the parameter optimisation is robust and hence, whether the optimised values for each parameter are meaningful and can be used to draw conclusions regarding the mechanisms that govern dCA.

Traditional sensitivity analysis methods look at whether changes in parameter values cause large changes in the model output, assumed to be a single scalar. Since the model output in this study is an IR, which is time-dependent, four characteristic metrics of the IR (Figure 3.4) were used as scalar model outputs:

1. Initial value of the IR (IRinit).

2. Peak (P): negative peak in the undershoot of the IR.
3. Time to peak (TTP): time taken to reach its negative peak.
4. Time to baseline (TTB): time taken for the dCA IR to return to baseline value of zero from the negative peak.

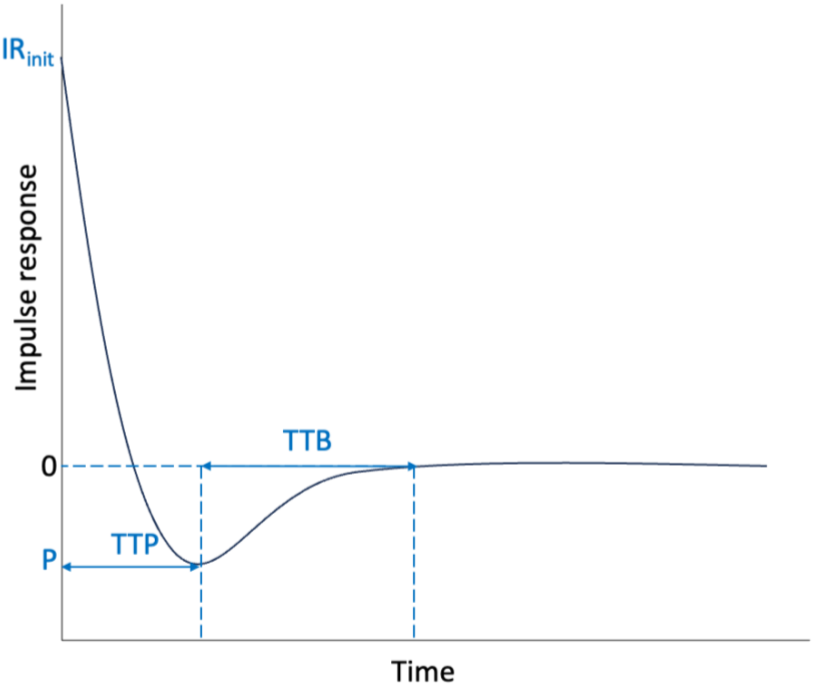

Figure 3.4. Illustration of dCA IR characteristic metrics. IRinit: Impulse response initial value, P: Peak, TTP: Time-to-peak, TTB: Time-to-baseline.

The Elementary Effects method was implemented to investigate how model parameters affect the variability of these characteristic metrics, using the SAFE toolbox [23]. This technique varies the values of the parameter values within their given ranges and calculates two sensitivity metrics to quantify their effect on the model output: the mean of elementary effects (EEs), which quantifies the influence of each parameter on the variability of the output; and the standard deviation of EEs, which quantifies the non-linearity and/or interaction effects of each parameter. Parameter ranges were set as ± 20% of their mean normocapnia values obtained in this study.

3.3.Results

3.3.1.Model fit[5]

The second and first order dCA models were fit to data-based IRs and the model fit and associated optimised parameter values were evaluated. The second order model produces the expected dCA IR, whereas neither of the first order models can produce the expected shape for unique parameter sets of optimised parameter values, as shown below. All subsequent analysis therefore uses the second order model.

3.3.1.1. Second order model

The second order model produces the characteristic shape of the pressure-flow IR with physiologically plausible parameter values (Figure 3.5). The IR shows the expected biphasic response, where the initial value is around one, followed by an undershoot, and a return to baseline [27]. The biphasic response is due to different timings of the quicker passive response (due to compliance of the vessels) and the slower active response (i.e., dCA). The initial value is approximately one, because a 1% change in ABP causes a change of around 1% in CBF during the passive response – and the IR shows the passive response at t=0. A second order model can therefore describe dCA, and the following subsection investigates whether a simplified first order model could also describe dCA.

---

[5] "Model fit" has been added as a results section in this chapter to allow space for discussion of the first order model fit in addition to the second order model fit. In the published article, the second order model fit is shown as part of the Materials and Methods section.

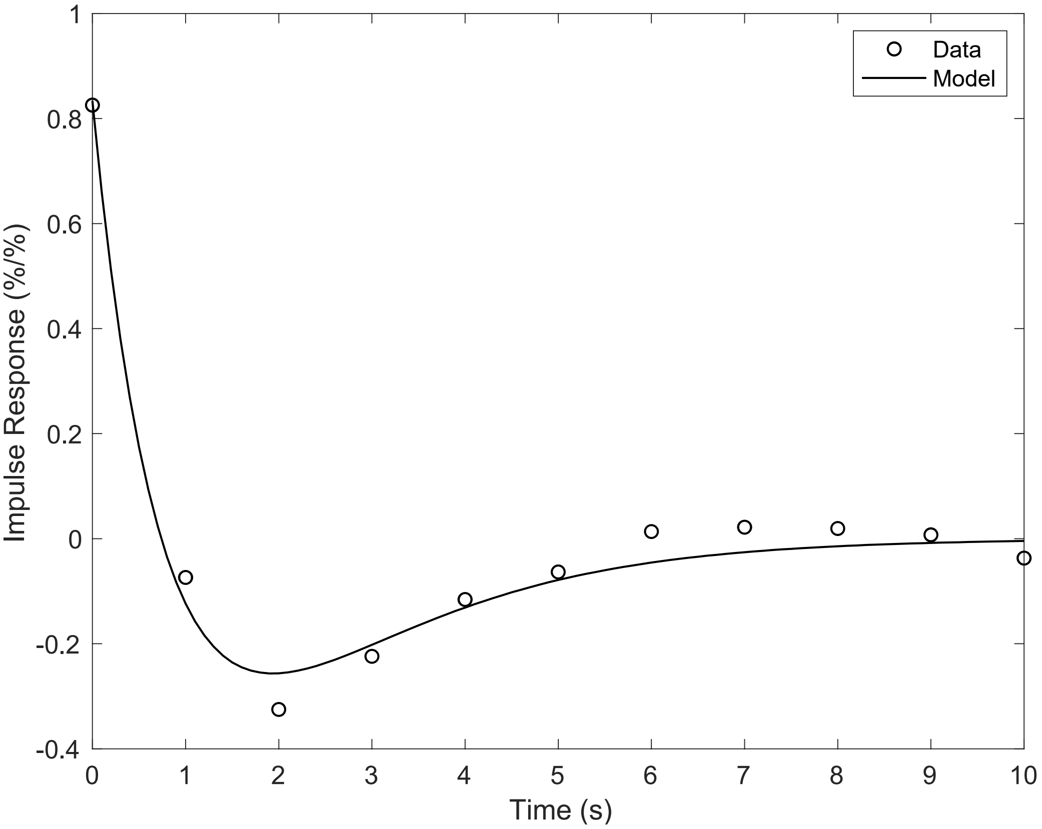

Figure 3.5. Optimal model fit to experimental pressure-flow impulse response of a representative recording. Values represent deviations from the baseline value.

3.3.1.2. First order models[2]

Two examples of a first order model were developed (see Section 3.2.1.2), primarily to investigate whether dCA can be described by a first order model. In the first case, only the myogenic response has a time constant, and the metabolic response is assumed to be instantaneous and in the second case only the metabolic response has a time constant, and the myogenic response is assumed to be instantaneous.

In the first case ($\tau_V = 0$), the expected shape for the IR could not be obtained. Only a negligibly small positive value could be obtained for the initial value of the IR while constraining the parameter values to be non-negative. This was confirmed using the initial value theorem, where the solution is provided in (3.23). The IR initial value can therefore only be positive if S_M is negligibly small, which means that the response containing the only time constant in this first order model tends to zero - meaning that the response is essentially happening instantaneously and fitting experimental data to this model while enforcing non-negative parameter values will always provide a nearly horizontal line instead of a first order response.

$$0 \leq S_M < 6.16 \times 10^{-16} \text{ and } S_V > \frac{-7.14\times10^{30}-4.76\times10^{46}S_M}{-7.72\times10^{30}+1.25\times10^{46}S_M} \text{ and } \tau_M > 0 \qquad (3.23)$$

In the second case ($\tau_M = 0$), the expected shape for the IR could be obtained, but no meaningful results could be obtained for parameter values. During the pre-fitting to the CARNet sample recordings (see Section 3.2.4), large differences in parameter values were observed for a negligible difference in SSE (Table 3.3). This indicates that the algorithm was finding local minimums of SSE instead of a global minimum - showing that dCA cannot be described using this first order model. All analysis in this chapter therefore uses the second order version of the model, where both the myogenic and metabolic responses have non-zero values of the time constants.

Table 3.3. Example of large differences in sets of parameter values with a negligible difference in SSE obtained when fitting the CARNet recordings to the first order model where $\tau_M = 0$.

S_M	S_V	τ_V	SSE
7.34	0.213	0.0369	0.162371
2510	40.1	0.0339	0.162371

3.3.2.Sensitivity analysis of model parameters

The results of the sensitivity analysis are plotted in Figure 3.6, where parameters closer to the origin have less effect on the model output than parameters further away. For the four characteristic metrics taken to represent the IR (i.e., the model output), none of the model parameters are consistently located closer or further away from the origin, which indicates that all four parameters are important. This corroborates that the values of these four parameters should be optimised individually.

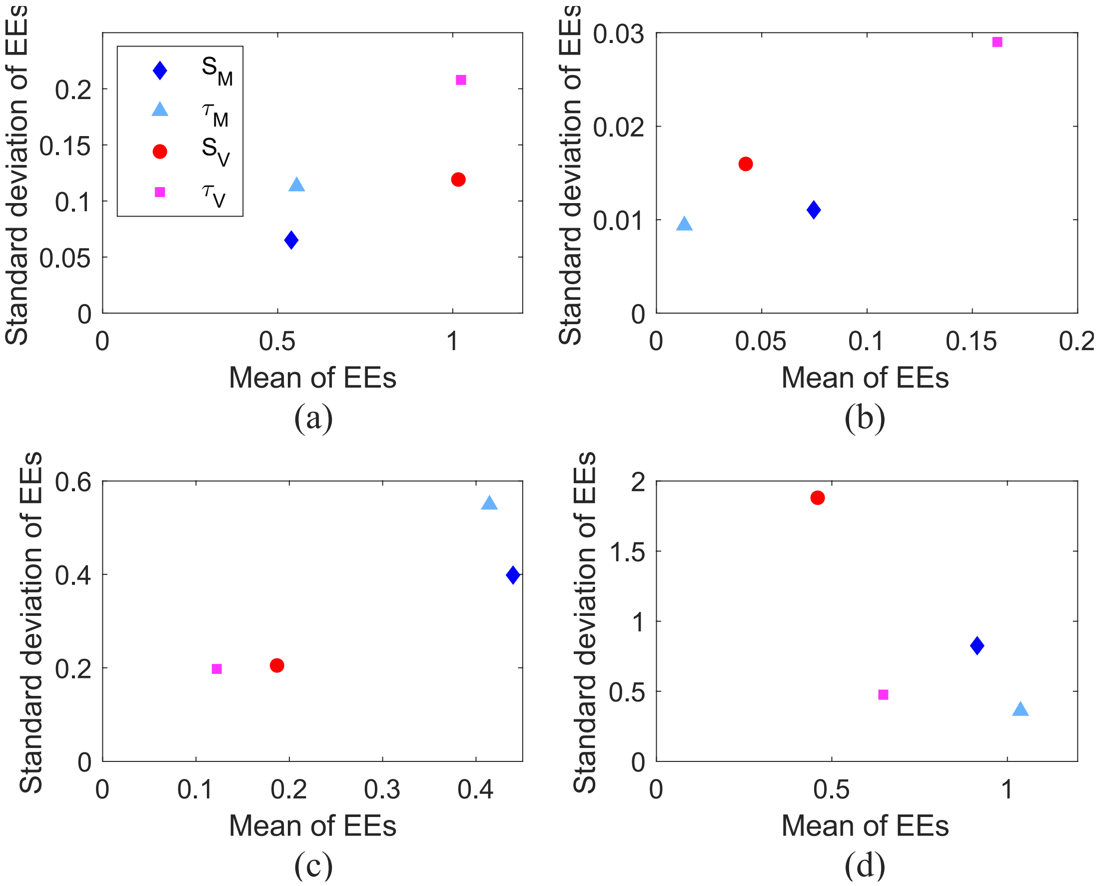

Figure 3.6. Sensitivity metrics to quantify the effects of model parameter values on model outputs: (a) Impulse response initial value (IRinit), (b) Peak (P), (c) Time to peak (TTP), (d) Time to baseline (TTB). EEs: Elementary effects.

The optimised values for S_M and τ_M have bimodal distributions, as shown in Figure 3.7A and Figure 3.7B. The bimodal distributions are not due to different physiological conditions, as they also occur within each physiological condition (Figure A.1 in Appendix A.2). The set of larger values for S_M corresponds to the set of larger values for τ_M, and vice versa, as shown by the normal distribution of the ratio S_M/τ_M in Figure 3.7D. It is not yet clear why corresponding bimodal distributions for S_M and τ_M occur. Interestingly, this effect does not occur with the pair of parameters that describe the metabolic response (S_V and τ_V), despite the fact that they are included in the model in a similar form to S_M and τ_M (i.e., as a first-order response). Since a bimodal distribution does not allow the removal of outliers using a measure of centrality and spread, and limits statistical comparison between conditions, the ratio S_M/τ_M is used for further analysis and interpretation.

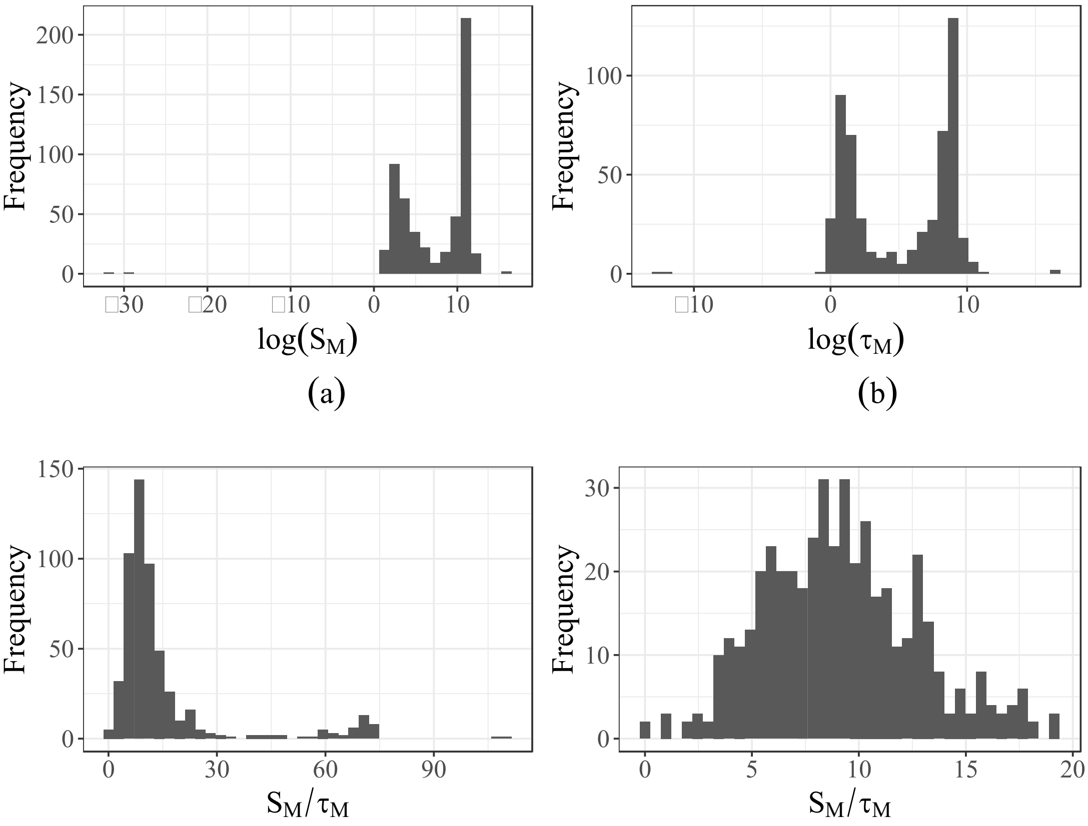

(a) (b)

(c) (d)

Figure 3.7. Histograms of S_M, τ_M, and S_M/τ_M values optimised from fitting impulse responses obtained from multivariate TFA to the dCA model. Results from all three conditions (normocapnia, thigh cuff, and hypercapnia) are grouped together here. (a) S_M. A log scale is used to emphasis the bimodal distribution. (b) τ_M. A log scale is used to emphasis the bimodal distribution. (c) S_M/τ_M before outliers were removed. (d) S_M/τ_M after outliers were removed.

3.3.3.Optimised model parameters

The three robust parameters were each optimised using experimentally derived IRs under three physiological conditions: normocapnia, thigh cuff, and hypercapnia. The results stemming from IRs obtained using u/v and m/v TFA are identified with the subscripts (u/v) and (m/v) respectively.

Linear mixed effects models were used to account for the non-independence in the data stemming from the use of multiple recordings per subject. Their residuals were tested for normality, as shown in Table 3.4. Residuals for the parameters $S_M/\tau_{M_{(u/v)}}$, $S_{V_{(u/v)}}$, $\tau_{V_{(u/v)}}$, and $\tau_{V_{(m/v)}}$ are normally distributed, indicating that variation in each of their optimised parameter values is fully described by effects from hemisphere and/or condition in the linear model. However, that is not true for $S_M/\tau_{M_{(m/v)}}$ and $S_{V_{(m/v)}}$, where the non-normality of residuals could be attributed to heteroscedasticity, non-linear relationships between the fixed effects and these physiological model parameters, or the influence of additional, unmodelled effects.

Table 3.4. The p-values from application of the D'Agostino-Pearson test for normality on residuals from fitting different transformations of the optimised parameter values to linear mixed effects models. Shaded cells indicate p-values that show the residuals are normally distributed.

Univariate TFA	$\boldsymbol{S_M/\tau_{M_{(u/v)}}}$	$\boldsymbol{S_{V_{(u/v)}}}$	$\boldsymbol{\tau_{V_{(u/v)}}}$
Original data	0.426	0.439	0.783
Multivariate TFA	$\boldsymbol{S_M/\tau_{M_{(m/v)}}}$	$\boldsymbol{S_{V_{(m/v)}}}$	$\boldsymbol{\tau_{V_{(m/v)}}}$
Original data	1.00e-06	0.0158	0.180
Square root	< 2.2e-16	0.0127	-
Cube root	< 2.2e-16	3.44e-10	-
Logarithm	< 2.2e-16	< 2.2e-16	-
Box Cox ($\boldsymbol{x_{transform} = x^{\lambda}}$)	0.794 [a]	0.000558 [b]	-

With Box Cox transformation parameters, $\boldsymbol{\lambda}$, of [a] 0.626 and [b] 0.788.

Residuals' normality can be achieved for $S_M/\tau_{M_{(m/v)}}$ by performing a Box Cox transformation before fitting to the linear mixed effects model (Table 3.4), which is therefore used in further statistical analysis. Although residuals normality could not be achieved for $S_{V_{(m/v)}}$ according to the D-Agostino-Pearson test, the original optimised $S_{V_{(m/v)}}$ values give a residual distribution with a skewness of -0.280, i.e., $|\text{skewness}| < 2.0$ [127], when fitted to a linear mixed effects model, which is accepted here and used for further analysis. Two-Way ANOVA was performed on the linear mixed effects models to determine whether brain hemisphere or physiological condition have a significant effect on optimised parameter values (Table 3.5). There is no significant interaction effect between hemisphere and condition, and no significant effect of hemisphere, on any parameters, optimised using u/v or m/v TFA, as expected. Condition, on the other hand, has a significant effect on all parameters except $S_{V(m/v)}$. Significant differences between conditions were investigated using *post-hoc* analyses and are discussed in the following sections.

Table 3.5. The p-values from the Two-Way ANOVA showing significance of hemisphere (left, right) and condition (normocapnia, thigh cuff, hypercapnia) on optimised parameter values. Shaded cells indicate a significant effect.

Univariate TFA	$\boldsymbol{S_M/\tau_M}_{(u/v)}$	$\boldsymbol{S_V}_{(u/v)}$	$\boldsymbol{\tau_V}_{(u/v)}$
Hemisphere	0.600	0.434	0.966
Condition	1.76e-11	0.653	1.79e-05
Multivariate TFA	$\boldsymbol{S_M/\tau_M}_{(m/v)}$	$\boldsymbol{S_V}_{(m/v)}$	$\boldsymbol{\tau_V}_{(m/v)}$
Hemisphere	0.866	0.509	0.458
Condition	<2e-16	0.000166	1.13e-08

3.3.3.1. Myogenic response

The myogenic response is represented by a single parameter, S_M/τ_M, taken as the ratios of the optimised values for S_M and τ_M (see Section 3.3.2), and its distribution is provided in Table 3.6. The mean value of $S_M/\tau_{M(u/v)}$ is significantly smaller in hypercapnia compared to normocapnia and thigh cuff, and there is no significant difference between normocapnia and thigh cuff. This indicates that the myogenic response is impaired in hypercapnia and supports the idea that dCA is impaired in hypercapnia. However, it directly links dCA impairment to myogenic response impairment – and since the myogenic response is associated with changes in resistance-area-product, this is not wholly in agreement with [63], which proposes that the impairment in dCA observed in hypercapnia is due to changes in critical closing pressure and not resistance-area-product. Furthermore, a decrease in S_M (i.e., dampening of the response) or an increase in τ_M (i.e., a slowing down of the response) can both decrease the ratio S_M/τ_M, making it only possible to state that the myogenic response is impaired in hypercapnia, but not whether this takes the form of an attenuated or slowed down response.

Table 3.6. Distribution of S_M/τ_M (s^{-1}) values optimised using univariate and multivariate TFA, for normocapnia (N), thigh cuff (TC) and hypercapnia (H). Shaded cells indicate statistically significant differences.

Cond.	$S_M/\tau_{M(u/v)}$		$S_M/\tau_{M(m/v)}$	
mean ± standard deviation				
	Left	Right	Left	Right
N	3.90 ± 0.824	3.92 ± 0.878	11.1 ± 3.14	11.0 ± 3.54
TC	3.82 ± 0.953	3.92 ± 0.938	8.89 ± 3.13	8.76 ± 2.88
H	3.35 ± 0.794	3.34 ± 0.781	7.06 ±3.45	7.26 ± 3.72
p-value (*post-hoc* analysis)				
N vs. TC	0.836		< 0.0001	
N vs. H	< 0.0001		< 0.0001	
TC vs. H	< 0.0001		< 0.0001	

The m/v TFA results show a significant decrease in the mean value of $S_M/\tau_{M(m/v)}$ between conditions in the order: normocapnia, thigh cuff, hypercapnia. This corroborates an impaired myogenic response in hypercapnia, but also shows impairment in thigh cuff compared to normocapnia.

3.3.3.2. Metabolic response

The metabolic response is represented by a separate gain and time constant, S_V and τ_V, and the distributions of their optimised values are provided in Table 3.7 and Table 3.8 respectively. The Two-Way ANOVA showed that condition does not have a significant effect on $S_{V(u/v)}$ (Table 3.5), which indicates that the metabolic response is not attenuated in hypercapnia. This does not contradict the idea that dCA is impaired in hypercapnia, since the myogenic response is impaired in hypercapnia, as discussed in the previous section. However, the mean value of $S_{V_{(m/v)}}$ is significantly larger in thigh cuff than in normocapnia, whereas there are no significant differences between hypercapnia and either of the other two conditions.

Table 3.7. Distribution of S_V values optimised using univariate and multivariate TFA, for normocapnia (N), thigh cuff (TC) and hypercapnia (H). Shaded cells indicate statistically significant differences.

Cond.	$S_{V_{(u/v)}}$		$S_{V_{(m/v)}}$	
mean ± standard deviation				
	Left	Right	Left	Right
N	6.07 ± 1.47	6.00 ± 1.56	4.70 ± 0.745	4.62 ± 0.825
TC	6.20 ± 1.81	6.06 ± 1.59	5.03 ± 0.906	4.94 ± 0.952
H	6.13 ± 1.87	6.02 ± 1.79	4.78 ± 0.967	4.83 ± 0.992
p-value (*post-hoc* analysis)				
N vs. TC	-		0.0001	
N vs. H	-		0.0713	
TC vs. H	-		0.2036	

Most notably, the mean value of $\tau_{V_{(u/v)}}$ is significantly larger in hypercapnia compared to normocapnia and thigh cuff, whereas no significant difference was found between normocapnia and thigh cuff (Table 3.8). Alongside $S_{V_{(u/v)}}$ being unaffected by condition (Table 3.5), this indicates that the metabolic response is not attenuated during impaired dCA, but rather that it is slower. Once again, the m/v TFA results show a difference in thigh cuff results, where $\tau_{V_{(m/v)}}$ is significantly larger in both hypercapnia and thigh cuff compared to normocapnia (Table 3.8), indicating that the metabolic response is not only slower in hypercapnia but also in thigh cuff. Notably, $\tau_{V_{(m/v)}}$ seems to be larger (i.e., slower metabolic response) in hypercapnia compared to thigh cuff, but this is not statistically significantly. It therefore appears that the metabolic response is slower in hypercapnia (i.e., impaired dCA), but also (although perhaps to a lesser extent) during the thigh cuff test.

Table 3.8. Distribution of $\tau_V\ (s)$ values optimised using univariate and multivariate TFA, for normocapnia (N), thigh cuff (TC) and hypercapnia (H). Shaded cells indicate statistically significant differences.

Cond.	$\tau_{V(u/v)}$		$\tau_{V(m/v)}$	
mean ± standard deviation				
	Left	Right	Left	Right
N	0.884 ± 0.133	0.878 ± 0.143	0.395 ± 0.115	0.394 ± 0.123
TC	0.872 ± 0.149	0.867 ± 0.147	0.460 ± 0.127	0.445 ± 0.123
H	0.936 ± 0.178	0.945 ± 0.146	0.483 ± 0.169	0.478 ± 0.156
p-value (*post-hoc* analysis)				
N vs. TC	0.6792		0.0001	
N vs. H	0.0005		< 0.0001	
TC vs. H	< 0.0001		0.1330	

3.4.Discussion

In this chapter, a simple physiological model and TFA of experimental data were used in a combined approach to investigate how the myogenic and metabolic responses are individually affected in different physiological conditions. The conditions termed normocapnia and thigh cuff represent intact dCA, and the hypercapnia condition represents impaired dCA, as it is known that dCA is impaired in hypercapnia [26], [27].

3.4.1.Main findings

This chapter's results support the idea that dCA is impaired in hypercapnia, where both the myogenic and metabolic responses are shown to be affected. For the myogenic response, the optimised values of S_M/τ_M are significantly smaller in hypercapnia compared to normocapnia and thigh cuff. An additional point of difference is observed in the m/v TFA results, where $S_M/\tau_{M(m/v)}$ is also significantly smaller in thigh cuff compared to normocapnia, and potential reasons for this are discussed later. This decrease in S_M/τ_M can be due to a decrease in S_M, indicating an attenuated myogenic response (i.e., vasoconstriction response in this model) or an increase in τ_M, indicating a slowed myogenic response, or a mixture of both. The results therefore show that the myogenic response is impaired in dCA but cannot differentiate whether this takes the form of an attenuated or slowed response.

For the metabolic response, S_V is not significantly different between normocapnia and hypercapnia, indicating that the metabolic response is not attenuated in impaired dCA. The m/v TFA results do show a significant difference between normocapnia and thigh cuff, which is discussed later. τ_V is observed to be larger in hypercapnia compared to normocapnia and thigh cuff, although significance was not found between thigh cuff and hypercapnia in the m/v TFA results. $\tau_{V_{(m/v)}}$ is also significantly larger in thigh cuff compared to normocapnia, which is discussed later. These results indicate that the metabolic response (i.e., vasodilation response in this model) is slowed down in impaired dCA. To the best of the author's knowledge, a difference in the timing of the metabolic response between intact and impaired dCA has not been reported before.

3.4.2.Univariate vs multivariate TFA results

Experimental pressure-flow IRs were derived using TFA: first u/v TFA and then m/v TFA to consider the effects of CO_2. Since arterial CO_2 concentration is known to have a large effect on CBF [3], the m/v TFA results are expected to be a more accurate representation of the underlying dCA mechanisms. However, Panerai *et al.* [71] stated that this is not the case, having observed that pressure-flow IRs derived with u/v and m/v (including $PetCO_2$) models were similar. They therefore argue that although $PetCO_2$ does have a large effect on CBF, it is not required when deriving the pressure-flow IR as a measure of dCA. The study explains that spontaneous $PetCO_2$ variations were not found to have a large effect on ABP, and in such weakly correlated signals, the second input (i.e., $PetCO_2$) typically does not have a strong influence on the individual IRs.

The u/v and m/v TFA IRs in this study (Figure 3.8) have similar shapes and initial values, but the size and timing of the undershoot and subsequent return to baseline differ. In the m/v TFA IR, the undershoot occurs just before one second and the return to baseline by around three seconds. In the u/v TFA IR, it takes approximately twice as long, where the undershoot occurs just before two seconds and the return to baseline by around six seconds. In fact, this difference in timing is also seen in the metabolic time constant, as $\tau_{V_{(m/v)}}$ is around half the value of $\tau_{V_{(u/v)}}$ (Table 3.8). The m/v model IR in [29] shows the undershoot occurring at around one second, agreeing with the m/v TFA IR in this study, and the u/v model IR is stated to be very similar, but is not shown for comparison. The IR reported by Panerai *et al.* [71], which has been described as highly characteristic by subsequent literature, [22], [3], also shows the undershoot occurring just before one second, again corresponding to the m/v TFA IRs in this study, but was based on a u/v model, not a m/v model. Fortunately, the most noteworthy findings in this chapter – impaired myogenic response and slower metabolic response in hypercapnia compared to normocapnia – were seen in both the u/v and m/v TFA results. However, other differences between the u/v and m/v results are still interesting and therefore briefly discussed.

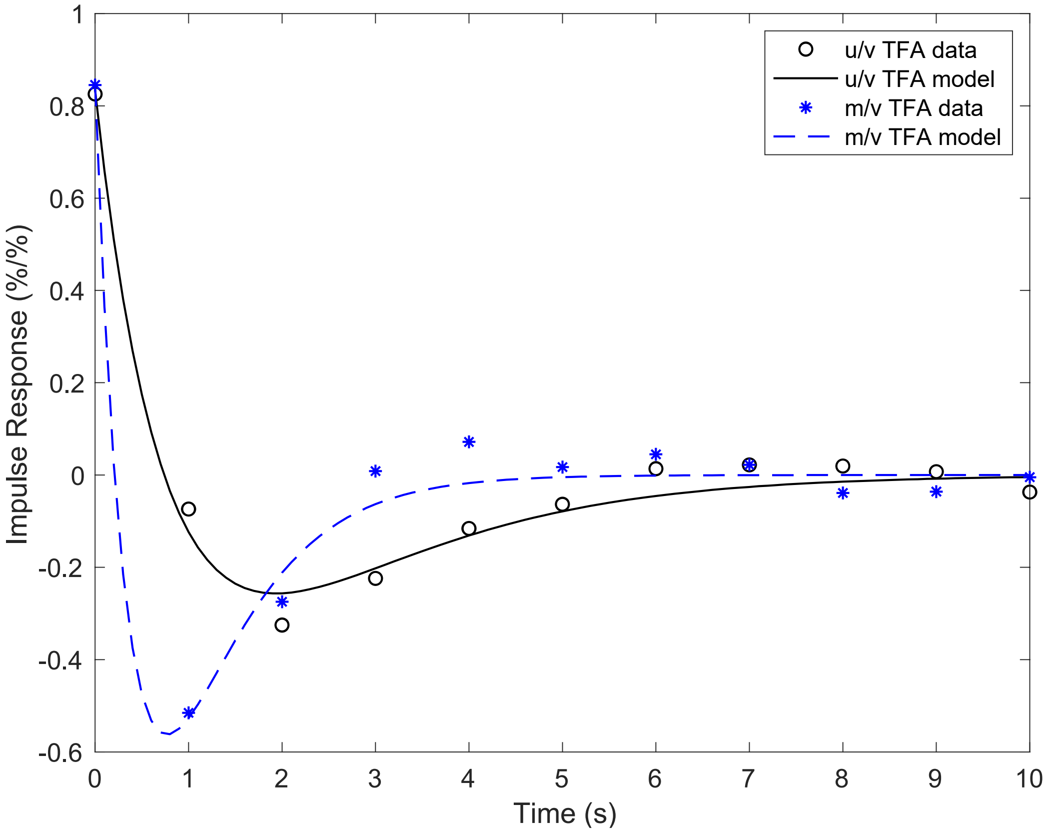

Figure 3.8. Representative pressure-flow impulse responses for a subject during normocapnia, where the experimental impulse response was derived using univariate TFA and multivariate TFA respectively. The normocapnia recording presented here is representative, as the same pattern is observed in the impulse responses for the thigh cuff and hypercapnia conditions. Values represent deviations from the baseline value.

First, the linear mixed effects models that were fitted to the optimised values for each parameter are considered. For two of the parameters optimised using m/v TFA IRs ($S_M/\tau_{M\,(m/v)}$, $S_{V\,(m/v)}$), the residuals are not normally distributed, which could be due to heteroscedasticity or nonlinear relationships between the fixed effects and these physiological model parameters, but alternatively, may indicate that other effect(s) affect these physiological model parameters. Notably this non-normality of the residuals is limited to parameters including a gain and optimised using m/v TFA. An additional effect may therefore be frequency, as a gain parameter is mostly important at higher frequencies and hence such a component would be affected by frequency. It is however not yet clear why m/v TFA, where the effects of CO_2 were regressed out, would highlight an additional effect on gain parameter values and more investigation will be required.

Next, the parameter values optimised using m/v TFA IRs are considered. The results show that the thigh cuff condition produces significant differences in dCA from normocapnia where only spontaneous fluctuations in ABP are present. Specifically, S_M/τ_M is smaller, S_V is larger, and τ_V is larger, indicating that the myogenic (i.e., vasoconstricting) response is attenuated and/or slowed down and the metabolic (i.e., vasodilating) response is larger but slowed down in thigh cuff compared to normocapnia. The thigh cuff condition therefore appears to introduce some additional complexities that appear to impair dCA, specifically when interacting with the CO_2 response. Two potential explanations for this distinction between normocapnia and thigh cuff, both expected to represent intact dCA, could be subjects breathing differently during the experience of thigh cuffs, or increased activation of the sympathetic nervous system in response to large changes in ABP induced by inflation and deflation of the thigh cuffs.

The effects of sympathetic activation have also been widely debated. For example, Jordan *et al.* [30] found that the sympathetic nervous system reduces the effects of CBF increase in response to CO_2 increase, whereas Peebles *et al.* [31] found that the sympathetic nervous system reduces the effects of CBF decrease in response to CO_2 decrease but not vice versa. However, Cassaglia *et al.* [32] showed that sympathetic nervous activation is only triggered in response to a substantial change in ABP, of the order of 50% - which is not achieved in ABP time series for the thigh cuff condition used in this chapter. Gierthmühlen *et al.* [33] also found a lack of sympathetic activation during the thigh cuff test.

3.4.3.Physiological and clinical implications

In this chapter, a simplified model that disentangles the myogenic and metabolic responses of dCA was produced. For the sake of simplicity, the myogenic response was taken to account only for vasoconstriction, as a response to direct stress, and the metabolic response to account only for vasodilation as a response to shear stress, although the true responses are likely a mixture of these pathways. S_M/τ_M represents the magnitude and timing of the myogenic response, where a larger value indicates a larger and/or faster response of vasoconstriction to direct stress when there are changes in ABP, and vice versa. S_V and τ_V represent the magnitude and timing of the metabolic response respectively, where a larger value of S_V indicates a larger response, and a larger value of τ_V indicates a slower response of vasodilation to shear stress when there are changes in ABP, and vice versa. The model indicates that the changes in the underlying dCA mechanisms in hypercapnia may take the form of: smaller and/or slower vasoconstriction in response to direct stress (smaller S_M/τ_M); no effect on the magnitude of vasodilation in response to shear stress (no effect on S_V); and slower vasodilation in response to shear stress (larger τ_V).

In this chapter, the model has been applied to healthy subjects under hypercapnia to simulate impaired dCA, but it can also be applied to subject groups with a known disease, such as stroke, dementia, sickle cell disease, or small vessel disease. The model can then be used to form new hypotheses regarding how underlying mechanisms are affected in specific diseased states.

3.4.4.Study limitations

This work in this chapter combines the use of a physiological model and data-driven analysis using experimental data, so its limitations stem from both model assumptions and practical measurement limitations. The model limitations are discussed in detail in [83], but briefly include no consideration of NVC or the sympathetic response, and the simplified labelling of the feedback mechanisms driving vasoconstriction and vasodilation purely as the myogenic and metabolic responses. In addition, dynamics are only introduced into the model via the myogenic and metabolic time constants, but these two mechanisms are not the only source of dynamics within the cerebral vasculature. Other sources of dynamics, such as the elastic (i.e., passive) response, sensing delays, and the neurogenic response, are therefore also subsumed within these parameters. However, the IRs obtained from the model appear from visual inspection to be second-order rather than of a higher order (Figure 3.5, Figure 3.8), which indicates that any other dynamics have similar time constants to one of the time constants in the model. The passive response occurs before any active autoregulation and the neurogenic response has previously been modelled as a feedforward control mechanism due to its speed [124], so both are possibly captured in the smaller time constant.

Measurement limitations refer to the measurements taken to represent CBF and $PaCO_2$. In this study CBv was taken to represent CBF, which is only true if the MCA cross-sectional area remains constant. $PetCO_2$ was taken to represent $PaCO_2$, as it has been shown that $PetCO_2$ closely resembles $PaCO_2$ measured by blood analysis when using a sequential gas delivery circuit [34]. However, $PetCO_2$ cannot capture the variation in $PaCO_2$ between breaths (which would occur as CO_2 is transported from the brain tissue to the lungs), since only one $PetCO_2$ measurement is available per breath. Time series consisting of interpolated $PetCO_2$ points were used in m/v TFA in this study, since a better non-invasive estimation of $PaCO_2$ is not currently available.

3.5.Conclusion

In this chapter, a simple physiological model was used in conjunction with TFA on experimental data to separate out the myogenic and metabolic responses and investigate how they are affected in impaired dCA. Both the myogenic and metabolic responses were found to be impaired, and the metabolic response to be specifically slowed down. Future work can incorporate the effects of changes in intracranial pressure in the model, extending this approach to consider dCA impairment in brain trauma patients. The differences between results from u/v and m/v TFA, including effects of CO_2, can also be further investigated.

CHAPTER 4

Modelling dynamic cerebrovascular reactivity under different physiological conditions

A version of this chapter is under review as:

- ***van Zijl, N.**, Bulte, D.P., Payne, S.J. 2024. Quantifying dynamic cerebrovascular reactivity under different physiological conditions. IEEE Transactions on Biomedical Engineering. (Under review)*

A version of the results in this chapter was presented at the following conference:

- ***van Zijl, N.**, Bulte, D.P., Payne, S.J. A model of dynamic cerebrovascular reactivity. BioMedEng24. September 5-6, 2024, London, United Kingdom.*

Abstract

CVR is the ability of the cerebral vasculature to respond to a vasoactive stimulus such as CO_2 and is known to be impaired in various pathologies. The dCVR response has been increasingly investigated from a data-driven perspective but with limited mechanistic insights. The objective of this study was to present a physiological model of dCVR that can be used in conjunction with experimental data to provide insights into the underlying physiology of dCVR and how it differs between conditions. A second order physiological model of dCVR was developed, where the response of the vasculature to changes in CO_2 was described by a gain and two time constants. Model parameters were optimised using experimentally derived CO_2-flow IRs under normocapnia and hypercapnia. The IRs were derived by applying a basis expansion technique to experimental recordings of $PetCO_2$ (capnograph), ABP (Finapres), and CBv (TCD in bilateral MCAs). The model produced *the CO_2-flow IR shape most commonly reported in previous data-driven literature. Key findings include that one time constant is significantly affected by physiological condition in all analyses (p-values < 0.001, except one analysis where p-value < 0.05), becoming smaller in hypercapnia compared to normocapnia, and potential sex-specific effects on the gain (p-value < 0.05) and time constants (p-values < 0.001). This study is the first link between the growing body of data-driven dCVR studies and its underlying physiology, allowing for insights into the physiology of dCVR and how it is affected under different physiological conditions.*

4.1.Introduction

CVR is the ability of the cerebrovasculature to dilate or constrict in response to a vasoactive stimulus, most commonly CO_2. It is a widely used biomarker of brain health, known to be impaired in ageing [36] and various pathologies including hypertension [38], stroke [37], and dementia [133]. More recently, interest in the temporal characteristics of CVR has grown [109], [107], [134], [47], [45] leading to the terms, dCVR and CO_2 dynamic vasomotor reactivity, which are used interchangeably in literature. Promising results have been reported, including differences in dCVR between subjects with mild-cognitive deficit and Alzheimer's disease [47], and between patients with Type-2 Diabetes Mellitus and healthy controls [45].

These studies are all from a data-driven perspective, often deriving the CO_2-flow IR [45], [116], [15], where some physiological interpretations can be assigned to its timing parameters. For example, the recent review by Shams *et al.* [116] points out that the time to peak and time to recover to baseline can reflect vasodilatory and vasoconstrictive ability and transit delays [106], and the width at half maximum can reflect a combination of the onset and recovery responsiveness of the vasculature [135]. However, physiological modelling is required for mechanistic insights into the underlying physiology of dCVR. Previous physiological models of CBF control have included the effects of both ABP, via dCA, and CO_2 on CBF, but the effects of CO_2 were modelled as a first order high-pass filter [34], [78], [81], which this study shows cannot produce the CO_2-flow IR shape reported in most previous dCVR studies. Daher and Payne [89] provide a more detailed physiological model of CVR, showing that the vasculature may respond to changes in tissue CO_2 rather than arterial CO_2 during hypercapnia, but the model has many parameters, limiting its use alongside experimental data.

This chapter therefore presents a novel model of dCVR that can produce the commonly reported shape of the CO_2-flow IR and has a physiological basis but remains simple enough for meaningful parameter values to be inferred from experimental data. This chapter takes advantage of the fact that considerable research has gone into deriving the CO_2-flow IR in recent years and the model is prepared in the IR form for parameter optimisation under different physiological conditions. The model is designed as a link between data-driven analysis of dCVR and the underlying physiological mechanisms of dCVR and can be applied under different physiological and pathophysiological conditions. It is intended to reveal specific physiological mechanisms and how they differ in different healthy and diseased states, once differences in its current, more generalised, parameters lead to new hypotheses that can then be tested by inclusion of specifically selected, more detailed pathways within the model.

The rest of this chapter is organised as follows: Section 4.2 describes the methods, including model development, experimental CO_2-flow IR derivation, parameter optimisation, and statistical and sensitivity analysis methods; Section 4.3 presents the results of the model fit, optimised model parameters, and the sensitivity analysis; Section 4.4 discusses the main findings and study limitations, placing them in the context of current literature; and Section 4.5 presents the conclusions and highlights directions for future work.

4.2.Materials and methods

4.2.1.Physiological model development

The haemodynamic model developed in this chapter is an extension of the equivalent electrical circuit model in [81] with compartments for the arteries, capillaries, and veins (Figure 4.1). All three compartments have compliance to allow for changes in blood volume. The arterial compartment is divided into two to allow for a distinction between the large arteries (down to but excluding the large pial arteries) that do not regulate CBF and the smaller arteries and arterioles where most CBF regulation occurs. Resistance and blood volume of the large arteries are therefore assumed to be constant, whereas they are variable for the small arteries and arterioles. A separate compartment for the capillaries with variable resistance and blood volume was modelled, as changes in these variables can play an important role in clinical conditions such as stroke or dementia. The venous compartment is assumed to have constant resistance but variable volume. Intracranial pressure (ICP) is assumed to be constant, as the time constants of changes in ICP are significantly different from those of dCVR. An overview of the model derivation is provided here, and a more detailed derivation is provided in Appendix B.3.

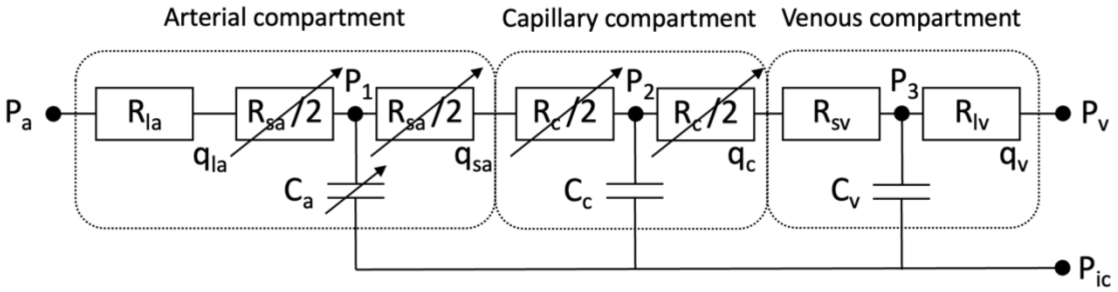

Figure 4.1. Schematic of haemodynamic model. Pa: systemic arterial pressure, R_{la}: resistance of large arteries compartment, P_1, R_{sa}, and C_a: pressure, resistance, and compliance of small (regulating) arteries, P_2, R_c, and C_c: pressure, resistance, and compliance of capillaries compartment, R_{sv}: resistance of small veins, C_v: venous compliance, P_3: small veins pressure; P_v and R_{lv}: pressure and resistance of large veins; P_{ic}, intracranial pressure, $q_{la:}$: large arteries flowrate, q_{sa}: small arteries flowrate, q_c: capillaries flowrate, q_v: veins flowrate.

Total arterial volume is assumed to consist of a constant volume, V_{la}, corresponding to the non-regulating vessels, and a variable volume, V_{sa}, corresponding to the regulating vessels:

$$V_a = V_{la} + V_{sa} \tag{4.1}$$

From the Poiseuille equation, relationships between volume and resistance can be obtained:

$$\frac{V_{sa}}{\overline{V}_{sa}} = \sqrt{\frac{\overline{R}_{sa}}{R_{sa}}} \tag{4.2}$$

$$\frac{V_c}{\overline{V}_c} = \sqrt{\frac{\overline{R}_c}{R_c}} \tag{4.3}$$

The definition of compliance provides relationships between volume and pressure:

$$\frac{dV_{sa}}{dt} = \frac{d}{dt}\left(C_a(P_1 - P_{ic})\right) \tag{4.4}$$

$$\frac{dV_c}{dt} = C_c\frac{d}{dt}(P_2 - P_{ic}) \tag{4.5}$$

$$\frac{dV_v}{dt} = C_v\frac{d}{dt}(P_3 - P_{ic}) \tag{4.6}$$

Volumes and pressures can then be calculated from volume balances in each compartment, assuming no significant changes in blood density:

$$\frac{\mathrm{dV}_{sa}}{dt}=\frac{P_a-P_1}{R_{la}+R_{sa}/2}-\frac{P_1-P_2}{R_{sa}/2+R_c/2} \tag{4.7}$$

$$\frac{\mathrm{dV}_{c}}{dt}=\frac{P_1-P_2}{R_{sa}/2+R_c/2}-\frac{P_2-P_3}{R_c/2+R_{sv}} \tag{4.8}$$

$$\frac{\mathrm{dV}_{v}}{dt}=\frac{P_2-P_3}{R_c/2+R_{sv}}-\frac{P_3-P_v}{R_{lv}} \tag{4.9}$$

CBF in the large arteries, which include the MCAs where the CBv recordings used in this study were measured, is calculated as:

$$q_{la}=\frac{P_a-P_1}{R_{la}+R_{sa}/2} \tag{4.10}$$

dCVR is assumed to modify arterial compliance in response to the logarithm of changes in CO2 pressure. The choice of logarithm follows the approach in [78] and emphasises that the response of the cerebral vasculature to CO2 is linearly correlated with pH in the perivascular space (as pH is related to $P_{a,CO2}$ via its logarithm). The control mechanism of dCVR is described by a second order model, with a gain, G_a, and two time constants, τ_{a1} and τ_{a2}:

$$\tau_{a1}^2\frac{d^2C_a(t)}{dt}+\tau_{a2}\frac{dC_a(t)}{dt}+C_a(t)=G_a\log_{10}\left(\frac{P_{a,CO2}(t)}{\bar{P}_{a,CO2}}\right) \tag{4.11}$$

A previous version of the model allowed dCVR to also modify capillary compliance, but preliminary results (available in Appendix B.1) showed no improvement in model fit compared to the simpler model with constant capillary compliance, so constant capillary compliance is assumed here. All model parameters are provided in Table 4.1. More detailed validation of the model can be performed in future, but all model parameter values are in line with previous studies, as shown in Appendix B.2.

Table 4.1. Haemodynamic model parameter values.

Parameter	Value	Description	Source
R_{la}	0.4 mmHg s/mL	Resistance of large (non-regulating) arteries	[81]
$\bar{R}_{sa}$	5.03 mmHg s/mL	Baseline resistance of small (regulating) arteries	[81]
R_{lv}	0.56 mmHg s/mL	Resistance of large veins	[81]
$\bar{P}_a$	100 mmHg	Baseline arterial blood pressure	[81]
P_v	6 mmHg	Venous outlet pressure	[81]
V_{la}	1 mL	Volume of large (non-regulating) arteries	[81]
$\bar{V}_{sa}$	12 mL	Baseline volume of small (regulating) arteries	[81]
P_{ic}	10 mmHg	Intracranial pressure	[81]
$\bar{C}_a$	0.205 mL/mmHg	Baseline arterial compliance	[81]
k_{ven}	0.186 mL^{-1}	Elastance coefficient for venous compliance	[81]
P_{v1}	-2.25 mmHg	Pressure offset for venous compliance	[81]
$\bar{P}_{a,CO2}$	40 mmHg	Baseline arterial CO_2 pressure	[81]
$\bar{R}_c$	0.107 mmHg s/mL	Baseline resistance of capillaries	App. B.2
$\bar{R}_{sv}$	1.21 mmHg s/mL	Baseline resistance of small veins	App. B.2
$\bar{V}_c$	4.79 mL	Baseline volume of capillary compartment	App. B.2
$\bar{C}_c$	0.162 mL/mmHg	Baseline capillary compliance	App. B.2
$\bar{P}_1$	62.5 mmHg	Steady state pressure in the arteries	App. B.2
$\bar{P}_2$	29.5 mmHg	Steady state pressure in the capillaries	App. B.2
$\bar{P}_3$	12.2 mmHg	Steady state pressure in the veins	App. B.2
$\bar{q}_{la}$	12.9 mL/s	Steady state flow rate through large arteries	App. B.2
$\bar{q}_{sa}$	12.9 mL/s	Steady state flow rate through small arteries	App. B.2
$\bar{q}_c$	12.9 mL/s	Steady state flow rate through capillaries	App. B.2
$\bar{q}_v$	12.9 mL/s	Steady state flow rate through veins	App. B.2

The model was linearised in terms of deviation variables (i.e., small changes from baseline) and converted to the Laplace domain for simplification (as shown in Appendix B.3). The overall CO_2-flow transfer function was derived analytically in the Laplace domain (available in Appendix B.3) and then converted back to the time domain using the inverse Laplace transform to obtain the model-based CO_2-flow IR.

4.2.2.Data

The analysed data are taken from an experimental vital-sign dataset[6] [125] recorded from 20 healthy subjects (10 males; age 25.5 ± 3.5 years, height 168 ± 12 cm, weight 64 ± 16 kg) in supine position with head elevation in Southampton General Hospital. Recordings were taken at rest under two physiological conditions: normocapnia (18 min) and hypercapnia, achieved with 5% inspired CO_2 (5 min). The multivariate recordings include $PetCO_2$ (infrared capnograph) and beat-averaged CBv (TCD in bilateral MCAs) and ABP (Finapres), all at a SF of 10 Hz. The dataset contains five multivariate recordings per subject, totalling 100 recordings per physiological condition, all used individually to increase the sample size. Due to poor quality or missing signals for any of the physiological measurements, three normocapnia and eight hypercapnia recordings were excluded, so 97 normocapnia and 92 hypercapnia recordings were used for analysis.

The $PetCO_2$ and beat-averaged CBv and ABP recordings were pre-processed to fill missing values where artefacts had been removed using linear interpolation, sub-sampled to 2 Hz for this chapter, and their z-scores were used for analysis. The SF of 2 Hz was selected as a compromise between a desired lower SF for $PetCO_2$ time series that has a true SF of around 0.2 Hz and a desired higher SF for improved temporal resolution in the basis functions during IR derivation (see Section 4.2.3) that must have the same SF as the input-output data.

---

[6] Data collection and pre-processing to produce beat-averaged CBv time series and end-tidal CO_2 time series were performed by Dr Dragana Nikolic, Prof David Simpson, and Dr Tony Birch. This is the same dataset that was used in Chapter 3, where a more detailed description is provided.

4.2.3.Data-based impulse response derivation

Two sets of CO_2-flow IRs were derived from the data: first using a single-input-single-output (SISO) approach where $PetCO_2$ is the input and CBv is the output; and second using a multiple-input-single-output (MISO) approach to regress out the effects of ABP, where $PetCO_2$ and ABP are inputs and CBv is the output. TFA produced CO_2-flow IRs with oscillations, as shown and discussed in Appendix B.4, and was therefore not used in this chapter. For the SISO approach, the CO_2-flow IRs were derived using a basis expansion method recommended by the recent review by Shams *et al.* [116], which is briefly outlined here. The IR, $h(m); m = 0, \dots, M-1$, is equivalent to the Volterra kernel of the first-order discrete Volterra Model (DVM):

$$\mathrm{y(n)} = \sum_{m=0}^{M-1} h(m)x(n-m) + \epsilon(n); n = 1, \dots, N \qquad (4.12)$$

where y is the output (CBv in this case), x is the input ($PetCO_2$ in this case), ϵ is noise, M is the memory of the system (i.e., the number of samples in the discrete IR), and N is the number of input-output sample points.

The IR was derived using a basis expansion technique in terms of an orthonormal basis set [136]:

$$\mathrm{h}(m) = \sum_{j=0}^{p-1} c_j b_j(m) \qquad (4.13)$$

where b_j is a set of p orthonormal basis functions (i.e., p is the model order):

$$\{b_j(m);\ j = 0, \dots, p-1;\ m = 0, \dots, M-1\} \qquad (4.14)$$

c_j is the set of unknown expansion coefficients of the basis functions. To solve for the unknown expansion coefficients, the DVM is expressed in a compact matrix form by combining (12) and (13) [15]:

$$\mathbf{y} = \mathbf{Vc} + \boldsymbol{\epsilon} \tag{4.15}$$

where **V** is a matrix of values which are convolutions of the input with the basis functions, and the vector **c** of unknown coefficients can be derived using ordinary least squares [15]:

$$\hat{\boldsymbol{c}}_{\boldsymbol{OLS}} = [\boldsymbol{V}^T\boldsymbol{V}]^{-1}\boldsymbol{V}^T\boldsymbol{y} \tag{4.16}$$

Spherical Laguerre basis functions [137] were used:

$$\mathrm{b_j}(n) = \sqrt{\frac{j!}{(j+2)!}\frac{e^{\frac{-n}{2\alpha}}}{\sqrt{\alpha^3}}}L_j^{(2)}(n/\alpha) \tag{4.17}$$

where α is the exponential decay parameter and $L_j^{(2)}$is the j-th generalised Laguerre polynomial of order two [137]:

$$L_j^{(2)}(n) = \sum_{r=0}^{j}\binom{j+2}{j-r}\frac{(-n)^r}{r!} \tag{4.18}$$

The spherical Laguerre basis functions $b_j(n)$ are orthonormal with respect to a radial inner product, whereas $n \times b_j(n)$ can be viewed as basis functions that are orthogonal in Cartesian coordinates [137] and are therefore used as the set of basis functions to derive the IR in this work. The length of the CO_2-flow IR (and hence the basis functions) was set to 25 seconds, corresponding to the length of the CO_2-flow IR derived using TCD data (as in this work; see Section 4.2.2) in [113].

Hyperparameters, α and p, were set as 0.7 and 3 respectively, selected as the average values of individual grid searches minimising the Bayesian Information Criterion

(BIC) for each recording, as recommended by the CARNet white paper [97], where BIC is [138]:

$$BIC = \ln\left(\frac{\sum_{n=1}^{N} e^2(n)}{N}\right) + \frac{p\ ln(N)}{N} \tag{4.19}$$

In the grid searches, values for α ranged from 0.5 to 0.9 with step size 0.1 and values for p ranged from 2 to 4, as in [116]. Only normocapnia recordings were used in each grid search, following the approach of [139] and [140], where global basis functions were selected using only the healthy control subjects.

For the MISO approach, the method explained above is extended to include ABP as a second input, now deriving both the CO2-flow IR, $h_{CO2}(m)$, and the pressure-flow IR, $h_p(m)$ [97], so (4.12) becomes:

$$\mathrm{y(n)} = \sum_{m=0}^{M_1-1} h_{CO2}(m)x(n-m) + \sum_{m=0}^{M_2-1} h_p(m)x(n-m) + \epsilon(n); n = 1, \dots, N \tag{4.20}$$

Laguerre basis functions were used for the pressure-flow IR, $h_p(m)$, as in [97], and its length was set to 10 seconds, corresponding to the length of pressure-flow IRs reported in literature [113], [141]. For the MISO approach, the hyperparameters, α and p, for $h_{CO2}(m)$ were kept the same as for the SISO approach, and the hyperparameters for $h_p(m)$ were set as 0.2 and 4 respectively, selected as the average values of a grid search minimising BIC over values of α ranging from 0.1 to 0.9 and values of p ranging from 1 to 8, as recommended by [97]. All IRs were derived using a custom function produced in MATLAB, which was tested and shown to correctly identify a known ground truth IR, as shown in Appendix B.5.

4.2.4.Data-based impulse response acceptance

Data-based IRs were accepted or rejected based on sets of criteria regarding (1) statistical significance, (2) physiological plausibility, (3) goodness of fit to the physiological model. Two sets of analyses were completed: the first where only the first two criteria had to be met for an IR to be accepted, and the second where all three criteria had to be met for an IR to be accepted. In the first analysis, a wider range of IRs can be included in the analysis, but results may be affected by poorer model fit; in the second analysis, a good model fit is required but fewer IRs can be included in the analysis. The number of IRs accepted in each analysis is shown in Table 4.2. The slight differences between the number of accepted left and right hemisphere IRs may be due to data quality, although in most cases IRs from pairs of hemispheres are either both accepted or both rejected, as shown in Appendix B.7.

Table 4.2. Number of IRs (out of 97 normocapnic and 92 hypercapnic IRs available per hemisphere) accepted for further analysis. SISO: single-input-single-output, MISO: multiple-input-single-output, LH: left hemisphere, RH: right hemisphere.

	Normocapnia				*Hypercapnia*			
	SISO		MISO		*SISO*		*MISO*	
	LH	RH	LH	RH	*LH*	*RH*	*LH*	*RH*
				Analysis 1				
Female	17	22	24	29	*33*	*34*	*41*	*40*
Male	27	26	35	33	*32*	*36*	*40*	*41*
				Analysis 2				
Female	10	15	12	16	*29*	*28*	*33*	*33*
Male	16	18	17	18	*12*	*19*	*21*	*23*

For the first criterion, the “boot-strapping” method from [45] was used to determine the statistical significance of the derived CO_2-flow IRs, since the basis expansion method for IR gives a results (that can resemble a plausible CO_2-flow shape) even if there is no relationship between the input and output time series, as shown in

Appendix B.6. Under the Null Hypothesis that there is no predictive relationship between the input and output time series, the output time series were randomly shuffled and 1000 "null" IRs and their corresponding predicted outputs and normalised mean square errors (NMSEs) were derived. The histogram of the "null" NMSEs was constructed and confidence intervals determined using the *t*-test at 5% significance level. For the MISO case, "null" ABP-flow IRs were first derived and then "null" CO_2-flow IRs were derived using the difference between the measured and predicted (using the ABP-flow IR) CBv time series as output. The lower limits of the "null" %NMSE confidence intervals were 96.5 and 91.0 for the SISO and MISO cases respectively. Derived CO_2-flow IRs with %NMSEs above the lower limit of the %NMSE threshold were excluded from further analysis.

For the second criterion, the derived CO_2-flow IRs were classified as "non-physiological" and excluded from further analysis if the initial response is negative. For the third criterion, only IRs with NMSE from fitting to the physiological model below or equal to 0.3, a metric proposed by Panerai *et al.* [126] for dCA SRs fitting to the model of Tiecks *et al.* [98], were accepted.

4.2.5.Model parameter optimisation

Model parameters were optimised by fitting the model to each of the data-based CO_2-flow IRs, using the lsqnonlin function in MATLAB. Optimising model parameters using an IR follows the approach from [114], and is advantageous because the IR is not affected by potential nonlinearities in the CO_2-flow relationship , as it represents the linear component independently from the non-linear components. The three parameters (G_a, τ_{a1}, τ_{a2}) that describe the dCVR response were constrained to be non-negative to maintain physiological plausibility. A set of initial conditions for the parameters were obtained by pre-fitting the model to the CO_2-flow IR reported in [113]. Since the data-based IRs in this study exhibit a faster response than in [113], a new set of initial conditions were obtained from a model fit to a recording in this study that had a small SSEs and fit well according to visual inspection.

4.2.6.Statistical analysis

Optimised values of each parameter further than three multiples of the quartile deviation from the median were removed as outliers in the first analysis (see Section 4.2.4). No parameter values were removed as outliers in the second analysis (see Section 4.2.4) to conserve larger sample sizes for statistical analysis, as a strict criterium for goodness of fit to the physiological model had already been applied.

In both analyses, the values of each model parameter were analysed using linear mixed effects models to account for the non-independence introduced into the data by multiple recordings from the same subject. Brain hemisphere, sex, and physiological condition were set as fixed effects and subject as a random effect:

$$\begin{aligned} MP = \beta_0 + \beta_1 * PC + \beta_2 * BH + \beta_3 * S + \beta_4 * (PC \times BH) + \beta_5 * (PC \times S) \\ + \beta_6 * (BH \times S) + \beta_7 * (PC \times BH \times S) + u_{subject} + \epsilon \end{aligned} \tag{4.21}$$

where MP is model parameter, PC is physiological condition, BH is brain hemisphere, S is sex, β_0 is the fixed effects intercept, $\beta_1, \beta_2, \dots, \beta_7$ are the coefficients for the fixed effects and their interactions, $u_{subject}$ is the random intercept for each subject, and ϵ is the residual error. Normality of the resulting residuals was tested for using the D'Agostino-Pearson test, as normally distributed residuals is a required condition for inferences to be made from linear mixed effects models. In cases where the residuals were not normally distributed, the linear mixed effects model was fitted to the transformed parameter values (the square, cube, logarithm, and Box Cox transformation) and the residuals checked for normality again.

Three-Way ANOVA was performed on each linear mixed effects model to test for significant effects of brain hemisphere, sex, and physiological condition. Since Three-Way ANOVA on the linear mixed effects model can only test whether a fixed effect or interaction effect (e.g., the interaction between physiological condition and sex) has a significant effect on the model parameter, but not between which pairs of group means the significant difference is (e.g., between normocapnia in men and hypercapnia in men, or between normocapnia in women and hypercapnia in women), *post-hoc* analysis was performed to assess the significance of differences between pairs of group means. Multiple comparisons were accounted for by using Tukey's correction during *post-hoc* analysis, as it is a popular choice to correct for multiple comparisons and more powerful than the Bonferroni correction. All statistical analyses were done using R statistical software version 4.2.2.

4.2.7.Sensitivity analysis

A sensitivity analysis was performed to investigate whether the value of each model parameter affects the model output to give an indication of the robustness of model parameter optimisation. The Elementary Effects method was implemented using the SAFE toolbox [23]. This technique varies the values of the parameter values within their given ranges and calculates two sensitivity metrics to quantify their effect on the model output: the mean of elementary effects (EEs), quantifying the influence of each parameter on the variability of the output; and the standard deviation of EEs, quantifying the non-linearity and/or interaction effects of each parameter. Parameter ranges were set as ± 20% of their mean normocapnia values obtained in this study.

Since EEs method is set up for a scalar model output and the model output in this study is a time-dependent IR, the CO_2-flow IR characteristic metrics summarised in [116] were used as scalar model outputs (Figure 4.2):

1. Time to peak (TTP): the time taken for the IR to reach its positive peak.
2. Time to half maximum (TTH): the time taken for the IR to recover to half of its positive peak.
3. Full width at half maximum (FWHM): the width of the IR at the points of half maximum.
4. Area under curve (AUC): the area under the curve, which corresponds to the magnitude of static CVR.

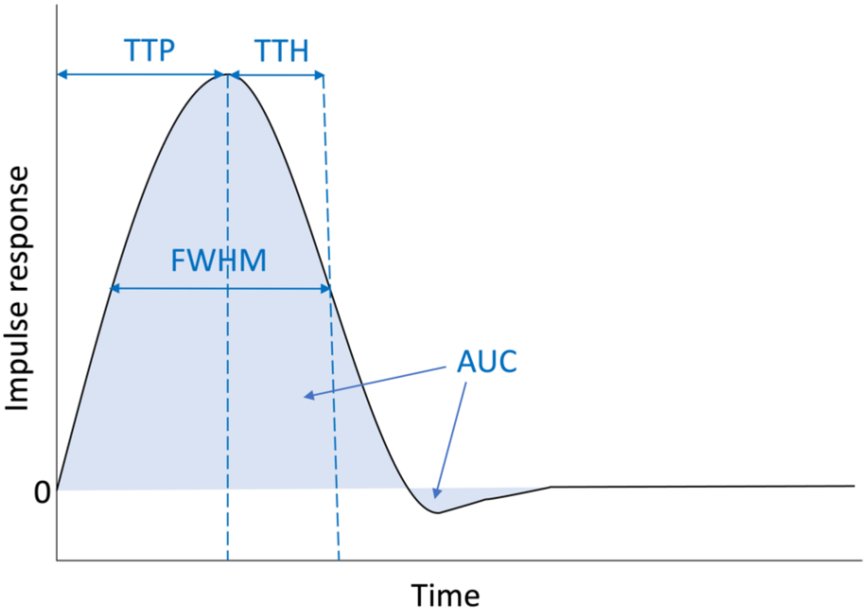

Figure 4.2. Illustration of the CO2-flow IR characteristic metrics based on the diagram in [116]. TTP: time to peak, TTH: time to half maximum, FWHM: full width at half maximum, AUC: area under curve.

4.3.Results

4.3.1.Model fit

The second order (SO) dCVR model proposed in this study produces the CO_2-flow IR shape reported in most previous studies that derived data-based CO_2-flow IRs,

[113], [142], [15], and used as the ground truth in the recent review paper by Shams *et al.* [116] that tested different CO_2-flow IR derivation methods on simulated data. The beginning of the IR, up until the first peak, is described by the model's first time constant, τ_{a1}, and the rest of the IR, settling to baseline after the first peak, is described by the model's second time constant, τ_{a2}. Figure 4.3 benchmarks the SO model against a first order (FO) model and a first order time delay (FOTD) model for the range of data-based CO_2-flow IR shapes obtained in this study, categorised as (a)-(h).

In Figure 4.3(a)-(b), the SO model fits the CO_2-flow IR well and is clearly an improvement on the FO and FOTD models, neither of which can produce the CO_2-flow IR shape described in [116]. In some cases that resemble Figure 4(b), the SO model struggles to fit to an undershoot that has a large amplitude or slower dynamics than the initial response and can only capture part of or the beginning of the undershoot. The SO model fit is poorer for the tail-end of IRs with overshoots, whether the overshoot is small and in the absence of an undershoot (Figure 4.3(d)) or large and in the presence of an undershoot as part of overall more oscillatory behaviour (Figure 4.3(c)), although it is still an improvement on the FO and FOTD models. If the data-based IR has a small initial overshoot (sometimes followed by a small undershoot), the SO model stretches its response (Figure 4.3(e)), resulting in a lower amplitude than the data-based IR but still a better fit than the FO and FOTD models.

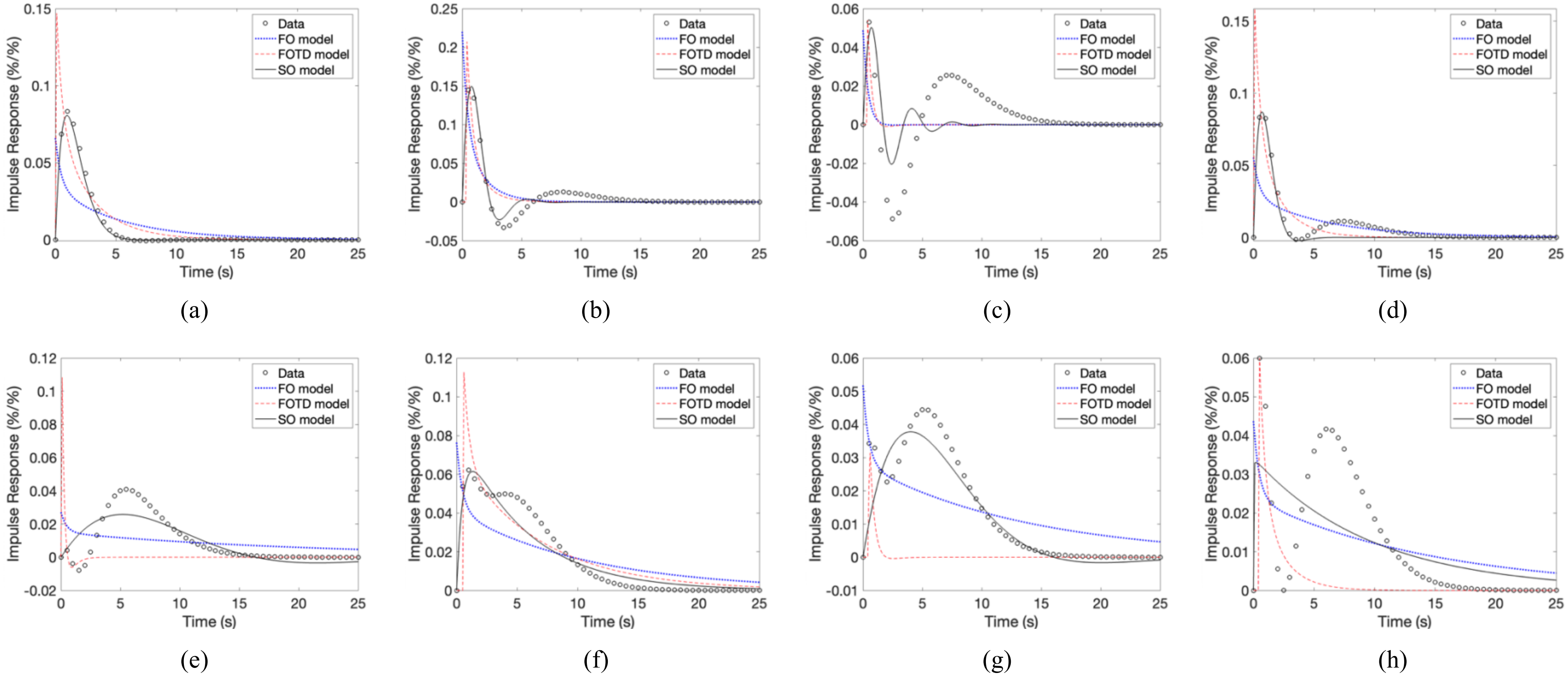

(a) (b) (c) (d)

(e) (f) (g) (h)

Figure 4.3. Representative model fit to data-based IRs with (a) no undershoot or overshoot, (b) an undershoot, (c), more oscillatory behaviour giving a larger undershoot and overshoot, (d) an overshoot, (e) an initial undershoot, (f) two peaks with similar amplitudes (where the first peak has the larger amplitude) and a small dip between them, (g) two peaks with similar amplitudes (where the second peak has the larger amplitude) and a small dip between them, (h) two peaks with similar amplitudes with a large dip (approaching or reaching the x-axis) between them.

If the data-based IR has two separate peaks with a shallow dip between them, the SO model fits one peak over both peaks, whether the first (Figure 4.3(f)) or second (Figure 4.3(g)) peak has the larger amplitude relative to the other, again producing a better fit than the FO and FOTD models. For IRs with a deeper dip (approaching or reaching the x-axis) between two peaks, the SO model produces a poorer overall fit, approaching the FO model fit (Figure 4.3(h)). Depending on the placement of the higher order dynamics (i.e., the undershoots, overshoots, and second peaks) in the data-based IRs, they can affect the values of τ_{a1} when they are in the beginning of the response (as seen in Figure 4.3(e),(g)), and τ_{a2}, when they are in the tail-end of the response (as seen in Figure 4.3(c),(f),(h)).

A sample of model fits to 10% of the 510 data-based IRs (accepted based on the first two criteria in Section 4.2.4, i.e., without goodness of fit requirements) were visually inspected and categorised according to the model fit in Figure 4 that they most closely resemble, as reported in Table 4.3. The sample consisted of 13 IRs per category: SISO CO_2-flow IR under normocapnia, SISO CO_2-flow IR under hypercapnia, MISO CO_2-flow IR under normocapnia, MISO CO_2-flow IR under hypercapnia).

Table 4.3. Distribution of 10% sample (i.e., 52 IRs) of model fits to the range of data-based IRs shown in Figure 4.3(a)-(h). N: normocapnia, H: hypercapnia.

		(a)	(b)	(c)	(d)	(e)	(f)	(g)	(h)
SISO	N	2	1	4	1	-	1	1	3
	H	-	2	9	1	-	-	-	1
MISO	N	2	-	1	4	1	1	-	4
	H	-	5	6	1	-	-	-	1
Total		3 (5.9%)	8 (15.7%)	20 (39.2%)	7 (13.7%)	1 (2.0%)	2 (3.9%)	1 (2.0%)	9 (17.6%)

Most (39.2%) of the model fits most closely resemble the behaviour in Figure 4(c), although it should be noted that many of those IRs had undershoots and overshoots with smaller amplitudes than the example shown in Figure 4(c). In the first analysis in this study (as defined in Section 4.2.4), no constraints were placed on the level of higher order dynamics exhibited by the data-based IRs and the full range of data-based IRs (and corresponding model fits) shown in Figure 4.3 (and quantified in Table 4.3) were included; in the second analysis, a requirement for goodness of fit to the SO physiological model was applied, which constrains the shape of accepted IRs and hence excludes cases that resemble Figure 4(c) (for cases with large undershoot and/or overshoot amplitudes) and Figure 4(h).

4.3.2.Optimised model parameter values

The three model parameters (G_a, τ_{a1}, τ_{a2}) were optimised using the normocapnic and hypercapnic, SISO (Table 4.5) and MISO (Table 4.7) CO_2-flow IRs accepted for each of the two analyses (as defined in Section 4.2.4). Linear mixed effects models were used to account for non-independence in the data stemming from multiple recordings per subject; their residuals were tested for normality (Table 4.4). The residuals are not normally distributed, which could be attributed to heteroscedasticity, non-linear relationships between the fixed effects and physiological model parameters, or the influence of additional, unmodelled effects. Residuals' normality was achieved for $\tau_{a1\ (Analysis\ 1,MISO)}$, $\tau_{a2\ (Analysis\ 2,SISO)}$, and $\tau_{a2\ (Analysis\ 2,MISO)}$ by taking the logarithm, and for all the other parameters by taking the Box Cox transformation, which are used for further analysis.

Three-Way ANOVA and, where significance was found, *post-hoc* analyses were performed on the linear mixed effects models for each of the dCVR model parameters, with the SISO and MISO results shown in Table 4.6 and Table 4.8 respectively. In the first analysis, where no constraint was placed on goodness of fit to the physiological model and a wider range of data-based IRs were included, the SISO and MISO Three-

Way ANOVA results both indicate that the gain parameter, G_a, is significantly affected by the interaction between physiological condition and sex. However, in both cases, *post-hoc* analysis with a correction for multiple comparisons reveals that G_a is not significantly different between normocapnia and hypercapnia in women or men.

Table 4.4. The p-values from application of the D'Agostino-Pearson test for normality on residuals from fitting different transformations of the optimised parameter values to linear mixed effects models. Shaded cells indicate p-values that show the residuals are normally distributed.

	Analysis 1			**Analysis 2**		
SISO	$\boldsymbol{G_a}$	$\boldsymbol{\tau_{a1}}$	$\boldsymbol{\tau_{a2}}$	$\boldsymbol{G_a}$	$\boldsymbol{\tau_{a1}}$	$\boldsymbol{\tau_{a2}}$
Original data	0.0225	8.76e-10	3.86e-10	0.00313	1.62e-12	1.96e-08
Square root	9.31e-9	6.62e-13	9.47e-15	3.76e-11	< 2.2e-16	< 2.2e-16
Cube root	8.75e-16	4.92e-16	< 2.2e-16	< 2.2e-16	< 2.2e-16	< 2.2e-16
Logarithm	3.18e-5	9.05e-7	0.0191	7.34e-07	4.96e-08	0.389
Box Cox ($\boldsymbol{x_{transform}} = \boldsymbol{x^{\lambda}}$)	0.851 ^{a}	0.117 ^{b}	0.183 ^{c}	0.838 ^{a}	0.224 ^{b}	-
MISO	$\boldsymbol{G_a}$	$\boldsymbol{\tau_{a1}}$	$\boldsymbol{\tau_{a2}}$	$\boldsymbol{G_a}$	$\boldsymbol{\tau_{a1}}$	$\boldsymbol{\tau_{a2}}$
Original data	0.00621	0.0327	1.78e-14	0.000198	< 2.2e-16	0.000373
Square root	3.66e-12	1.38e-5	< 2.2e-16	2.23e-15	< 2.2e-16	3.94e-12
Cube root	< 2.2e-16	3.86e-9	< 2.2e-16	< 2.2e-16	< 2.2e-16	< 2.2e-16
Logarithm	2.04e-14	0.190	0.00326	0.000108	5.55e-14	0.779
Box Cox ($\boldsymbol{x_{transform}} = \boldsymbol{x^{\lambda}}$)	0.332 ^{d}	-	0.856 ^{e}	0.597 ^{f}	0.195 ^{g}	-

With Box Cox parameters, $\boldsymbol{\lambda}$, of ^{a} 0.586, ^{b} -2, ^{c} -0.424, ^{d} 0.545, ^{e} -0.303, ^{f} 0.424, ^{g} 0.384.

The first analysis' SISO and MISO results also show that both time constants, τ_{a1} and τ_{a2}, are significantly affected by physiological condition. Interestingly, the means of τ_{a1} are larger and the means of τ_{a2} are smaller in hypercapnia compared to normocapnia, indicating that part of the dCVR response is sped up and another part is slowed down in hypercapnia. The SISO results show that τ_{a1} is significantly affected by the interaction between physiological condition and sex, and the MISO results show that is the case for both τ_{a1} and τ_{a2}. The *post-hoc* analysis results show that the significant difference of τ_{a1} in hypercapnia compared to normocapnia is specifically found in women and not in men (in both the SISO and MISO results); and that the significant difference of τ_{a2} in hypercapnia compared to normocapnia is specifically found in men and not in women (in the MISO results).

In the second analysis, where a requirement for goodness of fit to the physiological model constrained the data-based IRs that could be included, the SISO results show that G_a is significantly affected by physiological condition and by the interaction between physiological condition and sex, where *post-hoc* analysis revealed that the difference between normocapnia and hypercapnia is in men but not women. The means of G_a in men are larger in hypercapnia compared to normocapnia, indicating that the magnitude of the dCVR response increases during hypercapnia, which is surprising and discussed more in Section 4.4.2. The MISO results, however, show that G_a is not significantly affected by physiological condition, sex, brain hemisphere or any interactions between them.

The second analysis' SISO results show that both time constants, τ_{a1} and τ_{a2}, are significantly affected by physiological condition, whereas the MISO show this only for τ_{a2}. In agreement with the first analysis, the means of τ_{a1} are larger (in the SISO results) and the means of τ_{a2} are smaller (in the SISO and MISO results) in hypercapnia compared to normocapnia. The second analysis' SISO results also show that two interaction effects significantly affect τ_{a1}: the interaction between physiological condition and sex, and the interaction between physiological condition and brain hemisphere. These findings are driven by values that are larger ($\tau_{a1} > 3$ s) than the main distribution of τ_{a1} (Figure 4.4). Although the strict physiological model goodness of fit requirement likely only resulted in physiologically plausible values, these larger values may have been affected by known vascular risk factors, such as body mass index, hyper- or hypotension, or smoking, that were not accounted for in this study. Furthermore, three of the eight $\tau_{a1} > 3$ s values in this study belong to the same subject (female, normocapnia, right hemisphere), indicated by a black outline in Figure 4.4. When the analysis is repeated without that subject, the significance of both interaction effects falls away (Table 4.6).

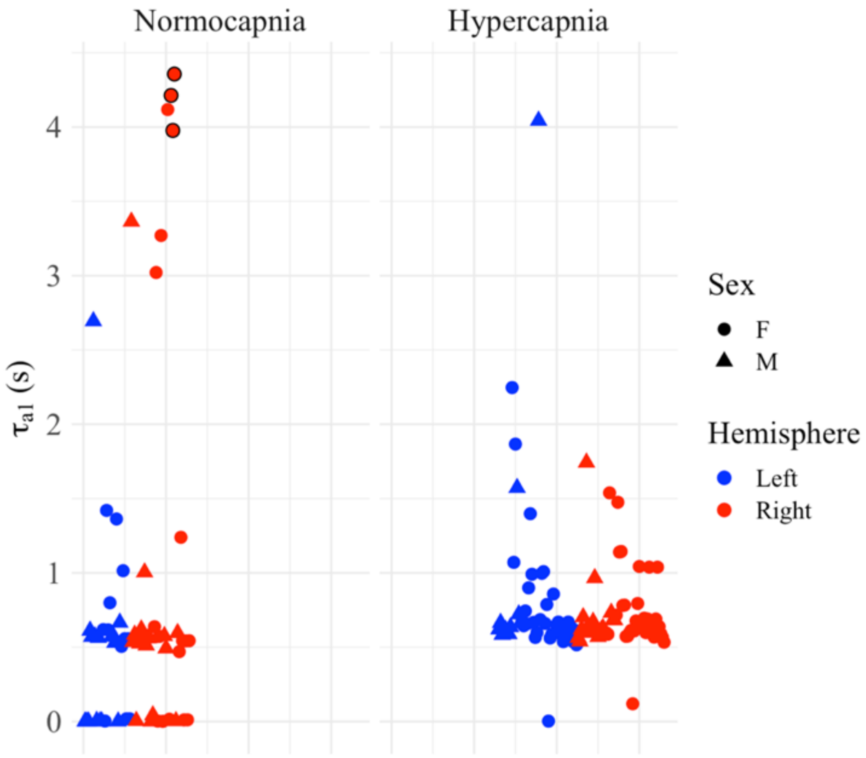

Figure 4.4. Scatter plot of the τ_{a1} values in the second analysis. The three large values from the same subject are indicated by a black outline. F: female, M: male.

Table 4.5. Distribution of parameter values according to sex, brain hemisphere, and physiological condition, optimised using impulse responses from the **SISO** approach. Values are **mean ± SD.** LH: left hemisphere, RH: right hemisphere, F: female, M: male.

		Analysis 1				**Analysis 2**			
		Normocapnia		*Hypercapnia*		Normocapnia		*Hypercapnia*	
		LH	RH	*LH*	*RH*	LH	RH	*LH*	*RH*
G_a	F	0.587 ± 0.393	0.679 ± 0.349	*0.683 ± 0.281*	*0.658 ± 0.296*	0.650 ± 0.340	0.645 ± 0.285	*0.611 ± 0.326*	*0.643 ± 0.308*
	M	0.582 ± 0.332	0.556 ± 0.296	*0.462 ± 0.308*	*0.491 ± 0.288*	0.519 ± 0.224	0.447 ± 0.277	*0.735 ± 0.320*	*0.716 ± 0.319*
τ_{a1} (s)	F	0.542 ± 0.0840	0.589 ± 0.147	*0.656 ± 0.105*	*0.638 ± 0.107*	0.625 ± 0.477	1.53 ± 1.72	*0.769 ± 0.388*	*0.739 ± 0.278*
	M	0.590 ± 0.0973	0.574 ± 0.0419	*0.569 ± 0.0694*	*0.576 ± 0.0607*	0.461 ± 0.663	0.617 ± 0.736	*0.994 ± 0.998*	*0.704 ± 0.268*
τ_{a2} (s)	F	1.87 ± 1.68	1.82 ± 1.76	*1.18 ± 0.882*	*1.21 ± 1.11*	3.52 ± 2.91	3.94 ± 2.52	*1.35 ± 1.55*	*1.08 ± 0.789*
	M	1.60 ± 1.54	1.76 ± 1.78	*0.511 ± 0.199*	*0.525 ± 0.211*	3.06 ± 3.20	2.80 ± 3.65	*1.04 ± 1.09*	*0.901 ± 0.692*

Table 4.6. The p-values from the Three-Way **ANOVA** and ***post-hoc*** for the **SISO** results. LH: left hemisphere, RH: right hemisphere, F: female, M: male, PC: physiological condition, BH: brain hemisphere, S: sex. Shaded cells indicate statistical significance.

	Analysis 1									**Analysis 2**								
	ANOVA							*post-hoc*		ANOVA							*post-hoc*	
	PC	BH	S	PC:BH	PC:S	BH:S	PC:BH:S	N vs. H (in F)	N vs. H (in M)	PC	BH	S	PC:BH	PC:S	BH:S	PC:BH:S	N vs. H (in F)	N vs. H (in M)
G_a	0.728	0.393	0.189	0.497	0.0432	0.533	0.152	0.679	0.281	0.0106	0.839	0.653	0.604	0.0413	0.306	0.656	0.980	0.0119
τ_{a1}	6.90e-4	0.381	0.649	0.363	1.37e-5	0.648	0.143	8.00e-4	0.889	0.00480	0.176	0.121	0.0360	0.0307	0.622	0.843	-	-
τ_{a1} [a]	-	-	-	-	-	-	-	-	-	2.33e-4	0.490	0.402	0.127	0.151	0.910	0.362	-	-
τ_{a2}	1.49e-3	0.755	0.152	0.771	1.87e-4	0.905	0.726	0.982	< 0.0001	1.75e-7	0.591	0.137	0.499	0.253	0.467	0.435	-	-

[a] When the three large values from one subject (see Figure 4.4) are excluded.

Table 4.7. The distribution of parameter values according to sex, brain hemisphere, and physiological condition, optimised using impulse responses from the **MISO** approach. Values are **mean ± SD.** LH: left hemisphere, RH: right hemisphere, F: female, M: male.

		Analysis 1				**Analysis 2**			
		Normocapnia		*Hypercapnia*		Normocapnia		*Hypercapnia*	
		LH	RH	*LH*	*RH*	LH	RH	*LH*	*RH*
G_a	F	0.458 ± 0.352	0.518 ± 0.341	*0.505 ±0.288*	*0.505 ±0.259*	0.675 ± 0.273	0.566 ± 0.243	*0.554 ±0.327*	*0.584 ±0.321*
	M	0.542 ± 0.285	0.474 ± 0.296	*0.395 ±0.270*	*0.425 ±0.288*	0.529 ± 0.192	0.448 ± 0.218	*0.579 ±0.326*	*0.657 ±0.328*
$\tau_{a1}\ (s)$	F	0.585 ± 0.114	0.541 ± 0.0608	*0.653 ±0.0815*	*0.653 ±0.0953*	0.844 ± 0.777	1.44 ± 1.51	*0.778 ±0.319*	*0.768 ±0.311*
	M	0.578 ± 0.0573	0.578 ± 0.0507	*0.591 ±0.0687*	*0.586 ±0.0864*	0.803 ± 1.10	1.13 ± 1.38	*0.703 ±0.247*	*0.873 ±0.755*
$\tau_{a2}\ (s)$	F	1.39 ± 1.55	1.65 ± 1.78	*1.23 ±0.805*	*1.09 ±0.835*	3.99 ± 2.48	3.74 ± 2.21	*1.13 ±0.738*	*1.07 ±0.763*
	M	1.48 ± 1.42	1.78 ± 1.67	*0.601 ±0.306*	*0.792 ±0.864*	3.10 ± 2.73	2.69 ± 2.02	*1.03 ±1.35*	*1.05 ±1.02*

Table 4.8. The p-values from the Three-Way **ANOVA** and ***post-hoc*** for the **MISO** results. LH: left hemisphere, RH: right hemisphere, F: female, M: male, PC: physiological condition, BH: brain hemisphere, S: sex. Shaded cells indicate statistical significance.

	Analysis 1									**Analysis 2**						
	ANOVA							*post-hoc*		ANOVA						
	PC	BH	S	PC:BH	PC:S	BH:S	PC:BH:S	N vs. H (in F)	N vs. H (in M)	PC	BH	S	PC:BH	PC:S	BH:S	PC:BH:S
G_a	0.350	0.805	0.605	0.797	0.0397	0.430	0.225	0.8753	0.1126	0.411	0.770	0.656	0.0908	0.124	0.804	0.767
τ_{a1}	3.54e-6	0.283	0.211	0.612	0.000645	0.517	0.428	< 0.0001	0.7611	0.290	0.0687	0.334	0.154	0.365	0.984	0.567
τ_{a2}	0.0436	0.611	0.448	0.350	2.36e-5	0.549	0.544	0.4196	< 0.0001	5.36e-16	0.754	0.116	0.837	0.141	0.558	0.909

4.3.3.Sensitivity analysis of model parameters

The results of the sensitivity analysis are plotted in Figure 4.5, where parameters closer to the origin have less effect on the model output than parameters further away. As expected, G_a is located near the origin and hence has less of an effect than τ_{a1} and τ_{a2} on the temporal IR metrics (TTP, TTH, FWHM). For AUC, where G_a is expected to play a role due to its direct effect on IR amplitude, it is not located near the origin. τ_{a1} and τ_{a2} are not consistently located closer to or further away from the origin, which indicates that both of them are important parameters in the model. Overall, all three model parameters are important for at least one aspect of the model output, corroborating that they should be optimised individually and that their values can be meaningfully interpreted.

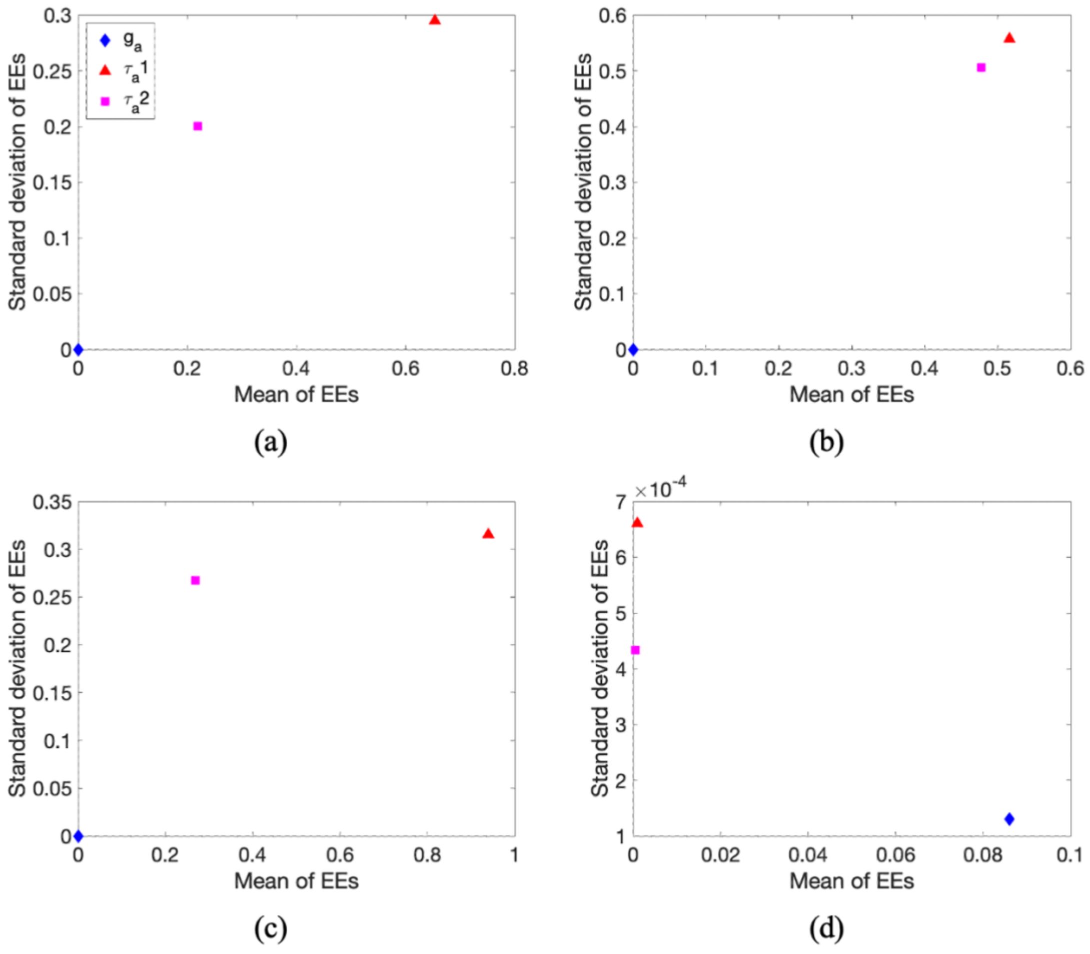

(a) (b)

(c) (d)

Figure 4.5. Sensitivity metrics to quantify the effects of model parameter values on model outputs: (a) Time to peak (TTP), (b) Time to half maximum (TTH), (c) Full width at half maximum (FWHM), (d) Area under curve (AUC). EEs: Elementary effects.

4.4.Discussion

In this chapter, a simple physiological model of dCVR was developed, CO_2-flow IRs were derived from experimental data, and then used in a combined approach to investigate potential differences between physiologically meaningful dCVR parameters under two different physiological conditions.

4.4.1.Physiological model fit to data-based CO_2-flow impulse responses

This chapter shows that a SO model is required to produce a CO_2-flow IR shape that starts at zero, rises to a positive peak, sometimes has an undershoot, and settles to baseline (Figure 4.3(a)-(b)), which is the shape reported in most previous studies that derived data-based CO_2-flow IRs, [113], [142], [15], and described as the ground truth in the recent review paper by Shams *et al.* [116] that tested different CO_2-flow IR derivation methods on simulated data. To the best of the author's knowledge, this has not been shown before and all previous physiological models that have included the effects of CO_2 on CBF, e.g., [78], [81], [89] have used a FO model to do so.

However, in addition to the CO_2-flow IR shape described in [116], some of the CO_2-flow IRs derived in this study exhibit higher order dynamics (Figure 4.3(c)-(h)). In these cases, the SO model is still an improvement over FO and FOTD models (Figure 4.3(a)-(f)), with only one exception for a data-based IR that exhibits two distinct peaks with a large dip between them, where all of the models (FO, FOTD, SOTD) produce a poor fit (Figure 4.3(g)). One other study, by Marmarelis *et al.* [45], also shows a data-based CO_2-flow IR (for healthy subjects) with a shape that deviates from the description in [116], starting at a positive value, decreasing, then rising to a positive peak and settling to baseline. There is therefore no hard consensus on the expected shape for a CO_2-flow IR shape in healthy subjects in current literature and more investigation is required, although three out of the four studies that show a data-based CO_2-flow IR, [113], [142], [15], report the shape described in [116], and, as argued by Panerai *et al.* [113], a CO_2-flow IR with a sharp transition at the origin is unlikely to be physiologically meaningful in light of CO_2 transport phenomena.

Since the IR is the derivative of the SR, the higher order dynamics in some of the IRs derived in this study (that deviate from the CO_2-flow IR description provided in [116] and result in poorer model fits) indicate that the velocity of CBF response to a step change in arterial CO_2 increases, then decreases (and if it becomes negative, indicates a change in the opposite direction to the CO_2 change) then increases again and decreases again before settling to baseline, which would correspond to a SR that approaches a plateau multiple times (and if the IR became negative, changes in the opposite direction) before reaching its new steady state. Although this behaviour has not been reported for step-like increases in CO_2, any increase in arterial CO_2 induced in an experimental setup (e.g., by increasing inspired CO_2) can only approximate a step increase and can in reality only be a ramp increase due to the nature of CO_2 transport in the body. It is therefore plausible that the sudden change of a true arterial CO_2 step change (although not physically taking place but theoretically represented by the IR), could elicit a stronger control response, which may exhibit higher order dynamics before settling and hence correspond to an IR with higher order dynamics. The true increase in arterial CO_2 may also not be the smooth ramp increase that is observable by $PetCO_2$. Since $PetCO_2$ is limited to one sample per breath, there may be changes in arterial CO_2 within a breath that are simply not measurable, so the true increase in arterial CO_2 may consist of a series of small SRs, which could result in higher order dynamics in the IR.

However, the higher order dynamics could also be artefacts from deriving CO_2-flow IRs using low SNR, steady state $PetCO_2$ data that was interpolated and resampled to produce a time series with an artificially high SF (2 Hz in this study) when the true SF of $PetCO_2$ is limited to breathing rate (around 0.1 Hz to 0.2 Hz), a concern highlighted by the CARNet white paper [97] and addressed in [113] by using different SFs for the input ($PetCO_2$) and output (CBv) data. The basis expansion method used for CO_2-flow IR derivation in this study was specifically selected as a robust option for steady state data, based on the recommendation by Shams *et al.* [116], and it does perform better than TFA (see Appendix B.4); but it requires the same SF for the basis functions and input-output data ($PetCO_2$-CBv time series), so a higher SF (2 Hz) was required for sufficient resolution in the basis functions. Interestingly, the average, hypercapnic IRs have less pronounced higher order dynamics than the average, normocapnia IRs (Figure 4.6), which may be due to differences in the underlying physiology between the two conditions, or because people tend to breath more quickly and deeply during hypercapnia, improving the SF and accuracy of the end-tidal values. Further investigation into the physiological plausibility of the higher order dynamics would therefore be useful and could be done by incorporating and testing specific hypotheses in the physiological model presented in this chapter in conjunction with data-based IRs that exhibit higher order dynamics.

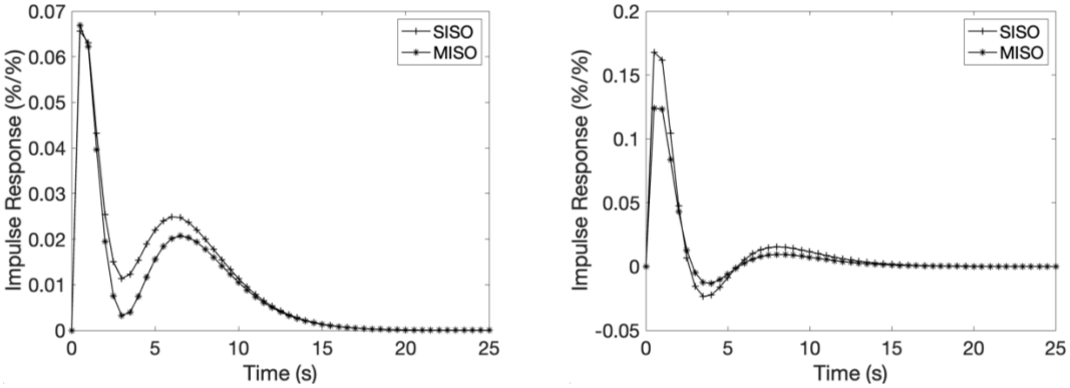

(a) (b)

Figure 4.6. Average accepted SISO and MISO impulse responses under (a) normocapnia, and (b) hypercapnia.

4.4.2.Main findings

The SO dCVR model parameters were optimised using two sets of CO_2-flow IRs: first derived using a SISO approach and then derived using a MISO approach to consider the effects of ABP. CBF is known to respond to changes in ABP via dCA, so the MISO CO_2-flow IRs are expected to be a more accurate representation of the dCVR mechanism. In light of the uncertainty around the variation in the data-based CO_2-flow IR shapes (see Section 4.4.1), two sets of analyses were performed, using the IR acceptance criteria described in Section 4.2.4: the first with no constraints on the level of higher order dynamics exhibited by the data-based IRs but where results may be influenced by poorer model fits, and the second with a requirement for sufficient goodness of fit to the physiological model proposed in this study but with fewer IRs accepted for analysis. The most trusted results are therefore the MISO results from the second analysis, although they may only represent part of the physiological range of dCVR behaviour.

The gain parameter, G_a, is not significantly affected by physiological condition in the first analysis' SISO (Table 4.6) or MISO (Table 4.8) results. It is, however, significantly affected by physiological condition in men in the second analysis' SISO results (Table 4.6), so the effect may be less pronounced in dCVR IRs with higher order dynamics or have been hidden by poorer model fits in the first analysis. The G_a mean values in men are larger in hypercapnia, indicating that the magnitude of the dCVR response becomes larger in hypercapnia. A larger dCVR response in hypercapnia compared to normocapnia may seem counterintuitive, as a state of hypercapnia would mean a more vasodilated baseline state and hence less remaining range for further vasodilation during dCVR. On the other hand, a more vasodilated baseline state would also allow for more range for vasoconstriction, which may be the reason for the larger magnitude of dCVR response in hypercapnia. However, the second analysis' MISO results also show that G_a is not significantly affected by physiological condition. The effect of hypercapnia on G_a may therefore be due to an interaction of the effects of ABP and CO_2 on CBF, and this should be investigated in a model where both dCA and dCVR are included.

The timing parameters, τ_{a1} and τ_{a2}, are both significantly affected by physiological condition in the first analysis' SISO (Table 4.6) and MISO (Table 4.8) results and in the second analysis' SISO results (Table 4.6), but the effect is only found in τ_{a2} in the second analysis' MISO results (Table 4.8). The effect of physiological condition on at least one time constant of dCVR, τ_{a2}, is therefore a key finding of this study, as it is present in the SISO and MISO results from both analyses. The effect of physiological condition on τ_{a1}, which is not present in the second analysis' MISO results, may be more pronounced in IRs with higher order dynamics (that were excluded in the second analysis), and/or be affected by the interaction between dCA and dCVR, and should be investigated in a model where both dCA and dCVR are included.

The interaction between physiological condition and sex was also shown to have a significant effect on the timing of dCVR in the first analysis' SISO and MISO results: τ_{a1} is affected by physiological condition in women but not men, and τ_{a2} is affected by physiological condition in men but not women. However, the second analysis does not show sex differences in its SISO (adjusted to exclude one subject, as explained in Section 4.3.2; Table 4.6) or MISO (Table 4.8) results. The sex differences may therefore either be spurious results due to poorer model fits in the first analysis or primarily occur in IRs with higher order dynamics (that were limited in the second analysis) and more investigation will be required. These potential differences in how the timing of dCVR is affected in men and women under different physiological and pathophysiological conditions motivate further investigation into sex differences in dCVR, while accounting for potentially confounding factors such as hormone differences and pregnancy history in women.

The mean values for τ_{a1} are consistently smaller than the mean values for τ_{a2} (Table 4.5, Table 4.7), indicating that τ_{a1} describes the faster response and τ_{a2} describes the slower response of dCVR. Interestingly, in the cases where significant differences were found between physiological conditions, the time constants' mean values differ in different directions in hypercapnia compared to normocapnia: τ_{a1} is larger and τ_{a2} is smaller, indicating that the faster response (related to τ_{a1}) slows down and the slower response (related to τ_{a2}) speeds up. This behaviour may be explained by allocating τ_{a1} (the faster response) mainly to vasoconstriction and τ_{a2} (the slower response) mainly to vasodilation, as vasodilation has been reported to be slower than vasoconstriction in response to changes in $PetCO_2$ [7]. Since hypercapnia corresponds to a state of greater baseline vasodilation and hence less remaining range for further vasodilation, τ_{a2} (the slower response) could be faster in hypercapnia because it takes less time to cover the smaller available range for vasodilation. Similarly, τ_{a1}(the faster response) could be slower in hypercapnia because it takes more time to cover the larger available range for vasoconstriction. Future work could extend the model to separate out the mechanisms of vasoconstriction and vasodilation in dCVR to investigate how each mechanism is individually affected and corroborate this hypothesis in men and women.

The values of both time constants obtained in this chapter are smaller than those reported in previous human studies that include the timing of CVR, although previous studies are also not consistent. Here, the mean values of τ_{a1} and τ_{a2} are less than a second and around 0.5 to four seconds respectively (Table 4.5, Table 4.7). Two studies that used CBv in the MCA as a surrogate for CBF (as in this study), [7], [78], report time constants of 45 s and 40 s respectively for the hypercapnic response; Severinghaus *et al.* [143], where CBF was calculated from the arterio-venous O_2 saturation difference, report a time constant of 18 s for the hypocapnic response; Holmes *et al.* [47], where BOLD from fMRI was used as a surrogate for CBF, report a time constant of 26.4 s and 23.7 s in two different brain regions respectively. However, these studies all used data where changes in $PetCO_2$ were induced using dynamic end-tidal forcing or hyperventilation, which may result in a different response than to the spontaneous fluctuations in steady state data used in this study.

CO_2-flow IRs from steady state data have been reported to exhibit an undershoot that is not present in end-tidal forcing IRs [15]. Importantly, based on visual inspection of the IRs shown in [15], both sets of IRs settle to baseline at around 30 s (just before 30 s for the end-tidal forcing IR; just after 30 s for the steady state IR), despite the fact that the steady state IR also has to fit an undershoot into that time. This is possible because the steady state IRs reach their positive peak faster than the end-tidal forcing IRs, although the difference is only around three seconds. The average CO_2-flow IRs obtained for normocapnia and hypercapnia in this study (Figure 4.6) settle to baseline just after and just before 15 seconds respectively, which is faster than in [15] where BOLD-fMRI data is used, but corresponds well to the CO_2-flow IR in [113], which settles to baseline at around 12 seconds and used CBv in the MCA (as in this study). The time constants in this study may therefore be smaller because they are mostly based on the first part of the response (with the undershoot only affecting the level of damping in the model, which can only be incorporated in τ_{a2} to a limited extent) for the majority of the model fits (see Table 4.3), whereas the time constants reported in previous studies likely encompass the entire response (i.e., until it settles to steady state in a SR or baseline in an IR).

4.4.3.Potential for physiological insights

This chapter presents a simple, physiological model of dCVR that can be used in conjunction with data-based CO_2-flow IRs. The model allows differences between conditions to be allocated to changes in the magnitude of the response (represented by G_a) or the slower (represented by τ_{a2}) or faster (represented by τ_{a1}) dynamics in the response. Here, the model was applied to different physiological conditions: the slower part of the dCVR response (τ_{a2}) was found to be faster in hypercapnia compared to normocapnia, and the magnitude (G_a) and faster part of the dCVR response (τ_{a1}) were found to be affected by the interaction between the effects of ABP and CO_2 on CBF, with potential sex-specific effects. New hypotheses of the underlying physiology can be formed and tested by including more detailed pathways within the dCVR control mechanism and optimising model parameters under different physiological conditions such as pregnancy and/or diseases such as stroke, dementia, or diabetes.

4.4.4.Study limitations

The model presented in this chapter describes the dCVR control mechanism with a second order model without detailed pathways that are tied more directly to the underlying physiology, although this serves the aim of a simple model that can be easily used in combination with experimental data. Although the effects of ABP were regressed out in the MISO analysis performed in this work, the model focusses only on dCVR and does not include consideration of CA or neural activation, so their potential interactions with dCVR could not be investigated. Both the model and the data-based IRs focus only on the linear relationship between $PaCO_2$ and CBF, although this is reasonable in conjunction with steady state data where only small fluctuations around baseline occur.

CBF and CO_2 in the brain cannot be measured directly, so surrogates were used. CBv recordings were taken to represent CBF in the MCAs, which is only true if the MCA cross-sectional area does not change. $PetCO_2$ recordings were taken to represent the CO_2 content in the brain, as $PetCO_2$ closely resembles $PaCO_2$ measured by blood analysis when using a sequential gas delivery circuit [34]. However, $PetCO_2$ recordings (and hence derived data-based IRs) may include dynamics that are not limited to only the brain, as recording timings will be affected by the difference in the time it takes for CO_2 to travel from the lungs to the capnograph and the time it takes for CO_2 to travel from the lungs to the brain. Although this delay may affect absolute values of the time constants, the comparison between the conditions (normocapnia vs hypercapnia) is not, as measurements were taken from the same subjects under the same experimental conditions. $PetCO_2$ recordings may also only represent a low-pass filter of dynamic changes in $PaCO_2$, as $PetCO_2$ recordings are inherently limited to one sample per breath.

Since the aim of this study is to gain insights into the underlying physiology of dCVR, data-based CO_2-flow IRs that were classified as “non-physiological” were excluded from model parameter optimisation. A negative initial response was termed “non-physiological”, which meant that only 50-80% of the available IRs could be included (Table 4.2). Previous studies have also reported CO_2-flow IRs with negative initial responses, but these studies used regional BOLD-fMRI data, so the “steal” effect could occur if different parts of the vasculature respond to different degrees and with different timings due to pathology, although it is still not expected in healthy subjects. In this work, CBv recordings that were measured in the MCAs were used, so each recording and resulting CO_2-flow IR represents the perfusion territory of a major cerebral artery, making the “steal” effect unlikely to occur in healthy subjects. Interestingly, the study by Marmarelis *et al.* [45] also used CBv recorded in the MCA to derive CO_2-flow IRs and reported an average IR for healthy subjects that starts at a positive value and initially decreases (without becoming negative), but the study does not discuss the shape of the IR itself, only comparing it between healthy subjects and patients. The prevalence of an initial decrease in data-based CO_2-flow IRs may be due to the limitations with data collection discussed above, such as the fact that $PetCO_2$ is taken to represent dynamic changes in $PaCO_2$ but cannot capture intra-breath variation in $PaCO_2$.

The model achieves a poorer fit to data-based IRs that, whilst not exhibiting a negative initial response, exhibit higher order dynamics than the shape described in [116] and found in most previous studies that show data-based CO_2-flow IRs, [113], [142], [15] (Figure 4.3); and it is currently not clear whether these higher order dynamics represent a larger physiological range or artefacts from the data-based IR derivation procedure (as discussed in Section 4.4.1). This limitation was addressed by performing a second analysis, where a data-based IR was only included if the NMSE from its fit to the physiological model was equal to or below 0.3 (see Section 4.2.4). However, the additional requirement meant that only 27-61% of the available IRs could be included in the second analysis (Table 4.2). An important avenue for future work is therefore a robust investigation into the physiological range of shapes expected for a CO_2-flow IR for, at first, young and healthy subjects, potentially in conjunction with expanded versions of the dCVR model developed in this study to test specific hypotheses.

A final limitation of this study is that confidence bounds were not determined for the data-based CO_2-flow IRs, which may have revealed uncertainty around the exhibited higher order dynamics (Figure 4.3). Since the expansion coefficients for the basis functions that make up the data-based IRs were estimated using ordinary least squares, confidence bounds could be calculated (for the expansion coefficients and hence the IRs) and this is recommended for future work that uses these methods.

4.5.Conclusion

In this chapter, a model of dCVR was developed that can produce the CO_2-flow IR described in [116] and found in most previous studies that show data-based CO_2-flow IRs, [113], [142], [15], where the effects of $PaCO_2$ on arteriolar vessel compliance are described by a gain and two time constants. This model is the first step in linking the recent research on data-driven approaches that investigate temporal characteristics of CVR with a physiological model where physiologically meaningful parameters can be optimised under different physiological and pathophysiological conditions. It has been shown that the model parameters can yield statistically different mean values under different physiological conditions, with a key finding that the slower part of the dCVR response is faster during hypercapnia, potentially due to a smaller remaining range for vasodilation. Potential sex-specific differences between normocapnia and hypercapnia were also found in the magnitude and timing of the dCVR response, motivating further investigation into sex differences in CBF control in different healthy and diseased states. Future work will extend the model to the BOLD-fMRI signal and parameter optimisation using BOLD-fMRI data to investigate spatial heterogeneity and better link with the growing body of dCVR research that uses BOLD-fMRI data.

CHAPTER 5

Modelling dynamic cerebrovascular reactivity using BOLD-fMRI

A subset of the results in this chapter are presented in a conference abstract:

- ***van Zijl, N.**, Pinto, J., Payne, S.J., Bulte, D.P. Modeling dynamic cerebrovascular reactivity in the postpartum period using BOLD-fMRI. Organization for Human Brain Mapping Annual meeting. June 24-28, 2025, Brisbane, Australia. (Accepted*)

Abstract

dCVR, which refers to transient CBF changes that occur in response to a vasoactive stimulus such as arterial CO_2*, is affected in different healthy and diseased states. However, most dCVR studies are from a data-driven perspective with limited mechanistic insights. In the previous chapter, a simple physiological model of dCVR was developed and meaningful physiological parameters were optimised using* CO_2*-flow IRs derived from TCD data. Since most CVR studies use BOLD data from fMRI, this chapter extended the physiological model and optimised its parameters with IRs derived from BOLD-fMRI data. A clinical imagining dataset was used in conjunction with the physiological model to perform group comparisons between postpartum women and women with no history of pregnancy at the brain hemisphere and MNI atlas brain region level. Although significant differences were not found between postpartum women and controls in the brain regions investigated in this study, brain region was found to have a significant effect on all model parameters (p-values* < 0.001*), highlighting the spatial heterogeneity of dCVR and*

motivating the application of this physiological model with BOLD-fMRI data. This chapter makes the physiological model of dCVR accessible to the CVR community that typically uses BOLD-fMRI data.

5.1.Introduction

CVR is widely accepted as an important biomarker of brain health. Recently, interest has grown in its temporal aspects, namely dCVR, although mostly from a data-driven perspective. In the previous chapter, a simple physiological model of dCVR was developed to serve as a link between the growing body of data-driven analyses of dCVR and its underlying physiological mechanisms. The model was used in conjunction with TCD data to perform a group comparison between normocapnic and hypercapnic conditions, finding statistically significant differences in model parameters.

However, most CVR research is performed with fMRI, as CVR can differ across brain regions [50]. This chapter therefore extends the physiological dCVR model from the previous chapter for application with BOLD-fMRI data. The model is tested by applying it with a clinical imagining dataset to perform a group comparison.

The group comparison aims to investigate potential neurovascular changes associated with the known brain anatomical changes in women that can occur due to pregnancy and last up to two years postpartum [144]. Two age-matched groups of women are therefore compared: postpartum women and women with no history of pregnancy. Comparisons are first performed at a brain hemisphere level to allow for comparison with TCD studies (as in the previous chapter), followed by an explorative, brain region level analysis to allow for spatial heterogeneity in dCVR.

The rest of this chapter is organised as follows: Section 5.2 describes the methods, including model extension, experimental CO_2-flow IR derivation and acceptance, parameter optimisation, and statistical and sensitivity analysis methods; Section 5.3 presents the results of the model fit, optimised model parameters, and the sensitivity analysis; Section 5.4 discusses the main findings and study limitations, placing them in the context of current literature; and Section 5.5 presents the conclusions and highlights directions for future work.

5.2.Materials and methods

5.2.1.Physiological model extension

The physiological model of dCVR developed in Chapter 4 (see Section 4.2.1) was extended for application to BOLD-fMRI data. The overall transfer function was derived analytically in Mathematica as the relationship between $PaCO_2$ and flow in the capillary compartment, as described in Appendix C.1. Capillary flow was selected, as BOLD-fMRI signal sensitivity shifts from predominantly veins at low magnetic field strengths to an increased sensitivity to capillaries at higher field strengths such as 3T [145] (as used in this study; see Section 5.2.2.1).

5.2.2.Data

5.2.2.1. Data collection and pre-processing

The dataset used for this chapter was from a BOLD-fMRI dataset collected as part of "The Maternal Brain Project" at the Welcome Centre for Integrative Neuroimaging[7] [146]. The cohort consisted of 23 women in two age-matched groups (Table 5.1): 13 postpartum women (postpartum period up to two years after giving birth) and 10 women with no history of pregnancy (i.e., controls). Data was collected[7] on a 3T Siemens Prisma Scanner (32 channel head coil), including a high-resolution structural image and BOLD-fMRI sequences with two protocols (Table 5.2):

1. At resting state (RS) (380 volumes, i.e., 5 min).
2. With a 5% CO_2 challenge protocol (Figure 5.1; 450 volumes, i.e., 6 min).

Table 5.1 Demographic and physiological features of the subjects in "The Maternal Brain" dataset [146]. *t*-tests were used for group comparisons[7], with $p < 0.05$ indicating significance.

	Control	Postpartum	p-value
Age	31.0 ± 6.7 years	33.6 ± 4.3 years	0.270
Post-partum period	NA	14.2 ± 6.2 months	NA
Baseline $PetCO_2$	49.3 ± 2.5 mmHg	51.2 ± 2.9 mmHg	0.120
Body mass index	26.1 ± 4.9 kg/m2	25.6 ± 5.5 kg/m2	0.830
Systolic blood pressure	99.5 ± 9.1 mmHg	105.6 ± 12.4 mmHg	0.210
Diastolic blood pressure	71.4 ± 8.6 mmHg	74.8 ± 12.5 mmHg	0.470
Heart rate	73.8 ± 11.0 bpm	73 ± 9.9 bpm	0.860

Expired CO_2 was sampled during acquisition of both BOLD-fMRI sequences[7]. Due to missing data of around half of the recording time, one control subject was excluded from the RS data, leaving 13 postpartum subjects and 9 controls for the RS analysis.

---

[7] Data collection was performed by Dr Joana Pinto, Genevieve Hayes, and Sierra Sparks. Dr Joana Pinto also performed pre-processing steps and analysis, which are all indicated by referencing this footnote.

Table 5.2. MRI acquisition parameters. TR: Repetition time, TE: Echo time.

	Structural image
Pulse sequence	Magnetisation prepared - rapid gradient echo (MP-RAGE)
Spatial resolution	1 mm × 1 mm × 1 mm
TR/TE	1900 ms / 3.97 ms
	BOLD-fMRI sequences
Pulse sequence	Gradient echo echo-planar imaging (GE-EPI)
Spatial resolution	2.4 mm × 2.4 mm × 2.4 mm
Multi-band acceleration factor	6
TR/TE	800 ms / 30 ms

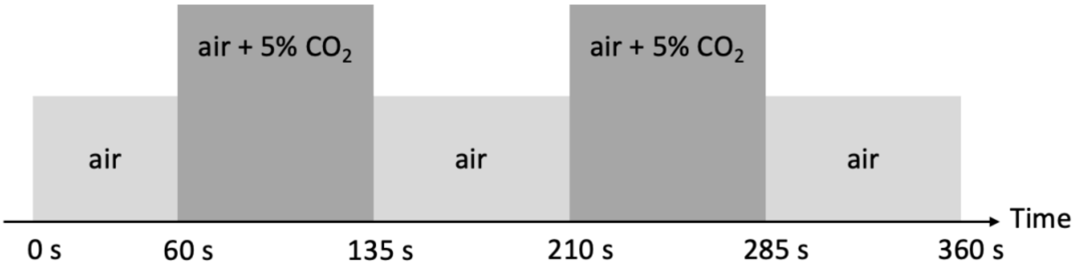

Figure 5.1. Protocol according to which participants inhaled alternating normocapnic air (0.04% CO_2) and air mixed with 5% CO_2 through a face mask. BOLD-fMRI data was collected from 0 s.

Preprocessing was performed in FSL [147] using the FEAT tool for motion correction (MCFLIRT tool), spatial smoothing (4 mm), and high-pass filtering (100 s)[7]. Co-registration to structural and Montreal Neurological Institute (MNI) template space was also performed within FEAT, using a linear method with 12 degrees of freedom (FLIRT)[7]. The first five volumes from each BOLD-fMRI sequence were deleted to allow for signal stabilisation. $PetCO_2$ values were extracted from the expired CO_2 trace, interpolated with a cubic spline, and resampled at the BOLD-fMRI SF of 1.25 Hz. Subject-specific $PetCO_2$ time shifts were obtained by cross-correlation with the average whole-brain BOLD-fMRI signals recorded under the 5% CO_2 protocol and applied to both the RS and 5% CO_2 protocol $PetCO_2$ time series[7].

5.2.2.2. Data preparation for time series analysis

In conjunction with the $PetCO_2$ time series, two sets of time series were prepared from each BOLD-fMRI sequence:

1. By averaging the voxel-wise BOLD-fMRI signals over each brain hemisphere using subject-specific masks (Figure 5.2, Figure 5.3), which allows for comparison with TCD studies (as in Chapter 4).
2. By averaging the voxel-wise BOLD-MRI signal over nine brain regions from the MNI atlas using subject-specific masks (Figure 5.4, Figure 5.5), which allows for more spatial heterogeneity.

The z-scores of the $PetCO_2$ and BOLD-fMRI times series were used for analysis.

Figure 5.2. Left and right hemispheres shown on the coronal and axial planes for a representative subject.

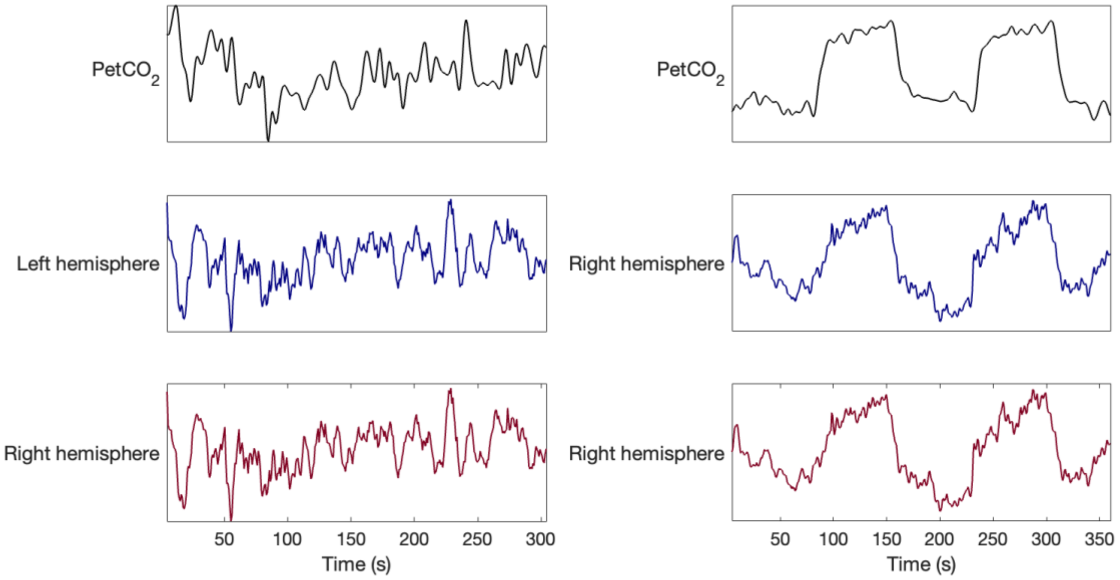

(a) (b)

Figure 5.3. $PetCO_2$ and brain hemisphere level BOLD-fMRI time series (shown as z-scores) for a representative subject under (a) resting state, and (b) the 5% CO_2 protocol (Figure 5.1). Colours correspond to brain hemispheres in Figure 5.2.

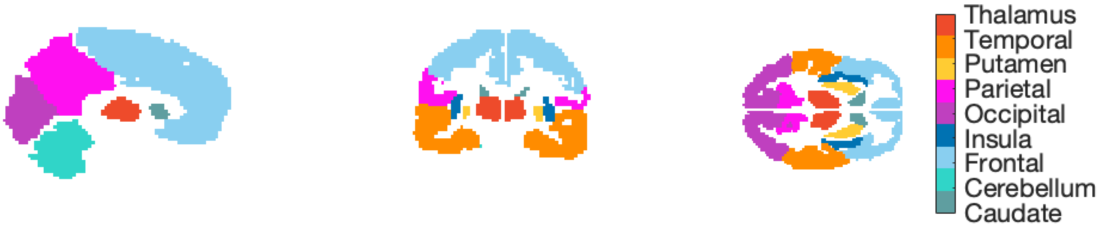

Figure 5.4. MNI atlas brain regions shown on the sagittal, coronal, and axial planes for a representative subject.

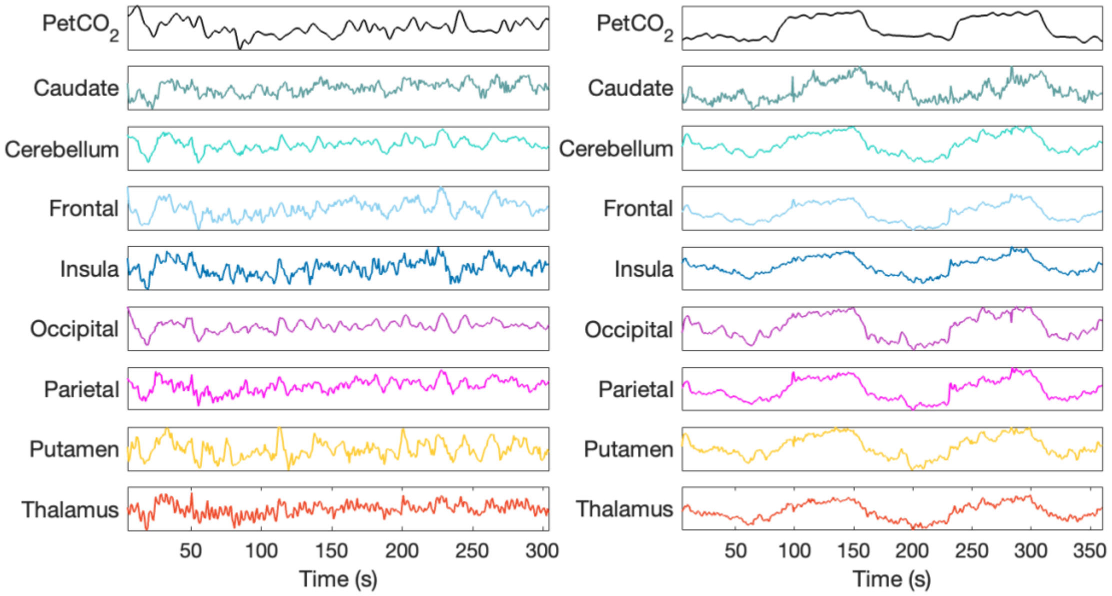

(a) (b)

Figure 5.5. PetCO₂ and brain region level BOLD-fMRI time series (shown as z-scores) for a representative subject under (a) resting state, and (b) the 5% CO₂ protocol (Figure 5.1). Colours correspond to brain regions in Figure 5.4.

5.2.3. Data-based impulse response derivation

Four sets of CO₂-flow IRs were derived: brain hemisphere level IRs using the RS data (Figure 5.3(a)) and using the 5% CO₂ protocol data (Figure 5.3(b)), and brain region level IRs using the RS data (Figure 5.5(a)) and 5% CO₂ protocol data (Figure 5.5(b)).

All the IRs were derived using the basis expansion technique with spherical Laguerre basis functions described in Chapter 4 (see Section 4.2.3). Hyperparameters, model order (p) and exponential decay (α) were selected as the average of the values of a grid search minimising the BIC for each subject, as recommended by the CARNet white paper [97], with values for α ranging from 0.5 to 0.9 with step size 0.1 and values for p ranging from 2 to 4, as in [116]. Only the RS data was included in hyperparameter selection and all subjects in both control and postpartum groups were included, as neither group is to be defined as normal. Individual sets of hyperparameters were selected for the hemispheres and for each brain region, to allow for spatial heterogeneity, and are reported in Table 5.3.

Table 5.3. Sets of hyperparameters selected for hemispheres and brain regions. p: model order, α: exponential decay parameter.

Brain Region	$\boldsymbol{p}$	$\boldsymbol{\alpha}$
Hemispheres	3	0.6
Caudate	2	0.4
Cerebellum	3	0.6
Frontal	3	0.6
Insula	2	0.4
Occipital	3	0.6
Parietal	3	0.5
Putamen	2	0.5
Temporal	3	0.6
Thalamus	2	0.5

5.2.4.Data-based impulse response acceptance

Data-based IRs were accepted or rejected based on three criteria: (1) statistical significance, (2) physiological plausibility, (3) goodness of fit to the physiological model. The first criterion could only be applied to IRs derived from the RS data (Figure 5.3(a) and Figure 5.5(a)), where IRs were accepted and rejected according to a %NMSE between the real and predicted output (BOLD-fMRI time series in this case) threshold determined by the "bootstrapping" method described for the single-input-single-output case in Chapter 4 (see Section 4.2.4). The thresholds were set as the lower limits of the "null"

%NMSE confidence intervals (Table 5.4), which were determined for the hemispheres and for each brain region to allow for potential heterogeneity introduced by different numbers of voxels averaged in the time series. For each region, IRs with a %NMSE above the lower limit of the "null" %NMSE confidence interval were excluded from further analysis.

Table 5.4. Lower limits of the null %NMSE confidence intervals used as thresholds for IR exclusion for hemispheres and brain regions. Values were obtained from the resting state data.

Brain region	**% NMSE threshold**
Hemispheres	94.4
Caudate	96.0
Cerebellum	94.7
Frontal	94.4
Insula	97.4
Occipital	95.1
Parietal	95.2
Putamen	97.5
Temporal	94.9
Thalamus	96.7

IRs derived from the 5% CO_2 data could not be accepted or rejected according to the "bootstrapping" method, as "null" IRs could not be derived. The Null Hypothesis requires there to be no predictive relationship between the input ($PetCO_2$ in this case) and output (BOLD-fMRI in this case) time series, but since the inspired CO_2 is changed at the same time points for all subjects during the 5% CO_2 protocol (Figure 5.1), all the input and output time series show the same trend. I.e., even when the output data is randomly shuffled, there is still a relationship between the input and output data due to the confounding variable of the external input from the experimental protocol. %NMSEs from the 5% CO_2 protocol IRs also cannot be compared to the null %NMSE threshold determined for the RS data, as the larger signal change improves the goodness of fit measure (typical values in this chapter: RS %NMSE > 90%, 30% < 5% CO_2 protocol

%NMSE < 40%), so the two are not comparable. However, also due to the larger signal changes, the 5% CO_2 protocol data have a better SNR, making it reasonable to expect meaningful derived IRs.

The second and third criteria were applied to IRs from both the RS data and 5% CO_2 protocol data, as described in Chapter 4 (see Section 4.2.4). IRs that exhibit an initial decrease were classified as “non-physiological” and excluded from further analysis. IRs with a NMSE from fitting to the physiological model above 0.3 were excluded from further analysis. The number of IRs accepted for further analysis is shown in Table 5.5. Differences in the number of accepted IRs per protocol and brain hemisphere/region are investigated in Appendix C.2.

Table 5.5. Number of IRs at brain hemisphere and brain region level accepted for further analysis.

	Resting state data		*5% CO_2 protocol data*	
	Control	Postpartum	*Control*	*Postpartum*
Left hemisphere	5	8	*10*	*13*
Right hemisphere	4	4	*10*	*13*
Caudate	0	5	*5*	*8*
Cerebellum	4	3	*10*	*10*
Frontal	2	5	*10*	*13*
Insula	2	8	*10*	*13*
Occipital	3	7	*10*	*13*
Parietal	2	4	*10*	*12*
Putamen	1	8	*10*	*13*
Temporal	3	5	*10*	*13*
Thalamus	3	5	*10*	*12*

5.2.5. Model parameter optimisation

Model parameters were optimised by fitting the model to each of the data-based CO_2-flow IRs using to the fitting procedure, constraints, and initial conditions described in Chapter 4 (see Section 4.2.5).

5.2.6.Statistical analysis

Two sets of statistical analyses were performed:

1. Using the parameters optimised at a brain hemisphere level.
2. Using the parameters optimised at a brain region level.

In both analyses, the values of each model parameter were analysed using linear mixed effects models to account for the non-independence between compared groups (e.g., parameters from different brain hemispheres/regions in the same subjects).

In the brain hemisphere level analysis, brain hemisphere, protocol (RS vs 5% CO_2), and group (control vs postpartum) were modelled as fixed effects and subject as a random effect:

$$\begin{aligned} MP = \beta_0 + \beta_1 * BH + \beta_2 * Pr + \beta_3 * Group + \beta_4 * (BH \times Pr) \\ +\beta_5 * (BH \times Group) + \beta_6 * (Pr \times Group) \\ +\beta_7 * (BH \times Pr \times Group) + u_{subject} + \epsilon \end{aligned} \tag{5.1}$$

where MP is model parameter, BH is brain hemisphere, Pr is protocol, β_0 is the fixed effects intercept, $\beta_1, \beta_2, \ldots, \beta_7$ are the coefficients for the fixed effects and their interactions, $u_{subject}$ is the random intercept for each subject, and ϵ is the residual error. Three-Way ANOVA was performed on each linear mixed effects model to test for significant main effects of brain hemisphere, protocol, and group.

In the brain region level analysis, the RS results were excluded from the statistical analysis due to inadequate sample sizes (Table 5.5). Brain region and group (control vs postpartum) were modelled as fixed effects and subject was modelled as a random effect:

$$MP = \beta_0 + \beta_1 * BR + \beta_2 * Group + \beta_3 * (BR \times Group) + u_{subject} + \epsilon \tag{5.2}$$

where MP is model parameter, BR is brain region, β_0 is the fixed effects intercept, $\beta_1, \beta_2, \dots, \beta_3$ are the coefficients for the fixed effects and their interaction, $u_{subject}$ is the random intercept for each subject, and ϵ is the residual error. Two-Way ANOVA was performed on each linear mixed effects model to test for significant main effects of brain region and group.

In both analyses, no optimised parameter values were removed as outliers, as none of the values were deemed physiologically implausible and may therefore reflect true variability in the data. Normality of the residuals was tested for using the D'Agostino-Pearson test, as normally distributed residuals is a required condition for inferences to be made from linear mixed effects models. In cases where the residuals were not normally distributed, the linear mixed effects model was fitted to the transformed parameter values (the square, cube, logarithm, and Box Cox transformation) and the residuals checked for normality again.

Since the ANOVAs on the linear mixed effects models can only test whether a fixed effect or interaction effect (e.g., the interaction between physiological condition and sex) has a significant effect on the model parameter, but not between which pairs of group means the significant difference is (e.g., between normocapnia in men and hypercapnia in men, or between normocapnia in women and hypercapnia in women), *post-hoc* analysis was performed to assess the significance of differences between pairs of group means. Multiple comparisons were accounted for by using Tukey's correction during *post-hoc* analysis, as it is a popular choice to correct for multiple comparisons and more powerful than the Bonferroni correction. All statistical analyses were done using R statistical software version 4.2.2.

5.2.7.Sensitivity analysis

A sensitivity analysis was performed to investigate whether the value of each model parameter affects the model output, which is the model-based IR relating $PaCO_2$ to capillary flow in this chapter. The procedure is explained in detail in Chapter 4 (see Section 4.2.7), but briefly, the Elementary Effects method was used, and the model output was represented by the CO_2-flow IR characteristic metrics: time to peak (TTP), time to half maximum (TTH), full width at half maximum (FWHM), and area under curve (AUC). Parameter ranges were set as ± 20% of the mean RS values obtained in this chapter.

5.3.Results

5.3.1.Model fit

The physiological model fits well to the $PetCO_2$-BOLD IRs derived in this chapter. Of the 66 hemisphere level IRs and 266 brain region level IRs accepted by the first two acceptance criteria (i.e., IR statistical significance and physiological plausibility; see Section 5.2.4), only two (3.03%) and six (2.26%) have $NMSE > 0.3$ from fitting to the model respectively. The NMSEs from the model fit to all data-based IRs are available in Appendix C.3. The model fit to the range of $PetCO_2$-flow IR shapes in this chapter is shown in Figure 5.6, and the number of model fits within each category is quantified in Table 5.6.

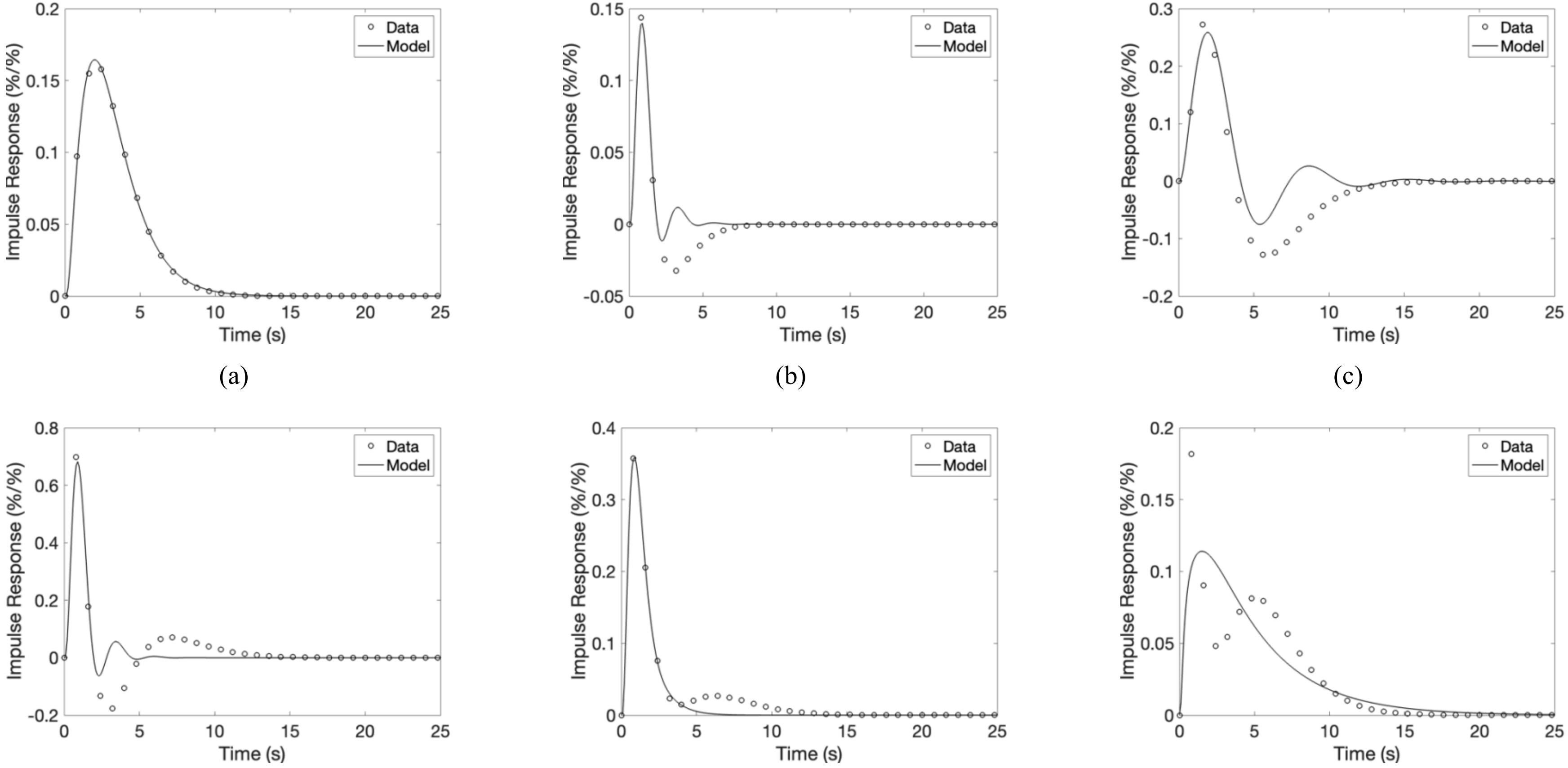

(a)

(b)

(c)

(d)

(e)

(f)

Figure 5.6. Examples of optimal model fit to PetCO$_2$-BOLD IRs, with (a) no secondary dynamics, (b) an undershoot with slower dynamics than the initial response, (c) an undershoot with dynamics similar to the initial response, (d) a combination of an undershoot and overshoot, (e) an overshoot or small second peak, (f) two peaks with large amplitudes and a shallow dip between them.

Table 5.6. Distribution of model fits to the range of $PetCO_2$-BOLD IRs shown in Figure 5.6(a)-(h) within the IRs accepted according to the first two acceptance criteria in Section 5.2.4. Model fits with NMSE > 0.3 are indicated in brackets.

		(a)	(b)	(c)	(d)	(e)	(f)	Total
Resting state	Left hemisphere	1	8	-	4 (1)	-	-	13 (1)
	Right hemisphere	-	3	2	2 (1)	-	-	7 (1)
	Caudate	13	2	-	-	-	-	5
	Cerebellum	-	2	2	4	-	-	8
	Frontal	-	2	1 (1)	4	-	-	7 (1)
	Insula	3	7	-	-	-	-	10
	Occipital	1	3	2 (1)	4	-	-	10 (1)
	Parietal	-	1	1	4	-	-	6
	Putamen	5	4	-	-	-	-	9
	Temporal	-	2	2 (1)	4	-	-	8 (1)
	Thalamus	3	5	-	-	-	-	8
	Total	26	39	10 (3)	26 (2)	-	-	91 (5)
5% CO_2 protocol	Left hemisphere	2	4	-	15	2	-	23
	Right hemisphere	3	5	-	12	3	-	23
	Caudate	11	2	-	-	-	-	13
	Cerebellum	-	-	-	18 (1)	2 (1)	(1)	20 (3)
	Frontal	3	9	-	9	2	-	23
	Insula	13	10	-	-	-	-	23
	Occipital	2	7	-	12	2	-	23
	Parietal	1	5	-	16	-	-	22
	Putamen	12	11	-	-	-	-	23
	Temporal	2	7	-	12	1	1	23
	Thalamus	16	6	-	-	-	-	23
	Total	65	66	-	94 (1)	12 (1)	1 (1)	239 (3)

The best fit occurs when there are no/small amplitude secondary dynamics (i.e., undershoots or overshoots) (Figure 5.6 (a)). The model struggles to fit data-based IRs that exhibit secondary dynamics at lower frequencies than the initial part of the response (i.e., the first peak), whether that takes the form of an undershoot (Figure 5.6(b)), a combination of an undershoot and overshoot (Figure 5.6(d)), or small second peak (Figure

5.6(e)), typically fitting mostly to the first part of the response. The model captures more of the secondary dynamics as their frequency approaches that of the initial response (Figure 5.6(c)), although the tail-end fit is still poorer, especially if the undershoot has a large amplitude. Under specific circumstances, where the data-based IR does not return close to baseline before reaching a second peak that has a sufficiently large amplitude, the model attempts to fit both peaks as one response, although this only occurs once in the accepted IRs in this chapter, as shown in Table 5.6.

5.3.2. Optimised model parameter values

Two sets of parameter values were optimised: first, at a brain hemisphere level to be comparable with TCD studies; second, at a brain region level to take advantage of the spatial information captured with BOLD-fMRI.

5.3.2.1. Optimised parameter values at brain hemisphere level

The three model parameters (G_a, τ_{a1}, τ_{a2}) were optimised using data-based CO_2-flow IRs obtained from RS data and data with externally induced CO_2 fluctuations (see Figure 5.1) for two groups of women: postpartum women and women who have never been pregnant (i.e., controls). Linear mixed effects models were used for statistical analysis and their residuals were tested for normality (Table 5.7). Residuals for the gain (G_a) are normally distributed, indicating that variation in each optimised parameter is fully described by effects from brain hemisphere, method (RS vs externally induced CO_2 fluctuations), and group (postpartum vs control) in the linear model. Although residuals' normality could not be achieved for τ_{a1} or τ_{a2} according to the D'Agostino-Pearson test, the Box Cox transformed values give residual distributions with a skewness of 1.00 and a skewness of 0.712 respectively, i.e., $|\text{skewness}| < 2.0$ [127], when fitted to a linear mixed effects model, which are accepted and used for further analysis.

Table 5.7. The p-values from application of the D'Agostino-Pearson test for normality on residuals from fitting transformations of the brain hemisphere-wise parameter values to linear mixed effects models. Shaded cells indicate p-values that show the residuals are normally distributed.

	$\boldsymbol{G_a}$	$\boldsymbol{\tau_{a1}}$	$\boldsymbol{\tau_{a2}}$
Original data	0.924	0.000281	1.51e-7
Square root	-	0.000672	4.70e-8
Cube root	-	0.00157	4.71e-8
Logarithm	-	0.000151	7.64e-5
Box Cox ($\boldsymbol{x_{transform} = x^{\lambda}}$)	-	0.000186 [a]	0.0171 [b]

With a Box Cox parameter, $\boldsymbol{\lambda}$, of [a] -2, [b] -1.27.

Three-Way ANOVA was performed on the linear mixed effects models to test whether brain hemisphere, protocol, or group have a significant effect on optimised parameter values (Table 5.8). Brain hemisphere does not have a significant effect on any of the parameters, as expected for young, healthy subjects. Group, which refers to the split between postpartum women and women who have never been pregnant, also has no significant effect on any of the parameters. The Three-Way ANOVA on the linear mixed effects model of τ_{a2} identified a main effect from the interaction between group and protocol, but the *post-hoc* analysis with Tukey's correction for multiple comparison revealed that there is no significant difference between the postpartum and control group in the RS or 5% CO_2 protocol data (Table 5.8).

Protocol, however, does have a significant effect on both G_a and τ_{a1}. G_a is larger and τ_{a1} is smaller for the 5% CO_2 protocol data than RS data, indicating that the dCVR magnitude is larger and one part of the response is faster in response to larger, externally induced CO_2 fluctuations compared to spontaneous fluctuations.

Table 5.8. Distribution of brain hemisphere-wise parameter values according to group, brain hemisphere, and method. Shaded cells indicate statistical significance.

		G_a		$\tau_{a1}\ (s)$		$\tau_{a2}\ (s)$	
		mean ± standard deviation					
		Control	Postpartum	Control	Postpartum	Control	Postpartum
Resting state	Left hemisphere	0.606 ± 0.174	0.778 ± 0.307	0.492 ± *0.254*	0.492 ± 0.227	0.315 ± 0.152	0.539 ± 0.409
	Right hemisphere	0.802 ± 0.0555	0.714 ± 0.405	0.397 ± *0.0514*	0.587 ± 0.371	0.287 ± 0.107	0.449 ± 0.200
5% CO_2 protocol	*Left hemisphere*	*1.64 ± 0.428*	*1.71 ± 0.601*	*0.460 ± 0.241*	*0.384 ± 0.0109*	*0.523 ± 0.530*	*0.364 ± 0.0869*
	Right hemisphere	*1.57 ± 0.360*	*1.78 ± 0.643*	*0.463 ± 0.245*	*0.386 ± 0.0116*	*0.578 ± 0.649*	*0.384 ± 0.112*
		Three-Way ANOVA (p-value)					
Group		0.236		0.459		0.260	
Brain hemisphere		0.327		0.828		0.647	
Protocol		< 2e-16		0.0298		0.354	
Group:Brain hemisphere		0.449		0.494		0.742	
Group:Protocol		0.203		0.432		0.00479	
Brain hemisphere:Protocol		0.308		0.775		0.873	
Group:Brain hemisphere:Protocol		0.800		0.465		0.773	
		***Post-hoc* analysis (p-value)**					
Postpartum vs. Control (in RS)		-		-		0.155	
Postpartum vs. Control (in 5% CO_2 protocol)		-		-		0.982	

5.3.2.2. Optimised parameter values at brain region level

An explorative analysis was performed by optimising the three model parameters (G_a, τ_{a1}, τ_{a2}) at a brain region level. The parameters were optimised using data-based CO_2-flow IRs obtained from only the 5% CO_2 protocol data for two groups of women: postpartum women and women who have never been pregnant (i.e., controls).

Linear mixed effects models were used for statistical analysis and their residuals were tested for normality (Table 5.9). Residuals for the gain (G_a) are normally distributed, indicating its variation is fully described by effects from brain region and group (postpartum vs control) in the linear model. Residuals for the time constants (τ_{a1}, τ_{a2}) are not normally distributed, which could be attributed to heteroscedasticity, non-linear relationships between the fixed effects and the time constants, or the influence of additional, unmodelled effects. Box Cox transformations achieved residuals' normality for τ_{a1} and τ_{a2} and are therefore used for all further analysis.

Table 5.9. The p-values from application of the D'Agostino-Pearson test for normality on residuals from fitting transformations of the brain region-wise parameter values to linear mixed effects models. Shaded cells indicate p-values that show the residuals are normally distributed.

SISO	$\boldsymbol{G_a}$	$\boldsymbol{\tau_{a1}}$	$\boldsymbol{\tau_{a2}}$
Original data	0.382	4.48e-9	< 2.2e-16
Square root	-	< 2.2e-16	< 2.2e-16
Cube root	-	< 2.2e-16	< 2.2e-16
Logarithm	-	< 2.2e-16	0.00100
Box Cox ($\boldsymbol{x_{transform} = x^{\lambda}}$)	-	0.856 [a]	0.463 [b]

With a Box Cox parameter, $\boldsymbol{\lambda}$, of [a] 0.545, [b] -0.788.

Two-Way ANOVA was performed on the linear mixed effects models to test whether brain region or group have a significant effect on any of the parameters. No significant differences were found between postpartum women and controls in any of the model parameters, overall or in specific brain regions (Table 5.10).

Table 5.10. Distribution of brain region-wise parameter values according to group and brain region, obtained from the 5% CO_2 protocol data. Shaded cells indicate statistical significance.

	G_a		τ_{a1} (s)		τ_{a2} (s)	
mean ± standard deviation						
	Control	Postpartum	Control	Postpartum	Control	Postpartum
Caudate	1.45 ± 0.392	1.36 ± 0.146	0.552 ± 0.362	0.518 ± 0.245	0.842 ± 0.570	0.943 ± 0.460
Cerebellum	1.25 ± 0.495	1.60 ± 0.543	0.335 ± 0.114	0.341 ± 0.114	0.314 ± 0.110	0.467 ± 0.474
Frontal	1.70 ± 0.424	1.85 ± 0.616	0.404 ± 0.0424	0.392 ± 0.0144	0.507 ± 0.417	0.412 ± 0.109
Insula	1.61 ± 0.274	1.63 ± 0.334	0.461 ± 0.274	0.402 ± 0.106	0.641 ± 0.421	0.582 ± 0.347
Occipital	1.56 ± 0.399	1.67 ± 0.624	0.491 ± 0.335	0.381 ± 0.0146	0.518 ± 0.467	0.362 ± 0.111
Parietal	1.74 ± 0.473	1.90 ± 0.773	0.353 ± 0.00819	0.355 ± 0.0082	0.257 ± 0.0725	0.265 ± 0.0634
Putamen	1.53 ± 0.213	1.62 ± 0.324	0.532 ± 0.311	0.488 ± 0.189	0.947 ± 0.572	0.811 ± 0.568
Temporal	1.67 ± 0.406	1.82 ± 0.563	0.349 ± 0.123	0.386 ± 0.00931	0.718 ± 1.13	0.364 ± 0.106
Thalamus	1.51 ± 0.170	1.56 ± 0.238	0.530 ± 0.216	0.523 ± 0.306	1.11 ± 0.561	0.916 ± 0.547
p-value (Two-Way ANOVA)						
Group	0.595		0.600		0.758	
Brain region	3.86e-10		0.000149		< 2e-16	
Group:Brain region	0.880		0.918		0.720	

Brain region, however, has a significant effect on all three model parameters (Table 5.10), and the *post-hoc* analysis results show significant differences between multiple pairs of brain region means (Table 5.11). These brain region differences may be affected by different numbers of voxels averaged and/or differences in hyperparameters (Table 5.3), although significant differences are also found between brain regions with the same hyperparameters (Table 5.11).

Table 5.11. p-values from *post-hoc* analysis to assess the significance of differences between pairs of brain region means for all three model parameters. Shaded cells indicate statistical significance. Bold indicates that the pair of brain regions have the same hyperparameters for the data-based IR derivation (see Table 5.3).

			G_a	τ_{a1}	τ_{a2}
Caudate	vs	Cerebellum	0.709	0.709	< 0.0001
Caudate	vs	Frontal	< 0.0001	< 0.0001	< 0.0001
Caudate	**vs**	**Insula**	**0.0022**	**0.0022**	**0.0496**
Caudate	vs	Occipital	0.00240	0.0024	< 0.0001
Caudate	vs	Parietal	< 0.0001	< 0.0001	< 0.0001
Caudate	vs	Putamen	0.0108	0.0108	1.00
Caudate	vs	Temporal	< 0.0001	< 0.0001	< 0.0001
Caudate	vs	Thalamus	0.105	0.105	1.00
Cerebellum	**vs**	**Frontal**	**0.0001**	**0.0001**	**0.345**
Cerebellum	vs	Insula	0.127	0.127	< 0.0001
Cerebellum	**vs**	**Occipital**	**0.137**	**0.137**	**0.944**
Cerebellum	vs	Parietal	< 0.0001	< 0.0001	0.0015
Cerebellum	vs	Putamen	0.385	0.385	< 0.0001
Cerebellum	**vs**	**Temporal**	**0.0005**	**0.0005**	**0.896**
Cerebellum	vs	Thalamus	0.928	0.928	< 0.0001
Frontal	vs	Insula	0.404	0.404	0.0877
Frontal	**vs**	**Occipital**	**0.383**	**0.383**	**0.974**
Frontal	vs	Parietal	1.00	1.00	< 0.0001
Frontal	vs	Putamen	0.130	0.130	< 0.0001
Frontal	**vs**	**Temporal**	**1.00**	**1.00**	**0.990**
Frontal	vs	Thalamus	0.0088	0.0088	< 0.0001
Insula	vs	Occipital	1.00	1.00	0.0027

			G_a	τ_{a1}	τ_{a2}
Insula	vs	Parietal	0.223	0.223	<.0001
Insula	vs	Putamen	1.00	1.00	0.0406
Insula	vs	Temporal	0.698	0.698	0.0048
Insula	vs	Thalamus	0.847	0.847	0.0003
Occipital	vs	Parietal	0.208	0.208	< 0.0001
Occipital	vs	Putamen	1.00	1.00	< 0.0001
Occipital	**vs**	**Temporal**	**0.677**	**0.677**	**1.00**
Occipital	vs	Thalamus	0.862	0.862	< 0.0001
Parietal	vs	Putamen	0.0574	0.0574	< 0.0001
Parietal	vs	Temporal	0.997	0.997	< 0.0001
Parietal	vs	Thalamus	0.0031	0.0031	< 0.0001
Putamen	vs	Temporal	0.322	0.322	< 0.0001
Putamen	**vs**	**Thalamus**	**0.990**	**0.990**	**0.894**
Temporal	vs	Thalamus	0.0348	0.0348	< 0.0001

5.3.3.Sensitivity analysis of model parameters

The sensitivity analysis results show how much of an effect each model parameter has on the model output relative to the other model parameters, where the model output (i.e., dCVR IR) is represented by four characteristic dCVR IR metrics: TTP (Figure 5.7(a)), TTH (Figure 5.7(b)), FWHM (Figure 5.7(c)), and AUC (Figure 5.7(d)). In each case, parameters closer to the origin have less effect on the respective model output than parameters further away.

The two time constants, τ_{a1} and τ_{a2}, are not consistently located closer to or further away from the origin, indicating that they are both important parameters. The gain parameter, G_a, is located near the origin and hence has less of an effect than τ_{a1} or τ_{a2} on the temporal metrics (TTP, TTH, FWHM), as expected for a parameter related to the magnitude of the response and not its timing. For AUC, which would be affected by the magnitude of the response, G_a is not located near the origin. Overall, each of the three model parameters is important for at least one characteristic metric of the dCVR IR, and hence their optimised values can be meaningfully interpreted.

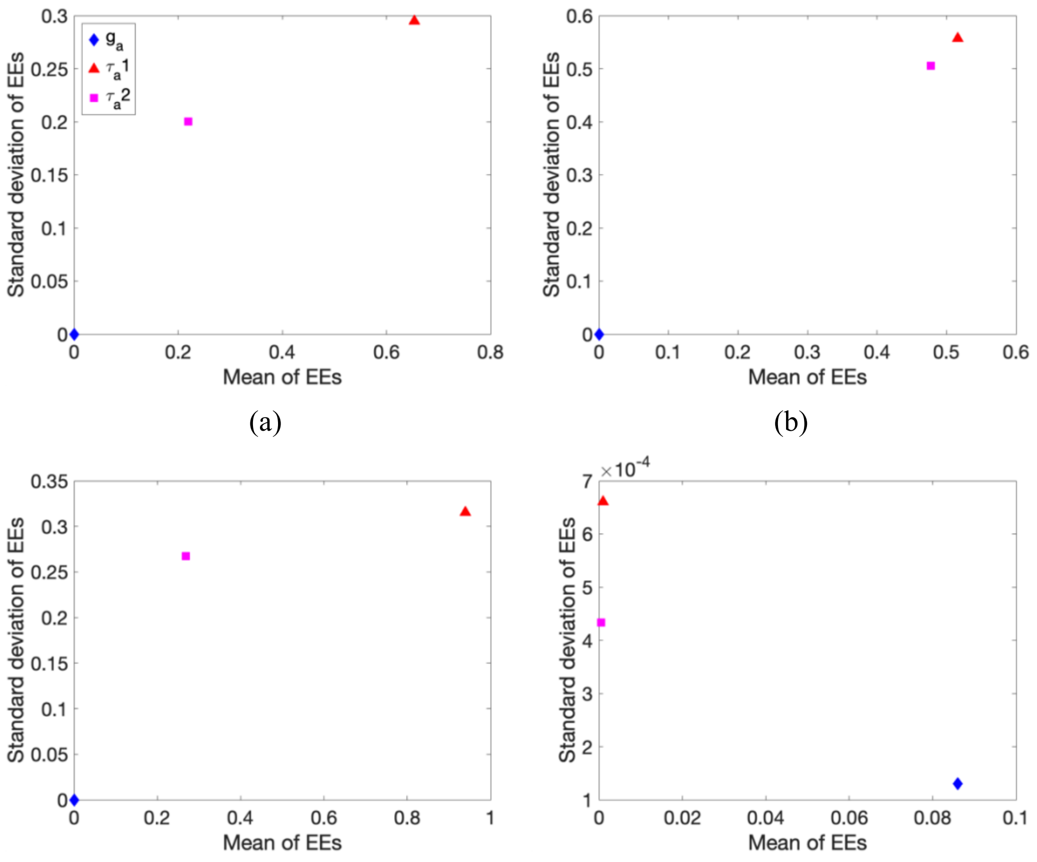

(a) (b)

(c) (d)

Figure 5.7. Sensitivity metrics to quantify the effects of model parameter values on model outputs: (a) Time to peak (TTP), (b) Time to half maximum (TTH), (c) Full width at half maximum (FWHM), (d) Area under curve (AUC). EEs: Elementary effects.

5.4.Discussion

In this chapter, the simple physiological model of dCVR was extended for use with BOLD-fMRI data. Data-based IRs were derived from a clinical imagining dataset and used in conjunction with the physiological model to investigate potential differences in dCVR between postpartum women and controls at a brain hemisphere and brain region level.

5.4.1.Main findings

The aim of this chapter was to apply the physiological dCVR model to BOLD-fMRI data by performing a group comparison between postpartum women and women with no history of pregnancy (i.e., controls) at a brain hemisphere and brain region level. No significant differences were found in optimised model parameters (G_a, τ_{a1}, τ_{a2}) between postpartum women and controls in brain hemispheres (Table 5.8) or any of the brain regions (Table 5.10), although this may be due to limited sample sizes in the dataset used in this study (Table 5.5).

Brain region, however, was found to have a significant effect on both the magnitude (captured by G_a) and timing (captured by τ_{a1} and τ_{a2}) of dCVR (Table 5.10). Although the main aim of this chapter was not to investigate the spatial variability of dCVR, but rather to take advantage of the spatial information provided by BOLD-fMRI to perform a group (postpartum vs control) comparison at a brain region level, this finding highlights the spatial variability of dCVR and motivates the use of BOLD-fMRI to capture spatial information. Spatial heterogeneity in dCVR is in line with previous reports, e.g., [15] [142], but in this chapter, these differences may be related to differences in IR derivation hyperparameter values and numbers of voxels averaged in the BOLD-fMRI data, although significant differences are also found between brain regions with the same hyperparameters (Table 5.10, Table 5.11), such as the caudate and insula (G_a, τ_{a1}, τ_{a2}), the cerebellum and frontal (G_a, τ_{a1}), and the cerebellum and temporal (G_a, τ_{a1}).

5.4.2.Data-based impulse responses from BOLD-fMRI data

The use of BOLD-fMRI data allowed spatial information to be incorporated by deriving data-based IRs at a brain region level. The physiological model fit these brain region level IRs well; only 2.26% of the IRs accepted according to the first two criteria (see Section 5.2.4) have a NMSE larger than 0.3 from fitting to the model.

However, in BOLD-fMRI data, better spatial resolution typically comes at the cost of poorer temporal resolution, and Prokopiou *et al.* [15] describes a TR of 1 s as "good". In this study, the BOLD-fMRI data have a TR of 0.8 s (i.e., SF of 1.25 Hz; Table 5.2), which, while faster than in [15], may seem too slow to capture potential higher frequency dynamics in the CO_2-flow IR. Fortunately, jittering occurs when the BOLD-fMRI signal from multiple voxels is averaged, increasing the "effective" SF. It is a known phenomenon in the averaged BOLD-fMRI signal that has been used to reliably show the initial dip in the haemodynamic response function (i.e., the response of CBF to neural activation) [148]. Due to the heterogenous cerebral vascular structure, the response from the different voxels are all slightly out of phase, and each voxel in one BOLD-fMRI sample captures a slightly different part of the response. When all those slightly different parts of the response are averaged, the response is characterised at a higher "effective" SF than the TR that the BOLD-fMRI data were acquired at. Jittering can therefore explain how dCVR time constants of less than one second (Table 5.8 and Table 5.10) were derived from BOLD-fMRI data in this study.

However, jittering only occurs when the BOLD-fMRI signal is averaged over multiple voxels (as in this study; see Section 5.2.2.2), and will not occur when IRs are derived within individual voxels. Voxel level IRs from BOLD-fMRI data with lower temporal resolution will therefore not be able to capture higher frequency dynamics, as seen in the study by Golestani *et al.* [142], where a CO_2-flow IR derived from BOLD-fMRI data with a TR of 0.323 s (i.e., a SF of 3.10 Hz) showed higher frequency components that were not present when the IR was derived from BOLD-fMRI data with a TR of 2 s (i.e., a SF of 0.5 Hz). The absence of jittering can also explain why the study by Holmes et al. [47], which optimised time constants per voxel with a TR of 2.4 s (i.e., a SF 0.42 Hz), reports larger mean time constants, of 26.4 s and 23.7 s in the temporal and parietal respectively, than in this study, where all the time constants are smaller than a second (Table 5.8 and Table 5.10).

Prokopiou *et al.* [15], however, derived brain region level IRs (i.e., averaged over multiple voxels), and found TTP (see Section 4.2.7) values of around five and eight seconds from BOLD-fMRI data at RS and with externally induced CO_2 fluctuations respectively, which is an order of magnitude larger than the time constants obtained in this study. The TTP (and hence τ_{a1}, which describes the first part of the IR) could be affected by how much the $PetCO_2$ time series was shifted to line it up with the BOLD-fMRI signal (see Section 5.2.2.1), as part of the dCVR response could be captured within the shift, and different studies use different methods to determine the shift, such as cross-correlation (as in this study), a breath-hold experiment with the experimental setup, or simply using a shift between three and six seconds as recommended by the CARNet white paper [97]. The difference in TTP could also be explained by the difference in basis functions, as the study by Prokopiou *et al.* [15] used custom Gamma basis functions with lower frequency components than the spherical Laguerre basis functions used in this study, so the choice of basis functions is an important one. Notably, Shams *et al.* [116] compared multiple IR derivation methods in simulated case studies with known IRs, and found the basis expansion method using spherical Laguerre basis functions (used in this study; see Section 5.2.3) to be superior to the basis expansion method using Gamma basis functions (used in [15]), although it was mentioned that the optimal Gamma basis functions may be cohort specific and were not customised for the simulated case studies.

5.4.3.Impulse responses from resting state vs 5% CO_2 protocol data

Data-based IRs were derived from $PetCO_2$ and BOLD-fMRI data under two protocols: RS, where there are only spontaneous fluctuations in CO_2, and a 5% CO_2 protocol (Figure 5.1), where there are externally induced fluctuations in CO_2. Experimental protocol was found to have a significant effect on the magnitude of dCVR (G_a) and the timing of one part of its response (τ_{a1}). G_a is larger and τ_{a1} is smaller in the 5% CO_2 protocol, which indicates that the magnitude of the dCVR response is larger and one part of the dCVR response is faster in response to larger, externally induced fluctuations in CO_2 compared to smaller, spontaneous fluctuations in CO_2. Care should therefore be taken when comparing findings from RS data and data with externally induced CO_2 fluctuations.

However, experimental protocol could only be compared at the brain hemisphere level, as too few RS IRs were accepted for statistical analysis. 64.6% of the RS brain region level IRs were rejected based on statistical significance, physiological plausibility, and goodness of fit to the physiological model (see Section 5.2.4), leaving between zero and eight brain region level IRs per group (Table 5.5). Although RS data is preferable, as there is no risk of discomfort or requirement for cooperation from potentially frail or unconscious subjects, RS $PetCO_2$ and BOLD-fMRI data may not have sufficient SNR for robust IR derivation at the brain region level, even with a basis expansion method such as the one used in this study. Averaging a larger number of voxels may help improve the SNR in BOLD-fMRI data, as fewer hemisphere level IRs (52.3%) were rejected, although this would need to be corroborated in a larger cohort. Importantly, the rejection of so many RS IRs emphasises the need to perform some form of test to determine whether IRs derived from RS data with a basis expansion method are meaningful (which is not done in all previous studies), as basis expansion methods will give a result even if there is no relationship between the input and the output (see Appendix B.6).

The 5% CO_2 protocol therefore seems to yield more robust IRs at the brain region level, as only 7% of the derived IRs were rejected (Table 5.5). However, the "bootstrapping" method (see Section 5.2.4), via which most of the RS IRs were rejected (Table C.1 in Appendix C.2), could not be applied to the 5% CO_2 protocol IRs. This is because the "bootstrapping" method involves deriving "null" IRs, which requires there to be no relationship between the inputs ($PetCO_2$) and outputs (BOLD-fMRI), but the confounding factor of the experimental 5% CO_2 protocol used in this study (Figure 5.1) causes a relationship between all inputs and outputs. Although the 5% CO_2 protocol IRs are likely meaningful, as IR derivation would be more robust for larger fluctuations in CO_2, it could not be checked in this study. Future studies should therefore use a different 5% CO_2 protocol, where inspired CO_2 is not increased and decreased at the same times for all subjects, so that the "bootstrapping" method can be applied. A multi-frequency sequence such as the one in [149] (which was used in [15]), where inspired CO_2 is varied in a way that spreads the power of $PetCO_2$ in the frequency domain to stimulate both the central and peripheral chemoreceptor [150], would be beneficial.

It would also be worth investigating experimental protocols that can optimise the SNR in $PetCO_2$ and BOLD-fMRI signals without the need to increase inspired CO_2, which may not be possible for frail patients. A potential target could be to increase breathing rate, which would increase SF of the $PetCO_2$ time series, as only one sample can be taken per breath. In this study, there is no correlation between NMSE (between the actual and predicted BOLD-fMRI signal) and breathing rate (Figure 5.8), but that may be due to a small range of breathing rates in this dataset, so this should be investigated with a protocol that cues changes in breathing rate.

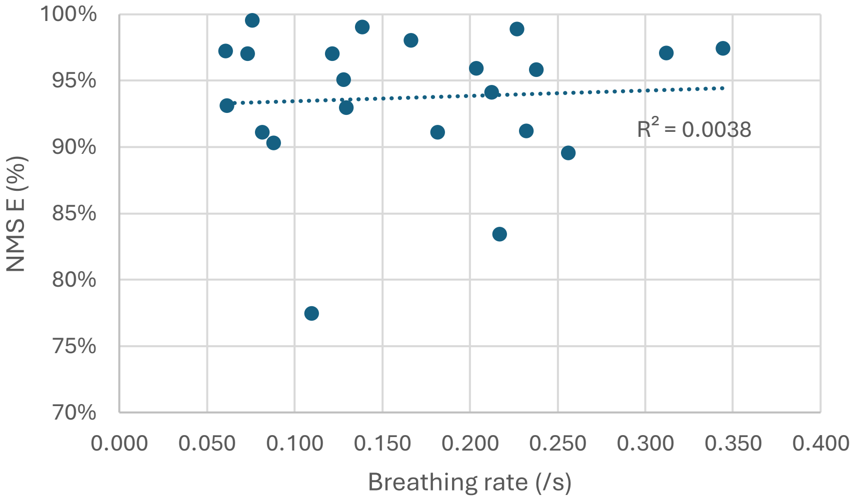

Figure 5.8. Normalised mean square error (between actual and predicted BOLD-fMRI time series) versus breathing rate for all subjects under resting state.

5.4.4.Potential for physiological insights

This chapter extends the simple physiological model of dCVR for use with BOLD-fMRI data, which incorporates spatial information. The model allows differences between groups to be allocated to changes in the magnitude of the response (represented by G_a) or the timing of the response (represented by τ_{a1} and τ_{a2}) within specific brain regions.

Here, the model was applied to postpartum women and women with no history of pregnancy (i.e., controls) in the structural brain regions from the MNI brain regions (Figure 5.4). Although differences between postpartum women and controls were not found in this cohort, differences between brain regions were found in all three model parameters, motivating the use of BOLD-fMRI data in conjunction with the physiological model. New hypotheses of the underlying physiology of dCVR can therefore be formed, implemented, and tested within the model at a brain region level. Specific structural or functional brain regions, such as the Default Mode Network [151], can be targeted under different physiological conditions or diseased states such as stroke, dementia, or diabetes.

5.4.5.Study limitations

This chapter has the same limitations stemming from the physiological model as described in Chapter 4. Briefly, the dCVR mechanism is currently a second order model without more detailed physiological pathways, neural activation and dCA are not modelled, and only the linear relationship between CO_2 and CBF is considered. In addition, the model does not take into account any spatial information beyond distinguishing between large arteries, small arteries and arterioles, capillaries, small veins and large veins, and rather relies on the spatial information from the BOLD-fMRI data to highlight spatial heterogeneity in the dCVR mechanism. In this chapter the model could not accommodate the “steal” effect, which can be captured by BOLD-fMRI data, as the gain was constrained to be non-negative during parameter optimisation, and data-based IRs with an initial decrease were excluded as “non-physiological”, because the “steal” effect is not expected in healthy subjects. It could, however, be incorporated in future studies if it is deemed reasonable by removing any constraints on the gain during parameter optimisation.

From the data side, dynamic $PetCO_2$ is used as a surrogate for dynamic arterial CO_2, although $PetCO_2$ is limited to one sample per breath and it is not clear whether intra-breath changes occur. Since the dataset used in this chapter also includes data collected under a CO_2 challenge protocol, sufficient SNR was available to line up the $PetCO_2$ and BOLD-fMRI time series using cross-correlation. This allowed the $PetCO_2$ time series to be shifted to limit the dynamics in the data-based CO_2-flow IRs to those stemming from only the brain (as opposed to including delays from the lungs to the capnograph and from the lungs to the brain), but the shift may capture part of the beginning of the dCVR response and so affect the optimised values of the model's first time constant. The BOLD-fMRI signal, which arises from a difference in deoxyhaemoglobin content in the blood and is hence affected by both CBF and metabolism, is used as a surrogate for CBF. The effects of ABP are not regressed out of the data-based IRs in this chapter, but ABP is not expected to affect the BOLD-fMRI signal, as it originates from the capillary bed, where changes in pressure have been attenuated by decreasing vessel diameters.

Data-based information is incorporated via IRs, which include only the linear relationship between CO_2 and CBF, but that is deemed reasonable, as the effects of CO_2 on the BOLD-fMRI signal have been found to be predominantly linear in both RS data and data with externally induced CO_2 fluctuations [15]. Lastly, confidence bounds were not estimated for the data-based CO_2-flow IRs. Since the expansion coefficients for the basis functions that make up the data-based IRs were estimated using ordinary least squares, confidence bounds could be calculated (for the expansion coefficients and hence the IRs) and this is recommended for future work that uses these methods.

5.5.Conclusion

In this chapter, the physiological model developed in Chapter 4 was extended and applied with BOLD-fMRI data to allow for spatial heterogeneity. This chapter links the growing body of dCVR studies using BOLD-fMRI data with a physiological model where physiologically meaningful parameters can be optimised under different physiological and pathophysiological conditions at a brain region level. Although the exploratory analysis in this chapter found no significant differences between postpartum women and women with no history of pregnancy in the MNI atlas brain regions, significant differences between brain regions were found in all model parameters, motivating the application of the model with BOLD-fMRI data. Future research should expand on this work by including a larger cohort and/or targeting specific regions known to be altered by pregnancy such as the Default Mode Network.

CHAPTER 6

Conclusions and future work

6.1.Thesis summary

The thesis objectives, listed in Chapter 1, were met in Chapter 3, Chapter 4, and Chapter 5. This section summarises and compares the key findings of this thesis, first by considering the modelling of dCA, second by considering the modelling of dCVR, and lastly by comparing the modelling of the two control mechanisms.

6.1.1.Modelling dynamic cerebral autoregulation

Recall that the first objective, listed in Chapter 1, is concerned with investigating the mechanisms of dCA by combining physiological modelling with time series analysis. This was addressed in Chapter 3, by developing a simple physiological model of dCA and using it in conjunction with TFA. The individual contributions of the two non-neurogenic mechanisms of dCA, the myogenic and metabolic responses, were disentangled by representing each mechanism by a gain and time constant within the physiological model. For simplicity, the myogenic response was taken to account only for vasoconstriction, as a response to direct stress, and the metabolic response to account only for vasodilation as a response to shear stress. The model was shown to produce the characteristic biphasic dCA IR. Two simplified versions of the physiological model were considered, by setting either the myogenic time constant or metabolic time constant to zero, but neither case could produce the characteristic biphasic IR of dCA with unique optimised parameter values, and the full model was selected.

Model parameters were optimised using data-based, pressure-flow IRs from u/v TFA and m/v TFA to regress out the effects of CO_2, applied to CBv (from TCD), ABP, and $PetCO_2$ data recorded under different physiological conditions: normocapnia and a thigh cuff condition to represent intact dCA, and hypercapnia to represent impaired dCA. Both the myogenic and metabolic responses were shown to be affected in hypercapnia compared to normocapnia. The ratio between the myogenic gain and time constant was found to be significantly smaller (p-values < 0.001 in u/v and m/v TFA results), indicating a smaller and/or slower vasoconstriction in response to direct stress. The metabolic gain was not affected, but the metabolic time constant was found to be larger (p-values < 0.001 in u/v and m/v TFA results), indicating that it is not the magnitude of vasodilation in response to shear stress that is affected in impaired dCA but rather the timing of the response that is slowed down – a key finding that has not been reported before. The thigh cuff condition was found to introduce some additional complexities that appear to impair dCA in the m/v TFA results, potentially due to differences in how subjects breathe during the experience of thigh cuffs or increased activation of the sympathetic nervous system.

The simple dCA model in combination with TFA, as presented in Chapter 3, can be used to form and test new hypotheses of how the myogenic and metabolic mechanisms of dCA are affected in specific healthy or diseased states. Model-based limitations include no consideration of NVC or the sympathetic response, the simplified allocation of vasoconstriction only to the myogenic response and vasodilation only to the metabolic response, and limiting all dynamics to the myogenic and metabolic time constants. Data-based limitations include using CBv in the MCA as a surrogate for CBF and using $PetCO_2$

as a surrogate for $PaCO_2$ although it cannot capture potential intra-breath variation in $PaCO_2$.

6.1.2.Modelling dynamic cerebrovascular reactivity

Recall that the second and third objectives, listed in Chapter 1, are concerned with investigating the mechanisms of dCVR by combining a physiological model with time series analysis of, first, TCD data, and second, BOLD-fMRI data, respectively.

6.1.2.1. Modelling dCVR with TCD

The second objective was addressed in Chapter 4, by developing a simple physiological model of dCVR and using it in conjunction with data-based, CO_2-flow IRs derived from a basis expansion method applied to TCD data. A compartmental physiological model was developed, with large arterial, small arterial and arteriole, capillary, and venous compartments. The control mechanism of dCVR was included as a second order response of arterial compliance to the logarithm of changes in arterial CO_2. A second order response was selected to produce a CO_2-flow IR that starts at zero, increases to a peak, decreases, sometimes has an undershoot, and settles to baseline, which is the shape that was obtained in most previous dCVR studies, [113], [142], [15] and used as the ground truth in the simulated case study of a recent review paper, [116].

Model parameters were optimised using data-based, CO_2-flow IRs obtained from a basis expansion method with spherical Laguerre basis functions applied to CBv (from TCD), $PetCO_2$, and ABP data in a SISO approach and a MISO approach to regress out the effects of ABP, under two physiological conditions: normocapnia and hypercapnia. The importance of testing whether data-based IRs derived from a basis expansion method are meaningful was highlighted, as the basis expansion method gives a result that may resemble a physiologically plausible shape even when white noise is used as the input and output. Only 50-80% of the derived data-based IRs were accepted for model parameter optimisation, based on a “bootstrapping” method and the absence of a non-physiological initial decrease.

The physiological model with the second order dCVR response was fitted to the accepted, data-based IRs and shown to be an improvement on both a first order dCVR response, as used in all previous studies that include the effects of CO_2, and a first order plus time delay dCVR response. However, the physiological model produced a poorer fit to data-based IRs that exhibited higher order dynamics than shown in most previous studies, [113], [142], [15]. Since it is currently unclear whether the higher order dynamics represent the underlying physiology of dCVR or an artefact from the data processing, where the $PetCO_2$ time series were up-sampled to an artificially high SF of 2 Hz, and data-based IR derivation, avenues for future work to investigate this are recommended in Section 6.3.3 and Section 6.3.4.

In Chapter 4, two analyses were performed: one with no requirement for goodness of fit to the physiological model, where a wider range of data-based IRs were included (50-80% of the derived IRs) but results may be affected by poorer model fits, and one where NMSE smaller than or equal to 0.3 was required from fitting to the physiological model, which is not affected by poor model fits but may only represent part of the physiological range of dCVR behaviour (including 27-61% of the derived IRs). A key finding is that the second time constant of dCVR was found to be significantly affected by physiological condition in all analyses (p-values < 0.001, except the second analysis' SISO results, where p-value < 0.05), becoming smaller, i.e., speeding up, in hypercapnia compared to normocapnia, potentially due to a smaller remaining range for vasodilation.

Potential sex differences on the gain and time constants were found in the first and second analyses, motivating further investigation into sex differences in CBF control in different healthy and diseased states. In the first analysis, the first time constant was found to decrease, i.e., speed up, in men (p-values < 0.001 in SISO and MISO results) and the second time constant was found to increase, i.e., slow down, in women (p-values < 0.001 in SISO and MISO results) during hypercapnia, but not in the second analysis. It was postulated that the sex differences may be spurious due to poorer model fits or primarily occur in IRs that exhibit higher order dynamics. In the second analysis, the gain was found to be significantly larger in men during hypercapnia compared to normocapnia, in the SISO results (p-value < 0.05) but not the MISO results where the effects of ABP were regressed out, so it should be further investigated in a model that includes both dCA and dCVR.

6.1.2.2. Modelling dCVR with BOLD-fMRI

The third objective was addressed in Chapter 5, by extending the physiological model of dCVR and using it in conjunction with BOLD-fMRI data, the most common modality in CVR studies. A clinical imagining dataset was used in conjunction with the physiological model to compare optimised model parameters between postpartum women and women with no history of pregnancy at the brain hemisphere and MNI atlas brain region level. The exploratory investigation in Chapter 5 did not find significant differences between postpartum women and controls in the MNI atlas brain regions. However, brain region was found to have a significant effect on all model parameters (p-values < 0.001), which highlights the spatial heterogeneity of dCVR and motivates the application of the dCVR physiological model with BOLD-fMRI data.

Chapter 5 also compared RS data and data from a 5% CO_2 protocol, and protocol-specific considerations were identified. First, RS data, despite being preferable in terms of patient comfort and cooperation, may not always have sufficient SNR for robust IR derivation at the brain region level. Too few brain level IRs derived from RS data passed the acceptance criteria to be included in the statistical analysis. This again highlighted the importance of testing whether data-based IRs are meaningful or not, and motivated the development of non-intrusive, experimental protocols that optimise RS $PetCO_2$ and BOLD-fMRI SNR. Second, the "bootstrapping" method could not be applied to determine whether the 5% CO_2 protocol IRs were meaningful, as the protocol increases and decreases the inspired CO_2 at the same times, so the $PetCO_2$ and BOLD-fMRI time series from all subjects are related and "null" IRs could not be derived, so recommendations for CO_2 protocols are provided in Section 6.3.3. Third, both the model gain and the first time constant are significantly affected by the experimental protocol at the brain hemisphere level, so care should be taken in comparing findings from RS data with findings from data with externally induced CO_2 fluctuations.

6.1.2.3. Modelling dCVR with TCD vs BOLD-fMRI

This thesis showed that the simple physiological model of dCVR can be used at a brain hemisphere level with TCD data and a brain hemisphere or brain region level with BOLD-fMRI data. New hypotheses of the underlying physiology of dCVR can be tested by including more detailed pathways within the control mechanism and using it in conjunction with either modality. The most obvious difference between the two modalities is that TCD is more cost effective than fMRI, so larger TCD datasets can be acquired more easily, as seen in the 100 recordings per physiological condition in Chapter 4 and 23 recordings, consisting of 10 postpartum and 13 controls, in Chapter 5. Dataset size was found to be an important consideration, as the RS brain region level parameter values in Chapter 5 could not be included in the statistical analysis due to small sample sizes of IRs accepted based on the "bootstrapping" method and the absence of an initial decrease that is non-physiological in young, healthy subjects.

Another consideration is that TCD has a high temporal resolution whereas fMRI provides spatial resolution but at the cost of high temporal resolution. However, data-based CO_2-flow IRs from both modalities exhibited high-frequency components, which is possible due to temporal jittering in the averaged BOLD-fMRI signal. Since jittering would not occur at a voxel level, analysis is limited to brain region level. The lower temporal resolution of BOLD-fMRI data, however, did limit the resolution of the Laguerre basis functions used in the basis expansion method for IR derivation, as the SF for the basis functions must equal the SF for the input-output data.

The physiological model of dCVR fit well to a larger proportion of the data-based IRs derived from the BOLD-fMRI dataset in Chapter 4 than from the TCD dataset in Chapter 5. Of the data-based IRs accepted by the "bootstrapping" method and with no initial decrease, 97.0% of the brain hemisphere level and 97.7% of the brain region level BOLD-fMRI IRs fit to the physiological model with a NMSE less than or equal to 0.3, whereas that was only the case for 62.7% of the TCD IRs. The difference in model fit stems from higher order dynamics, which the physiological model struggles to accommodate, occurring in more TCD IRs than BOLD-fMRI IRs. The two modalities also yield different ranges for the optimised time constants: for the BOLD-fMRI data in Chapter 5, both time constants are mostly less than a second (in the brain hemisphere level and brain region level analyses, except for the thalamus, where the time constant is around one second), whereas the TCD analyses in Chapter 4 also yield a first time constant of less than a second but a second time constant that ranges from less than a second up to four seconds. Importantly, these differences are present where an almost direct comparison can be made between TCD and BOLD-fMRI in this thesis, which is between the normocapnia results in Chapter 4 and the RS control results in Chapter 5. The comparison is, however, not entirely direct, as the steady state $PetCO_2$ and CBv time series in Chapter 4 were not lined up (and hence their dynamics were not limited only to the brain) but the higher SNR, 5% CO_2 protocol $PetCO_2$ and BOLD-fMRI time series in Chapter 5 could be used to perform cross-correlation to identify shifts that were then applied to both the RS and 5% CO_2 protocol $PetCO_2$ time series (and hence their dynamics were limited only to the brain, but perhaps shortened if the shift included part of the response time).

The findings in this thesis therefore highlighted the fact that, although they describe the same control system, data-based CO_2-flow IRs derived from TCD data and BOLD-fMRI data are different and are both only approximations of the response of CBF in the arterioles. Firstly, a TCD IR describes the response of CBv in a single artery, whereas a BOLD-fMRI IR describes the response of perfusion in a spatially diffuse capillary bed. Secondly, although the TCD data is beat-averaged to remove the cardiac effect, a TCD IR describes the response of high-pressure, fast-flowing, pulsatile blood flow, whereas a BOLD-fMRI IR describes the response of low-pressure, slow-moving blood flow. It was therefore important to regress out the effects of ABP in TCD data, as in the MISO approach in Chapter 4, but not in the BOLD-fMRI data in Chapter 5. Thirdly, a TCD IR is based on a measurement taken upstream from the dCVR control mechanism in the arterioles, whereas a BOLD-fMRI IR is based on a measurement taken downstream from the dCVR control mechanism. Since another consideration is that the higher order dynamics may be an artefact from artificially up-sampling the $PetCO_2$ time series, the lower SF of 1.25 Hz used in the BOLD-fMRI IR derivation may also explain the occurrence of fewer higher order dynamics. Interestingly, the average, hypercapnic, TCD IRs also exhibit less pronounced higher dynamics than the average, normocapnic, TCD IRs, and it was postulated that this may be due to differences in the underlying physiology between the two conditions or due to improved quality of the hypercapnic $PetCO_2$ time series, as people tend to breath more quickly and deeply in hypercapnia, improving the SF and accuracy of the $PetCO_2$ values.

6.1.2.4. Limitations of modelling dCVR

Limitations of the dCVR investigations in both Chapter 4 and Chapter 5 include the fact that the dCVR control mechanism was modelled as a second order response without detailed pathways that are tied more directly to the underlying physiology, although it was an important first step to link data-based dCVR studies with a physiological model. The model also does not consider dCA or neural activation, so their potential interactions with dCVR could not be investigated. The “steal” effect was not considered in this thesis, as all data were from young, healthy subjects. However, if the dCVR model is applied to a patient population where the “steal” effect is plausible, it can be accommodated by not constraining the gain parameter to be non-negative during parameter optimisation. A poorer model fit is obtained to data-based IRs that exhibit higher order dynamics, although it is not yet clear whether the higher order dynamics are artefacts or stem from the underlying physiology, and avenues for further investigation, potentially in conjunction with extended versions of the dCVR model presented in this thesis, are recommended in Section 6.3.3 and Section 6.3.4. Confidence bounds may have revealed uncertainty around the higher order dynamics, and the fact that they were not calculated is a key limitation of this study. In addition, only the linear range of the relationship between CO_2 and CBF was considered.

From the data side, CBv and BOLD-fMRI were used as surrogates for CBF in Chapter 4 and Chapter 5 respectively. Dynamic $PetCO_2$ was used as a surrogate for dynamic CO_2 content in the brain, although it is limited to one sample per breath, and its timing may include dynamics that are not limited to only the brain, such as the difference in the time it takes for CO_2 to travel from the lungs to the capnograph and the time it takes for CO_2 to travel from the lungs to the brain. In Chapter 4, where only low SNR, steady state recordings were available, these additional dynamics were not excluded from the derived data-based CO_2-flow IRs, although recordings were taken from the same subjects using the same experimental setup under the different physiological conditions, so any differences between physiological conditions are limited to the brain dynamics. In Chapter 5, 5% CO_2 protocol recordings were available, so there was sufficient SNR to line up the $PetCO_2$ and BOLD-fMRI time series using cross-correlation, but part of the dCVR response may then be captured in the shift.

There is currently not a best practice to account for CO_2 transport dynamics in $PetCO_2$ measurements, and even when the $PetCO_2$ time series is shifted (as in Chapter 5), it may still affect the derived CO_2-flow IR. Although the recent white paper published on behalf of CARNet [97] now recommends incorporating a $PetCO_2$ shift of some sort, and simply using three to six seconds if a shift cannot be identified from the recorded data, care should still be taken when comparing CO_2-flow IRs derived from different experimental setups, as it is not clear whether the delay from the lungs to the capnograph or the delay from the lungs to the brain is longer, so the true $PetCO_2$ shift that should be applied could be forwards or backwards.

6.1.3.Modelling dynamic cerebral autoregulation vs modelling dynamic cerebrovascular reactivity

Recall that the aim of this thesis was to investigate the mechanisms of dynamic CBF control by combining physiological and data-driven modelling approaches. The two main global CBF control mechanisms, dCA and dCVR, were specifically targeted and simple physiological models of both were developed and used in conjunction with time series analysis to gain physiological insights into their underlying mechanisms.

Various physiological models of dCA exist in literature, so a more detailed model of dCA could be derived, separating out the effects of two of its underlying mechanisms, the myogenic and metabolic responses. The underlying mechanisms of dCVR are less well understood and this thesis presented the first link between the growing body of data-driven dCVR studies to a simple physiological model, where a second order model with a gain and two time constants characterises the response of arterial compliance (which modulates CBF) to a change in arterial CO_2. It is, however, known that the response of CBF to changes in arterial CO_2 is correlated to changes in pH, so the dCVR control mechanism was modelled as a response to the logarithm of a change in arterial CO_2.

The application of TFA to analyse dCA is well established, and the data-based pressure-flow IRs that describe the linear part of dCA consistently produced the characteristic biphasic dCA IR from TFA in this thesis. Data-based CO_2-flow IRs that describe the linear part of dCVR, however, produced a range of IR shapes when derived from the basis expansion method used in this thesis, sometimes exhibiting the shape found in most previous dCVR studies and sometimes exhibiting higher order dynamics. The range of dCVR IR shapes were found when using both a SISO and MISO approach with TCD data and when using a SISO approach with BOLD-fMRI data, although the higher order dynamics occurred less often with BOLD-fMRI data. This thesis therefore highlighted the fact that, despite the recently growing body of data-driven dCVR studies, different methodologies are used for IR derivation, which complicates comparisons between studies, and as a result, a firm consensus on the CO_2-flow IR shape expected for young, healthy subjects is yet to be agreed upon.

The physiological models of dCA and dCVR were both purposefully kept simple enough for model parameter optimisation with the IRs derived from experimental data. dCA was investigated using only one modality, TCD, whereas dCVR was investigated using two modalities, TCD as well as BOLD-fMRI that can give spatial information, as the effects of CO_2 can be observed in the MCA and the capillary bed, but the effects of ABP are attenuated in the low pressure environment of the capillary bed. Parameters for both the dCA and dCVR models included gains and time constants, and in both cases, three parameters could be robustly interpreted. For dCA, it was the ratio of the optimised values for the myogenic gain and time constant, and the metabolic gain and metabolic time constant; for dCVR, it was the gain and two time constants.

Optimised values for the metabolic time constant in dCA and the two time constants in dCVR were found to be of the same order of magnitude, all less than a second, except for the second time constant in Chapter 4, which was found to be up to four seconds. This may be unexpected, as dCVR is known to affect CBF at lower frequencies than dCA. The dCVR IRs also exhibit shorter TTP values than observed in previous dCVR studies, although direct comparisons are difficult due to differences in methodologies. However, in addition to the speed with which CBF changes in response to changes in $PaCO_2$, the rate at which $PaCO_2$ changes can be measured also affects the frequencies at which $PaCO_2$ can be observed to affect CBF. Since $PaCO_2$ is measured as

$PetCO_2$, which is limited to one sample per breath (i.e., around 0.1 Hz), the SF of $PetCO_2$ is the limiting factor, and it is possible that CBF changes quickly in a response to $PaCO_2$ that can only be measured around every 10 seconds. The dCVR time constant values found in this thesis therefore do not contradict existing knowledge that the observable effect of $PaCO_2$ on CBF is at the lower frequencies.

6.2.Key contributions and clinical context

This thesis produced both methodological and scientific contributions. Methodologically, this thesis showed that combining physiological and data-driven modelling can produce new insights into how the underlying mechanisms of CBF control are affected in different physiological conditions. A workflow was developed, where parameter values of novel models of dCA and dCVR were optimised with data-based IRs derived under different physiological conditions, yielding statistically significant differences.

Regarding dCA, the key scientific contribution is that the metabolic response of dCA is slowed down in hypercapnia, a known surrogate state for impaired dCA. Regarding dCVR, both analyses (with and without goodness of fit requirements to the model) found that part of the response is faster in hypercapnia. Potential sex-specific effects on the dCVR gain and time constants were also found, although they were not present in both analyses and should be investigated further.

The models and workflow produced in this thesis can be used by researchers to test new hypotheses about dCA and dCVR in health and disease, improving the understanding of the complexities of these mechanisms for incorporation in future clinical trials and targeted treatment development. This thesis showed use-cases comparing between different physiological conditions in healthy subjects, using TCD data for dCA and both TCD and BOLD-fMRI data for dCVR. However, key limitations should be born in mind for future work, especially when extrapolating the use-case to compare between more clinically relevant groups, such as patient or elderly groups, and healthy controls.

For use-cases involving patient or elderly groups, model assumptions, fixed parameter values, and workflow implementation should be reconsidered, and, where necessary, updated. Regarding model assumptions, assuming a Newtonian fluid and no significant change in blood density throughout the cerebral vasculature may not be plausible in patients with sickle cell disease, due to the clumping of red blood cells in smaller blood vessels like the capillaries, for example. Regarding fixed model parameters, hypertensive patients will have elevated mean ABP, elderly subjects may have lower baseline arterial compliance due to arterial stiffening that occurs with age, sickle cell patients will have elevated baseline resistance to blood flow and blood viscosity due to red blood cell clumping, and so forth. Regarding workflow implementation, the presence of pathophysiology, whether known in patient groups or perhaps unknown in “healthy” elderly groups, the “steal” effect is plausible and should be accounted for. Data-based, CO_2-flow IRs with initial decreases should therefore not be excluded from analysis, and the dCVR gain parameter in the model should not be constrained to be nonnegative.

The workflow developed in this thesis can also be applied with extended or alternative models of CBF control. Currently, neither of the models account for blood inertia, which may contribute to the unexpected observed dynamics in the data-based CO_2-flow IRs, and could be modelled as inductance in the equivalent electrical models. The effects of pulsatility, where inertia is particularly relevant, were regressed out in this thesis by using beat-averaged recordings of ABP and CBv, but inertia may still play a role in the transient responses of dCA and dCVR, especially in the higher frequency components. Another source of dynamics, that may contribute to the unexpected observed dynamics in the data-based IRs but is currently not included in the models, is physiological sensor dynamics (e.g., sensing direct or shear stress on vessel walls, or sensing pH changes). Dynamics such as higher order behaviour or an initial decrease are not intuitively physiological for the response of CBF to $PaCO_2$ but may be due to the dynamics involved in sensing changes in pH, and this should be investigated.

The workflow could also be applied to another aspect of CBF control, namely NVC, which is the response of CBF to changes in neural activation. A physiological model of NVC could be identified from literature or developed, and TCD or BOLD-fMRI data could be collected alongside electroencephalography (EEG) data. Since NVC is a local response, BOLD-fMRI would be the better option for data collection, and it may be worth including some more detailed spatial information within the physiological model. The neural task could be selected to activate a specific part of the brain and spatial information of only that part could be included in the model, in order to keep the number of free parameters in the model low.

A key limitation of the workflow presented in this thesis, is that it is designed to only investigate one aspect of CBF control at a time. Instead of adding additional complexity to the physiological models, the effects of other factors are regressed out of the data-based IRs using a multivariate approach. This serves the purpose of obtaining physiological models that remain simple enough to be used in conjunction with experimental data, but it does mean that the workflow cannot be used to investigate the interaction of different aspects of CBF control.

Lastly, the workflow presented in this thesis only considers the linear components of dCA and dCVR, whereas the nonlinear components may be of particular relevance in clinical populations, such as patients or elderly subjects, with less remaining vasodilatory ability. The basis expansion method that derives the IR as the first kernel of the DVM can be used to derive higher order kernels that would incorporate nonlinear dynamics, although this approach would then require the physiological model to also be separated into the linear and nonlinear components, which is not intuitive - yet.

6.3.Future work

During the course of this thesis, interesting avenues for future work were discovered and are briefly presented here.

6.3.1.Investigating sex differences in dCA and dCVR

Women’s health is an important topic that has only recently started attracting more attention and funding. In light of this, the scientific community has been encouraged to include sex as an independent variable in analyses to investigate potential sex differences. Sex was included in the dCVR investigation in Chapter 4 and potential sex differences were found in both the magnitude and timing of dCVR. However, sex was not included in the dCA investigation in Chapter 3, and future work should repeat the statistical analysis with a Three-Way ANOVA where sex is included as a potential main effect.

Future studies of dCA and dCVR should also include additional sex-specific information. For example, information about potentially confounding factors such as a history of pregnancy or hormonal effects in women should be asked for during the data collection stage and, if sufficient granularity can be obtained, accounted for in analyses.

6.3.2.Extending the physiological dCA model

The dCA model in Chapter 3 was purposefully kept simple so that it could be used in conjunction with time series analysis for model parameter optimisation. However, it could be extended to widen its application domain. Since the main case where dCA is currently monitored in a clinical setting is for patients with traumatic brain injury [152], a useful extension would be to include variable intracranial pressure.

The current dCA model only includes the non-neurogenic mechanisms of dCA, the myogenic and metabolic responses. Future work could extend the model to include the neurogenic response. The main challenge is robust optimisation of a larger number of model parameters, as scaling was observed in the preliminary results of Chapter 3 where an additional parameter for the elastic response was included. This could be addressed by adjusting the model to write and optimise the myogenic gain and time constant as one parameter (i.e., their ratio), since their optimised values already had to be interpreted as a combined value (i.e., their ratio) due to their bimodal distributions in Chapter 3.

6.3.3.Comparing data-based CO_2-flow impulse response derivation methods and hyperparameters

The characteristic biphasic pressure-flow IR is well established in literature but, despite the recent increase in interest, only a few studies, [113] [142], [15], [45], and Chapter 4 and Chapter 5 in this thesis, have derived the CO_2-flow IR. Although a range of different timings were included, the recent review paper by Shams *et al.* [116] used a CO_2-flow IR that starts at zero, rises to a peak, potentially has an undershoot, and settles to baseline, as the ground truth in a simulated case study, which is why a physiological dCVR model that can produce that CO_2-flow IR shape was developed in Chapter 4.

However, the CO_2-flow IRs derived in this study, using the method recommended by Shams *et al.* [116], exhibited that shape in addition to higher order dynamics in some of the IRs, especially when derived from TCD data. Marmarelis et al. [45], also showed an average CO_2-flow IR for healthy subjects that exhibited higher order dynamics, although it also did not start at zero. Currently it is unclear whether higher order dynamics represent the underlying physiology of dCVR or an artefact from deriving the IR from low SNR $PetCO_{2}$- time series that has been artificially up-sampled. An important avenue for future work is therefore two-fold: robust investigations are required to (1) identify the CO_2-flow IR shape or range of shapes that can be expected for young, healthy subjects, as discussed in Section 6.3.4, and (2) compare different methods that can be used to derive those CO_2-flow IRs, as discussed here.

Shams *et al.* [116] made a start to the second point by comparing different model-based CO_2-flow IR derivation methods on simulated data with a known ground truth. Model-based methods are recommended for use with low SNR RS data, but they impose an underlying shape (which differs for different model-based methods) on the resulting IR, so knowledge of the expected range of CO_2-flow shape is particularly important if this type of method is to be used. Future work should extend the comparison by Shams *et al.* [116] to include purely data-based methods, such as TFA or direct IR derivation, and apply the methods to real-world data in addition to simulated data. A white paper that reviews all the methods for CO_2-flow IR derivation and provides recommendations for implementation, such as the ones published on behalf of CARNet for dCA, [153], [111], [97], would be particularly beneficial, so that future dCVR studies can follow recommended guidelines and their results can be easily compared.

In addition to comparing different methods, the effects of specific aspects of the methods also need to be investigated and recommendations provided for consistency in the dCVR community. In model-based methods, important aspects that require investigation include the choice of basis functions (where applicable), hyperparameter selection, and SF, which are all interlinked. A specific recommendation for the basis expansion method with spherical Laguerre basis functions that was used in Chapter 4 and Chapter 5, is to investigate whether the use of larger values of the decay parameter, α, still yields CO_2-flow IRs with higher order dynamics. In Chapter 4 and Chapter 5, the range for α was limited to 0.5 to 0.9, as in [116], but a range of larger values, of up to five for example, would result in slower dynamics in the spherical Laguerre basis functions and so allow them to be sufficiently captured by a lower SF (Figure 6.1), which would, in turn, allow a lower SF to be used for the $PetCO_2$ time series. Ideally, the SF would not be higher than 1 Hz, as recommended by the CARNet white paper, [97], for the inclusion of CO_2 in a multivariate analysis of dCA. Of course, the slower dynamics in the basis functions would also limit the dynamics that can appear in the derived IRs, and the maximum allowable value for α was not selected during hyperparameter selection in any of the cases in Chapter 4 or Chapter 5, although that may be due to a local minimum. The NMSE between the actual and predicted output (CBv or BOLD-fMRI) and BIC values for the case with larger α values should therefore be compared with the NMSE and BIC values for the case with smaller α values to determine which derived IRs provide a better description of the CO_2-flow relationship. Whenever possible, confidence bounds should be estimated for the data-based IRs. For basis expansion methods, this can be done by estimating confidence intervals for the expansion coefficients (and hence resulting IRs) using a least squares criterion.

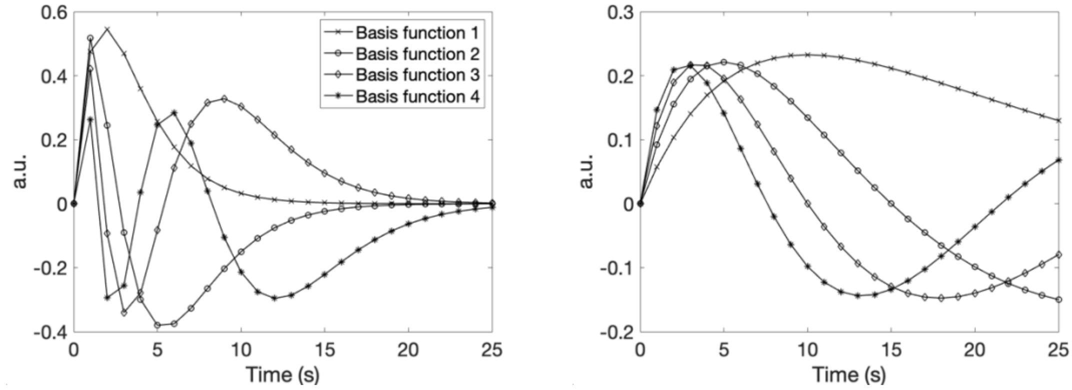

(a) (b)

Figure 6.1. Spherical Laguerre basis functions created with a sampling frequency SF of 1 Hz, where the decay parameter, α, is (a) 0.9, and (b) 5.

In purely data-based methods, the effect of SF should also be investigated. The main challenge in deriving CO_2-flow IRs from purely data-driven methods is that they typically require inversion of the autocorrelation matrix of $PetCO_2$, which becomes ill-conditioned if collinearities are introduced by over-sampling. This could be addressed by investigating methods where different SFs can be used for different inputs, such as direct finite IR derivation in [113], so that a lower SF can be used for $PetCO_2$. If the purely data-based methods struggle to derive the CO_2-flow IR from low SNR, RS data, data from different experimental protocols should be included as case studies for the comparison between methods and aspects of methods. A guided breathing protocol that encourages participants to breathe each breath out fully could improve the quality of the $PetCO_2$ values and so increase SNR. Alternatively, CO_2 fluctuations can be externally induced by changing the inspired CO_2, as in the dataset used in Chapter 5, although this may not be usable down the line in a clinical setting with frail patients. Importantly, if inspired CO_2 protocol data is to be used with model-based methods, the inspired CO_2 should be increased and decreased at random times, so that all the $PetCO_2$ and TCD or BOLD-fMRI time series are not related and “null” IRs can be derived for the “bootstrapping” approach to determine if the derived IRs are meaningful.

6.3.4.Investigating the shape of CO_2-flow IRs with extensions of the dCVR physiological model

In addition to robust investigations of implementations of the different methods available for.CO_2-flow IR derivation, as discussed in Section 6.3.3, future work should investigate the physiological plausibility of the higher order dynamics in the CO_2-flow IRs in conjunction with extensions of physiological models such as the one derived in Chapter 4. Simply modelling the response of arteriolar compliance to changes in arterial CO_2 as a higher order model, such as a third order model, may improve the physiological model fit to the data-based IRs that exhibit higher order dynamics, but that may be overfitting to potentially non-physiological features.

Rather, future work should add specific detail to the physiological model of dCVR presented in this thesis to test hypotheses of potential physiological causes for the higher order dynamics observed in some of the data-based IRs. Model parameters can be allocated to specific parts of the underlying physiology to investigate whether model parameter optimisation yields physiologically plausible values. One possibility is to separate out the contributions of vasodilation and vasoconstriction in dCVR. Another possibility is to extend the model to include a tissue compartment and include diffusion dynamics, to investigate the postulation by Daher *et al.* [89] that dCVR may respond to changes in tissue CO_2 rather than arterial CO_2.

6.3.5.Directly comparing between TCD and BOLD-fMRI data

The physiological model of dCVR was applied in conjunction with TCD data and BOLD-fMRI data in Chapter 4 and Chapter 5 respectively. Interestingly, differences in the data-based IRs and optimised model parameters were noted between the two modalities, as discussed in Section 6.1.2.3. However, the comparison was largely limited by the different demographics and physiological conditions captured in the two datasets. Since statistically significant differences were found in the dCVR model parameters between steady state normocapnia and hypercapnia, it would be valuable to repeat the analysis in Chapter 5 with a BOLD-fMRI dataset (with sufficient temporal resolution) that has also be acquired under steady state normocapnia and hypercapnia conditions. It would be particularly interesting to investigate whether the same differences in parameter values can be identified from both modalities. Ideally, a dataset could be acquired where both TCD and BOLD-fMRI data are recorded from the same cohort.

6.4.Concluding remarks

This thesis investigated both dCA and dCVR using a combination of physiological and data-driven modelling approaches. Both physiological and data-driven modelling of dCA are established in current literature, and this thesis separated out the effects of the myogenic and metabolic responses in intact and impaired dCA. The mechanism of dCVR itself has only recently gathered more interest, where previous studies mostly investigated static CVR or incorporated dCVR as part of a multivariate investigation of dCA. This thesis provides the first step in linking the recently growing body of data-driven studies of dCVR with a physiological model where physiologically meaningful parameters can be optimised under different physiological and pathophysiological conditions. The model was implemented in conjunction with both TCD data, making it accessible to the dCA community that typically uses TCD data and may expand their interests to include dCVR, and BOLD-fMRI, making it accessible to the CVR community that typically uses BOLD-fMRI data and appear to be expanding their interests to include the dynamic aspects of CVR.

References

[1] S. S. Kety and C. F. Schmidt, ‘The nitrous oxide method for the quantitative determination of cerebral blood flow in man: theory, procedure and normal values 1’, *J Clin Invest*, vol. 27, no. 4, pp. 476–483, Jul. 1948.

[2] M. E. Watts, R. Pocock, and C. Claudianos, ‘Brain energy and oxygen metabolism: Emerging role in normal function and disease’, *Frontiers in Molecular Neuroscience*, vol. 11, pp. 1–13, 2018, doi: 10.3389/fnmol.2018.00216.

[3] S. J. Payne, *Cerebral blood flow and metabolism: a quantitative approach*. World Scientific Publishing, 2018.

[4] P. N. Ainslie and J. Duffin, ‘Integration of cerebrovascular CO2 reactivity and chemoreflex control of breathing: Mechanisms of regulation, measurement, and interpretation’, *American Journal of Physiology - Regulatory Integrative and Comparative Physiology*, vol. 296, no. 5, pp. 1473–1495, 2009, doi: 10.1152/ajpregu.91008.2008.

[5] R. B. Panerai, ‘Cerebral autoregulation: from models to clinical applications’, *Cardiovasc Eng*, vol. 8, no. 1, pp. 42–59, Mar. 2008, doi: 10.1007/s10558-007-9044-6.

[6] A. Battisti-Charbonney, J. Fisher, and J. Duffin, ‘The cerebrovascular response to carbon dioxide in humans’, *J Physiol*, vol. 589, no. Pt 12, pp. 3039–3048, Jun. 2011, doi: 10.1113/jphysiol.2011.206052.

[7] M. J. Poulin, P. J. Liang, and P. A. Robbins, ‘Dynamics of the cerebral blood flow response to step changes in end-tidal PCO2 and PO2 in humans’, *Journal of Applied Physiology*, vol. 81, no. 3, pp. 1084–1095, Sep. 1996, doi: 10.1152/jappl.1996.81.3.1084.

[8] P. Liu, J. B. De Vis, and H. Lu, ‘Cerebrovascular reactivity (CVR) MRI with CO2 challenge: A technical review’, *NeuroImage*, vol. 187, pp. 104–115, Feb. 2019, doi: 10.1016/j.neuroimage.2018.03.047.

[9] WHO, ‘Global Health Estimates 2016: Disease burden by Cause, Age, Sex, by Country and by Region, 2000-2016’, Geneva: World Health Organisation, 2018.

[10] A. E. van Rijssel *et al.*, ‘Effect of Antihypertensive Treatment on Cerebral Blood Flow in Older Adults: a Systematic Review and Meta-Analysis’, *Hypertension*, vol. 79, no. 5, pp. 1067–1078, May 2022, doi: 10.1161/HYPERTENSIONAHA.121.18255.

[11] B. Widder, B. Kleiser, and H. Krapf, ‘Course of cerebrovascular reactivity in patients with carotid artery occlusions.’, *Stroke*, vol. 25, no. 10, pp. 1963–1967, Oct. 1994, doi: 10.1161/01.STR.25.10.1963.

[12] J. M. Serrador, F. A. Sorond, M. Vyas, M. Gagnon, I. D. Iloputaife, and L. A. Lipsitz, ‘Cerebral pressure-flow relations in hypertensive elderly humans: transfer gain in

different frequency domains', *Journal of Applied Physiology*, vol. 98, no. 1, pp. 151–159, Jan. 2005, doi: 10.1152/japplphysiol.00471.2004.

[13] A. D. Wijnhoud, P. J. Koudstaal, and D. W. J. Dippel, 'Relationships of transcranial blood flow Doppler parameters with major vascular risk factors: TCD study in patients with a recent TIA or nondisabling ischemic stroke', *Journal of Clinical Ultrasound*, vol. 34, no. 2, pp. 70–76, 2006, doi: 10.1002/jcu.20193.

[14] A. Xie, J. B. Skatrud, R. Khayat, J. A. Dempsey, B. Morgan, and D. Russell, 'Cerebrovascular Response to Carbon Dioxide in Patients with Congestive Heart Failure', *American Journal of Respiratory and Critical Care Medicine*, Dec. 2012, doi: 10.1164/rccm.200406-807OC.

[15] P. C. Prokopiou, K. T. S. Pattinson, R. G. Wise, and G. D. Mitsis, 'Modeling of dynamic cerebrovascular reactivity to spontaneous and externally induced CO2 fluctuations in the human brain using BOLD-fMRI', *NeuroImage*, vol. 186, pp. 533–548, Feb. 2019, doi: 10.1016/j.neuroimage.2018.10.084.

[16] Openstax, *Anatomy and Physiology*. 2020. [Online]. Available: https://openstax.org/books/anatomy-and-physiology

[17] A. Crossman and D. Neary, *Neuroanatomy: an Illustrated Colour Text*, 6th ed. in An Illusrtated Colour Text Series. Elsevier Science Health Science Division, 2018.

[18] B. Alpers, R. Berry, and R. Paddison, 'Anatomical studies of the circle of Willis in normal brain', *AMA Arch Neurol Psychiatry*, vol. 81, no. 4, pp. 409–418, 1959.

[19] V. Papantchev *et al.*, 'The role of Willis circle variations during unilateral selective cerebral perfusion: a study of 500 circles', *Eur J Cardiothorac Surg*, vol. 44, no. 4, pp. 743–753, 2013.

[20] H. L. McConnell, C. N. Kersch, R. L. Woltjer, and E. A. Neuwelt, 'The Translational Significance of the Neurovascular Unit *', *Journal of Biological Chemistry*, vol. 292, no. 3, pp. 762–770, Jan. 2017, doi: 10.1074/jbc.R116.760215.

[21] J. A. H. R. Claassen, D. H. J. Thijssen, R. B. Panerai, and F. M. Faraci, 'Regulation of cerebral blood flow in humans: physiology and clinical implications of autoregulation', *Physiological reviews*, vol. 101, no. 4, pp. 1487–1559, 2021, doi: 10.1152/physrev.00022.2020.

[22] R. B. Panerai, 'Assessment of cerebral pressure autoregulation in humans - A review of measurement methods', *Physiological Measurement*, vol. 19, pp. 305–338, 1998, doi: 10.1088/0967-3334/19/3/001.

[23] O. Paulson, S. Strandgaard, and L. Edvinsson, 'Cerebral autoregulation', *Cerebrovasc Brain Metab Rev*, vol. 2, pp. 161–192, 1990.

[24] K. Intharakham, L. Beishon, R. B. Panerai, V. J. Haunton, and T. G. Robinson, 'Assessment of cerebral autoregulation in stroke: A systematic review and meta-analysis of studies at rest', *Journal of Cerebral Blood Flow and Metabolism*, vol. 39, pp. 2105–2116, 2019, doi: 10.1177/0271678X19871013.

[25] A. H. E. A. Van Beek, J. A. H. R. Claassen, M. G. M. O. Rikkert, and R. W. M. M. Jansen, 'Cerebral autoregulation: An overview of current concepts and methodology

with special focus on the elderly', *Journal of Cerebral Blood Flow and Metabolism*, vol. 28, pp. 1071–1085, 2008, doi: 10.1038/jcbfm.2008.13.

[26] R. B. Panerai, 'System identification of human cerebral blood flow regulatory mechanisms', *Cardiovascular Engineering*, vol. 4, no. 1, pp. 59–71, 2004, doi: 10.1023/B:CARE.0000025123.43747.e1.

[27] S. J. Payne, *Cerebral Autoregulation. Control of Blood Flow in the Brain*, vol. s7-IV. Berlin: Springer Briefs in Bioengineering, Springer, 2016. doi: 10.1093/nq/s7-IV.95.328-b.

[28] A. Silverman and N. H. Petersen, *Physiology, Cerebral Autoregulation*. StatPearls Publishing, Treasure Island (FL), 2021. Accessed: Nov. 23, 2021. [Online]. Available: https://www.ncbi.nlm.nih.gov/books/NBK553183/

[29] C. Iadecola, 'The Neurovascular Unit Coming of Age: A Journey through Neurovascular Coupling in Health and Disease', *Neuron*, vol. 96, no. 1, pp. 17–42, Sep. 2017, doi: 10.1016/j.neuron.2017.07.030.

[30] M. E. Raichle and M. A. Mintun, 'Brain work and brain imaging', *Annual Review of Neuroscience*, vol. 29, pp. 449–476, 2006, doi: 10.1146/annurev.neuro.29.051605.112819.

[31] D. Attwell and C. Iadecola, 'The neural basis of functional brain imaging signals', *Trends in Neurosciences*, vol. 25, pp. 621–625, 2002, doi: 10.1016/S0166-2236(02)02264-6.

[32] R. L. Hoiland, J. A. Fisher, and P. N. Ainslie, 'Regulation of the Cerebral Circulation by Arterial Carbon Dioxide', in *Comprehensive Physiology*, vol. 9, Wiley, 2019, pp. 1101–1154. doi: 10.1002/cphy.c180021.

[33] A. M. Harper and H. I. Glass, 'Effect of alterations in the arterial carbon dioxide tension on the blood flow through the cerebral cortex at normal and low arterial blood pressures', *J Neurol Neurosurg Psychiatry*, vol. 28, no. 5, pp. 449–452, Oct. 1965, doi: 10.1136/jnnp.28.5.449.

[34] M. Ursino and C. A. Lodi, 'Interaction among autoregulation, CO2 reactivity, and intracranial pressure: a mathematical model', *Am J Physiol*, vol. 274, no. 5, pp. H1715-1728, May 1998, doi: 10.1152/ajpheart.1998.274.5.H1715.

[35] J. A. H. R. Claassen, R. Zhang, Q. Fu, S. Witkowski, and B. D. Levine, 'Transcranial Doppler estimation of cerebral blood flow and cerebrovascular conductance during modified rebreathing', *Journal of Applied Physiology*, vol. 102, pp. 870–877, 2007, doi: 10.1152/japplphysiol.00906.2006.

[36] K. B. Miller *et al.*, 'Age-Related Reductions in Cerebrovascular Reactivity Using 4D Flow MRI', *Front. Aging Neurosci.*, vol. 11, no. 281, Oct. 2019, doi: 10.3389/fnagi.2019.00281.

[37] I. Uwano *et al.*, 'Assessment of Impaired Cerebrovascular Reactivity in Chronic Cerebral Ischemia using Intravoxel Incoherent Motion Magnetic Resonance Imaging', *Journal of Stroke and Cerebrovascular Diseases*, vol. 30, no. 12, p. 106107, Dec. 2021, doi: 10.1016/j.jstrokecerebrovasdis.2021.106107.

[38] H. J. Walsh, R. T. Junejo, G. Y. H. Lip, and J. P. Fisher, ‘The effect of hypertension on cerebrovascular carbon dioxide reactivity in atrial fibrillation patients’, *Hypertens Res*, vol. 47, no. 6, pp. 1678–1687, Jun. 2024, doi: 10.1038/s41440-024-01662-2.

[39] R. L. GRUBB, M. E. RAICHLE, J. O. EICHLING, and M. M. TER-POGOSSIAN, ‘The Effects of Changes in PaCO2 Cerebral Blood Volume, Blood Flow, and Vascular Mean Transit Time’, *Stroke*, vol. 5, no. 5, pp. 630–639, Sep. 1974, doi: 10.1161/01.STR.5.5.630.

[40] M. Reivich, ‘Arterial Pco2 and cerebral hemodynamics’, *American Journal of Physiology-Legacy Content*, vol. 206, no. 1, pp. 25–35, Jan. 1964, doi: 10.1152/ajplegacy.1964.206.1.25.

[41] L. J. Kemna, S. Posse, L. Tellmann, T. Schmitz, and H. Herzog, ‘Interdependence of Regional and Global Cerebral Blood Flow during Visual Stimulation: An O-15-Butanol Positron Emission Tomography Study’, *J Cereb Blood Flow Metab*, vol. 21, no. 6, pp. 664–670, Jun. 2001, doi: 10.1097/00004647-200106000-00004.

[42] K. J. Cummings, M. Swart, and P. N. Ainslie, ‘Morning attenuation in cerebrovascular CO2 reactivity in healthy humans is associated with a lowered cerebral oxygenation and an augmented ventilatory response to CO2’, *Journal of Applied Physiology*, vol. 102, no. 5, pp. 1891–1898, May 2007, doi: 10.1152/japplphysiol.01437.2006.

[43] K. Ide, M. Eliasziw, and M. J. Poulin, ‘Relationship between middle cerebral artery blood velocity and end-tidal PCO2 in the hypocapnic-hypercapnic range in humans’, *Journal of Applied Physiology*, vol. 95, no. 1, pp. 129–137, Jul. 2003, doi: 10.1152/japplphysiol.01186.2002.

[44] K. C. Peebles, A. M. Richards, L. Celi, K. McGrattan, C. J. Murrell, and P. N. Ainslie, ‘Human cerebral arteriovenous vasoactive exchange during alterations in arterial blood gases’, *J Appl Physiol (1985)*, vol. 105, no. 4, pp. 1060–1068, Oct. 2008, doi: 10.1152/japplphysiol.90613.2008.

[45] V. Z. Marmarelis, D. C. Shin, Y. Kang, and V. Novak, ‘Data-based modeling of cerebral hemodynamics quantifies impairment of cerebral blood flow regulation in type-2 diabetes’, *J Cereb Blood Flow Metab*, vol. 44, no. 11, pp. 1288–1301, May 2024, doi: 10.1177/0271678X241254716.

[46] T. Peng, A. B. Rowley, P. N. Ainslie, M. J. Poulin, and S. J. Payne, ‘Multivariate System Identification for Cerebral Autoregulation’, *Ann Biomed Eng*, vol. 36, no. 2, pp. 308–320, Feb. 2008, doi: 10.1007/s10439-007-9412-9.

[47] K. R. Holmes *et al.*, ‘Slowed Temporal and Parietal Cerebrovascular Response in Patients with Alzheimer’s Disease’, *Canadian Journal of Neurological Sciences*, vol. 47, no. 3, pp. 366–373, May 2020, doi: 10.1017/cjn.2020.30.

[48] J. Leung, J. Duffin, J. A. Fisher, and A. Kassner, ‘MRI-based cerebrovascular reactivity using transfer function analysis reveals temporal group differences between patients with sickle cell disease and healthy controls’, *Neuroimage Clin*, vol. 12, pp. 624–630, Sep. 2016, doi: 10.1016/j.nicl.2016.09.009.

[49] R. L. Hoiland, A. R. Bain, M. G. Rieger, D. M. Bailey, and P. N. Ainslie, 'Hypoxemia, oxygen content, and the regulation of cerebral blood flow', *Am J Physiol Regul Integr Comp Physiol*, vol. 310, no. 5, pp. R398-413, Mar. 2016, doi: 10.1152/ajpregu.00270.2015.

[50] A. A. Bhogal *et al.*, 'Examining the regional and cerebral depth-dependent BOLD cerebrovascular reactivity response at 7 T', *NeuroImage*, vol. 114, pp. 239–248, Jul. 2015, doi: 10.1016/j.neuroimage.2015.04.014.

[51] O. Sobczyk *et al.*, 'A conceptual model for CO2-induced redistribution of cerebral blood flow with experimental confirmation using BOLD MRI', *NeuroImage*, vol. 92, pp. 56–68, May 2014, doi: 10.1016/j.neuroimage.2014.01.051.

[52] D. M. Mandell *et al.*, 'Selective reduction of blood flow to white matter during hypercapnia corresponds with leukoaraiosis', *Stroke*, vol. 39, no. 7, pp. 1993–1998, 2008, doi: 10.1161/STROKEAHA.107.501692.

[53] V. C. Hachinski, P. Potter, and H. Merskey, 'Leuko-Araiosis: An Ancient Term for a New Problem', *Canadian Journal of Neurological Sciences*, vol. 13, no. S4, pp. 533–534, Nov. 1986, doi: 10.1017/S0317167100037264.

[54] C. B. Early, R. C. Dewey, H. P. Pieper, and W. E. Hunt, 'Dynamic pressure-flow relationships of brain blood flow in the monkey', *Journal of Neurosurgery*, vol. 41, pp. 590–596, 1974, doi: 10.3171/jns.1974.41.5.0590.

[55] S. Kety, J. Hafkenschiel, W. Jeffer, I. Leopold, and H. Shenkin, 'The blood flow, vascular resistance, and oxygen consumption of the brain in essential hypertension', *The Journal of clinical investigation*, vol. 27, pp. 511–514, 1948, doi: 10.1172/JCI101998.

[56] J. W. Gooch, 'Hagen-Poiseuille Equation', in *Encyclopedic Dictionary of Polymers*, New York, NY: Springer, 2011, pp. 355–355. doi: 10.1007/978-1-4419-6247-8_5752.

[57] M. J. Davis, G. A. Meininger, and D. C. Zawieja, 'Stretch-induced increases in intracellular calcium of isolated vascular smooth muscle cells', *Am J Physiol*, vol. 263, no. 4 Pt 2, pp. H1292-1299, Oct. 1992, doi: 10.1152/ajpheart.1992.263.4.H1292.

[58] D. A. Hartmann, V. Coelho-Santos, and A. Y. Shih, 'Pericyte Control of Blood Flow Across Microvascular Zones in the Central Nervous System', *Annual Review of Physiology*, vol. 84, no. 1, pp. 331–354, 2022, doi: 10.1146/annurev-physiol-061121-040127.

[59] V. Krishnamurthy *et al.*, 'The Utility of Cerebrovascular Reactivity MRI in Brain Rehabilitation: A Mechanistic Perspective', *Front Physiol*, vol. 12, p. 642850, Mar. 2021, doi: 10.3389/fphys.2021.642850.

[60] F. A. Zeiler, J. Donnelly, L. Calviello, P. Smielewski, D. K. Menon, and M. Czosnyka, 'Pressure autoregulation measurement techniques in adult traumatic brain injury, part II: a scoping review of continuous methods', *Journal of Neurotrauma*, vol. 34, pp. 3224–3237, 2017, doi: 10.1089/neu.2017.5086.

[61] S. Purkayastha and F. Sorond, ‘Transcranial Doppler Ultrasound: Technique and Application’, *Semin Neurol*, vol. 32, no. 4, pp. 411–420, Sep. 2012, doi: 10.1055/s-0032-1331812.

[62] P. Maggio, A. Salinet, R. B. Panerai, and T. Robinson, ‘Does hypercapnia-induced impairment of cerebral autoregulation affect neurovascular coupling? A functional TCD study’, *Journal of Applied Physiology*, vol. 115, no. 4, pp. 491–497, 2013.

[63] R. B. Panerai *et al.*, ‘The critical closing pressure contribution to dynamic cerebral autoregulation in humans: influence of arterial partial pressure of CO2’, *The Journal of Physiology*, vol. 598, no. 24, pp. 5673–5685, 2020, doi: 10.1113/JP280439.

[64] S.-G. Kim and S. Ogawa, ‘Biophysical and physiological origins of blood oxygenation level-dependent fMRI signals’, *J Cereb Blood Flow Metab*, vol. 32, no. 7, pp. 1188–1206, Jul. 2012, doi: 10.1038/jcbfm.2012.23.

[65] H. Jahanian *et al.*, ‘Measuring vascular reactivity with resting-state blood oxygenation level-dependent (BOLD) signal fluctuations: A potential alternative to the breath-holding challenge?’, *J Cereb Blood Flow Metab*, vol. 37, no. 7, pp. 2526–2538, Jul. 2017, doi: 10.1177/0271678X16670921.

[66] N. H. Petersen, S. Ortega-Gutierrez, A. Reccius, A. Masurkar, A. Huang, and R. S. Marshall, ‘Comparison of non-invasive and invasive arterial blood pressure measurement for assessment of dynamic cerebral autoregulation’, *Neurocritical Care*, vol. 20, no. 1, pp. 60–68, 2014, doi: 10.1007/s12028-013-9898-y.

[67] E. L. Sammons *et al.*, ‘Influence of noninvasive peripheral arterial blood pressure measurements on assessment of dynamic cerebral autoregulation’, *Journal of Applied Physiology*, vol. 103, no. 1, pp. 369–375, 2007, doi: 10.1152/japplphysiol.00271.2007.

[68] S. Ito *et al.*, ‘Non-invasive prospective targeting of arterial PCO2 in subjects at rest’, *J Physiol*, vol. 586, no. Pt 15, pp. 3675–3682, Aug. 2008, doi: 10.1113/jphysiol.2008.154716.

[69] D. M. Simpson, S. J. Payne, and R. B. Panerai, ‘The INfoMATAS project: Methods for assessing cerebral autoregulation in stroke’, *Journal of Cerebral Blood Flow and Metabolism*, pp. 1–19, 2021, doi: 10.1177/0271678X211029049.

[70] J. S. Minhas, N. F. Syed, V. J. Haunton, R. B. Panerai, T. G. Robinson, and A. K. Mistri, ‘Is dynamic cerebral autoregulation measurement using transcranial Doppler ultrasound reproducible in the presence of high concentration oxygen and carbon dioxide?’, *Physiological Measurement*, vol. 37, no. 5, pp. 673–682, 2016, doi: 10.1088/0967-3334/37/5/673.

[71] R. B. Panerai, S. Deverson, P. Mahony, P. Hayes, and D. Evans, ‘Effects of CO2 on dynamic cerebral autoregulation measurement’, *Physiological Measurement*, vol. 20, no. 3, pp. 265–275, 1999.

[72] P. Maggio, A. S. M. Salinet, T. G. Robinson, and R. B. Panerai, ‘Influence of CO2 on neurovascular coupling: Interaction with dynamic cerebral autoregulation and cerebrovascular reactivity’, *Physiological Reports*, vol. 2, no. 3, 2014, doi: 10.1002/phy2.280.

[73] M. Ursino, ‘A mathematical study of human intracranial hydrodynamics part 1—The cerebrospinal fluid pulse pressure’, *Annals of Biomedical Engineering*, vol. 16, no. 4, pp. 379–401, Jul. 1988, doi: 10.1007/BF02364625.

[74] M. Ursino, ‘A mathematical study of human intracranial hydrodynamics. Part 2--Simulation of clinical tests’, *Ann Biomed Eng*, vol. 16, no. 4, pp. 403–416, 1988, doi: 10.1007/BF02364626.

[75] S. K. Kirkham, R. E. Craine, and A. A. Birch, ‘A new mathematical model of dynamic cerebral autoregulation based on a flow dependent feedback mechanism’, *Physiol Meas*, vol. 22, no. 3, pp. 461–473, Aug. 2001, doi: 10.1088/0967-3334/22/3/305.

[76] M. S. Olufsen, A. Nadim, and L. A. Lipsitz, ‘Dynamics of cerebral blood flow regulation explained using a lumped parameter model’, *Am J Physiol Regul Integr Comp Physiol*, vol. 282, no. 2, pp. R611-622, Feb. 2002, doi: 10.1152/ajpregu.00285.2001.

[77] M. Ursino and M. Giulioni, ‘Quantitative assessment of cerebral autoregulation from transcranial Doppler pulsatility: a computer simulation study’, *Med Eng Phys*, vol. 25, no. 8, pp. 655–666, Oct. 2003, doi: 10.1016/s1350-4533(02)00251-5.

[78] M. Ursino, A. Ter Minassian, C. A. Lodi, and L. Beydon, ‘Cerebral hemodynamics during arterial and CO2 pressure changes: in vivo prediction by a mathematical model’, *American Journal of Physiology-Heart and Circulatory Physiology*, vol. 279, no. 5, pp. H2439–H2455, Nov. 2000, doi: 10.1152/ajpheart.2000.279.5.H2439.

[79] S. L. Harper, H. G. Bohlen, and M. J. Rubin, ‘Arterial and microvascular contributions to cerebral cortical autoregulation in rats’, *Am J Physiol*, vol. 246, no. 1 Pt 2, pp. H17-24, Jan. 1984, doi: 10.1152/ajpheart.1984.246.1.H17.

[80] E. T. MacKenzie, J. K. Farrar, W. Fitch, D. I. Graham, P. C. Gregory, and A. M. Harper, ‘Effects of hemorrhagic hypotension on the cerebral circulation. I. Cerebral blood flow and pial arteriolar caliber’, *Stroke*, vol. 10, no. 6, pp. 711–718, Dec. 1979, doi: 10.1161/01.str.10.6.711.

[81] S. J. Payne, ‘A model of the interaction between autoregulation and neural activation in the brain’, *Mathematical Biosciences*, vol. 204, no. 2, pp. 260–281, Dec. 2006, doi: 10.1016/j.mbs.2006.08.006.

[82] B. Spronck, E. G. H. J. Martens, E. D. Gommer, and F. N. van de Vosse, ‘A lumped parameter model of cerebral blood flow control combining cerebral autoregulation and neurovascular coupling’, *Am J Physiol Heart Circ Physiol*, vol. 303, no. 9, pp. H1143-1153, Nov. 2012, doi: 10.1152/ajpheart.00303.2012.

[83] S. J. Payne, ‘Identifying the myogenic and metabolic components of cerebral autoregulation’, *Medical Engineering and Physics*, vol. 58, pp. 23–30, 2018, doi: 10.1016/j.medengphy.2018.04.018.

[84] F.-A. B. Robles, R. B. Panerai, E. Katsogridakis, and M. Chacón, ‘Superior Fitting of Arterial Resistance and Compliance Parameters With Genetic Algorithms in Models of Dynamic Cerebral Autoregulation’, *IEEE Transactions on Biomedical Engineering*, vol. 69, no. 1, pp. 503–512, Jan. 2022, doi: 10.1109/TBME.2021.3100288.

[85] M. Banaji, I. Tachtsidis, D. Delpy, and S. Baigent, ‘A physiological model of cerebral blood flow control’, *Math Biosci*, vol. 194, no. 2, pp. 125–173, Apr. 2005, doi: 10.1016/j.mbs.2004.10.005.

[86] M. Catherall, ‘Modelling the Role of Nitric Oxide in Cerebral Autoregulation’, University of Oxford, Oxford, 2014. Accessed: Nov. 24, 2021. [Online]. Available: http://arxiv.org/abs/1512.09160

[87] S. J. Payne, H. Morris, and A. Rowley, ‘A combined haemodynamic and biochemical model of cerebral autoregulation’, *Conf Proc IEEE Eng Med Biol Soc*, vol. 2005, pp. 2295–2298, 2005, doi: 10.1109/IEMBS.2005.1616923.

[88] M. Ursino, P. Di Giammarco, and E. Belardinelli, ‘A mathematical model of cerebral blood flow chemical regulation--Part I: Diffusion processes’, *IEEE Trans Biomed Eng*, vol. 36, no. 2, pp. 183–191, Feb. 1989, doi: 10.1109/10.16465.

[89] A. Daher and S. J. Payne, ‘The conducted vascular response as a mediator of hypercapnic cerebrovascular reactivity: A modelling study’, *Computers in Biology and Medicine*, vol. 170, p. 107985, Mar. 2024, doi: 10.1016/j.compbiomed.2024.107985.

[90] E. Gao, W. L. Young, J. Pile-Spellman, E. Ornstein, and Q. Ma, ‘Mathematical considerations for modeling cerebral blood flow autoregulation to systemic arterial pressure’, *Am J Physiol*, vol. 274, no. 3, pp. H1023-1031, Mar. 1998, doi: 10.1152/ajpheart.1998.274.3.H1023.

[91] R. Lampe, N. Botkin, V. Turova, T. Blumenstein, and A. Alves-Pinto, ‘Mathematical Modelling of Cerebral Blood Circulation and Cerebral Autoregulation: Towards Preventing Intracranial Hemorrhages in Preterm Newborns’, *Computational and Mathematical Methods in Medicine*, vol. 2014, p. e965275, Jul. 2014, doi: 10.1155/2014/965275.

[92] C. Lucas, ‘An anatomical model of the cerebral vasculature and blood flow’, http://purl.org/dc/dcmitype/Text, Oxford University, UK, 2012. Accessed: Nov. 24, 2021. [Online]. Available: https://ora.ox.ac.uk/objects/uuid:37d408b6-b804-4085-b420-a9704aeb97eb

[93] M. Ursino and M. Giannessi, ‘A model of cerebrovascular reactivity including the circle of willis and cortical anastomoses’, *Ann Biomed Eng*, vol. 38, no. 3, pp. 955–974, Mar. 2010, doi: 10.1007/s10439-010-9923-7.

[94] W. K. El-Bouri and S. J. Payne, ‘Multi-scale homogenization of blood flow in 3-dimensional human cerebral microvascular networks’, *J Theor Biol*, vol. 380, pp. 40–47, Sep. 2015, doi: 10.1016/j.jtbi.2015.05.011.

[95] S. Milanovic, K. Shaw, C. Hall, and S. J. Payne, ‘Investigating the role of pericytes in cerebral autoregulation: a modeling study’, *Physiol. Meas.*, vol. 42, no. 5, p. 054003, May 2021, doi: 10.1088/1361-6579/abfb0a.

[96] A. Coccarelli, I. Polydoros, A. Drysdale, O. F. Harraz, and C. Kadapa, ‘A new computational model for quantifying blood flow dynamics across myogenically-active cerebral arterial networks’, Nov. 13, 2024, *arXiv*: arXiv:2411.09046. Accessed: Nov. 19, 2024. [Online]. Available: http://arxiv.org/abs/2411.09046

[97] K. Kostoglou *et al.*, 'Time-domain methods for quantifying dynamic cerebral blood flow autoregulation: Review and recommendations. A white paper from the Cerebrovascular Research Network (CARNet)', *J Cereb Blood Flow Metab*, vol. 44, no. 9, pp. 1480–1514, Apr. 2024, doi: 10.1177/0271678X241249276.

[98] F. P. Tiecks, A. M. Am, R. Aaslid, and D. W. Newell, 'Comparison of Static and Dynamic Cerebral Autoregulation Measurements', *Stroke*, vol. 26, pp. 1014–1019, 1995.

[99] R. Aaslid, K. Lindegaard, W. Sorteberg, and H. Nornes, 'Cerebral autoregulation dynamics in humans', *Stroke*, vol. 20, no. 1, pp. 45–52, 1989.

[100]M. Czosnyka, P. Smielewski, P. Kirkpatrick, D. Menon, and J. Pickard, 'Monitoring of cerebral autoregulation in head-injured patients', *Stroke*, vol. 27, no. 10, pp. 1829–1834, 1996.

[101]R. Steinmeier, C. Bauhuf, U. Hubner, R. Hofmann, and R. Fahlbusch, 'Continuous cerebral autoregulation monitoring by cross-correlation analysis: evaluation in healthy volunteers', *Critical Care Medicine*, vol. 30, no. 9, pp. 1969–1975, 2002.

[102]S. O *et al.*, 'Assessing cerebrovascular reactivity abnormality by comparison to a reference atlas', *Journal of cerebral blood flow and metabolism : official journal of the International Society of Cerebral Blood Flow and Metabolism*, vol. 35, no. 2, Feb. 2015, doi: 10.1038/jcbfm.2014.184.

[103]J. Poublanc *et al.*, 'Vascular Steal Explains Early Paradoxical Blood Oxygen Level-Dependent Cerebrovascular Response in Brain Regions with Delayed Arterial Transit Times', *Cerebrovascular Diseases Extra*, vol. 3, no. 1, p. 55, Apr. 2013, doi: 10.1159/000348841.

[104]B. Np, D. Id, F. St, F. Ja, and G. Pa, 'An improved method for acquiring cerebrovascular reactivity maps', *Magnetic resonance in medicine*, vol. 65, no. 5, May 2011, doi: 10.1002/mrm.22719.

[105]C. H. B. van Niftrik *et al.*, 'Iterative analysis of cerebrovascular reactivity dynamic response by temporal decomposition', *Brain and Behavior*, vol. 7, no. 9, p. e00705, 2017, doi: 10.1002/brb3.705.

[106]M. J. Donahue, M. K. Strother, K. P. Lindsey, L. M. Hocke, Y. Tong, and B. deB Frederick, 'Time delay processing of hypercapnic fMRI allows quantitative parameterization of cerebrovascular reactivity and blood flow delays', *J Cereb Blood Flow Metab*, vol. 36, no. 10, pp. 1767–1779, Oct. 2016, doi: 10.1177/0271678X15608643.

[107]J. Poublanc *et al.*, 'Measuring Cerebrovascular Reactivity: The Dynamic Response to a Step Hypercapnic Stimulus', *J Cereb Blood Flow Metab*, vol. 35, no. 11, pp. 1746–1756, Nov. 2015, doi: 10.1038/jcbfm.2015.114.

[108]M. Poulin, P. Liang, and P. Robbins, 'Fast and slow components of cerebral blood flow response to step decreases in end-tidal PCO2 in humans', *Journal of applied physiology (Bethesda, Md. : 1985)*, vol. 85, no. 2, Aug. 1998, doi: 10.1152/jappl.1998.85.2.388.

[109]J. Duffin, O. Sobczyk, A. P. Crawley, J. Poublanc, D. J. Mikulis, and J. A. Fisher, 'The dynamics of cerebrovascular reactivity shown with transfer function analysis', *NeuroImage*, vol. 114, pp. 207–216, Jul. 2015, doi: 10.1016/j.neuroimage.2015.04.029.

[110]R. B. Panerai *et al.*, 'Chasing the evidence: the influence of data segmentation on estimates of dynamic cerebral autoregulation.', *Physiological measurement*, 2020, doi: 10.1088/1361-6579/ab7ddf.

[111]R. B. Panerai *et al.*, 'Transfer function analysis of dynamic cerebral autoregulation: A CARNet white paper 2022 update', *J Cereb Blood Flow Metab*, vol. 43, no. 1, pp. 3–25, Jan. 2023, doi: 10.1177/0271678X221119760.

[112]J. Liu *et al.*, 'A Data-Driven Approach to Transfer Function Analysis for Superior Discriminative Power: Optimized Assessment of Dynamic Cerebral Autoregulation', *IEEE Journal of Biomedical and Health Informatics*, vol. 25, no. 4, pp. 909–921, 2021, doi: 10.1109/JBHI.2020.3015907.

[113]R. B. Panerai, D. M. Simpson, S. T. Deverson, P. Mahony, P. Hayes, and D. H. Evans, 'Multivariate dynamic analysis of cerebral blood flow regulation in humans', *IEEE Trans. Biomed. Eng.*, vol. 47, no. 3, pp. 419–423, Mar. 2000, doi: 10.1109/10.827312.

[114]S. J. Payne and L. Tarassenko, 'Combined transfer function analysis and modelling of cerebral autoregulation', *Annals of Biomedical Engineering*, vol. 34, no. 5, pp. 847–858, 2006, doi: 10.1007/s10439-006-9114-8.

[115]R. B. Panerai, M. Eyre, and J. F. Potter, 'Multivariate modeling of cognitive-motor stimulation on neurovascular coupling: transcranial Doppler used to characterize myogenic and metabolic influences', *American Journal of Physiology-Regulatory, Integrative and Comparative Physiology*, vol. 303, no. 4, pp. R395–R407, Aug. 2012, doi: 10.1152/ajpregu.00161.2012.

[116]S. Shams, P. Prokopiou, A. Esmaelbeigi, G. D. Mitsis, and J. J. Chen, 'Modeling the dynamics of cerebrovascular reactivity to carbon dioxide in fMRI under task and resting-state conditions', *NeuroImage*, vol. 265, p. 119758, Jan. 2023, doi: 10.1016/j.neuroimage.2022.119758.

[117]A. Sarwal, C. Robba, C. Venegas, W. Ziai, M. Czosnyka, and D. Sharma, 'Are We Ready for Clinical Therapy based on Cerebral Autoregulation? A Pro-con Debate', *Neurocrit Care*, vol. 39, no. 2, pp. 269–283, May 2023, doi: 10.1007/s12028-023-01741-1.

[118]C. H. Brown *et al.*, 'Effect of Targeting Mean Arterial Pressure During Cardiopulmonary Bypass by Monitoring Cerebral Autoregulation on Postsurgical Delirium Among Older Patients', *JAMA Surg*, vol. 154, no. 9, pp. 819–826, Sep. 2019, doi: 10.1001/jamasurg.2019.1163.

[119]C. W. Hogue *et al.*, 'Personalized Blood Pressure Management During Cardiac Surgery With Cerebral Autoregulation Monitoring: A Randomized Trial', *Semin Thorac Cardiovasc Surg*, vol. 33, no. 2, pp. 429–438, Summer 2021, doi: 10.1053/j.semtcvs.2020.09.032.

[120]N. H. Petersen *et al.*, ‘Fixed Compared With Autoregulation-Oriented Blood Pressure Thresholds After Mechanical Thrombectomy for Ischemic Stroke’, *Stroke*, vol. 51, no. 3, pp. 914–921, Mar. 2020, doi: 10.1161/STROKEAHA.119.026596.

[121]M. Ursino, P. Di Giammarco, and E. Belardinelli, ‘A mathematical model of cerebral blood flow chemical regulation--Part II: Reactivity of cerebral vascular bed’, *IEEE Trans Biomed Eng*, vol. 36, no. 2, pp. 192–201, Feb. 1989, doi: 10.1109/10.16466.

[122]C. A. Giller and M. Mueller, ‘Linearity and non-linearity in cerebral hemodynamics’, *Medical Engineering and Physics*, vol. 25, no. 8, pp. 633–646, 2003, doi: 10.1016/S1350-4533(03)00028-6.

[123]R. B. Panerai, ‘The critical closing pressure of the cerebral circulation’, *Medical Engineering & Physics*, vol. 25, no. 8, pp. 621–632, Oct. 2003, doi: 10.1016/S1350-4533(03)00027-4.

[124]S. J. Payne, ‘A model of the interaction between autoregulation and neural activation in the brain’, *Mathematical Biosciences*, vol. 204, no. 2, pp. 260–281, Dec. 2006, doi: 10.1016/j.mbs.2006.08.006.

[125]J. E. D. Bryant, A. A. Birch, R. B. Panerai, D. Nikolic, D. Bulters, and D. M. Simpson, ‘Estimating confidence intervals for cerebral autoregulation: a parametric bootstrap approach’, *Physiol. Meas.*, vol. 42, no. 10, p. 104004, Oct. 2021, doi: 10.1088/1361-6579/ac27b8.

[126]R. B. Panerai, V. J. Haunton, M. F. Hanby, A. S. M. Salinet, and T. G. Robinson, ‘Statistical criteria for estimation of the cerebral autoregulation index (ARI) at rest’, *Physiol Meas*, vol. 37, no. 5, pp. 661–672, May 2016, doi: 10.1088/0967-3334/37/5/661.

[127]W. M. Trochim and J. P. Donnelly, *The research methods knowledge base*, 3rd ed. Mason, Ohio: Atomic Dog/Cengage Learning, 2008.

[128]R. B. Panerai, D. M. Simpson, S. T. Deverson, P. Mahony, P. Hayes, and D. H. Evans, ‘Multivariate dynamic analysis of cerebral blood flow regulation in humans’, *IEEE Transactions on Biomedical Engineering*, vol. 47, no. 3, pp. 419–423, Mar. 2000, doi: 10.1109/10.827312.

[129]J. Jordan *et al.*, ‘Interaction of Carbon Dioxide and Sympathetic Nervous System Activity in the Regulation of Cerebral Perfusion in Humans’, *Hypertension*, vol. 36, no. 3, pp. 383–388, Sep. 2000, doi: 10.1161/01.HYP.36.3.383.

[130]K. C. Peebles, O. G. Ball, B. A. MacRae, H. M. Horsman, and Y. C. Tzeng, ‘Sympathetic regulation of the human cerebrovascular response to carbon dioxide’, *Journal of Applied Physiology*, vol. 113, no. 5, pp. 700–706, Sep. 2012, doi: 10.1152/japplphysiol.00614.2012.

[131]P. A. Cassaglia, R. I. Griffiths, and A. M. Walker, ‘Sympathetic nerve activity in the superior cervical ganglia increases in response to imposed increases in arterial pressure’, *American Journal of Physiology-Regulatory, Integrative and Comparative Physiology*, vol. 294, no. 4, pp. R1255–R1261, Apr. 2008, doi: 10.1152/ajpregu.00332.2007.

[132]J. Gierthmühlen, A. Allardt, M. Sawade, R. Baron, and G. Wasner, ‘Dynamic cerebral autoregulation in stroke patients with a central sympathetic deficit’, *Acta Neurol Scand*, vol. 123, no. 5, pp. 332–338, May 2011, doi: 10.1111/j.1600-0404.2010.01424.x.

[133]C. Wang, G. Reid, C. E. Mackay, G. Hayes, D. P. Bulte, and S. Suri, ‘A systematic review of the association between dementia risk factors and cerebrovascular reactivity’, *Neuroscience & Biobehavioral Reviews*, vol. 148, p. 105140, May 2023, doi: 10.1016/j.neubiorev.2023.105140.

[134]K. L. West *et al.*, ‘BOLD hemodynamic response function changes significantly with healthy aging’, *NeuroImage*, vol. 188, pp. 198–207, Mar. 2019, doi: 10.1016/j.neuroimage.2018.12.012.

[135]R. F. Leoni, K. C. Mazzeto-Betti, K. C. Andrade, and D. B. de Araujo, ‘Quantitative evaluation of hemodynamic response after hypercapnia among different brain territories by fMRI’, *NeuroImage*, vol. 41, no. 4, pp. 1192–1198, Jul. 2008, doi: 10.1016/j.neuroimage.2008.03.035.

[136]V. Z. Marmarelis, ‘Identification of nonlinear biological systems using laguerre expansions of kernels’, *Annals of Biomedical Engineering*, vol. 21, no. 6, pp. 573–589, 1993, doi: 10.1007/BF02368639.

[137]B. Leistedt and J. D. McEwen, ‘Exact Wavelets on the Ball’, *IEEE Transactions on Signal Processing*, vol. 60, no. 12, pp. 6257–6269, Dec. 2012, doi: 10.1109/TSP.2012.2215030.

[138]D. C. Montgomery, *Introduction to Time Series Analysis and Forecasting*. Newark, United States: John Wiley & Sons, Incorporated, 2015.

[139]V. Z. Marmarelis, D. C. Shin, T. Tarumi, and R. Zhang, ‘Comparison of Model-Based Indices of Cerebral Autoregulation and Vasomotor Reactivity Using Transcranial Doppler versus Near-Infrared Spectroscopy in Patients with Amnestic Mild Cognitive Impairment’, *J Alzheimers Dis*, vol. 56, no. 1, pp. 89–105, 2017, doi: 10.3233/JAD-161004.

[140]V. Z. Marmarelis, D. C. Shin, M. Oesterreich, and M. Mueller, ‘Quantification of dynamic cerebral autoregulation and CO2 dynamic vasomotor reactivity impairment in essential hypertension’, *Journal of Applied Physiology*, vol. 128, no. 2, pp. 397–409, Feb. 2020, doi: 10.1152/japplphysiol.00620.2019.

[141]G. D. Mitsis, R. Zhang, B. D. Levine, and V. Z. Marmarelis, ‘Modeling of nonlinear physiological systems with fast and slow dynamics. II. Application to cerebral autoregulation’, *Annals of Biomedical Engineering*, vol. 30, no. 4, pp. 555–565, 2002, doi: 10.1114/1.1477448.

[142]A. M. Golestani, C. Chang, J. B. Kwinta, Y. B. Khatamian, and J. Jean Chen, ‘Mapping the end-tidal CO2 response function in the resting-state BOLD fMRI signal: Spatial specificity, test–retest reliability and effect of fMRI sampling rate’, *NeuroImage*, vol. 104, pp. 266–277, Jan. 2015, doi: 10.1016/j.neuroimage.2014.10.031.

[143]J. W. Severinghaus and N. Lassen, ‘Step Hypocapnia to Separate Arterial from Tissue Pco2 in the Regulation of Cerebral Blood Flow’, *Circulation Research*, vol. 20, no. 2, pp. 272–278, Feb. 1967, doi: 10.1161/01.RES.20.2.272.

[144]L. Pritschet *et al.*, ‘Neuroanatomical changes observed over the course of a human pregnancy’, *Nat Neurosci*, vol. 27, no. 11, pp. 2253–2260, Nov. 2024, doi: 10.1038/s41593-024-01741-0.

[145]J. Goense, Y. Bohraus, and N. K. Logothetis, ‘fMRI at High Spatial Resolution: Implications for BOLD-Models’, *Front. Comput. Neurosci.*, vol. 10, Jun. 2016, doi: 10.3389/fncom.2016.00066.

[146]J. Pinto, S. Suri, S. Sparks, G. Hayes, and D. Bulte, ‘Cerebrovascular reactivity dynamics in the postpartum period: a pilot study’, in *Proceedings of the International Society for Magnetic Resonance in Medicine*, Honolulu, USA, 2025.

[147]M. Jenkinson, C. F. Beckmann, T. E. J. Behrens, M. W. Woolrich, and S. M. Smith, ‘FSL’, *NeuroImage*, vol. 62, no. 2, pp. 782–790, Aug. 2012, doi: 10.1016/j.neuroimage.2011.09.015.

[148]M. Watanabe, A. Bartels, J. H. Macke, Y. Murayama, and N. K. Logothetis, ‘Temporal Jitter of the BOLD Signal Reveals a Reliable Initial Dip and Improved Spatial Resolution’, *Current Biology*, vol. 23, no. 21, pp. 2146–2150, Nov. 2013, doi: 10.1016/j.cub.2013.08.057.

[149]K. T. S. Pattinson *et al.*, ‘Determination of the human brainstem respiratory control network and its cortical connections *in vivo* using functional and structural imaging’, *NeuroImage*, vol. 44, no. 2, pp. 295–305, Jan. 2009, doi: 10.1016/j.neuroimage.2008.09.007.

[150]M. E. F. Pedersen, M. Fatemian, and P. A. Robbins, ‘Identification of fast and slow ventilatory responses to carbon dioxide under hypoxic and hyperoxic conditions in humans’, *J Physiol*, vol. 521, no. Pt 1, pp. 273–287, Nov. 1999, doi: 10.1111/j.1469-7793.1999.00273.x.

[151]L. E. Mak, L. Minuzzi, G. MacQueen, G. Hall, S. H. Kennedy, and R. Milev, ‘The Default Mode Network in Healthy Individuals: A Systematic Review and Meta-Analysis’, *Brain Connectivity*, vol. 7, no. 1, pp. 25–33, Feb. 2017, doi: 10.1089/brain.2016.0438.

[152]F. A. Zeiler, M. Aries, M. Czosnyka, and P. Smielewski, ‘Cerebral Autoregulation Monitoring in Traumatic Brain Injury: An Overview of Recent Advances in Personalized Medicine’, *Journal of Neurotrauma*, vol. 39, no. 21–22, pp. 1477–1494, Nov. 2022, doi: 10.1089/neu.2022.0217.

[153]A. S. S. Meel-van den Abeelen *et al.*, ‘Between-centre variability in transfer function analysis, a widely used method for linear quantification of the dynamic pressure–flow relation: The CARNet study’, *Medical Engineering & Physics*, vol. 36, no. 5, pp. 620–627, May 2014, doi: 10.1016/j.medengphy.2014.02.002.

[154]P. W. Rand, E. Lacombe, H. E. Hunt, and W. H. Austin, ‘Viscosity of normal human blood under normothermic and hypothermic conditions’, *Journal of Applied Physiology*, vol. 19, no. 1, pp. 117–122, Jan. 1964, doi: 10.1152/jappl.1964.19.1.117.

[155]F. Cassot, F. Lauwers, C. Fouard, S. Prohaska, and V. Lauwers-Cances, ‘A Novel Three-Dimensional Computer-Assisted Method for a Quantitative Study of Microvascular Networks of the Human Cerebral Cortex’, *Microcirculation*, vol. 13, no. 1, pp. 1–18, 2006, doi: 10.1080/10739680500383407.

[156]A. Løkkegaard, J. R. Nyengaard, and M. J. West, ‘Stereological estimates of number and length of capillaries in subdivisions of the human hippocampal region’, *Hippocampus*, vol. 11, no. 6, pp. 726–740, 2001, doi: 10.1002/hipo.1088.

[157]W. Li, D. Liu, P. C. M. van Zijl, and Q. Qin, ‘Three-dimensional whole-brain mapping of cerebral blood volume and venous cerebral blood volume using Fourier transform–based velocity-selective pulse trains’, *Magnetic Resonance in Medicine*, vol. 86, no. 3, pp. 1420–1433, 2021, doi: 10.1002/mrm.28815.

[158]E. Lüders, H. Steinmetz, and L. Jäncke, ‘Brain size and grey matter volume in the healthy human brain’:, *NeuroReport*, vol. 13, no. 17, pp. 2371–2374, Dec. 2002, doi: 10.1097/00001756-200212030-00040.

[159]T. Kubíková, P. Kochová, P. Tomášek, K. Witter, and Z. Tonar, ‘Numerical and length densities of microvessels in the human brain: Correlation with preferential orientation of microvessels in the cerebral cortex, subcortical grey matter and white matter, pons and cerebellum’, *Journal of Chemical Neuroanatomy*, vol. 88, pp. 22–32, Mar. 2018, doi: 10.1016/j.jchemneu.2017.11.005.

[160]H. Ito *et al.*, ‘Arterial fraction of cerebral blood volume in humans measured by positron emission tomography’, *Ann Nucl Med*, vol. 15, no. 2, pp. 111–116, Apr. 2001, doi: 10.1007/BF02988600.

[161]T. W. Barber, J. A. Brockway, and L. S. Higgins, ‘The Density of Tissues in and About the Head’, *Acta Neurologica Scandinavica*, vol. 46, no. 1, pp. 85–92, 1970, doi: 10.1111/j.1600-0404.1970.tb05606.x.

APPENDICES

Appendix A

A.1. Overall pressure-flow transfer function derivation

This appendix starts with a derivation of the sCA model by Payne [83], with additional detail, to aid with understanding of its extension to the dCA model. Thereafter, the extension to the dCA model (including the linearised transfer functions written in terms of deviation variables) and the derivation of the overall pressure-flow transfer function are described in detail.

A.1.1. sCA model derivation

First, a single arteriole is considered, as CBF regulation occurs at the arteriolar level. According to Laplace's law, direct stress on the vessel wall, σ, is related to internal pressure, p, vessel radius, r, and vessel wall thickness, h:

$$\sigma = \frac{pr}{h} \tag{A1}$$

The step-by-step linearisation of (A1) in terms of deviation variables, and re-writing it with variables as fractions of their baseline values is shown below. The notation used in [83] is adopted in this thesis for consistency, so Δ is used to indicate a deviation variable (i.e., a small change from baseline), a superscript star is used to indicate that a variable is written as a fraction of its baseline value., and a bar over a variable is used to indicate a baseline value. Linearising (A1):

$$\Delta\sigma = \frac{\bar{r}}{\bar{h}}\Delta p + \frac{\bar{p}}{\bar{h}}\Delta r - \frac{\bar{p}\bar{r}}{\bar{h}^2}\Delta h = \frac{\bar{r}}{\bar{h}}\Delta p + \frac{\bar{p}}{\bar{h}}\Delta r - \frac{\bar{p}\bar{r}}{\bar{h}}\Delta h^*$$

Multiplying both sides of the equation by $\frac{\bar{h}}{\bar{\sigma}\bar{p}\bar{r}}$:

$$\frac{\bar{h}}{\bar{p}\bar{r}}\Delta\sigma^* = \frac{1}{\bar{\sigma}}\ \Delta p^* + \frac{1}{\bar{\sigma}}\Delta r^* - \frac{\bar{p}\bar{r}}{\bar{h}}\Delta h^*$$

Rearranging:

$$\frac{\bar{\sigma}\bar{h}}{\bar{p}\bar{r}}\Delta\sigma^* = \Delta p^* + \Delta r^* - \Delta h^*$$

Taking (A1) at baseline: $\frac{\bar{\sigma}\bar{h}}{\bar{p}\bar{r}} = 1$, so that:

$$\Delta\sigma^* = \Delta p^* + \Delta r^* - \Delta h^* \tag{A2}$$

Similarly, the vessel wall force is a function of internal pressure and vessel radius:

$$\mathrm{F = pr} \tag{A3}$$

Using the same approach that obtained (A2) from (A1), (A3) can be linearised and written in terms of deviation variables that are fractions of their baseline values:

$$\Delta F^* = \Delta p^* + \Delta r^* \tag{A4}$$

Assume that vessel wall force is dependent in some (not yet specified) way upon smooth muscle cell stiffness, k, and the stretch, λ, such that small perturbations in wall force can be written as:

$$\Delta F^* = S_{F,k}\Delta k^* + S_{F,\lambda}\Delta\lambda^* \tag{A5}$$

where stretch, λ, is related to changes in vessel radius, r, through geometric considerations:

$$\Delta\lambda^* = S_{\lambda,r}\Delta r^* \tag{A6}$$

The vessel wall volume, V_{wall} is:

$$V_{wall} = [\pi(r+h)^2 - \pi r^2]L \tag{A7}$$

where r is the luminal radius (previously referred to as simply vessel radius), and h is the vessel wall thickness. Linearising (A7) and writing it in terms of deviation variables (for a given vessel length, L):

$$\Delta V_{wall} = \left[2\pi\bar{L}(\bar{r}+\bar{h}) - 2\pi\bar{L}\bar{r}\right]\Delta r + \left[2\pi\bar{L}(\bar{r}+\bar{h})\right]\Delta h = \left[2\pi\bar{L}\bar{h}\right]\Delta r + \left[2\pi\bar{L}(\bar{r}+\bar{h})\right]\Delta h$$

Assuming that the vessel wall volume remains constant:

$$0 = \left[2\pi\bar{L}\bar{h}\right]\Delta r + \left[2\pi\bar{L}(\bar{r}+\bar{h})\right]\Delta h$$

$$0 = \bar{h}\Delta r + (\bar{r}+\bar{h})\Delta h$$

Multiplying by $\frac{1}{\bar{r}\bar{h}}$ on both sides of the equation:

$$0 = \Delta r^* + \Delta h^* + \frac{\bar{h}}{\bar{r}}\Delta h^*$$

Assuming that vessel radius is much larger than vessel wall thickness at baseline (i.e., $\bar{r} \gg \bar{h}$, so that $\frac{\bar{h}}{\bar{r}} \sim 0$):

$$0 = \Delta r^* + \Delta h^* \tag{A8}$$

Assume vessel wall stiffness, k, responds to direct stress, σ, and shear stress, τ, on the vessel wall, acting in opposite directions, so that small perturbations in k can be written as:

$$\Delta k^* = S_{k,\sigma}\Delta\sigma^* - S_{k,\tau}\Delta\tau^* \tag{A9}$$

where shear stress, τ is a function of radius and pressure gradient, ∇p:

$$\Delta\tau^* = \Delta \mathrm{r}^* + (\nabla \mathrm{p})^* \tag{A10}$$

The notation used for shear stress, τ, and pressure gradient, ∇p, have been taken from [83] for consistency. Note that τ here refers to shear stress on the vessel wall. It should not be confused with the time constants, τ_M and τ_V, which will be introduced later. The symbol that is typically used for divergence, ∇, is used here to indicate gradient instead – because the symbol typically used to indicate gradient, Δ, is already being used to indicate a deviation variable.

Rearranging (A4):

$$\Delta r^* = \Delta F^* - \Delta p^* \tag{A11}$$

Then substituting the linearised equations, (A2), (A4), (A5), (A6), (A8), (A9), and (A10), into (A11):

$$\Delta r^* = \frac{1-(s_{F,k}s_{k,\sigma})}{2(s_{F,k}s_{k,\sigma})-(s_{F,k}s_{k,\tau})+(s_{F,\lambda}s_{\lambda,r})-1}\Delta p^* + \frac{(s_{F,k}s_{k,\tau})}{2(s_{F,k}s_{k,\sigma})-(s_{F,k}s_{k,\tau})+(s_{F,\lambda}s_{\lambda,r})-1}(\nabla p)^* \tag{A12}$$

Since (A12) is linear and written in terms of deviation variables, it can be readily converted to the Laplace domain:

$$\Delta r^*(s) = \frac{1-(s_{F,k}s_{k,\sigma})}{2(s_{F,k}s_{k,\sigma})-(s_{F,k}s_{k,\tau})+(s_{F,\lambda}s_{\lambda,r})-1}\Delta p^*(s) \\ + \frac{(s_{F,k}s_{k,\tau})}{2(s_{F,k}s_{k,\sigma})-(s_{F,k}s_{k,\tau})+(s_{F,\lambda}s_{\lambda,r})-1}(\nabla p)^*(s) \tag{A13}$$

Assuming that the myogenic response is purely the response to direct stress, let the sensitivity coefficient of the myogenic response be defined as the magnitude of response to direct stress (i.e., the effect of direct stress on wall force):

$$\mathrm{S_M} = s_{F,k}s_{k,\sigma} \tag{A14}$$

Assuming that the metabolic response is purely the response to shear stress, let the sensitivity coefficient of the metabolic response be defined as the magnitude of the response to shear stress (i.e., the effect of shear stress on wall force):

$$S_V = S_{F,k} S_{k,\tau} \tag{A15}$$

Let the sensitivity coefficient of the elastic response (i.e., the passive response of the vessel wall) be defined as the magnitude of the effect of vessel radius on wall force:

$$S_E = S_{F,\lambda} S_{\lambda,r} \tag{A16}$$

Incorporating the definitions of S_M, S_V, and S_E, (A13) becomes:

$$\Delta r^*(s) = \frac{1-S_M}{2S_M-S_V+S_E-1}\Delta p^*(s) + \frac{S_V}{2S_M-S_V+S_E-1}(\nabla p)^*(s) \tag{A17}$$

Let $S_{r,p}$ and $S_{r,\nabla p}$ be defined as simplifying parameters for the effect of internal pressure on radius and the effect of pressure gradient on radius respectively:

$$S_{r,p} = \frac{1-S_M}{2S_M-S_V+S_E-1} \tag{A18}$$

$$S_{r,\nabla p} = \frac{S_V}{2S_M-S_V+S_E-1} \tag{A19}$$

(A17) can then be written as:

$$\Delta r^*(s) = S_{r,p}\Delta p^*(s) + S_{r,\nabla p}(\nabla p)^*(s) \tag{A20}$$

which is the form provided in (3.1) in Chapter 3.

Next, a lumped compartmental model of the full cerebral vasculature is considered as an equivalent electric circuit (Figure A.1). The model of the single arteriole derived above is linked to this model of the full cerebral vasculature via the arteriolar (regulating) compartment. The internal pressure in the single arteriole and pressure gradient across the length of the single arteriole are taken as equivalent to the pressure in the arteriolar (regulating) compartment and the pressure drop across the arteriolar (regulating) compartment in the model of the full vasculature.

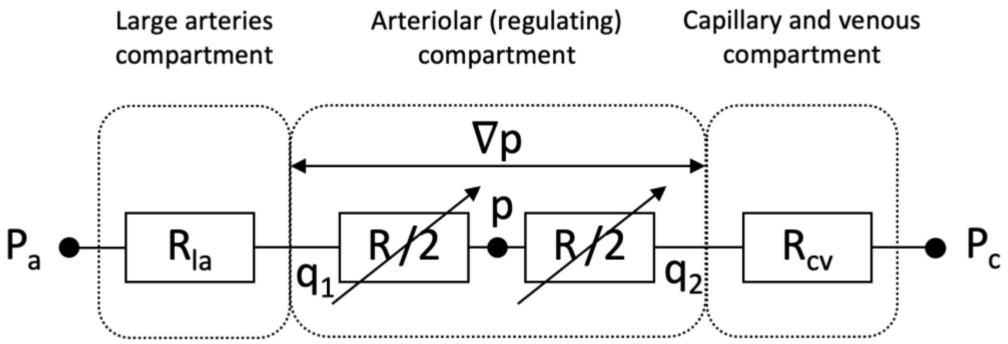

Figure A.1. Schematic of vascular model, adapted from [83]. Pa: systemic arterial pressure, Pc: critical closing pressure, p: pressure in arteriolar (regulating) compartment, ∇p: pressure drop across arteriolar (regulating) compartment, R_{la}: resistance of large arteries, R: resistance of arterioles, R_{cv}: resistance of capillaries and veins, q_1: flow rate into arteriolar (regulating) compartment, q_2: flow rate out of arteriolar (regulating) compartment.

The Poiseuille equation (A21) relates hydraulic resistance, R, to vessel radius, r, where hydraulic resistance is the opposition to fluid flow in a hydraulic system (equivalent to electrical resistance in an electric circuit), defined as the ratio of pressure drop, ∇p, to flow rate, q. The Poiseuille equation is derived from the Navier-Stokes equation for an incompressible Newtonian fluid by assuming steady state flow, a negligible advection term, absence of body forces, purely axial flow (i.e., negligible radial or circumferential velocity components), and uniform pressure over the cross-sectional area, and solving with boundary conditions of no-slip (i.e., zero velocity at the vessel wall) and symmetry at the flow centreline. For a detailed derivation of the Poiseuille equation, the reader is referred to the book by Payne [3].

$$\frac{8\mu L}{\pi r^4} = \frac{\nabla p}{q} = R \tag{A21}$$

Assuming constant blood viscosity, μ, and vessel length, L, and using the same approach that was used to obtain (A2) from (A1), (A21) can be linearised and written in terms of deviation variables that are fractions of their baseline values:

$$\Delta R^* = -4\Delta r^* \tag{A22}$$

According to (A21), pressure drop, ∇p, is directly proportional to hydraulic resistance, R:

$$\nabla p \propto R \tag{A23}$$

From (A23), a relationship between pressure drops and hydraulic resistances can be written:

$$\frac{\nabla p_1}{\nabla p_2} = \frac{R_1}{R_2} \tag{A24}$$

Applying the relationship in (A24) to obtain a ratio of pressure drop across the arteriolar (regulating) compartment to pressure drop across the full cerebral vasculature:

$$\frac{\nabla p}{P_a - P_c} = \frac{R}{R_T} \tag{A25}$$

where R_T is total resistance of the cerebral vasculature:

$$R_T = R_{la} + \frac{R}{2} + \frac{R}{2} + R_{cv} \tag{A26}$$

Assuming constant volume in the compartments and no significant change in blood density, the flow rates throughout the cerebral vasculature are equal:

$$q = q_1 = q_2 \tag{A27}$$

where q_1 denotes the flow rate into the arteriolar (regulating) compartment, q_2 denotes the flow rate out of the arteriolar (regulating) compartment, and q simply denotes the flow rate throughout the full cerebral vasculature. According to the definition of hydraulic resistance, R, and its equivalence to electrical resistance in an electric circuit, the equivalence of Ohm's law can be applied:

$$q_1 = \frac{P_a - p}{R_{la} + \frac{R}{2}} \tag{A28}$$

$$q_2 = \frac{p - P_c}{\frac{R}{2} + R_{cv}} \tag{A29}$$

$$\mathrm{q} = \frac{P_a - P_c}{R_T} \tag{A30}$$

Substituting (A28) and (A29) in (A27) and rearranging:

$$\mathrm{p} = \frac{1}{\left(R_{la}+\frac{R}{2}+\frac{R}{2}+R_{cv}\right)}\left(P_a\left(\frac{R}{2}+R_{cv}\right)+P_c\left(R_{la}+\frac{R}{2}\right)\right) \tag{A31}$$

Then substituting (A26) in (A31):

$$\mathrm{p} = \frac{1}{R_T}\left(P_a\left(\frac{R}{2}+R_{cv}\right)+P_c\left(R_{la}+\frac{R}{2}\right)\right) \tag{A32}$$

Similarly to the approach used to obtain (A2) from (A1), and assuming constant critical closing pressure (P_c): (A25), (A26), (A30), and (A31) can be linearised and written in terms of deviation variables that are fractions of their baseline values:

$$\Delta(\nabla p)^* = \Delta R^* - \Delta R_T^* + \frac{\bar{P}_a}{\bar{P}_a - \bar{P}_c}\Delta P_a^* \tag{A33}$$

$$\Delta R_T^* = \bar{f}_a \Delta R^* \tag{A34}$$

$$\Delta q^* = \frac{\bar{P}_a}{\bar{P}_a - \bar{P}_c}\Delta P_a^* - \Delta R_T^* \tag{A35}$$

$$\Delta \mathrm{p}^* = \left[\frac{-f_r\bar{P}_a - 2f_v\bar{P}_a - 2f_a\bar{P}_c - f_r\bar{P}_c}{2\bar{p}}\right]\Delta R_T^* + \left[\frac{f_r\bar{P}_a + 2f_v\bar{P}_a}{2\bar{p}}\right]\Delta P_a^* + \left[\frac{f_a\bar{P}_a + f_a\bar{P}_c}{2\bar{p}}\right]\Delta R^* \tag{A36}$$

where f_a, f_r, f_v are resistance fractions defined as:

$$f_a = \frac{R_{la}}{\bar{R}_T} \tag{A37}$$

$$f_r = \frac{\bar{R}}{\bar{R}_T} \tag{A38}$$

$$f_v = \frac{R_{cv}}{\bar{R}_T} \tag{A39}$$

Converting (A22), and (A33)-(A36) to the Laplace domain:

$$\Delta R^*(s) = -4\Delta r^*(s) \tag{A40}$$

$$\Delta(\nabla p)^*(s) = \Delta R^*(s) - \Delta R_T^*(s) + \frac{\bar{P}_a}{\bar{P}_a - \bar{P}_c}\Delta P_a^*(s) \tag{A41}$$

$$\Delta R_T^*(s) = \bar{f}_a \Delta R^*(s) \tag{A42}$$

$$\Delta q^*(s) = \frac{\bar{P}_a}{\bar{P}_a - \bar{P}_c}\Delta P_a^*(s) - \Delta R_T^*(s) \tag{A43}$$

$$\Delta \mathrm{p}^*(s) = \left[\frac{-f_r\bar{P}_a - 2f_v\bar{P}_a - 2f_a\bar{P}_c - f_r\bar{P}_c}{2\bar{p}}\right]\Delta R_T^*(s) + \left[\frac{f_r\bar{P}_a + 2f_v\bar{P}_a}{2\bar{p}}\right]\Delta P_a^*(s) + \left[\frac{f_a\bar{P}_a + f_a\bar{P}_c}{2\bar{p}}\right]\Delta R^*(s) \qquad \text{(A44)}$$

Substituting (A20), (A40)-(A42), and (A44) in (A43) and rearranging:

$$\frac{\Delta q^*(s)}{\Delta P_a^*(s)} = S_{q,a} \qquad \text{(A45)}$$

where $S_{q,a}$ is:

$$S_{q,a} = \left(\frac{\bar{P}_a}{\bar{P}_a - \bar{P}_c}\right)\left[\frac{\frac{1}{4f_r} + \left(\frac{\bar{P}_a - \bar{P}_c}{2\bar{p}}\right)S_{r,p} + \frac{1}{f_r}S_{r,\nabla p}}{\frac{1}{4f_r} + \left(\frac{\bar{P}_a - \bar{P}_c}{2\bar{p}}\right)(1 - f_r - 2f_v)S_{r,p} + \left(\frac{1}{f_r} - 1\right)S_{r,\nabla p}}\right] \qquad \text{(A46)}$$

Note that (A45) and (A46) are (3.4) and (3.5) presented in Chapter 3.

A.1.2. Extension to dCA model & pressure-flow transfer function derivation

The sCA model derived above was extended to a dCA model by incorporating dynamics in the myogenic and metabolic responses. This was done by modelling the response of wall force to direct stress (i.e., the myogenic response) and the response of wall force to shear stress (i.e., the metabolic response) each as first order responses instead of merely sensitivity coefficients, so that (A13) and (A14) become:

$$\frac{S_M}{\tau_M s + 1} = S_{F,k}S_{k,\sigma} \qquad \text{(A47)}$$

$$\frac{S_V}{\tau_V s + 1} = S_{F,k}S_{k,\tau} \qquad \text{(A48)}$$

where S_M and S_V still represent the magnitudes of the myogenic and metabolic responses respectively, and τ_M and τ_V can be thought of as time constants of the myogenic and metabolic responses respectively. This is of course a simplification, as the timing of the response of smooth muscle stiffness, k, to direct stress, σ, and the timing of the response of wall force, F, to smooth muscle stiffness, k, have been lumped together in one time constant, τ_M. Similarly, the timing of the response of smooth muscle stiffness, k, to shear stress, τ, and the timing of the response of wall force, F, to smooth muscle stiffness, k, have been lumped together in one time constant, τ_V. Furthermore, no other dynamics are added to the model, although there are other sources of dynamics in the cerebral vasculature (e.g., elastic response, sensing delays), and the assumptions made during derivation of the sCA model (e.g., constant volumes in the lumped compartments shown in Figure A.1) are maintained. These simplifications and assumptions likely do not fully reflect the true physiology, but serve the purpose of obtaining a model of dCA that can disentangle the contributions of the myogenic and metabolic responses whilst remaining simple enough for use in conjunction with experimental data.

Incorporating the new definitions in (A47) and (A48) into (A12):

$$\Delta r^*(s) = \frac{1-\frac{S_M}{\tau_M s+1}}{2\frac{S_M}{\tau_M s+1}-\frac{S_V}{\tau_V s+1}+S_E-1}\Delta p^*(s) + \frac{\frac{S_V}{\tau_V s+1}}{2\frac{S_M}{\tau_M s+1}-\frac{S_V}{\tau_V s+1}+S_E-1}(\nabla p)^*(s) \tag{A49}$$

(A49) can then be written as:

$$\Delta r^*(s) = S_{r,p}(s)\Delta p^*(s) + S_{r,\nabla p}(s)(\nabla p)^*(s) \tag{A50}$$

where $S_{r,p}(\mathrm{s})$ and $S_{r,\nabla p}(s)$ are now also functions of s:

$$S_{r,p}(\mathrm{s}) = \frac{1-\frac{S_M}{\tau_M s+1}}{2\frac{S_M}{\tau_M s+1}-\frac{S_V}{\tau_V s+1}+S_E-1} \tag{A51}$$

$$S_{r,\nabla p}(s) = \frac{\frac{S_V}{\tau_V s+1}}{2\frac{S_M}{\tau_M s+1}-\frac{S_V}{\tau_V s+1}+S_E-1} \tag{A52}$$

Note that (A50) is (3.1) in the case of the dCA model, and (A51) and (A52) are (3.2) and (3.3) respectively.

Substituting (A51) and (A52) in (A45) and (A46) gives the overall transfer function relating changes in ABP to changes in flow rate through the cerebral vasculature:

$$\frac{\Delta q^*(s)}{\Delta P_a^*(s)} = c_0 \frac{a_0 s^2 + a_1 s + a_2}{a_3 s^2 + a_4 s + a_5} \tag{A53}$$

where the coefficients are provided in (A54) - (A59):

$$a_0 = \tau_M \tau_V (c_2 S_E - c_2 + c_1) \tag{A54}$$

$$a_1 = \tau_M(-c_2 S_V + c_2 S_E - c_2 + c_1 + 4c_2 S_V) + \tau_V(2c_2 S_M + c_2 S_E - c_2 + c_1 - c_1 S_M) \tag{A55}$$

$$a_2 = 2c_2 S_M - c_2 S_V + c_2 S_E - c_2 + c_1 - c_1 S_M + 4c_2 S_V \tag{A56}$$

$$a_3 = \tau_M \tau_V (c_2 S_E - c_2 + c_1 c_3) \tag{A57}$$

$$a_4 = \tau_M[-c_2 S_V + c_2 S_E - c_2 + c_1 c_3 + (4c_2 - 1)S_V] + \tau_V[2c_2 S_M + c_2 S_E - c_2 + c_1 c_3 - c_1 c_3 S_M] \tag{A58}$$

$$a_5 = 2c_2 S_M - c_2 S_V + c_2 S_E - c_2 + c_1 c_3 - c_1 d c_3 + (4c_2 - 1)S_V \tag{A59}$$

where c_0, c_1, c_2, and c_3 are simplifying parameters, defined as in (A60) - (A63):

$$c_0 = \frac{\overline{\overline{P_a}}}{\overline{P_a} - \overline{P_c}} \tag{A60}$$

$$c_1 = \frac{\bar{P}_a - \bar{P}_c}{2\bar{p}} \tag{A61}$$

$$c_2 = \frac{1}{4f_r} \tag{A62}$$

$$c_3 = 1 - f_r - 2f_v. \tag{A63}$$

The transfer function in (A53) is not strictly proper, as both the denominator and numerator are second-order polynomials of s. Obtaining a transfer function with equal orders for the numerator and denominator to describe CA is in agreement with [122]. The theoretical reason that the numerator degree cannot be lower than the denominator degree is because that would send the limit of the transfer function where s tends to infinity to zero, which by the initial value theorem means that the initial value of a SR would be zero, and so does not correspond to the observation that a sudden increase (or decrease) in ABP produces a sudden increase (or decrease) in CBF. Similarly, based on the observation that a sudden increase (or decrease) in CBF is accompanied by a sudden change in ABP, the degree of the denominator cannot be lower than that of the numerator – and both these conditions can only be met if the numerator and denominator degrees are equal.

However, a proper transfer function was required to optimise model parameters using experimental data, and this was obtained using the methodology outlined in [114] and implemented in [113], where the transfer function in (A53) is rewritten as (A64):

$$\frac{\Delta q^*(s)}{\Delta P_a^*(s)} = K + H(s) \tag{A64}$$

where K is a constant and $H(s)$ is a strictly proper transfer function of the form (A65):

$$H(s) = \frac{b_0 s + b_1}{b_2 s^2 + b_3 s + b_4} \tag{A65}$$

The strictly proper transfer function, $H(s)$, was used for all further analysis.

A.2. Histograms of myogenic parameter values

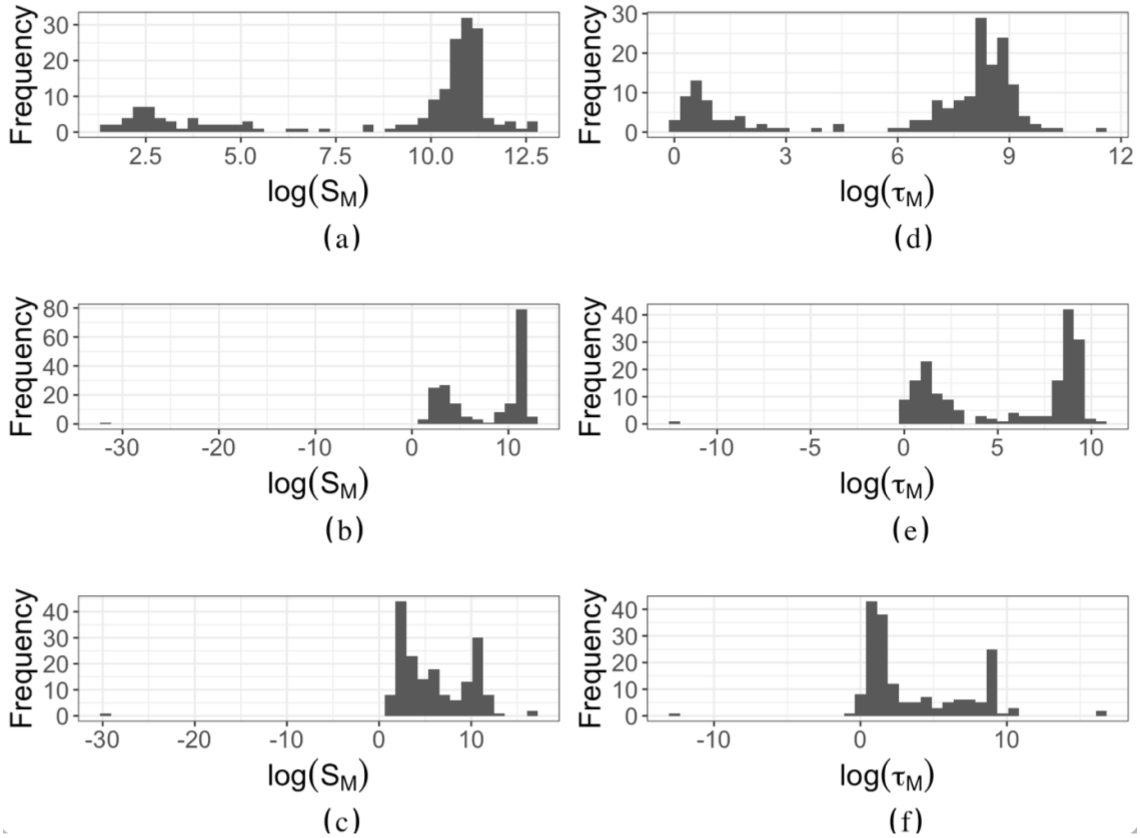

(a) (d)

(b) (e)

(c) (f)

Figure A.2. Histograms of S_M and τ_M values optimised by fitting impulse responses obtained from multivariate TFA to the dCA model. Log scales are used to emphasis the bimodal distributions. (a) S_M results using normocapnia data. (b) S_M results using thigh cuff data. (c) S_M results using hypercapnia data. (d) τ_M results using normocapnia data. (e) τ_M results using thigh cuff data. (f) τ_M results using hypercapnia data.

Appendix B

B.1. Preliminary results showing that capillary compartment control does not improve dCVR model fit

A previous version of the model presented in Chapter 4 allowed dCVR to also modify capillary compliance:

$$\tau_{c1}^2 \frac{d^2 C_c(t)}{dt} + \tau_{c2} \frac{dC_c(t)}{dt} + C_c(t) = G_c \log_{10}\left(\frac{P_{a,CO2}(t)}{\bar{P}_{a,CO2}}\right) \tag{B1}$$

Preliminary analysis was performed by fitting the model to the IR reported in [71]. Initial conditions for the two gains and four time constants were set as the values for the gain (i.e., 8) and time constant (i.e., 40 s) from the first order dCVR model in [113]. The model fit and optimised arterial parameter values are the same whether capillary compliance is modifiable or kept constant, as shown in Figure B.1 and Table B.1.

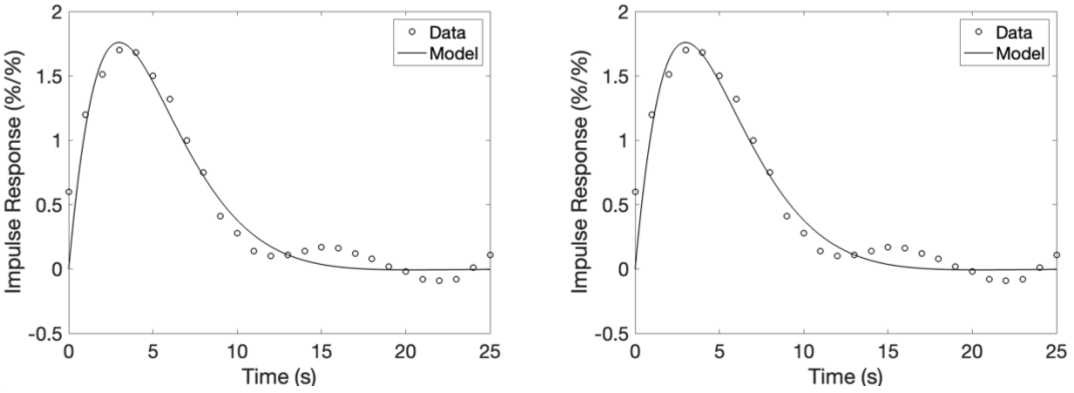

(a) (b)

Figure B.1. Optimal fit to CO_2-flow impulse response from [113] for the dCVR model with (a) modifiable capillary compliance and (b) constant capillary compliance. Values represent deviations from the baseline value.

Since a range of data-based IR shapes (with some including higher order dynamics) were observed in Chapter 4 and Chapter 5, the model with variable capillary compliance was also fitted to the range of IR shapes shown in Figure 4.3. The initial conditions for the arterial parameters from Chapter 4 were used for both the arterial and capillary compartments. In some of the cases, there are slight differences in model fit and optimised arterial parameter values, as shown in Figure B.2 and Table B.2, but the largest difference in SSE is of the order 1e-6, meaning that there are no notable differences in the goodness of fit between the models. The simpler version of the model with constant capillary compliance was therefore used for all further analysis

Table B.1. Optimised parameter values and SSEs for model fit with modifiable and constant capillary compliance to IR from [71].

	G_a	τ_{a1}	τ_{a2}	G_c	τ_{c1}	τ_{c2}	SSE
Modifiable C_c	33.9	2.74 s	4.77 s	2.39e-14	40 s	40 s	0.549
Constant C_c	33.9	2.74 s	4.77 s	-	-	-	0.549

Table B.2. Optimised parameter values and SSEs for model fit with modifiable and constant capillary compliance to IRs in Figure 4.3.

		G_a	τ_{a1}	τ_{a2}	G_c	τ_{c1}	τ_{c2}	SSE
(a)	Modifiable C_c	0.572	0.917	1.65	0.0779	0.486	0.529	6.09e-6
	Constant C_c	0.572	0.919	1.64	-	-	-	4.42e-6
(b)	Modifiable C_c	0.507	0.622	0.624	0.249	0.486	0.529	0.0032
	Constant C_c	0.544	0.640	0.657	-	-	-	0.0032
(c)	Modifiable C_c	0.107	0.512	0.269	0.187	0.486	0.529	0.0116
	Constant C_c	0.116	0.520	0.286	-	-	-	0.0116
(d)	Modifiable C_c	0.387	0.635	0.963	0.116	0.486	0.529	0.0011
	Constant C_c	0.387	0.634	0.963	-	-	-	0.0011
(e)	Modifiable C_c	0.65	4.39	4.71	6.59e-11	0.486	0.529	0.0028
	Constant C_c	0.655	4.37	4.75	-	-	-	0.0028
(f)	Modifiable C_c	1.31	1.67	5.99	0.00260	0.486	0.529	0.0013
	Constant C_c	1.31	1.66	6.01	-	-	-	0.0013
(g)	Modifiable C_c	0.911	3.61	5.11	0.0979	0.486	0.529	0.0014
	Constant C_c	0.911	3.61	5.11	-	-	-	0.0014
(h)	Modifiable C_c	1.06	0.0557	9.27	0.0563	0.486	0.529	0.0068
	Constant C_c	1.02	6.77e-4	9.7	-	-	-	0.0068

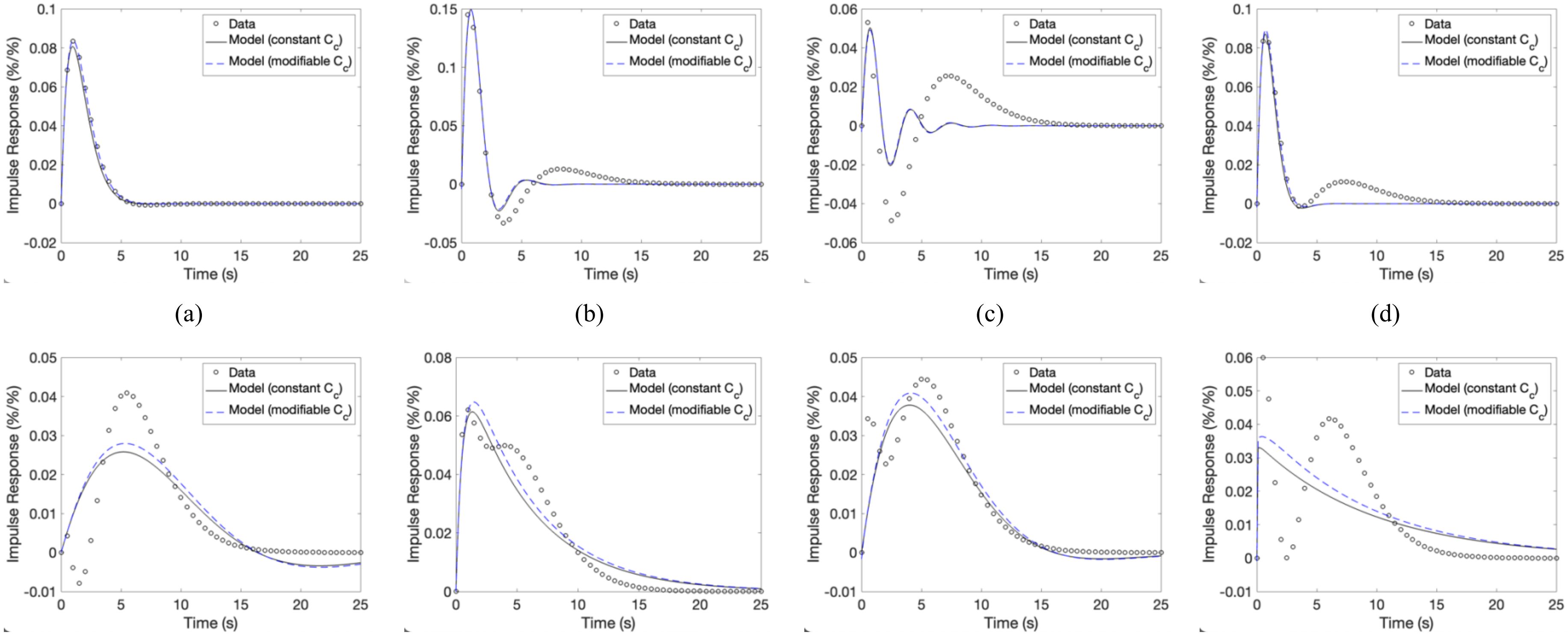

(a) (b) (c) (d)

(e) (f) (g) (h)

Figure B.2. Optimal fit to the range of CO_2-flow impulse responses observed in Chapter 4 (see Figure 4.3) for the dCVR model with modifiable capillary compliance and constant capillary compliance. Values represent deviations from the baseline value.

B.2. Fixed dCVR model parameters

B.2.1. Parameter values

All model parameters are provided in Table 3.1 in Chapter 4. Parameters from the validated haemodynamic model by [154] were used where applicable, but values for four parameters ($\overline{R_c}$, $\overline{R_{sv}}$, $\overline{V_c}$, $\overline{C_c}$) had to be selected for the extended model used in this work.

These four additional parameter values were calculated using suitable literature values provided in Table B.3 and reasonable assumptions as discussed below. Baseline resistance of the capillaries was calculated by approximating the capillary bed as a set of identical capillaries in parallel. The resistance of an individual capillary was calculated using the Poiseuille equation (B2), as it is the best tool available even though blood flow through capillaries does not strictly adhere to the assumption of laminar flow of a Newtonian fluid (since the plasma and red blood cells do not move in phase).

$$\overline{\mathrm{R}}_{\text{one c apillary}} = \frac{8\mu L}{\pi r^4} \tag{B2}$$

Table B.3. Literature values used to calculate capillary compartment parameter values for the hemodynamic model.

Parameter	Description	Value	Source
μ	Dynamic viscosity of blood (45% haematocrit)	4×10^{-3} Pa s	[92]
L	Capillary length	149.97 μm	[155]
r	Capillary radius	3.25 μm	[156]
D_c	Capillary density	805 mm^{-3}	[3]
V_{brain}	Brain volume	1195 mL	[157]
CBV_{GM}	Cerebral blood volume in grey matter	5.4 mL/100 g	[158]
VF_{GM}	Grey matter volume fraction	0.5505 L/L	[81]

Total baseline resistance of the capillaries was then calculated as that of identical resistors in parallel (B3):

$$\overline{R_c} = \frac{\overline{R_{one\ capillary}}}{D_c \times V_{brain}} \tag{B3}$$

Baseline resistance of the small veins was calculated as the difference between the combined resistance value for the capillary bed and small veins in [81], 1.32 mmHg s/mL, and the baseline resistance of the capillaries calculated above (B4), as the capillary bed and small veins are functionally in series in the electrical equivalent haemodynamic model.

$$\overline{R_{sv}} = \overline{R_{sv+c}} - \overline{R_c} \tag{B4}$$

The values obtained for the baseline resistance of the capillaries and the small veins fall within the ballpark of what is expected. Firstly, the calculated capillaries' resistance is smaller than the combined capillaries and small veins resistance reported in [78]. Secondly, the small veins' resistance calculated here is comparable to the value of a similar parameter, the resistance of the proximal cerebral veins, reported as 0.880 mmHg s/mL in [155]. However, it should be noted that the capillary resistance (and hence the small veins resistance) calculation is sensitive to the values of the parameters in Table B.3, which are not well established in literature. For example, [3] reports a characteristic capillary length of 60.3 μm; [159] reports a capillary density of 8000 mm^{-3} in the brain; and [159] reports capillary densities in the cortical and subcortical grey matter that average to 1331 mm^{3}. These model parameter values (Table 3.1) can therefore be updated according to what becomes available in literature in future.

Baseline volume of the capillaries was also calculated by approximating the capillary bed as a set of identical cylindrical capillaries (B5):

$$\overline{V_c} = (\pi r^2 L) \times (D_c \times V_{brain}) \tag{B5}$$

where suitable parameter values were identified from literature and are provided in Table B.3. To validate the value obtained for baseline volume of the capillaries, CBV fractions were calculated for each compartment in the haemodynamic model (B6) and are reported in Table B.4. Physiological ranges for CBV fractions were found for arteries and capillaries and veins together, and the calculated values both fall within those ranges.

$$CBV\ fraction = \frac{CBV_{compartment}}{CBV_{whole\ brain}} \tag{B6}$$

CBV values for each compartment are shown in Table B.4, where the absolute value for CBV of the whole brain was converted from suitable values found in literature (Table B.3). Notably, CBV is typically reported in mL (blood)/100 g (tissue), as is the case in [157], and therefore had to be converted using brain tissue mass. Furthermore, the value reported in [81] was obtained using MRI of grey matter, so only grey matter mass was considered in the conversion. Focusing on grey matter is reasonable, because most metabolism in the brain occurs in grey matter so most vasculature is found in the grey matter. All calculations are provided in Section B.2.2 of this appendix.

Table B.4. Comparison of compartmental volume fractions to literature values.

Compartment	Baseline CBV		Baseline CBV fraction		
	Value	Source	Calculated value	Literature values	Source
Whole brain (grey matter)	35.5 mL	Section B.2.2	1	1	-
Arteries	13 mL	[160]	0.37	0.30-0.37	[160]
Capillaries	4.8 mL	(B5)	0.13	-	-
Veins	-	-	0.50	-	-
Capillaries + veins	-	-	0.63	0.63-0.70	[160]

Baseline capillary compliance was calculated as the ratio between baseline volume of the capillaries and baseline pressure in the capillaries (B7):

$$\overline{C_c} = \frac{\overline{V_c}}{\overline{P_c}} \tag{B7}$$

where the baseline pressure in the capillaries is provided as $\overline{P_2}$ in Table 4.1 in Chapter 4. It should be noted that the true definition of compliance is the ratio of the change in volume and the change in pressure, but multiple volume and pressure values are not available, so (B7) is an approximation. The calculated value of baseline compliance of the capillaries is accepted as a reasonable, since it is smaller than that of the arteries but of the same order, and an order of magnitude smaller than that of the veins, as expected (Table B.5), where baseline compliance of the veins is assumed to be inversely proportional to transmural pressure as in [78] (B8) and P_{ic}, P_v, and $\overline{P_3}$ are described and provided in Table 4.1 in Chapter 4.

$$\overline{C_v} = \frac{1}{k_{ven}(\overline{P_3} - P_{ic} - P_v)} \tag{B8}$$

Table B.5. Baseline compliance of arteries, capillaries, and veins.

Compartment	Baseline compliance
Arteries	0.205 mL/mmHg
Capillaries	0.162 mL/mmHg
Veins	1.21 mL/mmHg

B.2.2. Parameter value calculations

Baseline resistance of one capillary:

$$\bar{R}_{one\ capillary} = \frac{8\mu L}{\pi r^4} = \frac{8(4\times10^{-3}\ Pa\ s)(149.97\mu m)}{\pi(3.25\ \mu m)^4} \times \frac{mmHg}{133.32\ Pa} \times \frac{\mu m^3}{1\times10^{-12} mL}$$

$$= 1.03 \times 10^8\ mmHg\ s/mL$$

Baseline resistance of capillary compartment:

$$\overline{R_c} = \frac{\overline{R_{one\ capillary}}}{D_c \times V_{brain}} = \frac{1.03\times10^8\ mmHg\ s/mL}{(805 mm^{-3})(1195\ mL)} \times \frac{mL}{1000\ mm^3} = 0.107\ mmHg\ s/mL$$

Baseline resistance of small veins:

$$\overline{R_{sv}} = \overline{R_{sv+c}} - \overline{R_c} = 1.32 - 0.107 = 1.21\ mmHg\ s/mL$$

Baseline volume of the capillary bed:

$$\overline{V_c} = (\pi r^2 L) \times (D_c V_{brain}) = \pi(3.25\ \mu m)^2(149.97\ \mu m) \times (805\ mm^{-3} \times 1195\ mL) \times \frac{1000\ mm^3}{mL} \times \frac{mL}{10^{12}\ \mu m^3} = 4.79\ mL$$

Whole brain (grey matter) cerebral blood volume, taking brain density as 1 g/mL [161]:

$$CBV_{whole\ brain} = \frac{5.4\ mL}{100\ g} \times \left(1195\ mL \times 1\frac{g}{mL}\right) \times 0.5505\ \frac{mL}{mL} = 35.5\ mL$$

Cerebral blood volume fraction of arteries:

$$CBV\ fraction_{arteries} = \frac{CBV_{arteries}}{CBV_{whole\ brain}} = \frac{13\ mL}{35.5\ mL} = 0.31$$

Cerebral blood volume fraction of capillaries:

$$CBV\ fraction_{capillaries} = \frac{CBV_{capillaries}}{CBV_{whole\ brain}} = \frac{4.79\ mL}{35.5\ mL} = 0.13$$

Cerebral blood volume fraction of veins:

$$CBV\ fraction_{veins} = 1 - CBV\ fraction_{arteries} - CBV\ fraction_{capillaries} = 1 - 0.37 - 0.13 = 0.50$$

Combined cerebral blood volume of capillaries and veins:

$$CBV\ fraction_{capillaries+veins} = CBV\ fraction_{capillaries} + BCV\ fraction_{veins} = 0.13 + 0.50 = 0.63$$

Baseline compliance of capillaries:

$$\overline{C_c} = \frac{\overline{V_c}}{\overline{P_c}} = \frac{4.79\ mL}{29.5\ mmHg} = 0.162\ mL/mmHg$$

Baseline compliance of veins:

$$\overline{C_v} = \frac{1}{k_{ven}(\overline{P_3} - P_{ic} - P_v)} = \frac{1}{0.186\ mL^{-1}(12.2\ mmHg - 10\ mmHg - 6\ mmHg)} = 1.21\ mL/mmHg$$

B.2.3. State variable baseline values

The baseline pressures were solved for using the Solver tool in Microsoft Excel and are provided in Table 4.1 in Chapter 4. Constraints were set so that the pressures decrease in the functional direction of flow ((B9) – (B12)):

$$\bar{P}_1 < \bar{P}_a \tag{B9}$$

$$\bar{P}_2 < \bar{P}_1 \tag{B10}$$

$$\bar{P}_3 < \bar{P}_2 \tag{B11}$$

$$P_v < \bar{P}_3 \tag{B12}$$

The objective function was set to achieve equal flow rates at steady state, as shown in (B13):

$$|\overline{q_{la}} - \overline{q_{sa}}| + |\overline{q_{sa}} - \overline{q_c}| + |\overline{q_c} - \overline{q_v}| = 0 \tag{B13}$$

where the steady state flow rates were calculated as the ratios between pressure differences and resistances (eqns (4.10) and (B14) – (B16)) and are provided in Table 4.1 in Chapter 4.

$$\overline{q_{sa}} = \frac{\overline{P_1} - \overline{P_2}}{\overline{R_{sa}}/2 + \overline{R_c}/2} \tag{B14}$$

$$\overline{q_c} = \frac{\overline{P_2} - \overline{P_3}}{\overline{R_c}/2 + R_{sv}} \tag{B15}$$

$$\overline{q_v} = \frac{\overline{P_3} - P_v}{R_{lv}} \tag{B16}$$

B.3. Overall CO$_2$-flow transfer function (using arterial flow) derivation

The overall transfer function describing the linear relationship between arterial CO$_2$ and arterial CBF is derived here. This derivation is intended to be read alongside the model description and Figure 4.1 provided in Section 4.2.1. More detailed derivations of the model equations, including the linearised transfer functions written in terms of deviation variables (i.e., small perturbations from baseline) in the Laplace domain, are provided here.

The Poiseuille equation is often used to model blood flow:

$$\frac{8\mu L}{\pi r^4} = \frac{dP}{q} = R \tag{B17}$$

where μ is blood viscosity, r is vessel radius, $\mathrm{d}P$ is pressure drop along the vessel length L, and q is volumetric flow rate. The ratio of pressure drop, dP, to flow rate, q, is known as the hydraulic resistance, R, which is the opposition to fluid flow in a hydraulic system, and is analogous to electrical resistance in an electrical circuit (i.e., it relates pressure drop and flow rate the same way electrical resistance relates voltage and current via Ohm's law). According to the Poiseuille equation, for a given vessel length and constant blood viscosity, hydraulic resistance is inversely proportional to vessel radius to the power of four:

$$R \propto \frac{1}{r^4} \tag{B18}$$

The blood vessel volume, $V,$ is the product of vessel length, L, and cross-sectional area, A_c:

$$V = L(A_c) = L(\pi r^2) \tag{B19}$$

Rearranging (B19) gives:

$$r^2 = \frac{V}{L\pi} \tag{B20}$$

Substituting (B20) in (B18) gives:

$$R \propto \frac{1}{\left(\frac{V}{L\pi}\right)^2} \tag{B21}$$

For a given vessel length, (B21) becomes:

$$R \propto \frac{1}{V^2} \tag{B22}$$

From (B22) the relationship between the ratio of two vessel volumes and the ratio of two corresponding hydraulic resistances can be written:

$$\frac{V_1}{V_2} = \frac{\sqrt{R_2}}{\sqrt{R_1}} \tag{B23}$$

The relationship in (B23) can be applied for the small arteries and for the capillaries in the haemodynamic model shown in Figure 4.1:

$$\frac{V_{sa}}{\bar{V}_{sa}} = \frac{\sqrt{\bar{R}_{sa}}}{\sqrt{R_{sa}}} \tag{B24}$$

$$\frac{V_c}{\bar{V}_c} = \frac{\sqrt{\bar{R}_c}}{\sqrt{R_c}} \tag{B25}$$

where an overscript indicates baseline value. Note that (B24) and (B25) are (4.2) and (4.3) in Chapter 4.

From the definition of compliance, the relationship between compliance, volume, and pressure can be written for the small arteries, capillaries, and veins:

$$\frac{dV_{sa}}{dt} = \frac{d}{dt}[C_a(P_1 - P_{ic})] \tag{B26}$$

$$\frac{dV_c}{dt} = \bar{C}_c \frac{d}{dt}(P_2 - P_{ic}) \tag{B27}$$

$$\frac{dV_v}{dt} = \bar{C}_v \frac{d}{dt}(P_3 - P_{ic}) \tag{B28}$$

where the arterial compliance, C_a is variable (according to (B.42) provided below), but the capillary compliance, $\bar{C}_c$, and venous compliance, $\bar{C}_v$, are written as their baseline values, as they are not adjustable by $\mathrm{P}_{\mathrm{a,CO2}}$ (since regulating CBF via adjusting vessel compliance is limited to the arterioles, as discussed in Section 2.2.3). In the previous version of this model (that was not used; see Appendix B.1), where capillary compliance was modifiable, (B27) took the same form as (B26), as C_c was not constant. Note that (B26)-(B28) are (4.4)-(4.6) in Chapter 4.

Assuming no significant changes in blood density, mass balances can be performed as volume balances over the nodes at P_1, P_2, and P_3 in Figure 4.1:

$$\frac{dV_{sa}}{dt} = q_{la} - q_{sa} \tag{B29}$$

$$\frac{dV_c}{dt} = q_{sa} - q_c \tag{B30}$$

$$\frac{dV_v}{dt} = q_c - q_v \tag{B31}$$

Since the haemodynamic model is treated as an equivalent electrical circuit model (see Section 2.4.1.1), the relationship between voltage, current, and electrical resistance given in Ohm's law can be applied to the relationship between pressure, flow rate, and hydraulic resistance (which corresponds to the definition of hydraulic resistance provided in (B17)):

$$q_{la} = \frac{P_a - P_1}{R_{la} + R_{sa}/2} \tag{B32}$$

$$q_{sa} = \frac{P_1 - P_2}{R_{sa}/2 + R_c/2} \tag{B33}$$

$$q_c = \frac{P_2 - P_3}{R_c/2 + R_{sv}} \tag{B34}$$

$$q_v = \frac{P_3 - P_v}{R_{lv}} \tag{B35}$$

Note that (B32) is (4.10) in Chapter 4. Then substituting (B32)-(B35) in (B29)-(B31) gives:

$$\frac{dV_{sa}}{dt} = \frac{P_a - P_1}{R_{la} + R_{sa}/2} - \frac{P_1 - P_2}{R_{sa}/2 + R_c/2} \tag{B36}$$

$$\frac{dV_c}{dt} = \frac{P_1 - P_2}{R_{sa}/2 + R_c/2} - \frac{P_2 - P_3}{R_C/2 + R_{sv}} \tag{B37}$$

$$\frac{dV_v}{dt} = \frac{P_2 - P_3}{R_c/2 + R_{sv}} - \frac{P_3 - P_v}{R_{lv}} \tag{B38}$$

Note that (B36)-(B38) are (4.7)-(4.9) in Chapter 4.

A differential equation for arterial compliance and pressure in the arterial compartment can be obtained by combining (B26) with (B36):

$$\bar{C}_a \frac{dP_1}{dt} + (\bar{P}_1 - P_{ic}) \frac{dC_a}{dt} = \frac{P_a - P_1}{R_{la} + R_{sa}/2} - \frac{P_1 - P_2}{R_{sa}/2 + R_c/2} \tag{B39}$$

Similarly, differential equations for pressures in the capillary and venous compartments can be obtained by combining (B27) with (B37) and combining (B28) with (B38) – except that the capillary and venous compliances are constant, so the derivative term for compliance falls away:

$$\bar{C}_c \frac{dP_2}{dt} = \frac{P_1 - P_2}{R_{sa}/2 + R_c/2} - \frac{P_2 - P_3}{R_C/2 + R_{sv}} \tag{B40}$$

$$\bar{C}_v \frac{dP_3}{dt} = \frac{P_2 - P_3}{R_c/2 + R_{sv}} - \frac{P_3 - P_v}{R_{lv}} \tag{B41}$$

dCVR is assumed to modify arterial compliance in response to the logarithm of changes in CO2 pressure (as the response may actually be to changes in pH, which relates to changes in CO2 via a logarithm, as described in Section 4.2.1):

$$\tau_{a1}^2 \frac{d^2 C_a}{dt} + \tau_{a2} \frac{dC_a}{dt} + C_a = G_a \log_{10}\left(\frac{P_{a,CO2}}{\bar{P}_{a,CO2}}\right) \tag{B42}$$

Note that (B42) is (4.11) in Chapter 4.

The equations (B24)-(B25), (B26)-(B27), (B32), (B39)-(B41), and (B42) can be linearised, written in terms of deviation variables (i.e., small perturbations from baseline, indicated by Δ), and converted to the Laplace domain to give:

$$\Delta \mathrm{R_{sa}}(s) = -2\frac{\bar{R}_{sa}}{\bar{V}_{sa}} \Delta V_{sa}(s) \tag{B43}$$

$$\Delta \mathrm{R}_c(s) = -2\frac{\bar{R}_c}{\bar{V}_c} \Delta V_c(s) \tag{B44}$$

$$\Delta V_{sa}(s) = \bar{C}_a \Delta P_1(s) + (\bar{P}_1 - P_{ic}) \Delta C_a(s) \tag{B45}$$

$$\Delta V_c(s) = \bar{C}_c \Delta P_2(s) \tag{B46}$$

$$\Delta q_{la}(s) = \left[\frac{1}{\mathrm{a}_2}\right] \Delta P_a(s) + \left[-\frac{1}{\mathrm{a}_2}\right] \Delta P_1(s) + \left[-\frac{q_{la}/2}{\mathrm{a}_2}\right] \Delta R_{sa}(s) \tag{B47}$$

$$\begin{aligned} \Delta P_1(s) = {} & \left[\frac{-(\bar{P}_1 - P_{ic})s}{\bar{\mathrm{C}}_\mathrm{a}(1/a_2 + 1/\mathrm{a}_0)\ s + 1}\right] \Delta C_a(s) + \left[\frac{1/\mathrm{a}_2}{\bar{\mathrm{C}}_\mathrm{a}(1/a_2 + 1/\mathrm{a}_0)\ s + 1}\right] \Delta P_a(s) + \\ & \left[\frac{1/\mathrm{a}_2}{\bar{\mathrm{C}}_\mathrm{a}(1/a_2 + 1/\mathrm{a}_0)\ s + 1}\right] \Delta P_2(s) + \left[\frac{\frac{-\frac{1}{2}(\bar{P}a - \bar{P}_1)}{(a_2)^2} + \frac{\frac{1}{2}\bar{q}a}{\mathrm{a}_0}}{\bar{\mathrm{C}}_\mathrm{a}(1/a_2 + 1/\mathrm{a}_0)\ s + 1}\right] \Delta R_{sa}(s) + \\ & \left[\frac{\frac{1}{2}\frac{\bar{q}sa}{\mathrm{a}_0}}{\bar{\mathrm{C}}_\mathrm{a}(1/a_2 + 1/\mathrm{a}_0)\ s + 1}\right] \Delta R_c(s) \end{aligned} \tag{B48}$$

$$\begin{aligned} \Delta P_2(s) = {} & \left[\frac{1/a_0}{\bar{C}_c(1/\mathrm{a}_0 + 1/\mathrm{a}_1)\, s + 1}\right] \Delta P_1(s) + \left[\frac{1/\mathrm{a}_0}{\bar{C}_c(1/\mathrm{a}_0 + 1/\mathrm{a}_1)\, s + 1}\right] \Delta P_3(s) + \\ & \left[\frac{-\frac{1}{2}\left(\frac{\bar{q}sa}{\mathrm{a}_0}\right) + \frac{1}{2}\left(\frac{\bar{q}c}{\mathrm{a}_1}\right)}{\bar{C}_c(1/\mathrm{a}_0 + 1/\mathrm{a}_1)\, s + 1}\right] \Delta R_c(s) + \left[\frac{-\frac{1}{2}\left(\frac{\bar{q}c}{\mathrm{a}_1}\right)}{\bar{C}_c(1/\mathrm{a}_0 + 1/\mathrm{a}_1)\, s + 1}\right] \Delta R_{sa}(s) \end{aligned} \tag{B49}$$

$$\Delta P_3(s) = \left[\frac{1/(\mathrm{C_v} a_1)}{\frac{\mathrm{a}_1}{C_v}s + 1}\right] \Delta P_2(s) + \left[\frac{\frac{\bar{P}_2 - \bar{P}_3}{2C_v}}{\frac{\mathrm{a}_1}{C_v}s + 1}\right] \Delta R_c(s) \tag{B50}$$

$$\Delta C_a(s) = \left[\frac{\frac{C_a G_a}{2\bar{P}_{a,CO2}\ln(10)}}{\tau_{a1}^2 s^2 + \tau_{a2}s + 1}\right] \Delta P_{a,CO2}(s) \tag{B51}$$

where $a_0 - a_2$ are simplifying parameters defined as in (B52) - (B54):

$$a_0 = \frac{\overline{r_{sa}}}{2} + \frac{\bar{r_c}}{2} \tag{B52}$$

$$a_1 = \frac{\bar{r_c}}{2} + r_{sv} \tag{B53}$$

$$a_2 = r_{la} + \frac{\overline{r_{sa}}}{2} \tag{B54}$$

An expression for flow rate in the large arteries (as a deviation variable), Δq_{la} can then be derived as a function of ABP (as a deviation variable), $\Delta \mathrm{P}_a$, and partial pressure of arterial CO2 (as a deviation variable), $\Delta P_{a,CO2}$, by combining equations (B43)-(B51):

$$\Delta q_{la}(s) = [TF_{ABP}]\Delta P_a + [TF_{CO2}]\Delta P_{a,CO2} \tag{B55}$$

where TF stands for transfer function. Since Chapter 4 focusses on investigating the response of flow to changes in $\mathrm{P}_{a,CO2}$, and the effects of changes in ABP are regressed out in the MISO model used to obtain the data-based CO2-flow IR (see Section 4.2.3), ABP is assumed to be constant. The deviation of ABP from baseline is therefore zero (i.e., $\Delta P_a = 0$), and (B55) simplifies to:

$$\Delta q_{la}(s) = [TF_{CO2}]\Delta P_{a,CO2} \tag{B56}$$

The overall CO2-flow transfer function, $\frac{\Delta q_{la}^*(s)}{\Delta P_{a,CO2}^*(s)}$, is then obtained by rearranging (B56) and multiplying by $\frac{\bar{P}_{a,CO2}}{\bar{Q}_{la}}$ on both sides of the equation, where the star superscript denotes a variable as a fraction of its baseline value. The transfer function is provided as the form derived by hand due to the complexity of the form organised in terms of orders of s that can be solved for in Mathematica:

$$\begin{aligned}
&\frac{\Delta q_{la}^*(s)}{\Delta P_{a,CO2}^*(s)} = \Big\{\overline{P_{a,CO2}}a_{24}G_a\Big(a_{25}(-a_{14}s + a_8a_{12}a_{14})\big((a_8s + 1)(a_{18}s + 1)(a_{16}s + \\
&1) + a_{21}(a_{16}s + 1) - a_{26}(a_{16}s + 1)(a_{18}s + 1)\big) + a_{25}a_{23}a_{11}a_{12}a_{14}(a_{18}s + \\
&1)(a_{16}s + 1) + a_{19}a_{12}a_{14}\Big((a_{17}s + 1)\big((a_8s + 1)(a_{18}s + 1)(a_{16}s + 1) + \\
&a_{21}(a_{16}s + 1) - a_{26}(a_{16}s + 1)(a_{18}s + 1)\big) - a_{23}a_{22}(a_{18}s + 1)(a_{16}s + 1) -
\end{aligned} \tag{B58}$$

$$a_8 a_{12}\overline{C_a}\big((a_8 s+1)(a_{18}s+1)(a_{16}s+1)+a_{21}(a_{16}s+1)-a_{26}(a_{16}s+$$

$$1)(a_{18}s+1)\big)\Big)\Big\}$$

$$/\Big\{\overline{q_{la}}(\tau_{a1}^2 s^2+\tau_{a2}s+1)\,\Big((a_{17}s+1)\big((a_8 s+1)(a_{18}s+1)(a_{16}s+1)+$$

$$a_{21}(a_{16}s+1)-a_{26}(a_{16}s+1)(a_{18}s+1)\big)-a_{23}a_{22}(a_{18}s+1)(a_{16}s+1)-$$

$$a_8 a_{12}\overline{C_a}\big((a_{16}s+1)(a_{18}s+1)(a_{16}s+1)+a_{21}(a_{16}s+1)-a_{26}(a_{16}s+$$

$$1)(a_{18}s+1)\big)\Big)\Big\}$$

where $a_0 - a_{25}$ are simplifying parameters defined as in (B52)-(B54) and (B59) - (B81):

$$a_3=\frac{1}{a_2}+\frac{1}{a_0} \tag{B59}$$

$$a_4=\frac{1}{a_0}+\frac{1}{a_1} \tag{B60}$$

$$a_5=k_{ven}\frac{\overline{P_3}}{a_1}-k_{ven}\frac{P_{ic}+P_{v1}}{a_1} \tag{B61}$$

$$a_6=-k_{ven}\frac{\overline{P_2}}{a_1}+2k_{ven}\frac{\overline{P_3}}{a_1}+2k_{ven}\frac{\overline{P_3}}{r_{lv}} \tag{B62}$$

$$a_7=\frac{1}{2}\frac{k_{ven}}{a_1}(-\overline{P_3}\bar{q}_c+(P_{ic}+P_{v1})\overline{P_2}-P_{ic}+P_{v1}) \tag{B63}$$

$$a_8=-\frac{1}{2}\frac{(\overline{P_a}-\overline{P_1})}{a_2^2}+\frac{1}{2}\frac{\overline{q_a}}{a_0} \tag{B64}$$

$$a_9=\frac{1}{2}\frac{\overline{q_a}}{a_0} \tag{B65}$$

$$a_{10}=-\frac{1}{2}\frac{\overline{q_a}}{a_0}+\frac{1}{2}\frac{\overline{q_c}}{a_1} \tag{B66}$$

$$a_{11}=-\frac{1}{2}\frac{\overline{q_c}}{a_1} \tag{B67}$$

$$a_{12}=-2\frac{\overline{r_{sa}}}{v_{sa}} \tag{B68}$$

$$a_{13}=-2\frac{\bar{r}_c}{\bar{v}_c} \tag{B69}$$

$$a_{14}=\bar{P}_1-P_{ic} \tag{B70}$$

$$a_{15} = \overline{P_2} - p_{ic} \tag{B71}$$

$$a_{16} = \frac{\overline{C_c}}{a_4} \tag{B72}$$

$$a_{17} = \frac{\overline{C_a}}{a_3} \tag{B73}$$

$$a_{18} = \frac{1}{a_6} \tag{B74}$$

$$a_{19} = -\frac{1}{2}\frac{\overline{q_{la}}}{a_3} \tag{B75}$$

$$a_{20} = \frac{1}{a_0} a_7 a_{13} a_{15} \tag{B76}$$

$$a_{21} = -\frac{1}{a_0}\left(a_5 + a_7 a_{13}\overline{C_c}\right) \tag{B77}$$

$$a_{22} = \frac{1}{a_0} + a_{11} a_{12}\overline{C_a} \tag{B78}$$

$$a_{23} = \frac{1}{a_2} + a_9 a_{13}\overline{C_c} \tag{B79}$$

$$a_{24} = \frac{\overline{C_a}}{2\overline{P_{a,CO2}}\ln(10)} \tag{B80}$$

$$a_{25} = -\frac{1}{a_2} + a_{19} a_{12}\overline{C_a} \tag{B81}$$

Eqn (B74) can be expanded as:

$$a_{18} = \frac{1}{a_6} = \frac{1}{k_{ven}\left(\frac{-\overline{P_2}+2\overline{P_3}}{\frac{\overline{R_C}}{2}+R_{sv}}+\frac{2\overline{P_3}}{R_{lv}}\right)}$$

$$= \frac{R_{lv}\left(\frac{\overline{R_C}}{2}+R_{sv}\right)}{k_{ven}\left(R_{lv}(2\overline{P_3}-\overline{P_2})+2\overline{P_3}\left(\frac{\overline{R_C}}{2}+R_{sv}\right)\right)} \times \frac{\overline{R_{total}}}{\overline{R_{total}}}$$

$$= \frac{\frac{R_{lv}}{\overline{R_{total}}}\left(\frac{\overline{R_C}}{2}+R_{sv}\right)}{k_{ven}\left(\frac{R_{lv}}{\overline{R_{total}}}(2\overline{P_3}-\overline{P_2})+2\overline{P_3}\left(\frac{\frac{\overline{R_C}}{\overline{R_{total}}}}{2}+\frac{R_{sv}}{\overline{R_{total}}}\right)\right)}$$

Since most of the resistance to flow takes place in the arteries, arterioles, and capillaries, whereas the venous vessels present little resistance to flow, the flow resistance fraction of the venous vessels, $\frac{R_{lv}}{R_{total}}$ could be assumed to be close to zero, which simplifies a_{18} to zero. The overall CO2-flow transfer function is then simplified to:

$$\begin{aligned}
&\frac{\Delta q_{la}^{*}}{\Delta P_{a,CO2}^{*}} = \{\overline{P_{a,CO2}}a_{24}G_a(a_{25}(-a_{14}s + a_8a_{12}a_{14})((a_8s + 1)(a_{16}s + 1) + \\
&a_{21}(a_{16}s + 1) - a_{26}(a_{16}s + 1)) + a_{25}a_{23}a_{11}a_{12}a_{14}(a_{16}s + 1) + \\
&a_{19}a_{12}a_{14}((a_{17}s + 1)((a_8s + 1)(a_{16}s + 1) + a_{21}(a_{16}s + 1) - a_{26}(a_{16}s + \\
&1)) - a_{23}a_{22}(a_{16}s + 1) - a_8a_{12}\overline{C_a}((a_8s + 1)(a_{16}s + 1) + a_{21}(a_{16}s + 1) - \\
&a_{26}(a_{16}s + 1))))\} \\
&/\{\overline{q_{la}}(\tau_{a1}^2s^2 + \tau_{a2}s + 1)((a_{17}s + 1)((a_8s + 1)(a_{16}s + 1) + a_{21}(a_{16}s + 1) - \\
&a_{26}(a_{16}s + 1)) - a_{23}a_{22}(a_{16}s + 1) - a_8a_{12}\overline{C_a}((a_{16}s + 1)(a_{16}s + 1) + \\
&a_{21}(a_{16}s + 1) - a_{26}(a_{16}s + 1)))\} \qquad \text{(B82)}
\end{aligned}$$

The non-simplified overall transfer function (B58) has an order of four in its numerator and six in its denominator; the simplified overall transfer (B82) has an order of three and five in its denominator.

B.4. Transfer function analysis to derive CO2-flow IRs

TFA was used to derive CO2-flow IRs but found to result in IR derivations with oscillations, as shown in Figure B.3. The oscillations may be due to the uncertainties associated with low SNR in steady state data (as used in this study). The recent review article by Shams et al. [116] recommends using a model-based method (i.e., a method that provides a shape to the derived IR) to overcome this limitation, and found the basis expansion technique using spherical Laguerre basis functions to perform the best out of all the model-based methods they tested. That method was therefore used in this work, as described in Section 4.2.3 in Chapter 4.

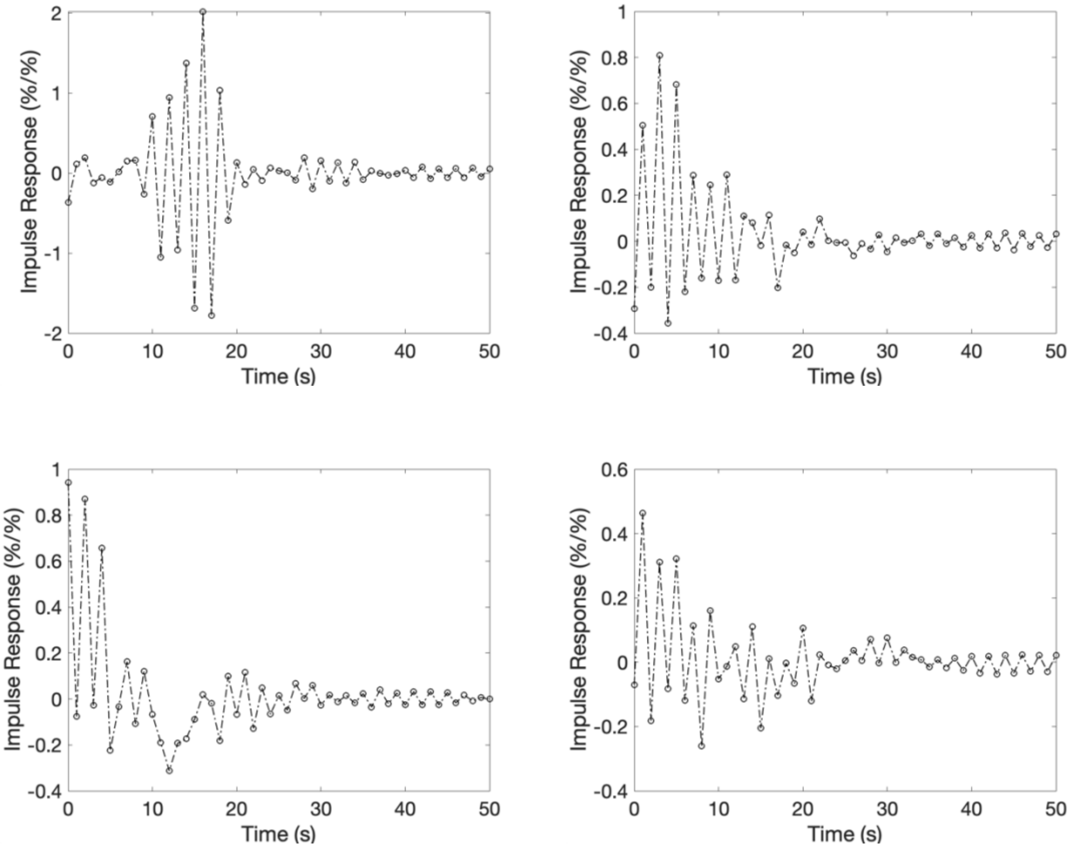

Figure B.3. CO_2-flow impulse responses derived using TFA from four representative recordings. The dashed line does not indicate a model fit and is only provided to assist with visualising the oscillations. Values represent deviations from the baseline value.

B.5. Testing implementation of the basis expansion method for impulse response derivation with a ground truth case

Implementation of the basis expansion method with spherical Laguerre basis functions in MATLAB was tested on a ground truth case. The ground truth case was constructed by using white noise as the input, an IR created using spherical Laguerre basis functions with known expansion coefficients, and an output created by convolving the input with the known IR. The input and output were then fed to the basis expansion method function in MATLAB and the derived IRs compared to the known IRs for two cases:

1. Using two basis functions.
2. Using three basis functions to increase complexity.

The hyperparameter ranges for α and p were set to 0.5 to 0.9 in increments of 0.1 and 2 to 4, as for the CO_2-flow IR derivation in Chapter 4.

Figure B.4 shows the input and output time series for the ground truth cases, and Figure B.5 shows the derived and ground truth IRs, which are exactly the same in both cases. The IR derivation method implemented with a custom function in MATLAB in this work has therefore been shown to correctly derive an IR for a simulated case where the ground truth is known.

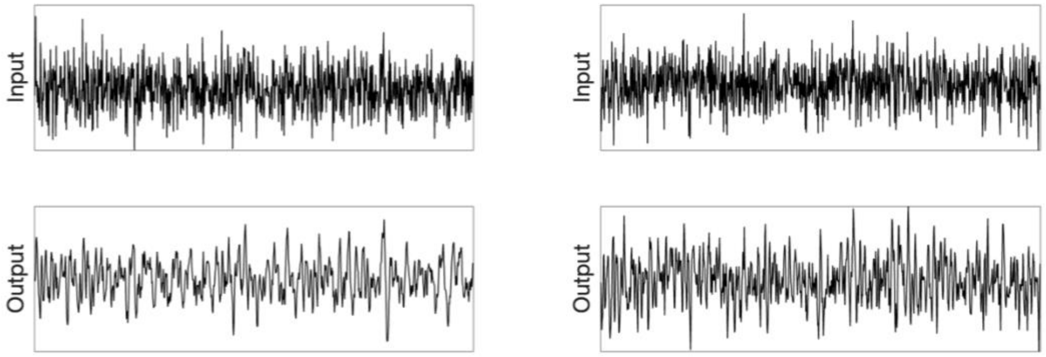

(a) (b)

Figure B.4. Input and output time series where the ground truth impulse response consists of (a) two basis functions, and (b) three basis functions.

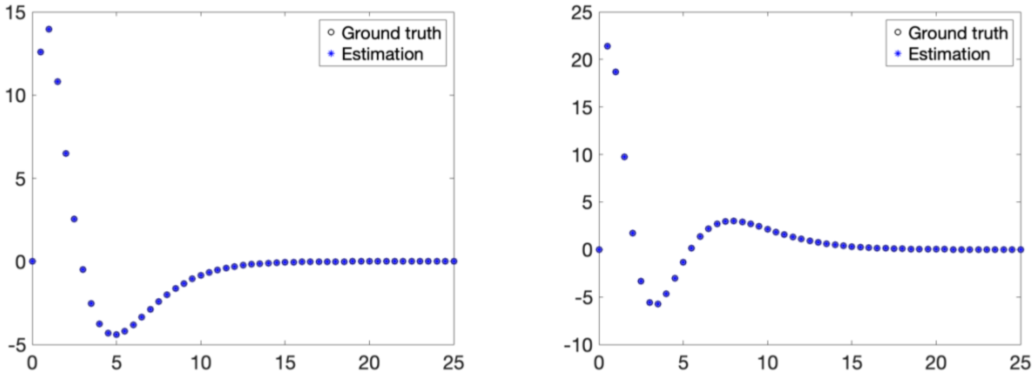

(a) (b)

Figure B.5. Comparison of ground truth and derived impulse responses where the ground truth consists of (a) two basis functions, and (b) three basis functions.

B.6. Testing basis expansion method with unrelated input and output

The basis expansion method using spherical Laguerre basis functions was tested to determine whether it would give a zero response (i.e., a flat line) when no relationship exists between the input and output. The test was performed by using independently generated white noise time series as the input and output, with an example shown in Figure B.6. The results (Figure B.7) show that the basis expansion method does not give a zero response when there is no relationship between the input and output, and in some cases, the derived IR resembles an expected shape of a CO_2-flow IR. It is therefore important to perform some form of test to determine whether a derived IR is meaningful or not.

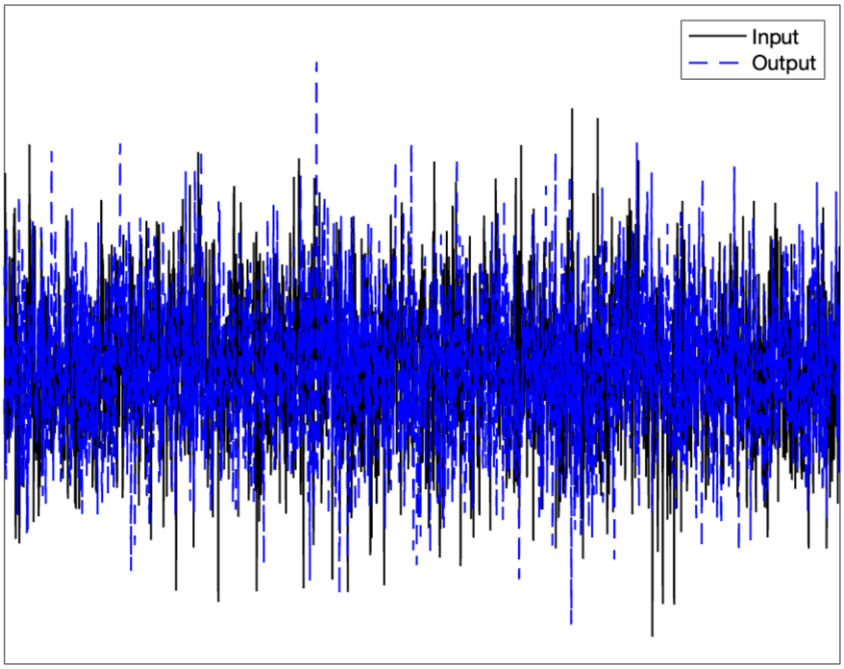

Figure B.6. Example of white noise time series that were used as the input and output.

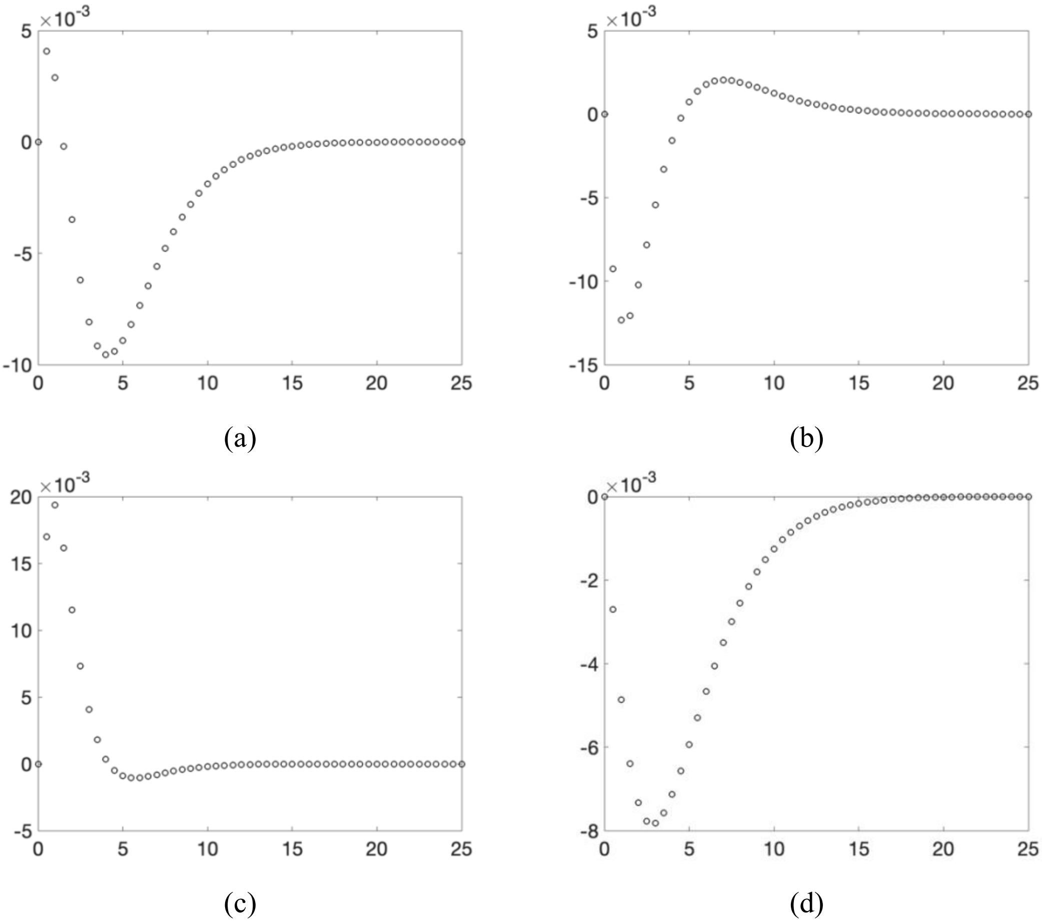

Figure B.7. Examples of impulse responses derived from white noise inputs and outputs using the basis expansion method with spherical Laguerre basis functions. (a) and (c) show cases that would be accepted according to the classification for a “physiological” impulse response (see Section 4.2.4 in Chapter 4), and (b) and (d) show cases that would be rejected.

B.7. Investigating data-based CO_2-flow impulse responses acceptance consistency over brain hemispheres

IRs were derived for the left and right brain hemispheres for each recording and it was noted that these pairs of hemispheres did not always both get accepted or both get rejected based on the criteria described in Section 4.2.4. A difference between IRs within a pair of hemispheres was not expected, as the subjects are young and healthy, and was therefore investigated. As shown in Table B.6, IRs from most (78% and above) pairs of hemispheres did both get accepted or both get rejected in the first and the second analysis, so the IR acceptance criteria are consistent in the majority of cases.

Table B.6. Breakdown of impulse responses that received the same classification (i.e., both left and right impulse responses are either accepted or rejected) or different classifications (i.e., one accepted and one rejected). SISO: single-input-single-output, MISO: multiple-input-single-output.

	Normocapnia		Hypercapnia	
	SISO	MISO	SISO	MISO
Analysis 1				
Both hemispheres accepted/rejected	79%	80%	84%	86%
One hemisphere accepted; one hemisphere rejected	21%	20%	16%	14%
Analysis 2				
Both hemispheres accepted/rejected	80%	78%	78%	83%
One hemisphere accepted; one hemisphere rejected	20%	22%	22%	17%

The small number of cases where one hemisphere is accepted and the other rejected may be due to data quality of the relevant time series. In some cases, the difference could be explained by sections of missing data in one of the CBv time series, with an example shown in Figure B.8. However, in other cases, there are no major differences between the left and right CBv time series, as shown by the example in Figure B.9. It is still possible that one of the CBv recordings contains more noise than the other (e.g., due to the angle of the TCD probe or movement during data acquisition), and this will require further investigation.

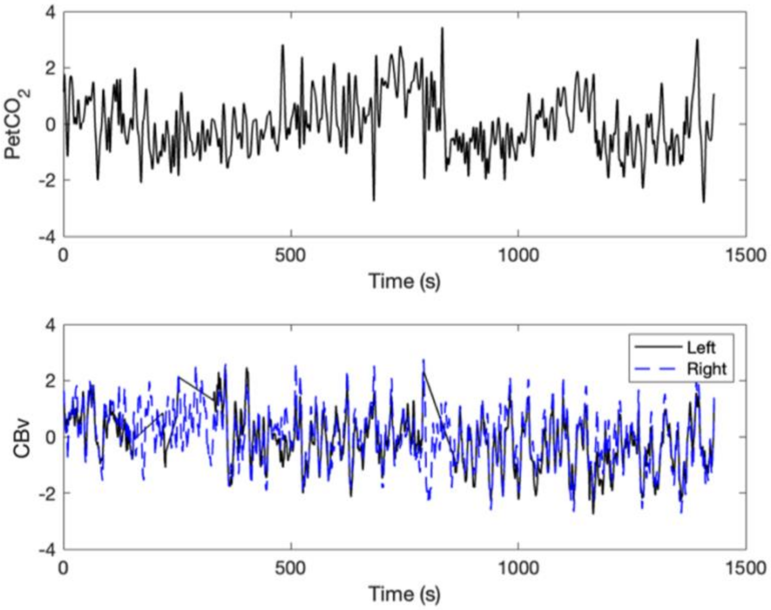

Figure B.8. A multivariate recording (shown as z-scores) that resulted in impulse responses with different classifications between hemispheres (i.e., one accepted and one rejected), likely due to missing data in the left CBv time series. CBv: cerebral blood velocity.

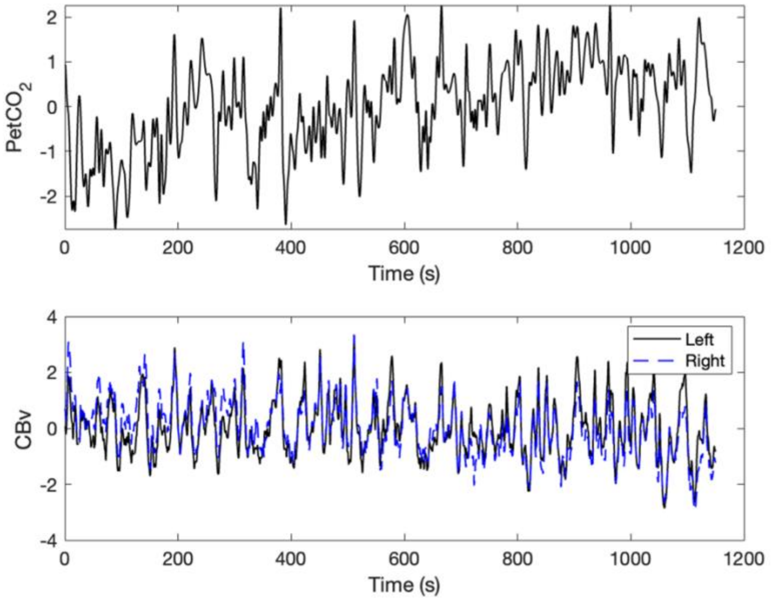

Figure B.9. A multivariate recording (shown as z-scores) that resulted in impulse responses with different classifications between hemispheres (i.e., one accepted and one rejected), despite no major differences between the left and right CBv time series. CBv: cerebral blood velocity.

Appendix C

C.1. Overall CO_2-flow transfer function (using capillary flow) derivation

The overall transfer function describing the linear relationship between arterial CO_2 and capillary CBF was derived using the same equations as provided in the full model derivation in Appendix B.3. The only difference is that the overall CO_2-flow transfer function in this case relates flow in the capillaries (instead of flow in the large arteries) to changes in $P_{a,CO2}$. One extra equation, (B34) in Appendix B.3, that provides the flow through the capillaries, therefore had to be linearised, written in terms of deviation variables (indicated by Δ), and converted to the Laplace domain:

$$\Delta q_c(s) = \frac{1}{a_1}\Delta P_2(s) - \frac{1}{a_1}\Delta P_3(s) - \frac{\overline{q_c}}{2a_1}\Delta R_c(s) \tag{C1}$$

where a_1 is a simplifying parameter defined in (B53) in Appendix B.3.

The equations (B43)-(B46) and (B48)-(B51) provided in Appendix B.3 (with the simplifying parameter a_{18} set to zero as explained in Appendix B.3) were solved simultaneously with (C1) to obtain an expression for $\frac{\Delta q_c(s)}{\Delta P_{a,CO2}(s)}$ using the "Eliminate" function in Mathematica. The most complete expression (i.e., with the highest orders of s in the numerator and denominator) provided by Mathematica was selected and written with the flowrate and $PaCO_2$ as fractions of their baseline values:

$$\frac{\Delta q_c^*}{\Delta P_{a,CO2}^*} = \frac{\Delta q_c}{\Delta P_{a,CO2}} \times \frac{\bar{P}_{a,CO2}}{\bar{q}_c} \tag{C2}$$

where the star superscript denotes a value as a fraction of its baseline value. Due to the complexity of the overall transfer function in terms of all its parameters, it could only be obtained with the numerical values of its constant parameters (Table 4.1) substituted in:

$$\frac{\Delta q_c^*}{\Delta P_{a,CO2}^*} = \{3.11G_a(5.66\times 10^{133} + 3.31\times 10^{133}s + 2.90\times 10^{132}s^2 - 1.22\times 10^{131}s^3)\}$$
$$/\{(3.73\times 10^{134} + 5.30\times 10^{134}s + 1.74\times 10^{134}s^2 + 2.09\times 10^{133}s^3 + 8.16\times 10^{131}s^4)(1 + s^2\tau_{a1}^2 + s\tau_{a2})\} \qquad \text{(C3)}$$

The order of the numerator is three and the order of the denominator is six.

C.2. Investigating resting state and 5% CO_2 protocol $PetCO_2$-BOLD impulse response acceptance

The derived $PetCO_2$-BOLD IRs were accepted or rejected based on three criteria: (1) a “bootstrapping” method, (2) physiological plausibility, and (3) goodness of fit to the physiological model (see Section 5.2.4). The rejected RS and 5% CO_2 protocol are categorised per criteria and subject in Table C.1. Here, IR acceptance consistency for different data collection protocols and over brain hemispheres/regions is investigated.

Regarding different data collection protocols, many of the RS IRs (57.9%) are rejected, whereas only few of the 5% CO_2 protocol IRs (5.93%) are rejected. However, it should be noted that the RS IRs were rejected based on all three criteria, whereas the 5% CO_2 protocol IRs could only be rejected based on two of the criteria, as the “bootstrapping method was not found suitable (see Section 5.2.4). The rejected 5% CO_2 protocol IRs are dominated by the caudate, where 10 out of the 23 caudate IRs (43.5%) are rejected, compared to zero to three IRs rejected for the other brain regions. This discrepancy between brain regions may be due to lower SNR in the caudate, as fewer voxels are averaged in the caudate compared to other brain regions (Figure 5.4).

Regarding brain hemisphere level IRs, none of the 5% CO_2 protocol IRs are rejected. Again, this may be influenced by the fact that the "bootstrapping" method could not be applied to the 5% CO_2 protocol IRs. In 16 out of the 22 (72.7%) RS hemisphere pairs, both the left and right IRs are either accepted or rejected based on the criteria described in Section 5.2.4), so the IR derivation method is consistent over hemispheres in the majority of cases. Of the six RS hemisphere pairs where only one IR was accepted, two are control subjects, whereas four are postpartum subjects. A history of pregnancy may therefore have affected dCVR in only one hemisphere or differently between hemispheres, although it is not expected, since none of the postpartum subjects have a history of pathology during their pregnancies. Alternatively, an IR from one one hemisphere being accepted may be due to different levels of noise in the hemisphere level BOLD-fMRI time series (e.g., due to artefacts or difficulty with subject-specific spatial registration to the MNI template), and this will require further investigation.

Also of note, the "bootstrapping" method appears to be effective in rejecting IRs that would be classified as "non-physiological" and/or produce a poor physiological model fit. For the RS hemisphere level IRs, all the IRs classified as "non-physiological" and all bar two IRs (from the same subject) with NMSE > 0.3 from fitting to the physiological model are already rejected by the "bootstrapping" method. For the RS brain region level IRs, only eight of the 35 IRs classified as "non-physiological" (22.9%) were not already rejected by the "bootstrapping" method, and only three of the 28 with NMSE > 0.3 from fitting to the physiological model (10.7%) were not already rejected by the "bootstrapping" method. It may therefore be sufficient to automate $PetCO_2$-BOLD IR rejection with the "bootstrapping" method without the need for additional classification according to physiological plausibility or goodness of fit to the physiological model in future studies.

Table C.1. IRs that were rejected based on (1) the "bootstrapping" method (indicated by shaded cells), (2) classification as "non-physiological" (indicated by "NP"), and (3) NMSE > 0.3 from fitting to the physiological model (indicated by diagonal line through cell) per subject. Blue indicates a control subject; orange indicates a postpartum subject. LH: left hemisphere, RH: right hemisphere, C: control, P: postpartum.

Subject	2	3	4	7	8	11	18	20	21	25	6	9	10	12	13	14	15	16	17	19	22	23	24
Group	C	C	C	C	C	C	C	C	C	C	P	P	P	P	P	P	P	P	P	P	P	P	P
Resting state data																							
LH			-			▨ NP	╱	▨ NP ╱		▨	▨	▨		▨ NP	▨		▨						
RH		▨	-		▨	▨ NP	╱	▨ NP ╱		▨	▨	▨	▨	▨ NP	▨ ╱		▨			▨ NP	▨		▨
Caudate	▨	▨	-	▨	▨	▨ NP ╱	▨	NP ╱	▨	▨	▨	▨	▨	▨ NP ╱			NP ╱			▨ NP	▨	▨	
Cerebellum	▨	NP	-			▨ NP ╱		NP ╱		▨	▨	▨	▨	▨ NP	▨		▨		▨	▨	▨		
Frontal	▨	▨	-	▨		▨	╱	▨ NP ╱		▨	▨ ╱	▨		▨	▨ ╱		▨			▨	▨		▨
Insula	▨		-	▨	▨	▨ NP ╱	▨	▨ NP ╱		▨	▨	▨	▨		▨ ╱		▨ NP ╱						
Occipital	▨		-		▨	▨ NP	╱	▨ ╱		▨	▨		▨	NP	▨ ╱		▨			▨ NP			
Parietal	▨	▨	-		╱	▨ NP	NP	▨ ╱		▨	▨	▨	▨	▨	▨		▨			▨	▨		▨
Putamen	▨		-	▨ NP	▨	▨ NP	▨ ╱	▨	▨	NP	▨	▨	▨		▨ NP ╱		▨ NP ╱						
Temporal	▨		-		▨	▨ NP	╱	NP ╱		▨	▨	▨ ╱	▨	▨ NP	▨		▨			▨	▨		
Thalamus			-	▨	▨	▨	▨	▨ ╱	▨		▨	▨		▨	▨ ╱	▨	▨ NP ╱			▨ NP	▨		
5% CO_2 data																							
LH																							
RH																							
Caudate		NP				NP	NP	NP ╱	NP		NP ╱	NP ╱	NP ╱		NP ╱						NP ╱		
Cerebellum											╱	╱	╱										
Frontal																							
Insula																							
Occipital																							
Parietal											NP												
Putamen																							
Temporal																							
Thalamus													NP										

C.3. NMSE from physiological model fit to $PetCO_2$-BOLD impulse responses

The NMSE from fitting each data-based IR to the physiological dCVR model are provided in Table C.2 and Table C.3 for the RS and 5% CO_2 protocol data respectively. Only NMSE from fitting to the physiological dCVR model is presented here; refer to Table C.1 in Appendix C.2 for a breakdown of individual IR acceptance/exclusion per acceptance/exclusion criteria (see Section 5.2.4).

Table C.2. NMSE for model fit to resting state $PetCO_2$-BOLD impulse responses. Shaded cells indicate NMSE > 0.3. LH: Left hemisphere, RH: Right hemisphere, Ca: Caudate, Ce: Cerebellum, Fr: Frontal, In: Insula, Oc: Occipital, Pa: Parietal, Pu: Putamen, Te: Temporal, Th: Thalamus.

Sub	2	3	4	6	7	8	9	10	11	12	13	14	15	16	17	18	19	20	21	22	23	24	25
LH	0.202	0.197	-	0.198	0.256	0.198	0.227	0.131	0.266	0.148	0.253	0.0681	0.257	0.112	0.057	0.358	6.88e-5	0.699	0.192	0.0152	0.118	0.167	0.144
RH	0.214	0.103	-	0.132	0.219	0.174	0.284	0.126	0.167	0.150	0.301	0.0742	0.115	0.124	0.0522	0.436	0.203	0.795	0.167	6.90e-3	0.143	0.157	0.112
Ca	0.198	0.00533	-	0.619	0.132	0.0732	8.13e-3	0.123	0.442	0.733	0.172	1.58e-4	0.438	0.0813	5.66e-3	0.186	0.294	0.730	0.191	0.138	0.108	1.29e-3	0.163
Ce	0.196	0.112	-	0.093	0.276	0.087	0.293	0.0664	0.379	0.235	0.101	0.0421	0.214	0.119	0.0707	0.238	3.47e-3	0.448	0.181	0.210	0.120	0.166	0.196
Fr	0.209	0.135	-	0.356	0.224	0.531	0.212	0.172	0.144	0.107	0.502	0.0892	0.277	0.111	0.0368	0.332	0.0285	0.891	0.219	0.0584	0.146	0.147	0.0469
In	0.138	4.57e-5	-	0.0284	0.135	0.0585	0.205	0.0832	0.528	0.0346	0.348	0.0196	0.305	0.0657	0.0854	0.228	1.62e-4	0.545	0.0348	5.85e-3	0.130	0.0392	0.0119
Oc	0.238	0.201	-	0.165	0.218	0.117	0.256	0.122	0.266	0.194	0.302	0.0559	0.186	0.0988	0.0761	0.431	0.176	0.383	0.129	2.83e-5	0.116	0.177	0.227
Pa	0.183	0.131	-	0.208	0.240	0.303	0.293	0.165	0.195	0.0425	0.255	0.111	0.154	0.148	0.0478	0.495	1.69e-3	0.639	0.195	0.0281	0.124	0.205	0.181
Pu	0.137	3.18e-5	-	0.135	0.536	0.0843	0.186	0.112	0.236	0.0437	0.588	0.0161	0.421	0.106	0.0815	0.181	0.0120	0.232	0.0298	0.0168	0.150	0.0298	0.101
Te	0.195	0.197	-	0.0695	0.209	0.155	0.349	0.116	0.241	0.219	0.246	0.0668	0.151	0.143	0.0934	0.370	0.0224	0.672	0.149	7.88e-3	0.132	0.138	0.0899
Th	0.161	0.0570	-	0.0621	0.0746	0.0958	0.196	0.0842	0.0376	0.0285	0.338	0.0145	0.406	0.0286	0.0770	0.225	0.0589	0.408	0.101	3.33e-4	0.119	0.0119	3.59e-4

Table C.3. NMSE for model fit to 5% CO_2 protocol $PetCO_2$-BOLD impulse responses. Shaded cells indicate NMSE > 0.3. LH: Left hemisphere, RH: Right hemisphere, Ca: Caudate, Ce: Cerebellum, Fr: Frontal, In: Insula, Oc: Occipital, Pa: Parietal, Pu: Putamen, Te: Temporal, Th: Thalamus.

Sub	2	3	4	6	7	8	9	10	11	12	13	14	15	16	17	18	19	20	21	22	23	24	25
LH	0.0612	0.0884	0.0174	2.6e-05	0.0715	0.0156	0.0657	0.118	0.126	0.0275	0.0407	0.0667	0.117	0.0939	0.0307	0.0722	0.128	0.0551	0.108	6.16e-3	0.0555	0.0942	4.06e-3
RH	0.0206	9.96e-4	3.18e-5	2.30e-5	0.0154	5.21e-3	0.0147	0.159	4.74e-5	9.50e-5	0.0221	0.0187	7.92e-4	7.39e-3	2.15e-3	3.84e-4	8.71e-3	1.33e-3	1.12e-4	2.81e-4	4.60e-3	0.0370	1.18e-4
Ca	9.4e-5	0.440	4.36e-5	0.348	0.0279	1.53e-3	0.368	0.466	0.0844	8.37e-3	0.362	8.27e-5	4.00e-4	2.00e-3	1.78e-4	0.251	1.35e-4	0.503	0.0596	0.430	8.10e-3	0.0196	7.71e-3
Ce	0.0461	0.106	0.0700	0.558	0.111	0.0116	0.398	0.301	0.154	0.0396	0.0280	0.0611	0.0893	0.128	0.123	0.182	0.147	0.0983	0.187	0.217	0.0603	0.131	0.126
Fr	0.0579	0.0974	0.0144	9.06e-6	0.0723	0.0211	9.04e-3	0.0427	0.120	0.0133	0.0437	0.0752	0.117	0.0951	0.0239	0.0370	0.0919	0.0307	0.112	5.99e-3	0.0379	0.104	5.18e-3
In	0.0333	2.04e-3	4.73e-5	0.0325	0.0196	9.95e-3	1.02e-4	3.48e-3	3.20e-4	2.81e-3	0.0270	0.0347	1.11e-4	0.0159	0.0236	4.75e-5	0.0225	4.93e-3	2.60e-3	3.38e-4	6.29e-3	0.0533	0.0331
Oc	0.0424	0.0374	0.0420	0.0749	0.126	0.0424	0.0702	0.114	0.0424	0.101	5.28e-3	0.0471	0.0901	8.16e-4	0.0424	0.0374	0.0420	0.0749	0.126	0.0423	0.0702	0.114	0.0424
Pa	0.0476	0.0573	0.0688	0.129	0.125	0.0238	0.0770	0.116	0.02156	0.128	3.92e-3	0.0661	0.107	0.0739	0.0476	0.0573	0.0688	0.129	0.125	0.0238	0.0770	0.116	0.0216
Pu	0.0335	6.75e-4	7.92e-3	8.01e-3	0.0176	0.0174	5.20e-5	3.38e-4	1.16e-3	5.57e-3	0.0323	0.0463	3.44e-3	0.0190	0.0159	1.28e-4	0.0201	1.45e-3	3.17e-5	8.11e-5	0.0256	0.0518	0.0175
Te	0.0791	0.0715	0.0320	0.161	0.0717	0.0151	0.0562	0.047	0.129	1.18e-3	0.0443	0.0909	0.0875	0.100	0.0424	0.0702	0.115	0.0535	0.0849	0.0317	0.0541	0.104	6.06e-3
Th	0.0206	9.96e-4	3.18e-5	2.30e-5	0.0154	5.21e-3	0.0147	0.159	4.74e-5	9.50e-5	0.0221	0.0187	7.92e-4	7.39e-3	2.15e-3	3.84e-4	8.71e-3	1.33e-3	1.12e-4	2.81e-4	4.60e-3	0.0370	1.18e-4